Transactions of the ASME

FLUIDS ENGINEERING DIVISION
Technical Editor
FRANK M. WHITE (1984)
Executive Secretary
L. T. NELSON (1984)
Calendar Editor
M. F. ACKERSON

Associate Editors
Fluid Machinery
AWATEF A. HAMED (1985)
WILLIAM E. THOMPSON (1984)
Fluid Measurements
THEODORE R. HEIDRICK (1984)
Fluid Mechanics
SHLOMO CARMI (1984)
KIRTI N. GHIA (1984)
THOMAS J. MUELLER (1985)
HASSAN M. NAGIB (1986)
Fluid Transients
M. HANIF CHAUDHRY (1983)
Multiphase Flow
JOHN T. JUREWICZ (1985)
OKITSUGU FURUYA (1984)
Review Articles
RICHARD A. BAJURA (1985)

FOREIGN CORRESPONDENTS
Europe and Russia
JACQUES CHAUVIN
Europe and Russia
JOHN H. HORLOCK
India and Middle East
ARUN PRASAD
Japan and China
YASUTOSHI SENOO

BOARD ON COMMUNICATIONS
Chairman and Vice President
K. N. REID, Jr.

Members-at-Large
W. BEGELL, J. T. COKONIS, W. G. GOTTENBERG, D. KOENIG, M. KUTZ, F. LANDIS, R. E. NICKELL, J. ORTLOFF, C. PHILLIPS, H. C. REEDER

President, G. KOTNICK
Executive Director
PAUL ALLMENDINGER
Treasurer,
ROBERT A. BENNETT

PUBLISHING STAFF
Mng. Dir. Publ., J. J. FREY
Dep. Mng. Dir. Publ.,
JOS. SANSONE
Managing Editor,
CORNELIA MONAHAN
Editorial Production Assistant,
MARISOL ANDINO

The Journal of Fluids Engineering (ISSN 0098-2202) is published quarterly for $100 per year by The American Society of Mechanical Engineers, 345 East 47th Street, New York, NY 10017. Second class postage paid at New York, NY and additional mailing offices. POSTMASTER: Send address changes to The Journal of Fluids Engineering, c/o THE AMERICAN SOCIETY OF MECHANICAL ENGINEERS, 22 Law Drive, Box 2300, Fairfield, NJ 07007-2300.
CHANGES OF ADDRESS must be received at Society headquarters seven weeks before they are to be effective. Please send old label and new address.
PRICES: To members, $24.00, annually: to nonmembers, $100. Add $6.00 for postage to countries outside the United States and Canada.
STATEMENT from By-Laws. The Society shall not be responsible for statements or opinions advanced in papers or . . . printed in its publications (B7.1, Par. 3),

COPYRIGHT © 1984 by The American Society of Mechanical Engineers. Reprints from this publication may be made on condition that full credit be given the TRANSACTIONS OF THE ASME, JOURNAL OF FLUIDS ENGINEERING and the author, and date of publication be stated.

INDEXED by the Engineering Index, Inc.

Journal of Fluids Engineering

Published Quarterly by The American Society of Mechanical Engineers

VOLUME 106 • NUMBER 4 • DECEMBER 1984

(Contents continued on page 409)

Downloaded 03 Jun 2010 to 171.66.16.159. Redistribution subject to ASME license or copyright; see http://www.asme.org/terms/Terms_Use.cfm

Contents (Continued)

Downloaded 03 Jun 2010 to 171.66.16.159. Redistribution subject to ASME license or copyright; see http://www.asme.org/terms/Terms_Use.cfm

Tetsuo Fujimoto
Professor,
Department of Electronic-Mechanical Engineering,
University of Nagoya, Furocho,
464 Nagoya, Japan

Masaru Usami
Research Associate,
Department of Mechanical Engineering,
University of Mie,
Kamihamacho, 514 Tsu, Japan

Rarefied Gas Flow Through a Circular Orifice and Short Tubes

Rarefied gas flow through a circular orifice and short tubes has been investigated experimentally, and the conductance of the aperture has been calculated for Knudsen number between 2×10^{-4} and 50. The unsteady approach was adopted, in which the decay of pressure in an upstream chamber was measured as a function of time. For flow with high pressure ratio, empirical equations of the conductance are proposed as a function of Reynolds number, or Knudsen number, and length-to-diameter ratio of the apertures.

1 Introduction

Many studies of rarefied gas flow through a circular orifice or a short tube have been reported over the past years. These studies form the basis of vacuum science and are especially indispensable to works of molecular beams or space technology. In a transition region, however, we have not yet found an analytical method that would lead to effective solutions. Furthermore, from the experimental point of view, there have been appreciable differences between existing data of many investigators as well as fluctuations in a series of data of one author. Those are mainly due to the difficulty caused by measurement of a small amount of gas flow through an aperture, and preclude establishment of the unified relation between the conductance and various physical conditions. The purpose of this paper is not only to supplement existing data, especially for short tubes of length-to-diameter ratio below 13, but also supply unified data and empirical equations over the whole range of rarefied gas flow.

To obtain the mass-flow rate, we have two fundamentally different approaches: steady approach and unsteady approach. In the former, establishing steady flow between the upstream and the downstream of an aperture, one measures the mass-flow by the rate of gas supply. In the latter, the decay of pressure caused by gas effusion through the aperture from a source chamber is measured at specified time interval and the flow rate is determined from a derivative of the decay curve. For necessity of the differentiation of the decay, a pressure measuring device (which operates continuously with high accuracy) is required. This is the reason why the approach has rarely been adopted in previous investigations. In the steady approach, on the other hand, the mass-flow measurement is also very difficult. When a burette mass-flow meter is used, very small amounts of gas at atmospheric pressure at the inlet must be measured in a near-free-molecular region. Various errors, therefore, arise from adhesion of an oil on the burette wall and/or a drift of gas temperature and pressure during the measurement. In short, the over-all error usually amounts to more than 10 percent.

To avoid the numerous errors which accompany the steady approach, the unsteady one is adopted in the present investigation. As mentioned above, it is necessary to use a highly accurate device. The Baratron diaphragm gauge was found to satisfy the requirements. In the unsteady approach, however, the outgassing from a surface of the wall has worse influence on the measurement than in the steady one. This is because the derivative of the pressure decay curve is very sensitive to the outgassing. We have tried several ways to suppress the effect, as will be mentioned in the following section. To increase the accuracy of sampling data, an automatic measurement with a microcomputer is employed. In this manner, a series of data over all region from continuum to free-molecular flow involving relatively small errors has been obtained by a run of the experiment in a short time. The final results on the conductance scatter less than those by the steady approach. This makes it possible to compare the conductance of the apertures of various geometry.

2 Experimental Apparatus

A schematic diagram of the apparatus is shown in Fig. 1. The vacuum tank, 60 cm in diameter, is divided by a partition into two parts: an expansion chamber (downstream), 160 cm long, and a source chamber (upstream), 40 cm long. An orifice or a short tube is mounted on the center of the partition. The two chambers are connected with a tube in which a bypass-valve is installed. The wall of the tank is nickel-plated to reduce the outgassing from the surface. Every test is carried out with air which is supplied through a drier filled with silicagel. The source pressure is measured mainly with two Baratron diaphragm gauges (310BHS-1 and 220BHS-100, MKS Instruments), which operate in the range from 1.33×10^{-3} to 133 Pa and from 13.3 to 1.33×10^{4} Pa, respectively. Using these gauges, we obtain a highly accurate measurement within 0.2 percent error of reading above 0.1 Pa, which is the lowest pressure in the present experiment. Sixteen or 40 or 400 ms is selected for the response time of Baratron gauges. The output of these gauges is fed into a digital volt meter with BCD output (Type 2502, YEW), and processed by a microcomputer (TK80BS, NEC). An ionization gauge, a Pirani gauge, and an oil U-tube manometer are used as

Contributed by the Fluids Engineering Division for publication in the JOURNAL OF FLUIDS ENGINEERING. Manuscript received by the Fluids Engineering Division, November 30, 1982.

Copyright © 1984 by ASME

Downloaded 02 Jun 2010 to 171.66.16.91. Redistribution subject to ASME license or copyright; see http://www.asme.org/terms/Terms_Use.cfm

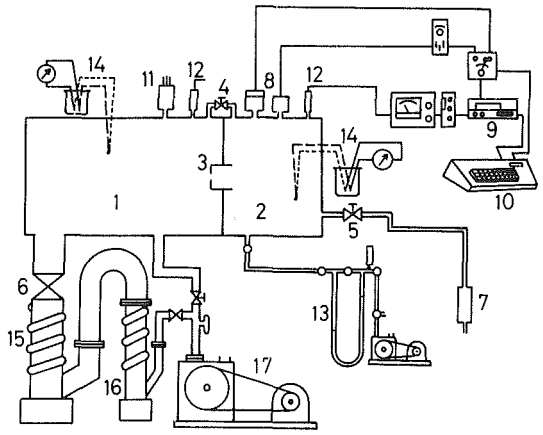

1. Expansion chamber
2. Source chamber
3. Test aperture
4. Bypass-valve
5. Leak valve
6. Main valve
7. Drier with silicagel
8. Baratron vacuum gauge
9. Digital volt meter
10. Microcomputer
11. Ionization gauge
12. Pirani gauge
13. Oil U-tube manometer
14. Thermocouple
15. Diffusion pump
16. Booster pump
17. Rotary pump

Fig. 1 Schematic diagram of the apparatus

supplements. Copper-constantan thermocouples are used to measure gas temperature in the chambers.

Several kinds of apertures (as shown in Table 1) are tested. A piece of thickness gauge stock, or a brass plate through which a circular hole is drilled, is sandpapered and glued on an element that is screwed with O-ring seal in a threaded portion of the partition. The diameter of the aperture is determined by the average of measurements in four or eight directions.

3 Methods of Measurement

3.1 Principles of the Unsteady Approach. Assuming a perfect gas with constant temperature, the mass-flow rate $\dot{m}$ is related to the flow rate $\dot{Q}$ which is used customarily in the vacuum science as follows:

$$\dot{Q}=P_s\dot{V}=\dot{m}RT_s, \tag{1}$$

where $\dot{V}$ is volume-flow rate, R is the gas constant, P_s and T_s are gas pressure and temperature in the source chamber, respectively. In this paper the unit of $\dot{Q}$ is [Pa•m^3]. When the gas effuses out through an aperture from the chamber, the rate of pressure decay is given by:

Table 1 Apertures used in tests

Diameter d (mm)	Length l (mm)	l/d
2.02±0.01	0.05±0.005	0.025±0.003
1.03±0.01	0.10±0.005	0.097±0.006
3.00±0.01	0.29±0.01	0.097±0.004
1.49±0.01	0.28±0.01	0.188±0.008
2.01±0.01	0.50±0.01	0.249±0.007
1.02±0.01	0.28±0.01	0.275±0.013
2.52±0.01	1.02±0.01	0.405±0.006
2.00±0.01	0.99±0.01	0.495±0.008
2.51±0.01	2.05±0.01	0.817±0.008
1.52±0.01	1.98±0.01	1.30 ±0.02
3.01±0.02	3.97±0.02	1.32 ±0.02
2.55±0.02	3.99±0.02	1.56 ±0.03
2.53±0.04	8.03±0.02	3.17 ±0.06
2.51±0.08	16.0 ±0.05	6.37 ±0.23
3.03±0.10	38.4 ±0.1	12.7 ±0.46
10.1 ±0.1	128.3 ±0.1	12.7 ±0.14

$$-dP_s/dt=\dot{m}RT_s/V_s, \tag{2}$$

where V_s is the volume of the chamber. Therefore, we have

$$\dot{Q}=-V_s(dP_s/dt). \tag{3}$$

On the other hand, the conductance F is defined by:

$$F=\dot{Q}/(P_s-P_e), \tag{4}$$

where P_e is the pressure in the expansion chamber. From these relations, it is basically possible to estimate the conductance by measuring the rate of pressure decay in the source chamber, the volume of the chamber, and the pressure difference between the upstream and the downstream.

In the present paper the pressure ratio is defined by:

$$P_r=(P_s-P_e)/P_s=\Delta P/P_s. \tag{5}$$

The experiments are divided into two cases according to the range of the pressure ratio. One is the case for $P_r > 0.99$, or $P_s/P_e > 100$; the downstream pressure can be neglected. The other is the case for Pr > 0.5, or $P_s/P_e > 2$; the downstream pressure should be considered.

3.2 Experimental Procedure for Cases of High Pressure Ratio

3.2.1 Situation Where the Outgassing From the Wall Can Be Ignored. For the flow from the transition to the continuum region, the source pressure is so high that the mass-flow rate is much larger than the rate of the outgassing from the wall of the source chamber. This situation makes the measurement comparatively straightforward. After a sufficient vacuum is achieved in the tank, the bypass-valve is closed and dry air is fed into the source chamber, through a leak valve, until desired pressure is attained. Then the leak

Nomenclature

A_0 = area of an aperture
C_D = discharge coefficient
d = diameter of an aperture
F = conductance
F_a = apparent conductance
F_{fm} = free-molecular conductance
F_{fm0} = theoretical free-molecular conductance of an orifice
Kn = Knudsen number
l = length of an aperture
$\dot{m}$ = mass-flow rate
$\dot{m}_{max}$ = maximum flow rate through an ideal nozzle
M = molecular weight
P_e = pressure in the expansion chamber (downstream pressure)
P_0 = equilibrium pressure
P_r = $(P_s-P_e)/P_s = \Delta P/P_s$ = pressure ratio
P_s = pressure in the source chamber (upstream pressure)
$\dot{Q}$ = flow rate
$\dot{Q}_a$ = apparent flow rate
$\dot{Q}_{og}$ = rate of outgassing
R = gas constant
Re = Reynolds number
t = time
T_s = temperature in the source chamber
u = mean flow velocity
v_a = mean molecular velocity
$\dot{V}$ = volume-flow rate
V_e = volume of the expansion chamber
V_s = volume of the source chamber
γ = ratio of specific heats
λ_s = mean free path in the source chamber
μ_s = coefficient of viscosity in the source chamber
ρ_s = density in the source chamber

Downloaded 02 Jun 2010 to 171.66.16.91. Redistribution subject to ASME license or copyright; see http://www.asme.org/terms/Terms_Use.cfm

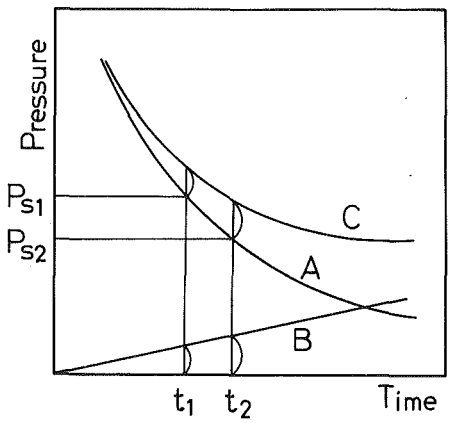

Fig. 2 Pressure decay curve in the source chamber. A: Decrease of pressure caused by only gas effusion. B: Increase of pressure by outgassing. C: Apparent change of pressure observed. Superimposing of curve A and B makes curve C.

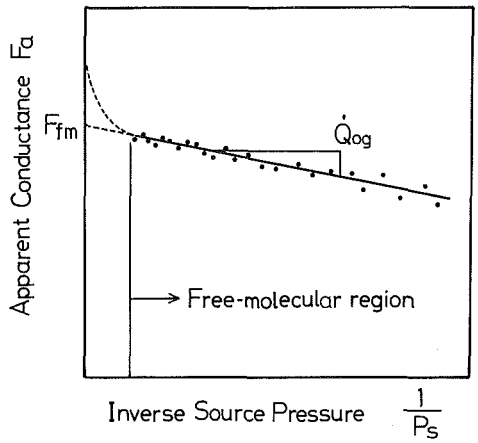

Fig. 3 Relation between the apparent conductance and the inverse source pressure

valve is closed and the pressure starts to fall. It is recorded intermittently and processed by a microcomputer.

Now, let us suppose the case where the source pressure P_{s1} at time t_1 decreases to P_{s2} at t_2, as shown in Fig. 2 by curve A. For the short time interval $\Delta t = t_2 - t_1$, equation (3) is approximated by:

$$\dot{Q} = V_s(P_{s1} - P_{s2})/(t_2 - t_1), \tag{6}$$

where $\dot{Q}$ is the flow rate at the state of the mean source pressure, $P_s = (P_{s1} + P_{s2})/2$. When the downstream pressure P_e is negligible compared with P_s, the conductance of the aperture F is given by:

$$F = \dot{Q}/P_s = V_s[(P_{s1} - P_{s2})/(t_2 - t_1)] \cdot 2/(P_{s1} + P_{s2}). \tag{7}$$

Since the flow rate is very small compared with the capacity of the source chamber, the decay of the pressure is so slow that the temperature in the source chamber can be assumed to be constant.

3.2.2 Situation Where the Outgassing Should be Considered. Near the free-molecular region, the outgassing from the wall cannot be neglected. This situation is illustrated in Fig. 2. In the figure, curve A shows the decay of the pressure caused by only gas effusion, and B shows the increase of the pressure by the outgassing. Curve C, plotted by superimposing these two curves, shows the apparent change of the pressure observed. The apparent conductance calculated from curve C is lower than the real one, especially for the lower source pressure, or the less mass-flow. The experiment should be performed at low temperature to decrease the outgassing. In addition to that, we adopt the following two steps to overcome it:

(*a*) Correction of Conductance for the Outgassing. The correction of data is carried out on the supposition that the rate of the outgassing does not change with time, and the conductance is constant in the free-molecular region. In this region, denoting the real flow rate by $\dot{Q}$ and the rate of the outgassing from the wall by $\dot{Q}_{og}$, the rate of the pressure decay dP_s/dt is given by:

$$V_s(dP_s/dt) = \dot{Q}_{og} - \dot{Q}. \tag{8}$$

The apparent flow rate and the apparent conductance are estimated by means of the rate of pressure decay as follows:

$$\dot{Q}_a = -V_s(dP_s/dt) \tag{9}$$

and

$$F_a = \dot{Q}_a/P_s = (\dot{Q} - \dot{Q}_{og})/P_s. \tag{10}$$

Therefore, the real conductance, $F = \dot{Q}/P_s$, is related to F_a by:

$$F_a = F - \dot{Q}_{og}/P_s. \tag{11}$$

Since F in this region and $\dot{Q}_{og}$ may be considered to be independent of the source pressure, F_a is a linear function of the reciprocal of the pressure, $1/P_s$, as shown in Fig. 3. Using all the experimental data obtained within the fully-free-molecular region, we determine $\dot{Q}_{og}$, the slope of the line in the figure, by a least-squares method, and then correct the results of a series of measurements for near-free-molecular region in terms of $\dot{Q}_{og}$.

The rate of the outgassing may be affected by the wall temperature and/or gas pressure. In these experiments, however, the wall temperature of the vacuum tank is kept constant. On the other hand, since the correction value for the outgassing is determined in the free-molecular-flow region, or at very low pressure, the rate of the outgassing for high source pressure may be different from that value. Because the relative rate of the outgassing with respect to the real flow rate becomes smaller as the source pressure rises, there is little possibililty of causing large errors by using the constant correction value.

(*b*) Adoption of a Multi-Aperture System. A multi-aperture system, composed of five or more apertures, is used to reduce the relative influence of the outgassing per one aperture. Since the distance between centers of the apertures is larger than five aperture-diameters, we are able to assume that the flows through each aperture have no interference with one another.

3.3 Experimental Procedure for Cases of Low Pressure Ratio. When the pressure ratio is low and the downstream pressure P_e cannot be neglected, the following procedure is adopted. At first, dry air is fed into the source chamber until the desired pressure is attained (in the same manner as the case for high pressure ratio). Then the main valve, which isolates the expansion chamber from the vacuum pumps, is closed at the same time as the leak valve is closed. In this case, the decrease of the source pressure causes the increase of the downstream pressure. After the decay of the source pressure for the prescribed region is attained, the bypass-valve is opened and the pressure in the two chambers is allowed to come to equilibrium. The downstream pressure P_e at any instant of the measurement is calculated by the following equation:

$$P_e = [P_0(1 + V_e/V_s) - P_s]/(V_e/V_s), \tag{12}$$

where P_0 is the equilibrium pressure; V_s and V_e are the volume of the source chamber and the expansion chamber, respectively. Now, suppose the source pressure P_{s1} and the downstream pressure P_{e1} at time t_1 change to P_{s2} and P_{e2} at

Downloaded 02 Jun 2010 to 171.66.16.91. Redistribution subject to ASME license or copyright; see http://www.asme.org/terms/Terms_Use.cfm

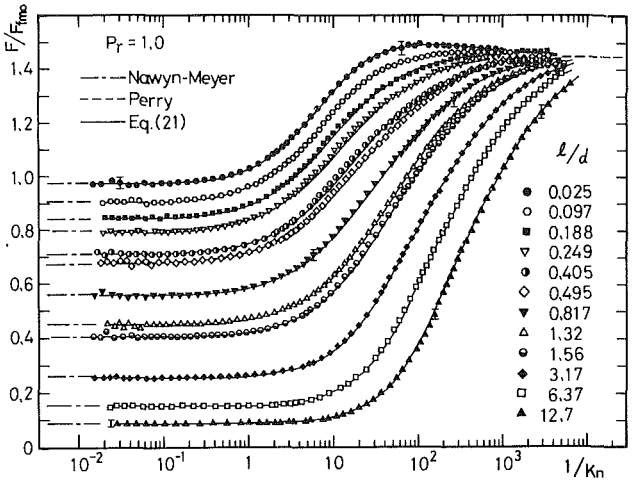

Fig. 4 Dependence of normalized conductance on inverse Kn-number for cases of high pressure ratio. Uncertainty: F/F_{fmo} ±2.0 percent ±0.01, 1/Kn ±1.0 percent (20:1 odds).

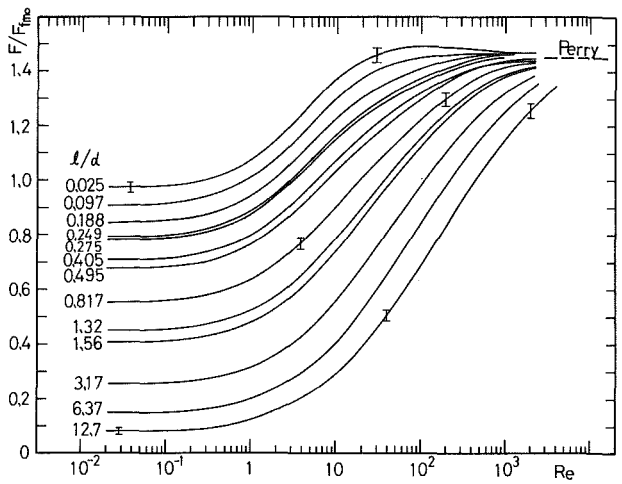

Fig. 5 Dependence of normalized conductance on Re-number for cases of high pressure ratio. Uncertainty: F/F_{fmo} ±2.0 percent ±0.01, Re ±3.0 percent (20:1 odds).

time t_2, respectively. For the short time interval $\Delta t = t_2 - t_1$), equation (4) is approximated by:

$$F = \frac{-V_s(P_{s1}-P_{s2})/(t_1-t_2)}{(P_{s1}+P_{s2})/2-(P_{e1}+P_{e2})/2}. \tag{13}$$

4 Experimental Results and Considerations

4.1 Conductance for the Cases of High Pressure Ratio. Figures 4 and 5 represent the dependence of aperture conductance normalized with the theoretical free-molecular conductance of an orifice, F_{fm0}, on inverse Knudsen number 1/Kn and Reynolds number Re, respectively:

$$F_{fm0} = (1/4)v_a A_0 = 3638 A_0 \sqrt{T_s/M} \quad [\mathrm{cm}^3/\mathrm{s}], \tag{14}$$

$$\mathrm{Kn} = \lambda_s/d, \tag{15}$$

λ_s : molecular mean free path

$$= \mu_s/[0.499 v_a P_s/(RT_s)], \tag{16}$$

v_a : mean molecular speed

$$= \sqrt{8RT_s/\pi}, \tag{17}$$

$$\mathrm{Re} = ud\rho_s/\mu_s = 0.501(1/\mathrm{Kn})(1/F_{fm0})\dot{V}, \tag{18}$$

or, if the condition $P_s >> P_e$ is satisfied,

$$\mathrm{Re} = 0.501(1/\mathrm{Kn})(F/F_{fm0}). \tag{19}$$

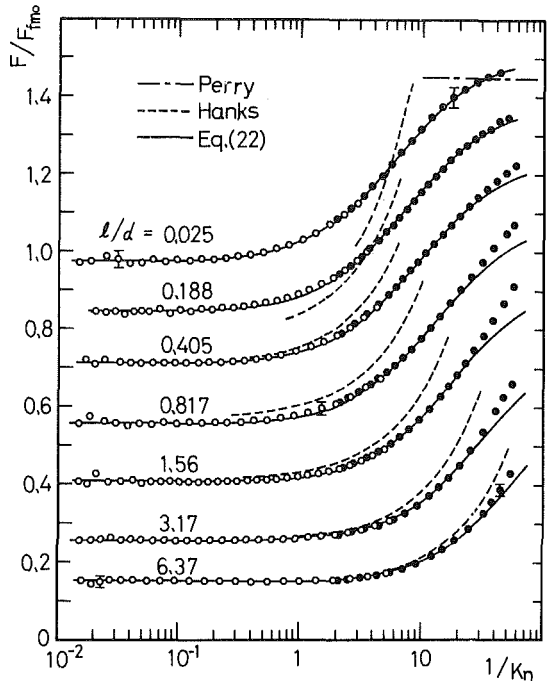

Fig. 6 Comparison between conductances obtained by two different methods. ●: Results without any consideration for outgassing. ○: Results with correction for outgassing obtained by a multi-aperture system. Uncertainty: F/F_{fmo} ±2.0 percent ±0.01, 1/Kn ±1.0 percent (20:1 odds).

In these figures the conductance changes smoothly from the free-molecular region to the continuum region. The experimental results agree well with the theoretical prediction by Nawyn-Meyer [1], or by Clausing [2], at the free-molecular region. Thus, the correction for the outgassing has been proved to be effective. They also approach to the semi-empirical value by Perry [3] at the continuum region. In Fig. 6, being part of Fig. 4, black dots represent the results obtained by a single-aperture; white dots represent the results by a multi-aperture system. Since there is no difference between them in the coexisting region, the flows through the multi-aperture have no interference with one another. In Fig. 6, the semi-empirical curves by Hanks [4], which are applied to short tubes in the transition region, are drawn. Their agreement with the present experimental results is rather poor. In a few cases with large l/d, however, the agreement is fair.

Uncertainty of data is mainly due to the deviation of the aperture from a true round, the error of the chamber volume and the error of the pressure gauge.

4.2 Effects of Downstream Pressure. The results of normalized conductance obtained in the situation where the downstream pressure cannot be neglected are shown in Figs. 7, 8, and 9, as a function of 1/Kn. Figures 10, 11, and 12 show the conversion of the conductance to the nondimensional mass-flow rate, or discharge coefficient C_D, which is normalized by the maximum flow rate [equation (20)] for an adiabatic expansion through an ideal nozzle [5].

$$\dot{m}_{\max} = \frac{A_0 P_s}{\sqrt{RT_s}} \sqrt{\gamma \left(\frac{2}{\gamma+1}\right)^{\frac{\gamma+1}{\gamma-1}}} \tag{20}$$

where γ is ratio of specific heats and is 1.4 for air.

In the case that length-to-diameter ratio of an aperture l/d is 1.3 (Fig. 10), the difference of mass-flow rate between different pressure ratios disappears rapidly as the inverse Kn-

Downloaded 02 Jun 2010 to 171.66.16.91. Redistribution subject to ASME license or copyright; see http://www.asme.org/terms/Terms_Use.cfm

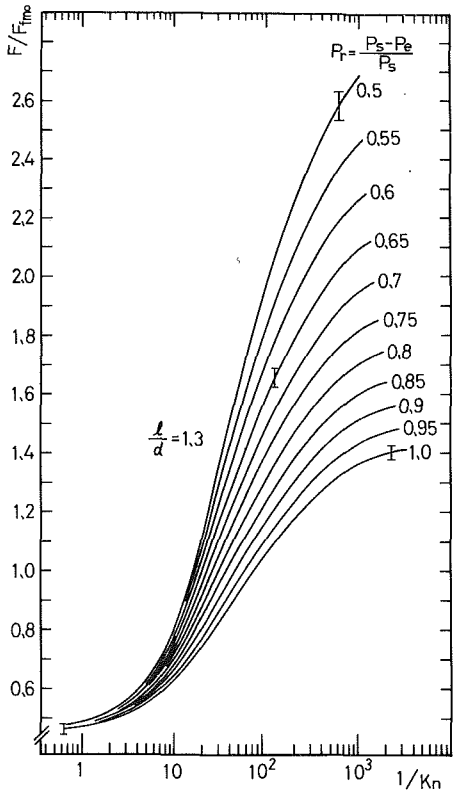

Fig. 7 Normalized conductance for cases of low pressure ratio. Length-to-diameter ratio l/d = 1.3. Uncertainty: F/F_{fmo} ±2.0 percent, 1/Kn ±1.0 percent (20:1 odds).

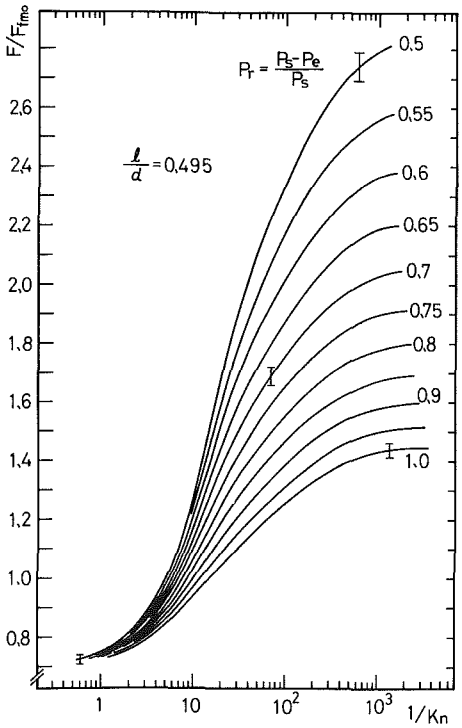

Fig. 8 Normalized conductance for cases of low pressure ratio. Length-to-diameter ratio l/d = 0.495. Uncertainty: F/F_{fmo} ±2.0 percent, 1/Kn ±1.0 percent (20:1 odds).

number increases: curves for pressure ratio $0.6 < P_r < 1.0$ converge to a single curve as the source pressure increases and curves for $P_r = 0.5$ and 0.55 tend to merge into the limiting

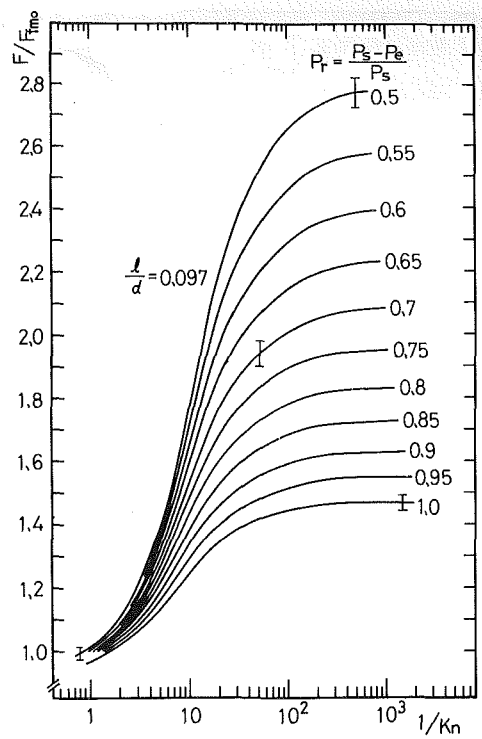

Fig. 9 Normalized conductance for cases of low pressure ratio. Length-to-diameter ratio l/d = 0.097. Uncertainty: F/F_{fmo} ±2.0 percent, 1/Kn ±1.0 percent (20:1 odds).

curve. In the case of $l/d = 0.097$ (Fig. 12), on the other hand, the difference of the mass-flow rate between different pressure ratios does not disappear so rapidly as that for the case of $l/d = 1.3$. Even though the source pressure further increases, the curves for the pressure ratio less than 0.6 have a tendency to maintain some difference from the curve of $P_r = 1.0$. In the case of $l/d = 0.025$ (Fig. 13), if each curve of different pressure ratios is extrapolated, it approaches Perry's limit [3] in the continuum region. It has been known that for the case of an adiabatic expansion through an ideal nozzle, the mass-flow is choked at the critical pressure ($P_r = 0.47$ for air). As far as the effect of the pressure ratio is concerned, the characteristics of the short tube with $l/d = 1.3$ are similar to those of the nozzle in the continuum region.

4.3 Effect of Gas Temperature. The experiments are carried out at gas temperature between 288 K and 298 K. Since the normalized conductances obtained at different temperatures agree well with one another, the temperature variation within 10 degrees does not appear to affect the present results.

4.4 Empirical Equations. In the range of Re < 2800, or 1/Kn < 4000, for $P_s/P_e > 100$, an empirical equation is proposed:

$$\left.\begin{aligned} \frac{F}{F_{fm0}} &= \frac{0.4733 + I\sqrt{1/(a\mathrm{Re})^c}}{1 + J/(a\mathrm{Re})^c + K/(a\mathrm{Re})^{2c}} b + \frac{F_{fm}}{F_{fm0}} \\ I &= 1.31(F_{fm}/F_{fm0})^{16},\ J = 8.537,\ K = 3.599 \end{aligned}\right\} \quad (21)$$

where F_{fm} is free-molecular conductance of an aperture and is a function of l/d given by either Nawyn-Meyer's or Clausing's theory. As a simplified expression of F_{fm}, the equations proposed by Henning [6] may be available. The factors a, b, and c are obtained using Table 2 as a function of F_{fm}/F_{fm0}. Values between adjacent entries in the table are to be decided

Downloaded 02 Jun 2010 to 171.66.16.91. Redistribution subject to ASME license or copyright; see http://www.asme.org/terms/Terms_Use.cfm

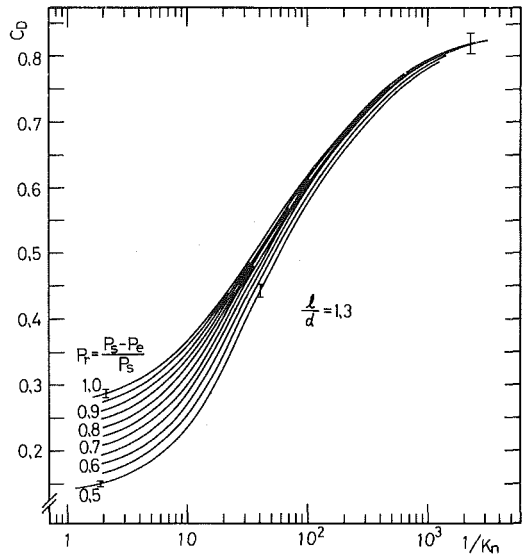

Fig. 10 Discharge coefficient for cases of low pressure ratio. *l/d* = 1.3. Uncertainty: C_D ±2.0 percent, 1/Kn ±1.0 percent (20:1 odds).

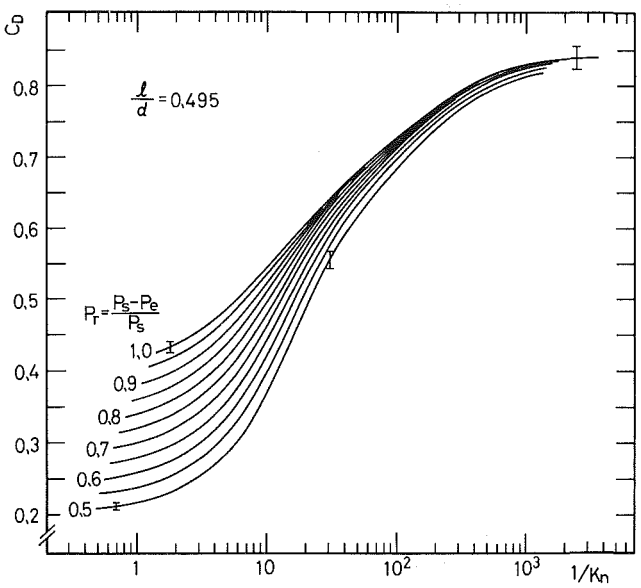

Fig. 11 Discharge coefficient for cases of low pressure ratio. *l/d* = 0.495. Uncertainty: C_D ±2.0 percent, 1/Kn ±1.0 percent (20:1 odds).

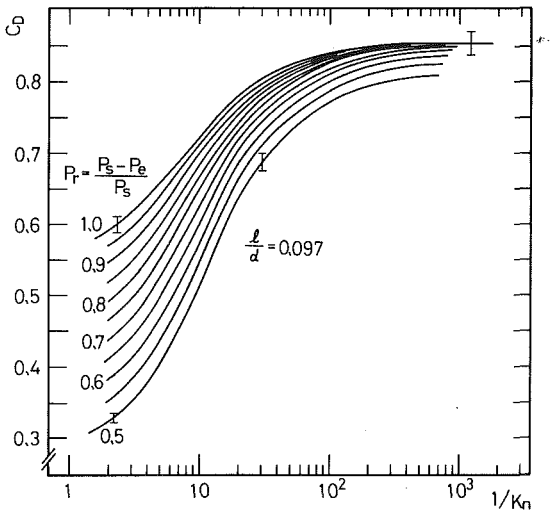

Fig. 12 Discharge coefficient for cases of low pressure ratio. *l/d* = 0.097. Uncertainty: C_D ±2.0 percent, 1/Kn ±1.0 percent (20:1 odds).

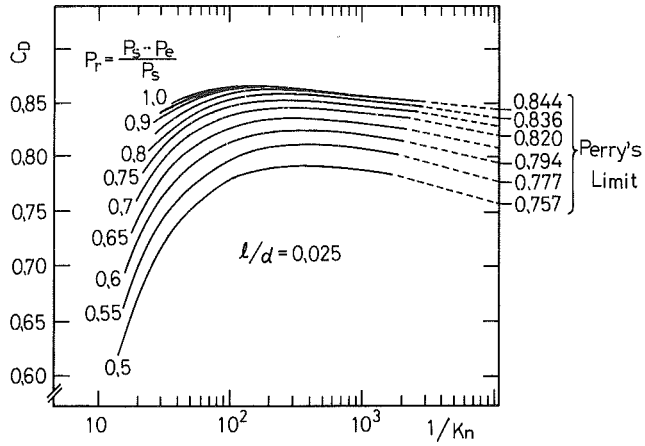

Fig. 13 Discharge coefficient for *l/d* = 0.025 and Perry's limit. Uncertainty: C_D ±2.0 percent, 1/Kn ±1.0 percent (20:1 odds).

Table 2 Factors *a*, *b*, and *c* in equation (21)

F_{fm}/F_{fm0}	*a*	*b*	*c*
0.05	0.188	3.245	0.527
0.1	0.287	3.060	0.573
0.15	0.379	2.894	0.596
0.2	0.476	2.760	0.607
0.25	0.573	2.635	0.615
0.3	0.686	2.505	0.622
0.35	0.805	2.385	0.628
0.4	0.935	2.276	0.634
0.45	1.067	2.165	0.639
0.5	1.220	2.059	0.642
0.55	1.399	1.950	0.645
0.6	1.570	1.838	0.650
0.65	1.751	1.730	0.661
0.7	1.935	1.621	0.683
0.75	2.150	1.510	0.713
0.8	2.178	1.400	0.754
0.85	2.058	1.291	0.839
0.9	1.745	1.175	0.934
0.95	1.291	1.057	0.983
1.0	0.700	0.932	1.013

by the method of proportional parts or linear interpolation. Although the conductance is derived from Re-number in the empirical equation, it is practical to derive the conductance from the source pressure, or the inverse Kn-number. In that case, it is necessary to calculate Re-number, substituting an arbitrarily prescribed value of conductance and 1/Kn into equation (19). If the derived conductance from equation (21) using the Re-number has any difference (which can not be disregarded) from the prescribed value, this procedure is repeated with the average of the two as the secondary prescribed value until a satisfactory value can be obtained. The curves calculated according to equation (21) are shown in Fig. 4.

From the practical point of view, equation (21) requires a cumbersome procedure to estimate flow rate. Therefore, another empirical equation is proposed, even though the range of applicability is restricted to $1/\mathrm{Kn} < 25$.

$$\left.\begin{aligned} &\frac{F}{F_{fm0}} = \frac{0.4733 + A\sqrt{1/(a/\mathrm{Kn})}}{1 + B/(a/\mathrm{Kn}) + C/(a/\mathrm{Kn})^2} + \frac{F_{fm}}{F_{fm0}} \\ &a = F_{fm}/F_{fm0} + 0.125\exp[-(12F_{fm}/F_{fm0} - 11.2)^2/2] \\ &\quad + 0.18\exp(-14.7F_{fm}/F_{fm0}) - 0.08, \\ &A = 0.907,\ B = 10.4,\ C = 16.1. \end{aligned}\right\} \quad (22)$$

The curves calculated by equation (22) are shown in Fig. 6.

Downloaded 02 Jun 2010 to 171.66.16.91. Redistribution subject to ASME license or copyright; see http://www.asme.org/terms/Terms_Use.cfm

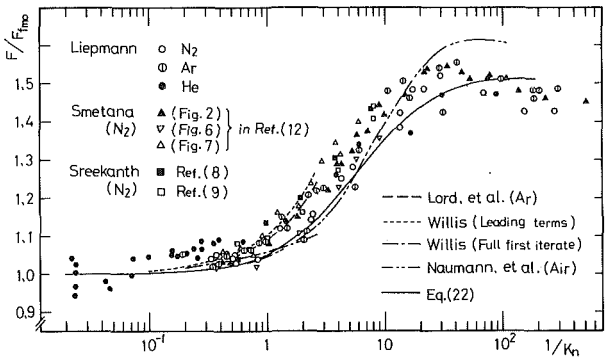

Fig. 14 Comparison between the results of orifices in references [7]-[13] and the present empirical equation (22) with $l/d = 0$

4.5 Comparison With Other Experiments. Figure 14 shows a comparison between the results of orifices in references [7]-[13] and the present empirical equation (22) with $l/d = 0$. Kn-number and the dimensionless mass-flow rate defined by various authors are given by:

$$\mathrm{Kn}_{(\mathrm{Naumann})} = 1/\mathrm{Re}_{(\mathrm{Liepmann,\ Willis})} = \mu_s\sqrt{RT_s}/P_s d$$

$$\mathrm{Kn}_{(\mathrm{Lord})} = \lambda_s/r = 2\lambda_s/d$$

$$\mathrm{Re}_{(\mathrm{Naumann,\ Smetana})} = 4\dot{m}/\pi d\mu_s \tag{23}$$

$$\mathrm{KR}_{(\mathrm{Naumann})} = \dot{m}\sqrt{RT_s}/P_s A_0$$

$$C_{D_{(\mathrm{Smetana})}} = \dot{m}/\dot{m}_{\max}$$

The recalculation of data in these references is carried out by means of the conversion of parameters as follows:

$$\begin{aligned}\mathrm{Kn}_{(\mathrm{present})} &= 1.256\,\mathrm{Kn}_{(\mathrm{Naumann})}\\ &= 1.256\,(1/\mathrm{Re})_{(\mathrm{Liepmann,\ Willis})}\\ &= 0.5\,\mathrm{Kn}_{(\mathrm{Lord})}\end{aligned} \tag{24}$$

$$\mathrm{Re}_{(\mathrm{Naumann,\ Smetana})} = 0.501(F/F_{fm0})(1/\mathrm{Kn})_{(\mathrm{present})} \tag{25}$$

$$\begin{aligned}(F/F_{fm0})_{(\mathrm{present})} &= 2.507\,\mathrm{KR}_{(\mathrm{Naumann})}\\ &= (\dot{m}/\dot{m}_{fm})_{(\mathrm{Willis,\ Lord,\ Sreekanth})}\\ &= (\Gamma/\Gamma_k)_{(\mathrm{Liepmann})}\\ &= 1.72\,C_{D_{(\mathrm{Smetana})}}\end{aligned} \tag{26}$$

The curve for the present results forms the lowest limit in the cloud of data and agrees well with Naumann's results [13] for $1/\mathrm{Kn} < 7$.

5 Conclusions

(1) For the cases of high pressure ratio, the conductance of apertures has been measured by the unsteady approach for Kn-number between 2.5×10^{-4} and 50 and length-to-diameter ratio l/d between 0.025 and 12.7.

(2) The correction for the outgassing near the free-molecular region has been proved to be effective.

(3) Empirical equations have been proposed as a function of Re-number, or Kn-number, and length-to-diameter ratio.

(4) In the continuum flow region for $1/\mathrm{Kn} > 1000$, the short tube of $l/d = 1.3$ is similar to an ideal nozzle, and the choking phenomena are observed for the pressure ratios larger than 0.6. On the other hand, the mass-flow rate for small l/d is affected considerably by the pressure ratio. Especially for $l/d = 0.025$, the mass-flow rates for different pressure ratios can approach each limit of Perry's.

References

1 Van Essen, D., and Heerens, W. C., "On the Transmission Probability for Molecular Gas Flow through a Tube," *Journal of Vacuum Science and Technology*, Vol. 13, No. 6, Nov/Dec. 1976, pp. 1183-1187.

2 Clausing, P., "Über die Strömung sehr verdünnter Gase durch Röhren von beliebiger Länge," *Annalen der Physik*, Band 12, 5.Folge, 1932, pp. 961-989.

3 Perry, J. A., Jr., "Critical Flow through Sharp-Edged Orifices," *Trans.* ASME, Vol. 71, Oct. 1949, pp. 757-764.

4 Hanks, R. W., and Weissberg, H. L., "Slow Viscous Flow of Rarefied Gases through Short Tubes," *Journal of Applied Physics*, Vol. 35, No. 1, Jan. 1964, pp. 142-144.

5 Shapiro, A. H., "Isentropic Flow," *The Dynamics and Thermodynamics of Compressible Fluid Flow*, Vol. 1, Ronald Press, New York, 1953, pp. 73-111.

6 Henning, H., "The Approximate Calculation of Transmission Probabilities for the Conductance of Tubulations in the Molecular Flow Regime," *Vacuum*, Vol. 28, No. 3, Mar. 1978, pp. 151-152.

7 Liepmann, H. W., "Gaskinetics and Gasdynamics of Orifice Flow," *Journal of Fluid Mechanics*, Vol. 10, 1961, pp. 65-79.

8 Sreekanth, A. K., "Some Experiments on the Flow of a Rarefied Gas through a Circular Orifice," *Proceedings of the 4th International Symposium on Rarefied Gas Dynamics*, De Leeuw, J. H., ed., Vol. 1, Academic Press, New York, 1964, pp. 621-629.

9 Sreekanth, A. K., "An Experimental Investigation of Mass Flow through Short Circular Tubes in the Transition Flow Regime," *Flight Sciences Laboratory Report No. 95*, D1-82-0427, Boeing Scientific Research Laboratories, Seattle, Apr. 1965.

10 Willis, D. R., "Mass Flow through a Circular Orifice and a Two-Dimensional Slit at High Knudsen Numbers," *Journal of Fluid Mechanics*, Vol. 21, Part 1, 1965, pp. 21-31.

11 Lord, R. G., Hurlbut, F. C., and Willis, D. R., "Nearly Free Molecule Flow through a Circular Orifice at High Pressure Ratios," *Proceedings of the 5th International Symposium on Rarefied Gas Dynamics*, Brundin, C. L., ed., Vol. 2, Academic Press, New York, 1966, pp. 1235-1242.

12 Smetana, F. O., Sherrill, W. A., II, and Schort, D. R., Jr., "Measurements of the Discharge Characteristics of Sharp-Edged and Round-Edged Orifices in the Transition Regime," ibid., pp. 1243-1251.

13 Naumann, A., and Chun, C. H., "Mass-Flow Measurements for Sharp-Edged Orifices in Low Density Flow," *Proceedings of the 9th International Symposium on Rarefied Gas Dynamics*, Becker, M., and Fiebig, M., eds., Vol. 2, DFVLR Press, Porz-Wahn, Germany, 1974, p. 21.

Downloaded 02 Jun 2010 to 171.66.16.91. Redistribution subject to ASME license or copyright; see http://www.asme.org/terms/Terms_Use.cfm

J. S. Weingarten[1]
Graduate Student.

A. J. Chapman
Professor.

W. F. Walker
Professor.

Department of Mechanical Engineering,
Rice University, Houston, Texas 77251

An Analysis of the Motion of Pigs Through Gas Pipelines

A one-dimensional, quasi-steady, model describing the motion of a pig moving in a gas pipeline is developed for the cases of a solid pig, which obstructs the cross section of the pipe, and one with a concentric hole through it. The resultant governing equations constitute a set of seven nonlinear differential equations. A numerical solution scheme, implemented by a computer program, is described. Results and discussion are presented for a set of typical cases.

Introduction

In natural gas pipelines, devices called "pigs" perform several maintenance operations. They may remove water and solid contaminants, apply protective or drag reducing coatings to the inside of the pipe, or inspect pipe for damage caused by corrosion or relative shifting of the pipeline. The pigs are propelled through the line by the gas being transported, thus eliminating the need to shut the line down for routine cleaning and inspection.

The pigs usually consist of two or more polyurethane rings attached to a cylindrical steel hub, although cylindrical pigs made of foam rubber are also used. The outer diameter of most pigs is slightly larger than the inner pipe diameter. This oversize provides a tight seal which creates a differential pressure across the pig, propelling it through the pipe. Variations on the basic pig shape depend on the particular use for which a pig is designed.

The typical configuration, described above, blocks the flow of gas in the pipeline, which reduces the gas flow rate. Furthermore, if a solid pig is used the pig velocity is determined by the operating conditions of the pipeline, and can be reduced only by increasing the interference between the pig and pipe diameters, which increases the friction. An inspection pig may have to travel very slowly in order to assess accurately the condition of the pipe. Increasing the friction on the pig to achieve this reduced velocity would result in drastically lower gas flow rates, as well as in excessive wear on the rubber rings. Thus, depending on the desired pig velocity, the amount of gas transported while the pig travels through the line may be appreciably less than that transported through the pipe without a pig. This solid configuration, which does not allow gas to flow past the pig, may be necessary for the cleaning pig, in order to keep water and debris ahead of the pig, but the inspection pig has no such constraint. Allowing some of the gas to flow through the pig, either through a hole or through an annular clearance between the pig and the pipe, could provide the required pig velocity, while keeping the gas flow rate high. Since the cost of routine pigging includes the amount of gas that is not transported, due to the decreased flow rate, any improvement in the gas flow rate lowers the cost of the operation and warrants investigation.

The problem of analyzing the flow of a cylindrical capsule through a pipe carrying an incompressible fluid has been studied extensively, (see bibliography of reference [1]), but the problem posed here, of motion in a compressible fluid, has been discussed in the literature only qualitatively, with design recommendations based primarily on field experience. It has been suggested that the speed of travel of a pig may be controlled by installing ports or jets in the pig which would open to allow gas to flow through, but no quantitative analysis or support for this practice has been published, and no reference in the literature has been made to the effect of this concept on the gas flow rate through the pipe.

The objectives of the analysis to be presented here are to propose a quantitative model for flow through a gas pipeline containing a pig, to derive the governing equations for the flow, and to provide a means of solving these equations for the flow parameters of interest. Such an analysis provides a rational basis for pig design, resulting in improved gas flow rates.

Many variations from the standard solid pig are possible, including those provided with a concentric annulus of uniform clearance, with a concentric hole of constant diameter, with a concentric hole of linearly decreasing diameter, and with both a hole and an annulus. All of these cases were studied, to varying degrees of completeness by Sullivan, [1][2]. However, for the sake of clarity and conciseness, only the cases of the solid pig and that with a concentric hole of constant diameter will be reported here. Only pigs of constant mass are considered; hence a cleaning pig that accumulates mass before it is not treated.

Analysis

This analysis considers a pig of known mass m and length l moving through a pipe of length L and diameter D. The pig

[1] Currently: Associate Research Engineer, ARCO Oil and Gas Company, Dallas, Texas 75221.

Contributed by the Fluids Engineering Division and presented at the Winter Annual Meeting, New Orleans, La., December 9-14, 1984, of THE AMERICAN SOCIETY OF MECHANICAL ENGINEERS. *Manuscript received by the Fluids Engineering Division, April 26, 1982. Paper No. 84-WA/FE-7.*

[2] J. M. Sullivan, reference [1], is now Jean S. Weingarten, senior author of this paper.

Copyright © 1984 by ASME

Downloaded 02 Jun 2010 to 171.66.16.91. Redistribution subject to ASME license or copyright; see http://www.asme.org/terms/Terms_Use.cfm

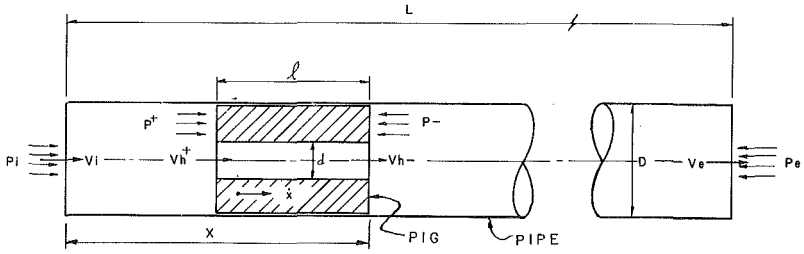

Fig. 1 The physical system

has a concentric hole of diameter d which may be made zero for the case of the solid pig. The pressures at the pipe inlet and exit P_i and P_e, respectively, are presumed known and fixed. Rubbing friction of a known amount exists between the pig and the pipe wall. Viscous frictional effects occur between the gas and the pipe wall, and between the gas and the pig surfaces. As the pig travels the length of the pipe, it is desired to describe its position, velocity and acceleration as well as the gas pressures immediately upstream and downstream of the pig and the pipe inlet and exit Mach numbers – all as functions of time.

Figure 1 depicts the pipe and pig, and shows some of the nomenclature used.

Assumptions. In order to facilitate the analysis, the following assumptions are made:

1. The gas flow is isothermal at a known temperature T.
2. The gas flow is quasi-steady.
3. The gas flow is taken to be one-dimensional, with uniform properties at each section of the pipe or pig hole.
4. Constant pressures are maintained at the pipe inlet and exit.
5. The gas is ideal.
6. There are negligible elevation changes along the length of the pipe.

The isothermal assumption is made, instead of the alternative adiabatic assumption, in order to simplify the analysis. Since most practical applications will be for flow Mach numbers that are significantly subcritical, and since most pipelines are not thermally insulated, this assumption is realistic.

The quasi-steady assumption is that at any instant of time, the steady state gas dynamic equations hold between the pipe inlet and the pig, through the pig hole (if it exists), and between the pig and the pipe exit. Since the pig moves, the gas flow is not truly steady, but if the pipeline is many orders of magnitude longer than the pig (a most likely condition) one may reasonably assume the quasi-steady state to exist with little error.

The remaining assumptions are self-explanatory and are customarily made in pipeline analyses.

Governing Equations: In the following paragraphs, the equations describing the gas flow and the pig motion will be presented. In order to provide a solution of a more general nature, these equations will be nondimensionalized. To do so, certain characteristic quantities must be selected. The characteristic length will be taken to be the pipe diameter, D; the characteristic pressure will be taken to be the specified pipe exit pressure, P_e; and the characteristic time will be $D/(\gamma RT)^{1/2}$. Thus, $(\gamma RT)^{1/2}$ will be a characteristic velocity and $(\gamma RT)/D$ will be a characteristic acceleration. The symbols γ and R represent the ratio of specific heats and the gas constant, respectively.

In general, a starred quantity will denote the dimensionless counterpart of an unstarred quantity. Thus,

$$L^* = L/D,\ l^* = l/D,\ d^* = d/D,\ P^* = P/P_e$$

$$x^* = x/D,\ \dot{x}^* = \dot{x}/(\gamma RT)^{1/2},\ \ddot{x}^* = \ddot{x}D/(\gamma RT)$$

(The existence of a dimensionless time $t^* = t(\gamma RT)^{1/2}/D$ is assumed, and x is the position of the pig measured from the pipe inlet.) An exception to this notation will be that the dimensionless gas velocities will be denoted by the traditional Mach number rather than V^*:

$$\mathrm{M} = V/(\gamma RT)^{1/2}.$$

Nomenclature

D = pipe diameter
d = pig hole diameter
d^* = d/D
F_f = pig frictional force
F_f^* = $4F_f/\pi d^2 P_e$
F_h, F_h^* = frictional force and dimensionless frictional force in pig hole
f_h, f_p = Fanning friction factor in pig hole and in pipe
L = pipe length
L^* = L/D
l = pig length
l^* = l/D
M = Mach number = $V/(\gamma RT)^{1/2}$
$\mathrm{M}_e, \mathrm{M}_i$ = Mach number at pipe exit and inlet
$\mathrm{M}_h^+, \mathrm{M}_h^-$ = hole Mach number at upstream and downstream ends of pig
$\bar{\mathrm{M}}^+, \bar{\mathrm{M}}^-$ = mean pipe Mach number at upstream and downstream ends of pig
m = pig mass
m^* = $4m\gamma RT/\pi d^3 P_e$
P = gas pressure
P_e, P_i = gas pressure at pipe exit and inlet
P^+, P^- = gas pressure at upstream and downstream ends of pig
P^* = P/P_e
P_i^*, P^{*+}, P^{*-} = $P_i/P_e, P^+/P_e, P^-/P_e$
R = gas content
T = gas temperature
V_e, V_i = gas velocity at pipe exit and inlet
V_h^+, V_h^- = gas velocity in pig hole at upstream and downstream ends of pig
V_R = relative velocity
$x, \dot{x}, \ddot{x}$ = position, velocity, and acceleration of pig
x^* = x/D
$\dot{x}^*$ = $\dot{x}/(\gamma RT)^{1/2}$
$\ddot{x}^*$ = $\ddot{x}D/\gamma RT$
γ = gas ratio of specific heats
δ = a generalized diameter
ρ = gas density
ξ = a generalized displacement

Downloaded 02 Jun 2010 to 171.66.16.91. Redistribution subject to ASME license or copyright; see http://www.asme.org/terms/Terms_Use.cfm

For the general case of a pig with a concentric hole, seven equations will be written to characterize the flow: continuity and momentum equations for the region upstream of the pig, for the flow through hole, and for the region downstream of the pig, plus a force and momentum balance on the pig. For given geometrical quantities, (see Fig. 1), the above equations will permit (for specified inlet and exit pressures, P_i and P_e) the determination of the inlet and exit gas velocities (V_i and V_e), the gas pressures immediately upstream and downstream of the pig (P^+ and P^-), the upstream and downstream velocities of gas in the pig hole (V_h^+ and V_h^-), along with the pig position (x) and its time derivatives – all as functions of time. Using the quasi-steady assumptions, the following equations result.

Continuity Equations. For steady, isothermal, flow of an ideal gas through a circular cross section of constant diameter, the continuity principle becomes:

$$P(\text{diameter})^2 V = \text{constant} \tag{1}$$

Application of this to the regions between the pipe inlet and the pig, the pig and the pipe exit, and the pig hole, gives, respectively:

$$P_i D^2 V_i = P^+ d^2 V_h^+ + P^+ (D^2 - d^2)\dot{x}$$
$$P_e D^2 V_e = P^- (D^2 - d^2)\dot{x} + P^- d^2 V_h^-$$
$$p^+ d^2 V_h^+ = P^- d^2 V_h^-$$

Introduction of the dimensionless variables defined in the foregoing yields:

$$P_i^* \mathrm{M}_i - P^{*+}[d^{*2}\mathrm{M}_h^+ + (1-d^{*2})\dot{x}^*] = 0 \tag{2}$$
$$P_e^* \mathrm{M}_e - P^{*-}[(1-d^{*2})\dot{x}^* + d^{*2}\mathrm{M}_h^-] = 0 \tag{3}$$
$$P^{*+}\mathrm{M}_h^+ - P^{*-}\mathrm{M}_h^- = 0 \tag{4}$$

Momentum Equations. The customary expression for the momentum principle applied to the steady one-dimensional flow of a gas, with friction, at constant area is [2]:

$$\frac{dP}{\rho} + VdV + \frac{4f}{\delta}\frac{V_R^2}{2}d\xi = 0$$

In the above equation f is the Fanning friction factor between the gas and the frictional surface, V_R is the relative gas velocity past the surface, $d\xi$ is a spatial displacement along the surface, and δ is the passage diameter. Using the fact that $P = \rho RT$ and that equation (1) implies $dP/P = -dV/V$, the above may be rearranged and nondimensionalized by introducing the Mach number $\mathrm{M} = V/(\gamma RT)^{1/2}$ to yield:

$$-\frac{d\mathrm{M}}{\mathrm{M}}\frac{1}{\gamma} + \mathrm{M}d\mathrm{M} + \frac{4f}{\delta}\left(\frac{1}{2}\frac{V_R{}^2}{\gamma RT}\right)d\xi = 0 \tag{5}$$

The relative velocity V_R is the gas velocity V in the regions upstream and downstream of the pig. However, in the pig hole V_R must be replaced with $V - x$. When applied to the hole, the form of equation (5) assumes that the gas flow through the hole is greater than the velocity of the pig.

When applied to the upstream region (between the pipe inlet and the pig), equation (5) may be integrated between $\xi = 0$ with $\mathrm{M} = \mathrm{M}_i$ to $\xi = x - l$ where M is denoted as some average value at the face of the pig, $\bar{\mathrm{M}}^+$. The result is:

$$4f_p(x^* - l^*) - (1/\gamma)\left[\frac{1}{\mathrm{M}_i^2} - \frac{1}{(\bar{\mathrm{M}}^+)^2}\right] - 2\ln\left(\frac{\mathrm{M}_i}{\bar{\mathrm{M}}^+}\right) = 0 \tag{6}$$

with the average Mach number at the upstream pig face given by:

$$\bar{\mathrm{M}}^+ = (1-d^{*2})\dot{x}^* + d^{*2}\mathrm{M}_h^+ \tag{7}$$

In equation (6), f_p represents the Fanning friction factor for the pipe, taken to be constant, and the fact that $\delta = D$ has been used.

In like fashion, equation (5) may be applied to the region between the downstream pig face (where $\xi = x$ and M is an average value $\bar{\mathrm{M}}^-$) and the pipe exit (where $\xi = L$ and $\mathrm{M} = \mathrm{M}_e$). The result of this integration yields

$$4f_p(L^* - x^*) + (1/\gamma)\left[\frac{1}{\mathrm{M}_e^2} - \frac{1}{(\bar{\mathrm{M}}^-)^2}\right] - 2\ln\left(\frac{\bar{\mathrm{M}}^-}{\mathrm{M}_e}\right) = 0 \tag{8}$$

with

$$\bar{\mathrm{M}}^- = (1-d^{*2})\dot{x}^* + d^{*2}\mathrm{M}_h^- \tag{9}$$

Finally, when equation (5) is applied to the pig hole (with $\delta = d$ and $V_R = V - \dot{x}$) it may be integrated over the pig length (from $\xi = 0$, $\mathrm{M} = \mathrm{M}_h^+$ to $\xi = l$, $\mathrm{M} = \mathrm{M}_h^-$) to give:

$$\frac{4f_h\gamma l^*}{2d^*} + \left[\frac{1}{\dot{x}^*} - (\gamma\dot{x}^*)\right]\left[\frac{1}{\mathrm{M}_h^+ - \dot{x}^*} - \frac{1}{\mathrm{M}_h^- - \dot{x}^*}\right]$$
$$+\left[\frac{1}{(\dot{x}^*)^2} + \gamma\right]\ln\left[\frac{\mathrm{M}_h^+ - \dot{x}^*}{\mathrm{M}_h^- - \dot{x}^*}\right] - \frac{1}{(\dot{x}^*)^2}\ln\left(\frac{\mathrm{M}_h^+}{\mathrm{M}_h^-}\right) = 0 \tag{10}$$

Here, f_h represents the Fanning factor in the hole, taken as constant. The integration leading to equation (10) assumes that $\dot{x}$ is constant. This assumption is consistent with the quasi-steady assumption noted earlier for flow through the pig hole even though $\dot{x}$ is not taken as constant when Newton's second law is applied to the motion of the pig.

Force Balance on Pig. The remaining necessary equation results from applying Newton's second law to the pig. The pig acceleration is balanced by upstream and downstream pressures, fluid friction in the pig hole (if it exists), and the frictional force between the pipe wall and the pig:

$$m\ddot{x} = (P^+ - P^-)\frac{\pi}{4}(D^2 - d^2) - F_f + F_h \tag{11}$$

In the above, F_f represents the frictional force between the pig and the pipe wall – a, presumably, given and known quantity. The term F_h represents the frictional drag of the gas flowing through the hole. The choice of sign on F_h is consistent with the basic assumption that the gas moves through the hole with a velocity greater than that of the pig. As a representative formulation for F_h, it was decided to base it on the average gas density and an average gas velocity in the hole:

$$F_h = 1/2\rho(x - \bar{V}_h)^2 f_h \pi dl$$

For an isothermal ideal gas this becomes

$$F_h = (1/2)\frac{P^+ + P^-}{2}\frac{1}{RT}\left(\dot{x} - \frac{V_h^+ + V_h^-}{2}\right)^2 f_h \pi dl$$

If equation (11) is nondimensionalized, one has

$$m^*\ddot{x}^* = (P^{*+} - P^{*-})(1-d^{*2}) - F_f^* + F_h^* \tag{12}$$

In equation (12) m^* and F_f^* are the dimensionless pig mass and wall force, specified quantities, defined as

$$m^* = \frac{4m\gamma RT}{\pi d^3 P_e} \tag{13}$$

$$F_f^* = \frac{F_f}{\frac{\pi}{4}d^2 P_e} \tag{14}$$

while the dimensionless hole drag force, F_h^*, is related to the other variables:

$$F_h^* = \frac{\gamma}{2}\frac{P^{*+} + P^{*-}}{2}\,4f_h\left(x^* - \frac{M_h^- + M_h^+}{2}\right)^2 d^* l^*$$

The seven equations (2), (3), (4), (6), (8), (10), and (12) may be solved at each time step for the seven unknowns: M_i, M_e, P^{*+}, P^{*-}, M_h^+, M_h^-, and x^*. If no hole exists in the pig, M_h^+ and M_h^- are removed from this list and equations (4) and (10) are not used. These equations form a system of nonlinear

Downloaded 02 Jun 2010 to 171.66.16.91. Redistribution subject to ASME license or copyright; see http://www.asme.org/terms/Terms_Use.cfm

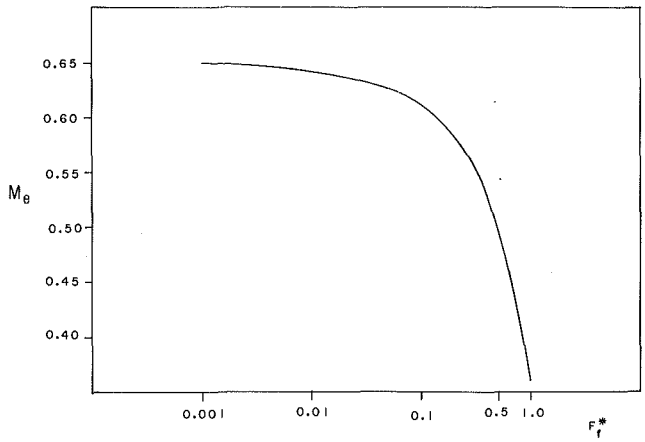

Fig. 2 Effect of friction on the exit Mach number for the solid pig

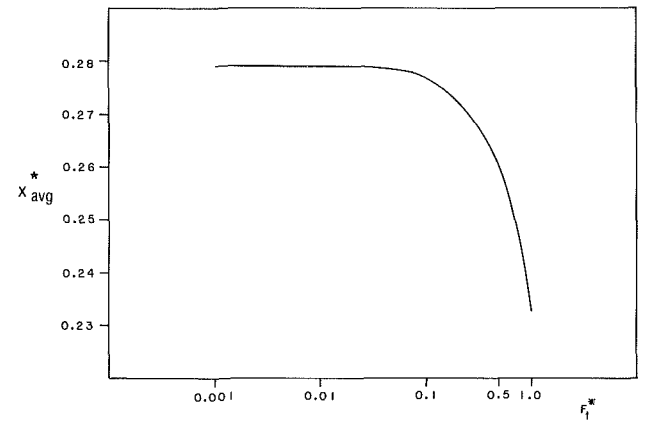

Fig. 3 Effect of friction on the average velocities of the solid pig

equations. In addition, they contain derivatives of x^* with respect to the dimensionless time t^*. Because of their complexity, these equations cannot be solved analytically and their solution must be found using numerical techniques.

Method of Solution

The governing equations presented in the foregoing describe the gas flow state and the pig's motion when the pig is located at a particular position in the pipe. The motion of the pig through the pipe may be simulated by solving these equations at successive locations. If time is set arbitrarily as zero when the pig is located at the pipe entrance, it is convenient to describe the motion at equal time increments, Δt^*, from that instant. The set of differential equations may be converted to a system of algebraic, nonlinear, equations by approximating the time derivatives of x^* by backward differences. This allows the velocity and acceleration of the pig to be expressed in terms of the current position, the previous positions, and the time step. If the subscript i denotes the current position and $i-1$ and $i-2$ the location one and two time steps previous, respectively, then the pig velocity and acceleration are approximated as

$$\dot{x}_i^* = \frac{x_i^* - x_{i-1}^*}{\Delta t^*}$$

$$\ddot{x}_i^* = \frac{x_i^* - 2x_{i-1}^* + x_{i-2}^*}{(\Delta t^*)^2}$$

With these representations, the set of seven equations may be used to solve for the current location x_i^* (along with M_i, M_e, M_h^+, M_h^-, p^{*+}, P^{*-}). After this solution is obtained, time may be incremented again, and the equations solved once more for a new pig position farther along the pipe.

Since the equations are second order in x^*, two initial conditions must be specified. These are

$$x_0^* = 0$$

$$\dot{x}_0^* = 0$$

With the set of governing equations thus reduced to an algebraic, nonlinear, set by introduction of the above approximations, a numerical solution may be carried out. The complete details of the numerical solution are given in reference [1]. In this work, the hybrid method of Powell [3, 4] has been incorporated into a Fortran program in which equations (2), (3), (4), (6), (8), (10), and (12) are solved at each resultant pig location for the variables M_i, M_e, P^{*+}, P^{*-}, M_h^+, M_h^-, and x^* (and its derivatives) for specified values of the dimensionless parameters P_i^*, m^*, γ, f_h, f_p, l^*, d^*, and F_f^* and a selected value of the dimensionless time increment Δt^*. This program was used to study, parametrically, the motion of a pig in a gas pipeline as a function of various parameters. The results of this study are reported in detail in reference [1], and were obtained using time steps sufficiently small that there was little effect on the answers. Some typical results are given in the next section.

Results and Discussion

Since nine dimensionless parameters are required to characterize a given pig performance problem, a comprehensive sampling of all possible flow conditions is not feasible. The results presented here represent only a fraction of the possible conditions, but will serve to illustrate some possible effects. The following dimensionless input parameters were used in all cases reported here:

$P_i^* = 3.3$ (the dimensionless pressure, P_i/P_e)
$m^* = 570$ (the dimensionless pig mass, $4m\gamma RT/\pi d^3 P_e$)
$\gamma = 1.3$ (the ratio of specific heats)
$f_h = 0.00025$ (the pig hole friction factor)
$f_p = 0.00025$ (the pipe friction factor)
$l^* = 3.0$ (the dimensionless pig length, l/D)
$L^* = 160{,}000$ (the dimensionless pipe length, L/D)

These were chosen to correspond, approximately, to the following physical quantities taken to represent a typical case:

$P_i = 22.75$ bar (pipe inlet pressure)
$P_e = 6.90$ bar (pipe exit pressure)
$T = 10°C$ (gas temperature)
$R = 0.520$ kJ/kg − °K (gas constant, typical of Methane)
$D = 0.3048$ m (pipe diameter)
$m = 45.36$ kg (pig mass)
$l = 9.144$ m (pig length)
$L = 48.28$ km (pipe length)

The values of $d^* = d/D$ (the ratio of the diameters of the pig hole and the pipe) and $F_f^* = 4F_f/\pi d^2 P_e$ (the dimensionless frictional force between the pig and the pipe) were varied while keeping the other parameters constant at the values stated above. Thus the mass of the pig was taken to the independent of the pig configuration as the concentric hole size was varied.

The average pig velocity and the gas flow rate are the two most important results to be obtained from the analysis. Since the pressure and cross sectional area at the pipe exit are constant, the mass flow rate at the exit is directly proportional to the exit Mach number, M_e. Thus, changes in the exit Mach number will be interpreted as changes in gas flow rates in the cases discussed in the following.

The velocity of the *solid* pig may be regulated only by adjusting the amount of friction between the outside of the pig and the pipe wall. This is achieved by changing the

Downloaded 02 Jun 2010 to 171.66.16.91. Redistribution subject to ASME license or copyright; see http://www.asme.org/terms/Terms_Use.cfm

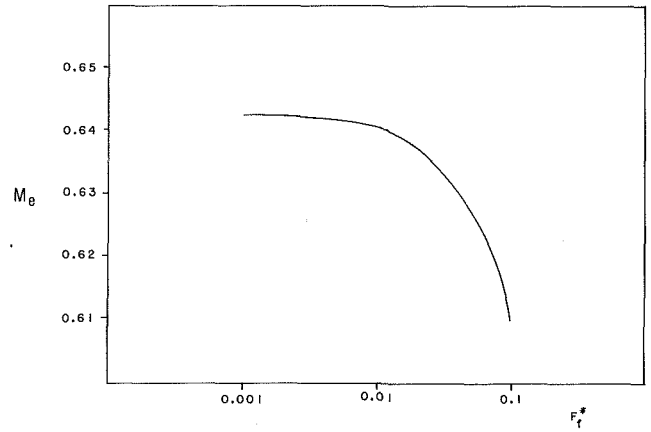

Fig. 4 Effect of friction on the exit Mach number for the pig with constant diameter hole, $d^* = 0.3$

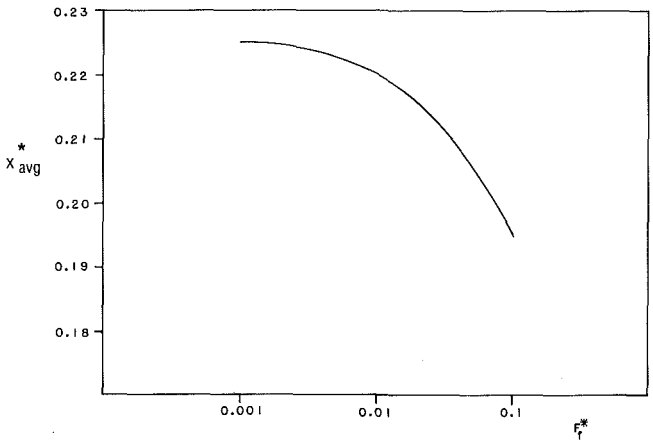

Fig. 5 Effect of friction on the average velocity of the pig with constant diameter hole, $d^* = 0.3$

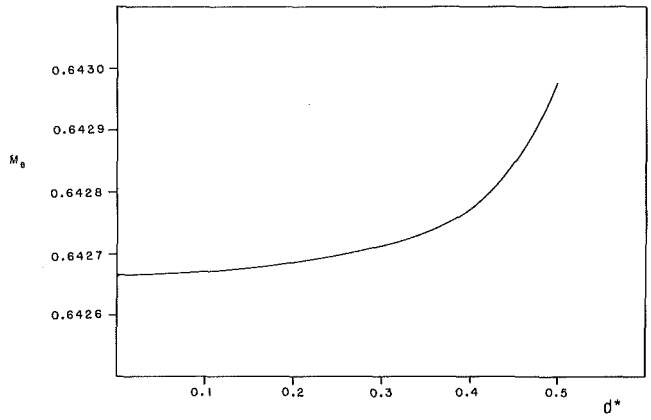

Fig. 6 Effect of hole diameter on exit Mach number $F_f^* = 0.001$

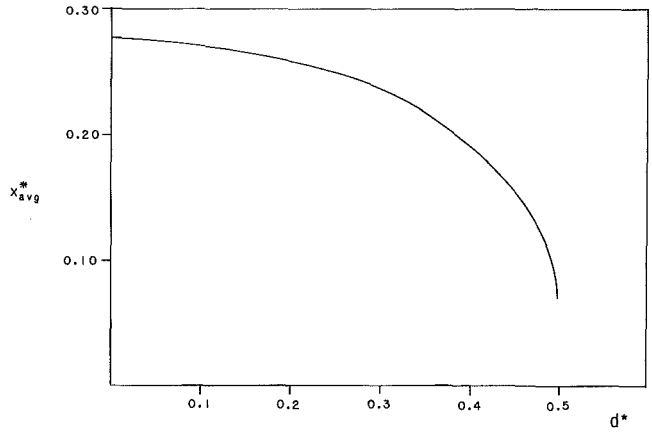

Fig. 7 Effect of hole diameter on pig velocity, $F_f^* = 0.001$

amount of interference between the outer diameter of the pig and the inner diameter of the pipe. Figures 2 and 3 illustrate the effect of friction on the exit Mach number and on the dimensionless average velocity of the solid pig. The exit Mach number for the pipe containing no pig is 0.64322. At low values of friction between the solid pig and the pipe, the exit Mach number for the pipe carrying the pig is slightly less. The average pig velocity and exit Mach number are nearly constant over the range $F_f^* = 0$ to $F_f^* = 0.1$. Increasing the amount of friction beyond $F_f^* = 0.1$ results in a rapid drop in both exit Mach number and average pig velocity, so that for an average pig velocity of 0.23, the exit Mach number is about half of that for the clear pipe. This method of slowing the pig, by increasing the friction between the pig and the pipe, is obviously unsatisfactory, due to the large decreases in gas flow rate.

Drilling a concentric, constant diameter hole through the solid pig would provide a better means of decreasing the pig velocity. Figures 4 and 5 illustrate the effect of friction on the exit Mach number and on the average pig velocity for a pig having a constant ratio of hole diameter to pipe diameter of 0.3. The shapes of these curves are similar to those obtained for the solid pig. But by adding the hole, the pig velocity of 0.23 is obtained with a small amount of friction between the pig and the pipe, and the exit Mach number is only slightly less than that for the pipe containing no pig. In addition, the exit Mach number is slightly higher than that for the solid pig with the same amount of friction.

A wide range of pig velocities may be obtained, simply by varying the size of the hole. Figures 6 and 7 demonstrate the

Table 1 Total mass of gas transferred for variable hole size

d^*	$M_{TOT,kg}$	Comment
0.0	113,829	solid pig
0.3	113,826	
0.4	113,822	
0.5	113,819	
1.0	113,861	unobstructed pipe

effect of hole size on exit Mach number and on average pig velocity for $F_f^* = 0.001$. As the hole size increases, the exit Mach number increases and the pig velocity decreases.

At the same value of F_f^*, the exit Mach number for the case of a pig with any size hole is greater than that for the case of the solid pig, but the pig with a hole travels more slowly through the pipe, obstructing the flow longer. Because the pigs with different hole sizes require different amounts of time to travel the length of the pipe, the effect of the hole size on the total amount of gas transported cannot be obtained by merely comparing the exit Mach numbers. The same time must be used to compare the different pigs. Let t^*_{max} be the dimensionless time needed for the slowest pig to travel through the pipe. A pig with a different hole diameter travels through the pipe in a faster dimensionless time, t^*. Until time t^*, the exit Mach number is that obtained for the pipe carrying this pig, but between times t^* and t^*_{max}, the exit Mach number is that for the unobstructed pipe. The expression for the total mass of gas transported over the length of time t^*_{max} is

$$m_{TOT} = \frac{\pi D^3 P_e}{4RT} [M_e t^* + M_{ep} (t^*_{max} - t^*)]$$

where M_e is the exit Mach number for the pipe carrying the

Downloaded 02 Jun 2010 to 171.66.16.91. Redistribution subject to ASME license or copyright; see http://www.asme.org/terms/Terms_Use.cfm

pig, M_{ep} is the exit Mach number for the clear pipe. A comparison of the total amounts of gas transferred, for the hole sizes presented earlier, is given in Table 1. F_f^* if 0.001, as before.

The total amount of gas transported decreases as the hole size increases from $d^* = 0$ to $d^* = 0.5$, since the pig is in the pipe for a longer time, but the amount of this decrease is not very significant when it is compared to the total amount transferred. Reducing the mass of the pig when the hole size is increased should make the differences in mass transferred even more negligible, since the lighter pig travels faster, and since the exit Mach number is greater for the lighter pig.

The results presented indicate that a pipe containing a pig with a constant diameter hole has a higher gas flow rate than the pipe carrying a solid pig, and the total amount of gas transferred over comparable time lengths is only slightly less than that for the pipe carrying the solid pig. This may be important in long pipelines where a consistently high flow rate may be required. More importantly, varying the diameter of the hole in the pig allows considerable versatility in regulating the pig velocity, while barely affecting the total amount of gas transported.

Conclusions

A model, and its governing equations, has been presented to describe the gas flow and pig motion in a gas pipeline. The governing equations form a set of nonlinear differential equations requiring numerical solution. Because of the large number of parameters involved, the results presented are limited to a few typical cases. However, these results do present interesting alternatives by which a desired pig motion may be obtained while maintaining a desirable mass flow through the pipeline.

The analysis presented here was limited to the case of the solid pig or one with a constant diameter concentric hole, allowing for gas through-flow. Similar analyses have been carried out [1] for pigs with tapered holes, annular passages, or both.

References

1 Sullivan,* J. M., "An Analysis of the Motion of Pigs Through Natural Gas Pipelines," MS thesis, Dept. of Mechanical Engineering, Rice Univ., Apr. 1981.

2 Chapman, A. J., and Walker, W. F., *Introductory Gas Dynamics*, Holt, New York, 1971.

3 Powell, M. J. D., "A Hybrid Method for Nonlinear Equations," *Numerical Methods for Nonlinear Algebraic Equations*, P. Rabinowitz, ed., Gordon and Breach, New York, 1970.

4 Powell, M. J. D., "A Fortran Subroutine for Solving Systems of Nonlinear Algebraic Equations," *Numerical Methods for Nonlinear Algebraic Equations*, P. Rabinowitz, ed., Gordon and Breach, New York, 1970.

*Now Jean S. Weingarten

Downloaded 02 Jun 2010 to 171.66.16.91. Redistribution subject to ASME license or copyright; see http://www.asme.org/terms/Terms_Use.cfm

Nonlinear Taylor Instability in a Cylindrical Vessel

I. Chang-Mateu

S. G. Bankoff

Chemical Engineering Department,
Northwestern University,
Evanston, Ill. 60201

A new class of Taylor-unstable waves, consisting of ring waves appearing at the interface of two fluids of differing densities within a around pipe when the interface is accelerated in the direction of the denser fluid, is considered. The analysis employs a generalized coordinate method introduced by Dienes [16]. The characteristic "bubble-spike" configuration is obtained, although the singularity corresponding to infinite spike tip velocity occurs at a later time than for the one-dimensional plane wave. In addition, it has been shown previously [19] that condensation of vapor at the interface produces negligible correction to the growth rate.

Introduction

Nonlinear Taylor instabilities have been treated by a number of authors, both experimentally [1–6] and theoretically [7–14]. Weak nonlinearities have been treated by multiple-scale expansions [15]. More recently, Dienes [16], following earlier work by Fermi [17] and Miles and Dienes [18], developed a generalized coordinate method which correctly predicts the "spike and bubble" shape observed experimentally in the late stages of the growth of the instability. Although his method is quite general, closed-form results can only be obtained by dropping all wavenumbers from the Fourier expansion except one, which is chosen to be the linearly fastest-growing wavenumber. The extension to two incompressible fluids with interfacial heat and/or mass transfer was made by Chang and Bankoff [19]. The Dienes method has great appeal, in that it allows time-varying accelerations, viscous and surface effects, as well as elastic and plastic deformations, all to be treated in an approximate, but consistent manner [20]. For example, the Taylor instability of the lower surface of a liquid layer which is accelerated upwards within a vertical pipe by the expansion of a gaseous phase contained below, can be treated. This problem is of current interest for hypothetical accident scenarios in the liquid-metal fast breeder reactor following a prompt-critical event, or possibly in the light-water reactor after a steam explosion. The energy absorption capability of the upper head of the reactor vessel must be sufficient to withstand the impact of the liquid slug which is thus generated. The kinetic energy of this slug may be greatly reduced by condensation of the hot gas/vapor onto the cold liquid surfaces. The liquid surface area can be increased by several orders of magnitude by droplet entrainment resulting from breakup of the Taylor "spikes" on the lower surface of the liquid slug. Other examples of liquids accelerated within a cylindrical container can be drawn from the liquid-fueled rocket field. In this paper a new class of Taylor waves, consisting of annular ring waves, are analyzed by the Dienes method.

Contributed by the Fluids Engineering Division for publication in the JOURNAL OF FLUIDS ENGINEERING. Manuscript received by the Fluids Engineering Division, April 7, 1983.

Statement of the Problem

Consider the incompressible fluids of differing densities, $\rho_1 > \rho_2$, contained in a vertical pipe of radius r_p, and subjected to a (possibly time-varying) acceleration, $g(t)$, directed from the light fluid to the heavy fluid. The following assumptions are made:

A1. The flow field in both fluids is axisymmetric, and can be described in terms of a velocity potential, except for boundary layers of negligible thickness at the pipe wall and at the interface.

A2. On the other hand, viscous dissipation in the bulk fluids can be included in the mechanical energy balance for the system.

A3. All physical properties of the bulk fluids and the interface between them are constant and independent of space and time.

A4. Velocities and gradients in the tangential direction are zero.

A5. The thickness of two fluid layers, h_1 and h_1, are large enough to have negligible influence on the interfacial instability. This implies that $kh_1 >> 1$, and $kh_2 >> 1$, where k is the fastest-growing wavenumber, to be specified later.

A6. The velocity potential can be aproximated by a single term of the wavenumber generalized-coordinate Fourier expansion, chosen to correspond to the fastest-growing waves.

The justification for A6 appeals entirely to experimental observations, where the later stages of Taylor instability correspond to the characteristic "bubble and spike" configuration with a wavelength close to the linear fastest-growing wavelength. No observations of unstable ring waves have been reported. This is in accord with the present theory, which predicts that the early nonlinear growth is faster for the ring waves, but that infinite velocities, correspond to sharp spikes, are attained later in real time for ring waves than for plane waves.

Analysis

With these assumptions, the velocity potential is approximated by

Copyright © 1984 by ASME

Downloaded 02 Jun 2010 to 171.66.16.91. Redistribution subject to ASME license or copyright; see http://www.asme.org/terms/Terms_Use.cfm

$$\phi(r,z,t) = F(r,z)\,\dot{q}(t)/k^2; \quad \dot{q} \equiv \frac{dq}{dt} \tag{1}$$

where the amplitude function, $q(t)$, may be looked upon as a generalized coordinate. From A1 and A4 it follows that

$$\frac{1}{r}\frac{\partial}{\partial r}\left(r\frac{\partial F}{\partial r}\right) + \frac{\partial^2 F}{\partial z^2} = 0 \tag{2}$$

Therefore, for the heavy fluid in the region $0 \le z \le h_1$ with

$$\phi_1(r,z,t) = \dot{q}\,J_0(kr)\,e^{-kz}/k^2 \tag{3}$$

whereas the light fluid lying in the region $-h_2 \le z \le 0$ has

$$\phi_2(r,z,t) = -\dot{q}\,J_0(kr)\,e^{kz}/k^2 \tag{4}$$

From equations (3) and (4):

$$v_{r1} = \dot{q}\,J_1(kr)\,e^{-kz}/k, \quad v_{z1} = \dot{q}\,J_0(kr)\,e^{-kz}/k \tag{5}$$

$$v_{r2} = -\dot{q}\,J_1(kr)\,e^{kz}/k, \quad v_{z2} = \dot{q}\,J_0(kr)\,e^{kz}/k \tag{6}$$

Therefore

$$\left(\frac{dz}{dr}\right)_1 = \frac{v_{z1}}{v_{r1}} = J_0(kr)/J_1(kr) \tag{7}$$

$$\left(\frac{dz}{dr}\right)_2 = \frac{v_{z2}}{v_{r2}} = -J_0(kr)/J_1(kr) \tag{8}$$

Upon integrating equation (7) from an initial point in the upper fluid (r_0, z_0) to a point (r, z) at time t, one obtains, after employing a well-known indentity

$$z = z_0 + \frac{1}{k}\ln\left[\frac{r\,J_1(kr)}{r_0\,J_1(kr_0)}\right] \tag{9}$$

where

$$r = r_0 + \int_0^t \frac{dr}{dt}\,dt = r_0 + \frac{q(t)}{k}\,e^{-kz_0}J_1(kr_0), \; z \ge 0 \tag{10}$$

Here it has been assumed, without loss of generality, that $q(0) = 0$. It should be noted that, since the path lines are, in general, not coincident with the stream lines in unsteady flow, this does not represent a Lagrangian coordinate system. However, since it is assumed that the particles in the interface remain there (approximately, in the case of interfacial vapor condensation or evaportion in the time scales of interest), equations (9) and (10) may be thought of as representing an implicit solution for the interface shape, if (r_0, z_0) are chosen to lie in the interface initially. It is convenient, but not necessary, to consider an initially planar surface.

Similarly, for the lower fluid we have

$$z = z_0 + \frac{1}{k}\ln\left[\frac{r_0\,J_1(kr_0)}{r\,J_1(kr)}\right] \tag{11}$$

and

$$r = r_0 - \frac{q(t)}{k}\,e^{kz_0}\,J_1(kr_0) \qquad z \le 0 \tag{12}$$

Consider the case where an initially planar surface ($z_0 = 0$) is given a velocity perturbation, and let $z = \eta(r, t)$ be the equation of the interfaces:

$$\eta_1 = \frac{1}{k}\ln[r\,J_1(kr)/r_0\,J_1(kr_0)] \qquad z \ge 0 \tag{13}$$

$$\eta_2 = \frac{1}{k}\ln[r_0\,J_1(kr_0)/r\,J_1(kr)] \qquad z \le 0 \tag{14}$$

Expanding $rJ_1(kr)$ and $r_0J_1(kr_0)$:

$$rJ_1(kr) \cong r_0J_1(kr_0) + k(r-r_0)r_0J_0(kr_0) + 0[k^2(r-r_0)^2] \tag{15}$$

$$r_0J_1(kr_0) \cong rJ_1(kr) + k(r_0-r)rJ_0(kr) + 0[k^2(r_0-r)^2] \tag{16}$$

and substituting

$$r - r_0 = \frac{q}{k}\,J_1(kr_0) \qquad \text{for the heavy fluid, } z \ge 0 \tag{17}$$

$$r_0 - r = \frac{q}{k}\,J_1(kr_0) \qquad \text{for the light fluid, } z \le 0 \tag{18}$$

the same approximate relationship between the interface shape and $q(t)$ is obtained for both fluids.

$$\eta(r,t) \cong \frac{1}{k}\ln[1 + q(t)\,J_0(kr)] \tag{19}$$

The "bubble" nose is at the centertline, where $kr = 0$ and $k\eta = \ln(1+q)$. The "spike" is at $kr_1 = 3.84$, where $J_0(kr)$ has its first minimum (-0.403) and $k\eta = \ln(1 - 0.403\,q)$. Therefore, $0 \le q \le 2.5$.

This analysis thus predicts that the annular ring wave at $kr_1 = 3.84$ will become infinite at a finite time, t_1, such that $q(t_1) = 2.5$. Other singularities will also appear at finite times, $t_j, j = 1, 2, \ldots n$ such that $\{r_j \le r_p$, the pipe radius; $J_1(kr_j) = 0$; $J_0(kr_j) < 0$; $q(t_j) = [-J_0(kr_j)]^{-1}\}$. One also sees from equations (5), (6), (15), and (16) that, to order $(r_j - r_{0j})^2$, the motion at $r = r_j$ is strictly vertical, and hence lies on the surface of a cylinder of radius r_j. For this conclusion to hold it is necessary that the interface motion be expressible in terms of a single fastest-growing wave set, determined by $J_1(kr_p) = 0$, which expresses the fact that radial velocities vanish at the pipe wall. The parameter k, chosen from an infinite set of eigenvalues, must satisfy the condition, to the nearest member of the set, that the growth rate at the first annular ring at $r = r_1$ be maximized.

Nomenclature

- Bo = Bond number, equation (27)
- g = gravity force
- h = height of fluid layer
- k = wave number
- k_m = fastest-growing wave number
- l = dimensionless wave number, $(= k/\beta)$
- l_c = dimensionless cut-off wave number $(= \theta^{-1/2})$
- l_m = dimensionless fastest-growing wave number, equation (25)
- n = linear growth constant equation (24)
- q = generalized coordinate defined by equation (1)
- r = radial distance
- r_p = pipe radius
- t = time
- V_r = radial velocity
- V_z = velocity in z direction
- x = planar coordinate parallel to undisturbed interface
- z = transverse direction
- $\beta = [(\rho_1 + \rho_2)\,g/\sigma]^{1/2}$
- η = height of interface at (r, t)
- $\theta = (\rho_2 - \rho_2)/(\rho_1 + \rho_2)$
- μ = viscosity
- ν = kinematic viscosity
- ρ = density
- σ = surface tension
- ϕ = velocity potential
- ξ = dimensionless composite physical parameter

Superscripts

- $\hat{}$ = dimensionless parameters, equations (26) and (27)
- $\cdot = \dfrac{d}{dt}$

Subscripts

- 1 = heavy fluid
- 2 = light fluid
- 0 = initial condition

Downloaded 02 Jun 2010 to 171.66.16.91. Redistribution subject to ASME license or copyright; see http://www.asme.org/terms/Terms_Use.cfm

Energy Balance

An energy integral is utilized to determine the differential equation satisfied by $q(t)$. An energy balance over the first annular ring, in the absence of mass transfer, states that

$$\sum_{i=1}^{2}\left(\frac{d}{dt}\left\{\int\left[\frac{\rho_i}{2}(v_{r_i}^2+v_{z_i}^2)+\rho_i g z\right]dV_i + \int_0^{r_1}\sigma\left[1+\left(\frac{\partial\eta}{\partial r}\right)^2\right]^{1/2}2\pi r dr-\sigma r_1\right\} + 2\rho_i\nu_i\int(v_{j,k}v_{j,k})_i dV_i\right)=0 \tag{20}$$

where

$$\int dV_1 = 2\pi\int_0^{r_1}\int_{\eta}^{h_1} r\,dr\,dz,\quad \int dV_2 = 2\pi\int_0^{r_1}\int_{-h_2}^{\eta} r\,dr\,dz$$

From the various velocity equations and the interface equation,

$$v_{r1}^2+v_{z1}^2=\frac{\dot q^2}{k^2}e^{-2kz}[J_1^2+J_0^2]$$

$$v_{r2}^2+v_{z2}^2=\frac{\dot q^2}{k^2}e^{2kz}[J_1^2+J_0^2]$$

$$(v_{j,k}v_{j,k})_1=\dot q^2 e^{-2kz}\left[2J_0^2-\frac{2}{kr}J_1J_0+2\left(\frac{J_1}{kr}\right)^2+2J_1^2\right]$$

$$(v_{j,k}v_{j,k})_2=2\dot q^2 e^{2kz}\left[J_0^2-\frac{J_1J_0}{kr}+\left(\frac{J_1}{kr}\right)^2+J_1^2\right]$$

$$\left[1+\left(\frac{\partial\eta}{\partial r}\right)^2\right]^{1/2}=\frac{[q^2J_1^2+(1+qJ_0)^2]^{1/2}}{1+qJ_0}$$

where the summation convention is used with (j, k) taking the meaning (r, z), the comma indicates differentiation, and J_0 and J_1 refer to $J_0(kr)$ and $J_1(kr)$, respectively. Again, $i = 1, 2$ refer to the heavy and light fluids. Equation (20) follows Dienes in balancing the rate of change of kinetic, potential, and surface energy by viscous dissipation. Dienes also shows how to include elastic and plastic deformation energies if one "fluid" is a solid. Upon making the appropriate substitutions for the velocities and the interface, one obtains:

$$\ddot q[\rho_1 A(q)+\rho_2 C(q)]+\dot q^2[\rho_2 D(q)-\rho_1 B(q)] +2kg(\rho_2-\rho_1)E(q)+2k^3\sigma F(q)+4k^2\dot q[\rho_1\nu_1 H(q)+\rho_2\nu_2 K(q)]=0 \tag{21}$$

where

$$\int_0^{r_1}\frac{[J_1^2+J_0^2]rdr}{(1+qJ_0)^2}\equiv A(q)$$

$$\int_0^{r_1}\frac{(J_1^2+J_0^2)J_0}{(1+qJ_0)^3}rdr\equiv B(q)$$

$$\int_0^{r_1}(1+qJ_0)^2(J_1^2+J_0^2)rdr\equiv C(q)$$

$$\int_0^{r_1}(1+qJ_0)J_0(J_1^2+J_0^2)rdr\equiv D(q)$$

$$\int_0^{r_1}\frac{J_0\ln(1+qJ_0)}{1+qJ_0}rdr\equiv E(q)$$

$$\int_0^{r_1}\frac{qJ_1^2rdr}{[q^2J_1^2+(1+qJ_0)^2]^{1/2}(1+qJ_0)^2}\equiv F(q)$$

$$\int_0^{r_1}\frac{\left[J_0^2-\frac{J_1J_0}{kr}+\left(\frac{J_1}{kr}\right)^2+J_1^2\right]rdr}{(1+qJ_0)^2}\equiv H(q)$$

$$\int_0^{r_1}(1+qJ_0)^2\left[J_0^2-\frac{J_1J_0}{kr}+\left(\frac{J_1}{kr}\right)^2+J_1^2\right]rdr\equiv K(q)$$

Note that the acceleration is not necessarily time-independent in equation (21).

The linearized form of equation (21) is

$$\ddot q[\rho_1+\rho_2]\int_0^{r_1}(J_1^2+J_0^2)rdr+2kg(\rho_2-\rho_1)q\int_0^{r_1}J_0^2\,rdr +2k^3\sigma q\int_0^{r_1}J_1^2\,rdr+4k^2\dot q(\rho_1\nu_1+\rho_2\nu_2)\int_0^{r_1}\left[J_0^2-\frac{J_0J_1}{kr}+\left(\frac{J_1}{kr}\right)^2+J_1^2\right]rdr=0 \tag{22}$$

Since r_1 is chosen such that kr_1 is the first zero of $J_1(kr)$, this reduces equation (22) further to

$$\ddot q+4\frac{(\mu_1+\mu_2)}{(\rho_1+\rho_2)}k^2\dot q+\left[\frac{\sigma k^3}{(\rho_1+\rho_2)}-\frac{\rho_1-\rho_2}{\rho_1+\rho_2}kg\right]q=0 \tag{23}$$

which is the same as the linearized equation for $q(t)$ in the Cartesian case [19]. Consequently, the linear growth constant is

$$n=\left[4\left(\frac{\mu_1+\mu_2}{\rho_1+\rho_2}\right)^2k^4-\frac{\sigma k^3}{(\rho_1+\rho_2)}+\frac{(\rho_1-\rho_2)kg}{(\rho_1+\rho_2)}\right]^{1/2} -2\left(\frac{\mu_1+\mu_2}{\rho_1+\rho_2}\right)k^2, \tag{24}$$

for two fluids, identical to the linear growth constant in the plane wave analysis. Let the dimensionless wavenumber l be

$$l=k/\beta,$$

$$\beta=\left[\frac{(\rho_1+\rho_2)g}{\sigma}\right]^{1/2}$$

$$\xi=4\left(\frac{\mu_1+\mu_2}{\rho_1+\rho_2}\right)^2\left[\frac{g(\rho_1+\rho_2)^3}{\sigma^3}\right]^{1/2}$$

$$\theta=(\rho_1-\rho_2)/(\rho_1+\rho_2)$$

In terms of these parameters, equation (24) becomes

$$n=2\beta^2\left(\frac{\mu_1+\mu_2}{\rho_1+\rho_2}\right)\left[\left(l^4+\frac{\theta l}{\xi}-\frac{l^3}{\xi}\right)^{1/2}-l^2\right]$$

Note that $l < l_c = \theta^{1/2}$ corresponds to the cut-off wavenumber. Setting $dn/dl = 0$, the fastest-growing wavenumber, l_m, is given implicity by

$$\xi=(\theta-3l_m^2)^2/8(\theta+l_m^2)\,l_m^3 \tag{25}$$

Define $\hat l_m \equiv l_m\,\theta^{-1/2}$ and $\hat\xi = \xi\theta^{1/2}$ equation (25) is transformed,

$$\hat\xi=(1-3\hat l_m^2)^2/8(1+\hat l_m^2)\hat l_m^3 \tag{26}$$

This agrees exactly with the results obtained by Dienes for a single fluid for two-dimensional plane interfacial waves [16]. Figure 1 shows $\hat l_m$ versus $\hat\xi$ according to equation (26). The linear growth constant described by equation (24) is also plotted in the same graph. For inviscid fluids ($\hat\xi = 0$), the most unstable wave is determined by $\hat l_m = 1/3^{1/2}$. For $\hat\xi > 2/27^{1/2}$, there is only a single unstable wave. For small values

Downloaded 02 Jun 2010 to 171.66.16.91. Redistribution subject to ASME license or copyright; see http://www.asme.org/terms/Terms_Use.cfm

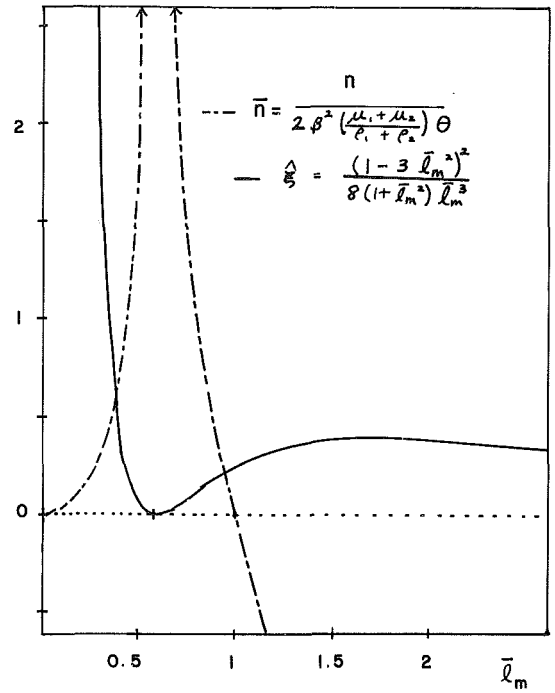

Fig. 1 Dimensionless fastest-growing wavenumber and linear growth constant

of $\hat{\xi}$, there are three possible solutions; one is stable, one is unstable, and one is dependent on the value of $\hat{\xi}$ for stability. It is obvious that only when $\hat{\xi} < 0.25$ do two unstable solutions exist. For the same values of $\hat{\xi}$, the long-wave solution has a more rapidly growing instability than the short-wave solution. Note that the second-fluid density is crucial in making $\hat{\xi}$ small enough to have two unstable modes.

It is assumed that the linearly fastest-growing wavenumber, obtained as the positive real root of $dn/dk = 0$, remains dominant and constant throughout the growth period. The large $\hat{l}_m$ solution (capillary waves) might be expected to show up in the nonlinear growth stage in addition to the long waves.

Equation (21) can be nondimensionalized by using:

$$\dot{Q} = \frac{dq}{d\hat{t}} = \left(\frac{\sigma}{g^3\rho_1}\right)^{1/4}\dot{q}, \quad \xi_1 = \nu_1 k^2\left(\frac{\sigma}{g^3\rho_1}\right)^{1/4}$$

$$\ddot{Q} = \frac{d^2q}{d\hat{t}^2} = \left(\frac{\sigma}{g^3\rho_1}\right)^{1/2}\ddot{q}, \quad \xi_2 = \nu_2 k^2\left(\frac{\sigma}{g^3\rho_1}\right)^{1/4} \tag{27}$$

$$\hat{\rho} = \frac{\rho_2}{\rho_1}, \quad \hat{t} = \left(\frac{g^3\rho_1}{\sigma}\right)^{1/4} t, \quad B_0 = \frac{\rho_1 g}{\sigma k^2}$$

Equation (21) is thus transformed to:

$$\ddot{Q}[A(q)+\hat{\rho}C(q)] + \dot{Q}^2[\hat{\rho}D(q)-B(q)] + 4\dot{Q}[\xi_1 H(q) + \hat{\rho}\xi_2 K(q)] + 2\frac{(\hat{\rho}-1)}{B_0^{1/2}}E(q) + \frac{2F(q)}{B_0^{3/2}} = 0 \tag{28}$$

A basic difficulty with the single-mode two-fluid approximation, as noted previously [19], is that a symmetry is predicted which cannot exist as the "bubble-and-spike" interfacial shapes develops. One sees from equations (7) and (8) that the stream lines are predicted to be mirror images of each other in the two fluids. Fortunately, as shown by the numerical results [19], the presence of the second fluid results in negligible correction to the single-fluid instability growth times if the second fluid is a gas. Even if ρ_1/ρ_2 is as small as 13 (mercury-water) the correction to the single-fluid growth time is only of the order of 10 percent. Hence an accurate description of the light fluid motion is not needed unless the density ratio is less than an order of magnitude.

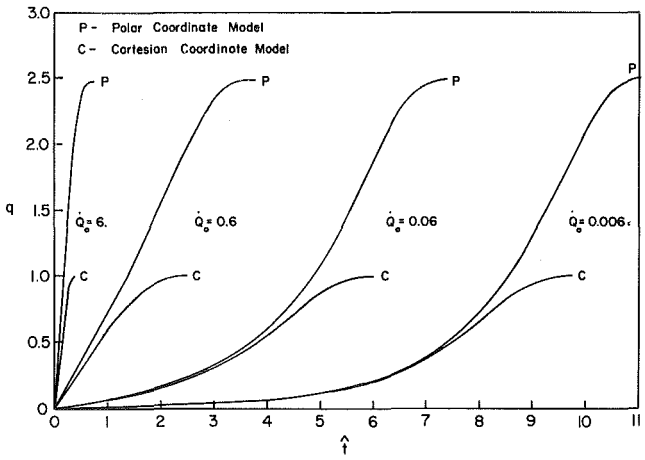

Fig. 2 Water-steam system at $k = k_m$

Numerical Results

The water/steam system at 107°C and 1.28 atmosphere was chosen for numerical calculations. The fastest-growing wavenumber based on equation (24), is then a function of acceleration; r_1 is also a function of acceleration, as shown below:

g (m/s^2)	k_m (m^{-1})	$r_1 = \frac{3.84}{k_m}$ (m)
9.8	238	.0161
98	754	.0051
980	2384	.00161

Choosing $\dot{Q}_0$ and g determines the initial conditions. Figure 2 shows the results of numerical integrations of equation (28), compared to the results of the plane wave [19] analysis, for various initial velocity perturbations, $\dot{Q}_0$.

The variation of dimensional time at which the spike velocity becomes effectively infinite for a range of values of $\dot{Q}_0$ and g is tabulated below:

	$g = 9.8$ m/s^2		$g = 98$ m/s^2		$g = 980$ m/s^2	
$\dot{Q}_0$	t_+	t_0	t_+	t_0	t_+	t_0
.6	6.2×10^{-3}	1.3×10^{-2}	1.1×10^{-3}	2.3×10^{-3}	2.0×10^{-4}	4.1×10^{-4}
.6	4.0×10^{-2}	5.9×10^{-2}	7.2×10^{-3}	1.1×10^{-2}	1.3×10^{-3}	1.9×10^{-3}
.06	9.6×10^{-2}	1.2×10^{-1}	1.7×10^{-2}	2.1×10^{-2}	3.0×10^{-3}	3.9×10^{-3}
.006	1.5×10^{-1}	1.8×10^{-1}	2.7×10^{-2}	3.2×10^{-2}	4.9×10^{-3}	5.9×10^{-3}

where t_+ is the plane wave time, and t_0 is the ring wave, both in seconds.

In practice the spike tips will detach, forming entrained droplets. One sees that the onset of entrainment from the annular waves, even though it is slower than from plane waves, is still very rapid for large accelerations, and is still in agreement with a preliminary steam-water shock tube study [21], in which the asymptotic regime was attained in a time less than 0.17 ms for all imposed acceleration on the order of 4000 m/s^2.

Downloaded 02 Jun 2010 to 171.66.16.91. Redistribution subject to ASME license or copyright; see http://www.asme.org/terms/Terms_Use.cfm

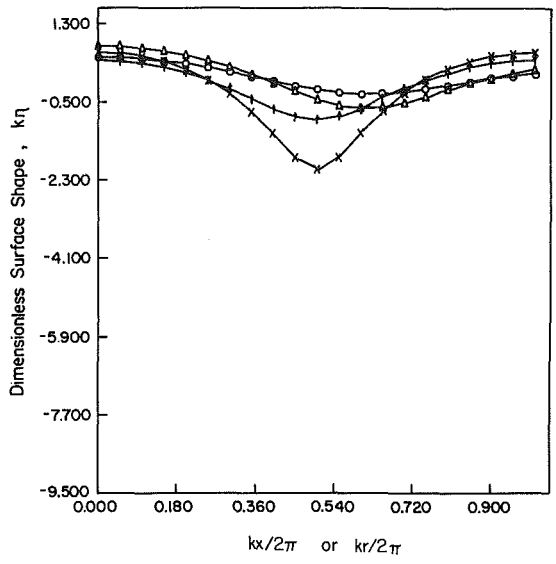

Fig. 3(a) Dimensionless surface interface

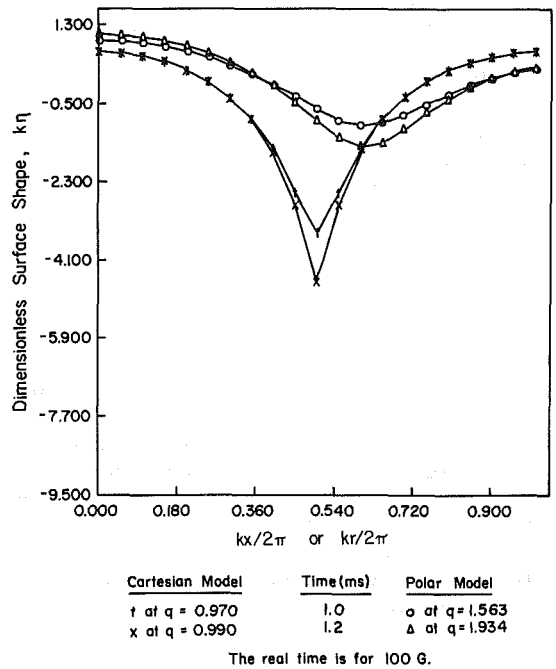

Fig. 3(b) Dimensionless surface interface

Figure 3 compares the deformation of the interface for the two types (plane and annular) of waves. It is of interest that the bubble growth for the annular waves at the pipe centerline is faster than for plane waves, and the spike position is shifted slightly.

Conclusions

The analysis shows that the linear growth constant for ring waves is the same as for plane waves. The present formulation also predicts infinite spike velocities ($q = 2.5$) at very small times ($\sim 10^{-3} - 10^{-4}$ s for 100 G). Even so, this is about ~ 1.2 times that predicted for plane waves for small initial perturbations, which may account for the fact annular Taylor

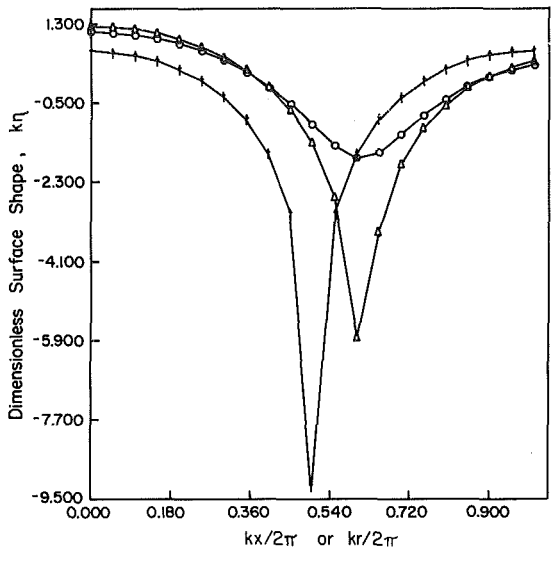

Fig. 3(c) Dimensionless surface interface

waves have not been reported experimentally in cylindrical geometries.

References

1 Lewis, D. J., "The Instability of Liquid Surfaces When Accelerated in a Direction Perpendicular to Their Planes, II," *Proc. Roy. Soc.* (London), Series A202, 1950, p. 81.

2 Emmons, H. W., Chang, C. T., and Watson, B. C., "Taylor Instability of Finite Surface Waves," *Journal of Fluid Mechanics*, Vol. 7, 1960, p. 177.

3 Cole, R. L., and Tankin, R. S., "Experimental Study of Taylor Instability," *Physics of Fluids*, Vol. 16, 1973, p. 1810.

4 Corradini, M. L., "Heat Transfer and Fluid Flow Aspects of Fuel-Coolant Interactions," Ph.D. thesis, Mass. Inst. of Tech., 1978.

5 Tobin, R. J., and Cagliostro, D. J., "Effects of Vessel Internal Structures on Simulated HCDA Bubble Expansions," SRI Project PYU-3929, 1978.

6 Christopher, D. M., "Transient Development of a Two Phase Jet," MS thesis, Purdue Univ., 1977.

7 Rayleigh, *Scientific Papers*, Vol. II, Cambridge, England, 1900, p. 200.

8 Lamb, H., *Hydrodynamics*, 6th ed., Dover, New York, 1932.

9 Taylor, G. I., "The Instability of Liquid Surfaces When Accelerated in a Direction Perpendicular to Their Planes, I," *Proc. Roy. Soc.* (London), Series A201, 1950, p. 192.

10 Bellman, R., and Pennington, R. H., "Effects of Surface Tension and Viscosity on Taylor Instability," *Quarterly Journal of Applied Mathematics*, Vol. 12, No. 2, 1954, p. 153.

11 Ingraham, R. L., "Taylor Instability of the Interface Between Superposed Fluids—Solution by Successive Approximations," *Proc. Phys. Soc.* (London), Series B67, 1954, p. 748.

12 Bankoff, S. G., *Physics of Fluids*, Vol. 2, 1959, p. 576.

13 Chandrasekhar, S., *Hydrodynamics and Hydromagnetic Stability*, Clarendon Press, Oxford, England, 1961, Chapter 10.

14 Daly, B. J., "Numerical Study of the Effect of Surface Tension on Interface Instability," *The Physics of Fluids*, Vol. 12, 1969, p. 1340.

15 Nayef, A. H., "On the Non-linear Lamb-Taylor Instability," *Journal of Fluid Mechanics*, Vol. 38, 1969, p. 619.

16 Dienes, J., "Method of Generalized Coordinates and an Application to Rayleigh-Taylor Instability," *The Physics of Fluids*, Vol. 21, 1978, p. 736.

17 Fermi, E., "Taylor Instability of an Incompressible Liquid," Appendixes to LA-1862, LA-1927, Los Alamos Scientific Laboratory, 1956.

18 Miles, J. W., and Dienes, J. K., "Taylor Instability in a Viscous Liquid," *The Physics of Fluids*, Vol. 9, 1966, p. 2518.

19 Chang, I. H. M., and Bankoff, S. G., "Nonlinear Taylor Instability of a Plane Interface between Two Incompressible Fluids with Interfacial Mass Transfer," *AIChE Journal*, Vol. 29, 1983, p. 95.

20 Cooper, F., and Dienes, J., "The Role of Rayleigh-Taylor Instabilities in Fuel-Coolant Interactions," *Nuclear Science and Engineering*, Vol. 68, 1978, p. 308.

21 Bankoff, S. G., Berthoud, G., Delhaye, J. M., and Pion, A., "Rayleigh-Taylor Instabilities with Condensation in a Steam-Water Shock Tube," presented at European Two-Phase Flow Group Meeting, Eindhoven, Netherlands, 1981.

Downloaded 02 Jun 2010 to 171.66.16.91. Redistribution subject to ASME license or copyright; see http://www.asme.org/terms/Terms_Use.cfm

On End Wall Effects in a Lid-Driven Cavity Flow

J. R. Koseff
Assistant Professor.

R. L. Street
Professor of Fluid Mechanics and Applied Mathematics. Mem. ASME

Department of Civil Engineering, Stanford University, Stanford, CA 94305

Experiments were conducted in a three-dimensional lid-driven cavity flow to study the effects of the end walls on the size of the downstream secondary eddy. The ratio of cavity depth to cavity width is 1:1. The span of the cavity was varied such that span-to-width ratios of 3:1, 2:1, and 1:1 were obtained. Flow visualization was accomplished by the thymol blue technique, and by rheoscopic liquid illuminated by laser-light sheets, for Reynolds numbers (based on lid speed and cavity width) between 1000 and 10,000. The results indicate that the corner vortices present at the end walls, in the region of the downstream secondary eddy, are a major influence on the size of this eddy. In addition, as the span of the cavity is reduced the size of the downstream secondary eddy at the symmetry plane becomes smaller with increasing Reynolds numbers, for Reynolds numbers greater than 2000.

1 Introduction

The lid-driven flow in a rectangular cavity has been used extensively by numerical modelers as a test bed for computational schemes. As a result of large differences in results obtained by the various schemes an experimental program was begun to provide a relevant data base for this flow. In previously reported studies [1, 2] we focused on, among others, the characteristics of the (so called) downstream secondary eddy (defined in detail below; see also Fig. 1) with extensive flow visualization studies. The ratio of cavity span to width, commonly referred to as spanwise-aspect-ratio (SAR), was 3:1 (for purely two-dimensional flow SAR = ∞:1).

Interestingly, when the sizes of the downstream secondary eddy (DSE) predicted by accurate two-dimensional (2-D) numerical simulations are compared over a range of flows to the experimental measurements made on the cavity symmetry plane, the agreement was qualitatively quite good and the trend was quantitatively represented. However, the experiments of Pan and Acrivos [3], performed in a cavity with a SAR of 1:1, showed an opposite trend. That is, the DSE shrank as Reynolds number (Re) increased. (Here, $\mathrm{Re} = U_B B/\nu$, where U_B is the velocity of the lid, B is the cavity width, and ν is the kinematic viscosity of the fluid.)

The three-dimensional (3-D) simulations by de Vahl Davis and Mallinson [4], Gresho and Upson [5], and Humphrey and To [see Koseff et al. (6)] raised some interesting questions concerning the specific nature of the three-dimensionality of the flow. For example, de Vahl Davis and Mallinson [4] demonstrated the sensitivity of the solution to the spanwise-aspect-ratio. They showed that, as this ratio becomes smaller, the strength of the symmetry plane flow was reduced. A similar result was obtained experimentally by Bogatyrev and Gorin [7] in a channel cut-out of square cross section. They found that for laminar flows the velocity distribution, in the symmetry plane, was dependent on the SAR of the cavity. For turbulent flows this dependence was less significant. They also found that the effect of the end-walls on the flow increased with decreasing SAR and that the three-dimensionality of the flow is (in part) due to the "decelerating effect of the end-wall."

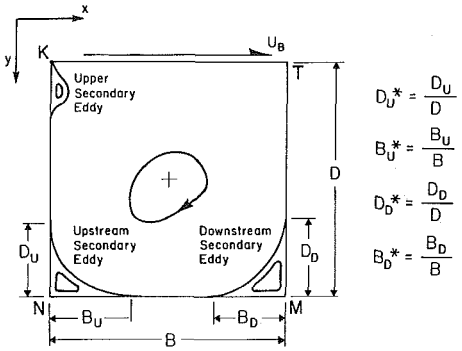

Fig. 1 Lid-driven cavity flow definition sketch

A further significant result was obtained by Koseff et al. [8, this issue] who made velocity measurements in a cavity with a spanwise-aspect-ratio of 3:1. They showed that the flow at the symmetry plane is significantly weaker, for a particular Re, than that predicted by the accurate 2 – D numerical solutions of Ghia et al. [9], Agarwal [10], Schreiber and Keller [11], and Gresho et al. [12].

In view of the above, we were led to perform visualization experiments to study the effects of the end walls on the flow, i.e., to study the effects of spanwise-aspect-ratio. A description of the experimental apparatus and visualization techniques used is given by Koseff and Street ([8], this issue). Subsequent sections of this paper describe the general features of the cavity flow which are relevant to this paper, and the observations made from the experiments. Our measurement program was focused on the size of the downstream secondary eddy as a function of Reynolds number and spanwise-aspect-ratio. Finally, we outline a physically-based rationale for the observed behavior in terms of cavity end-wall effects.

2 Observations

2.1. General Comments. Figure 2 is a schematic

Contributed by the Fluids Engineering Division for publication in the JOURNAL OF FLUIDS ENGINEERING. Manuscript received by the Fluids Engineering Division, October 17, 1983.

Copyright © 1984 by ASME

Downloaded 02 Jun 2010 to 171.66.16.91. Redistribution subject to ASME license or copyright; see http://www.asme.org/terms/Terms_Use.cfm

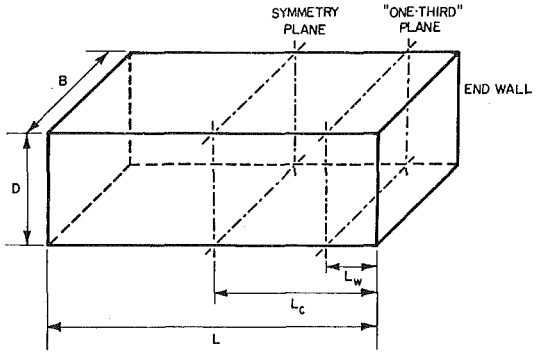

SAR	3:1	2:1	1:1
$\frac{L}{(cm)}$	45	30	15
$\frac{L_c}{(cm)}$	22.5	15	7.5
$\frac{L_w}{(cm)}$	7.5		

Fig. 2 Schematic showing cavity dimensions for various spanwise-aspect-ratios

showing the cavity dimensions for the various spanwise-aspect-ratios. (See Koseff and Street [8] in this issue for cavity definition sketches.) The typical time-averaged flow structure on a central vertical plane that is parallel to the direction of lid motion is sketched in Fig. 1. This plane is the symmetry plane.

Significant three-dimensional motions are present; some were described in Koseff and Street [1]. Because the end-walls appear to be an important reason for the three-dimensionality of the flow, this study focuses on a closer examination of the end-wall effects, particularly their effect on the size of the downstream secondary eddy (DSE). In the following sections we examine the dependence of the nondimensional DSE size D_D^* ($=D_D/D$: see Fig. 1) on Reynolds number (Re) and spanwise-aspect-ratio (SAR) in the case in which the vertical cross-section is square, i.e., $D=B$.

The quantitative data was obtained from a set of experiments in which Re was varied from 1000 to 10,000 for each specific SAR. To achieve the variable SAR we designed a false-wall insert which, when in place, forms two cavities, one with a SAR of 2:1 and one with a SAR of 1:1. In this fashion results for spanwise-aspect-ratios of 1:1, 2:1 and 3:1 were obtained. The experiments involved varying Re and SAR and determining the size of the downstream secondary eddy by analysis of the flow visualization photographs. Figure 3 shows the two different views of the cavity which were photographed; View A is an end view of the cavity, while View B is a side view. Since the flow is symmetric about the center plane, only half of the side view was photographed.

The dimensions of the secondary eddies, D_D, B_D, D_U, and B_U (see Fig. 1) were obtained from scaling large photographs of the flow. Average values obtained from 3 or 4 different photographs of the flow at each Re were used in the plot of D_D^* versus Re shown in Fig. 4. Because of the difficulty in locating the exact position of the separation and reattachment

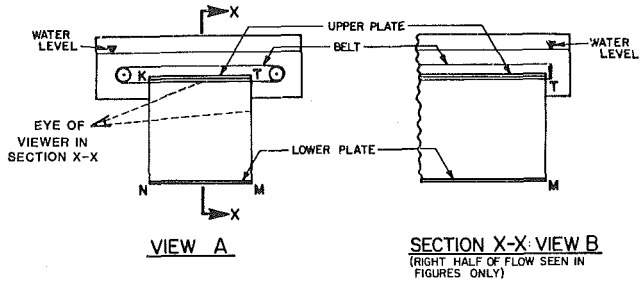

Fig. 3 Schematic of cavity planes depicted in photographs

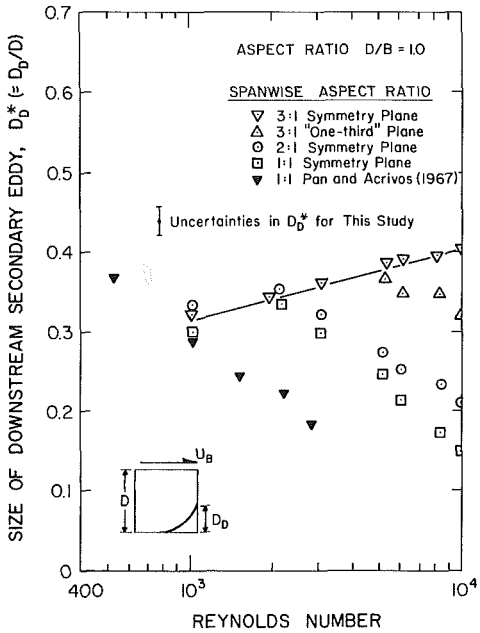

Fig. 4 Downstream secondary eddy as a function of Re and SAR

"points" from a pathline photograph (see, for example, Fig. 5) a fairly large uncertainty was ascribed to this procedure. The uncertainty in D_D^* (see Fig. 4), which is typical for all secondary eddy dimensions, is ± 0.04.

2.2 Downstream Secondary Eddy. The quantitative results obtained from the experiments are shown in Fig. 4, in which the variation in the size of the DSE (D_D^*) is plotted as a function of Re. On the symmetry plane D_D^* decreases with increasing Re (>2000) for spanwise-aspect-ratios of 2:1 and 1:1 in contrast to the trend for a SAR of 3:1. This result is illustrated by two sets of photographs.

First, by comparing Figs. 5(*a*) and 5(*b*), which show the flow at the symmetry plane for Reynolds numbers of 3300 and 5700, respectively, and an SAR = 1:1, we can see that D_D^* now decreases, as Re increases, from 0.28 (Re = 3300) to 0.23 (Re = 5700). Second, by comparing Figs. 6 and 5(*a*), which show the flow at the symmetry plane for spanwise-aspect-ratios of 3:1 and 1:1, respectively, and a Re = 3300, we can see that D_D^* is larger for the SAR = 3:1 case (0.35) than for

Nomenclature

B = width of the cavity
B_D = horizontal extent of downstream secondary eddy
B_U = horizontal extent of upstream secondary eddy
BL = boundary layer
D = depth of cavity
D_D = vertical extent of downstream secondary eddy
D_U = vertical extent of upstream secondary eddy
d_r = reattachment length
DSE = downstream secondary eddy
h = step height
L = span of the cavity
L_C = distance from end wall to symmetry plane
L_w = distance from end wall to "one-third" plane
Re = Reynolds number ($=U_B B/\nu$)
SAR = spanwise aspect ratio, L/B
U_B = speed of cavity lid
ν = kinematic viscosity of the fluid
ψ_{max} = maximum value of the stream function
$*$ = non-dimensional variable

Downloaded 02 Jun 2010 to 171.66.16.91. Redistribution subject to ASME license or copyright; see http://www.asme.org/terms/Terms_Use.cfm

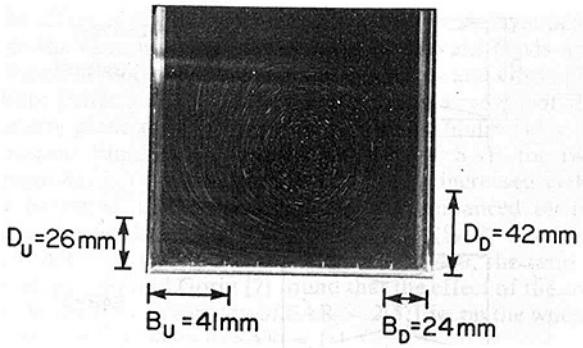

Fig. 5(*a*)

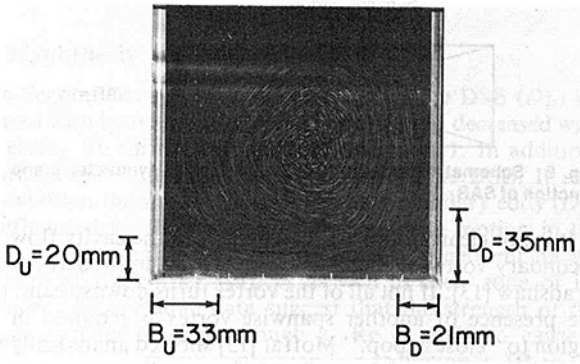

Fig. 5(*b*)

Fig. 5 Flow at symmetry plane for (*a*) Re = 3300, and (*b*) Re = 5700, SAR = 1:1. (View A, Fig. 3)

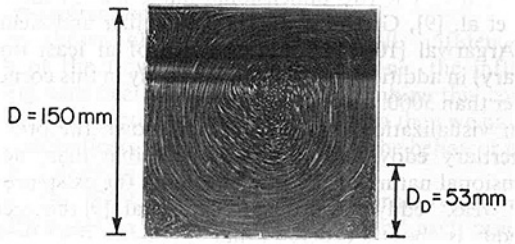

Fig. 6 Flow in symmetry plane for Re = 3300, SAR = 3:1 (View A, Fig. 3)

the SAR = 1:1 case (0.28). This trend is also present in the "one-third" plane (SAR = 3:1) at a Re of 5000 and above. The "one-third" plane (see Fig. 2) is parallel to the end-wall and 7.5 cm from it. (As a point of interest, because the distance to the symmetry plane is 7.5 cm for an SAR of 1:1, the 3:1 "one-third" plane and 1:1 symmetry plane are physically "coincident.")

2.3 Corner Vortex. A fourth major secondary structure, which is not seen when the flow is studied from View A (see Fig. 3), has a significant influence on the flow and is the most evident manifestation of three-dimensionality in the flow. The structure, which is termed the "corner vortex," originates from the adjustment of the shear and pressure forces acting on the recirculating fluid to the no-slip condition imposed by the presence of the end-walls. An example of a corner vortex is shown in Fig. 6(*b*) of Koseff and Street ([8], this issue), for a flow with Re = 6000 and SAR = 3:1. In this picture the flow in a plane parallel to the downstream wall of the cavity and 35 mm from it is visualized from View B (see Fig. 3) using rheoscopic liquid; the corner vortex is on the right edge of the flow. The other significant structures present are Taylor-Görtler-like vortices [1, 2].

2.4. Spanwise Motions. The spiralling motion of the fluid in the downstream secondary eddy (DSE) is illustrated in Fig. 7. Figure 7(*a*) (View A in Fig. 3) shows a dye streak marking a counter-clockwise spiral moving toward the end-wall for a Re of 5000 and SAR = 3:1. [This streak was generated using the thymol blue technique with a wire electrode in the region of the DSE (see Koseff and Street, [1, 8].) This outflow, which has a spiralling character, seemed to be more pronounced in the region of the end-wall and became stronger with increasing Re. The outflow then seems to become part of the corner vortex at the end-wall as shown in Fig. 7(*c*).

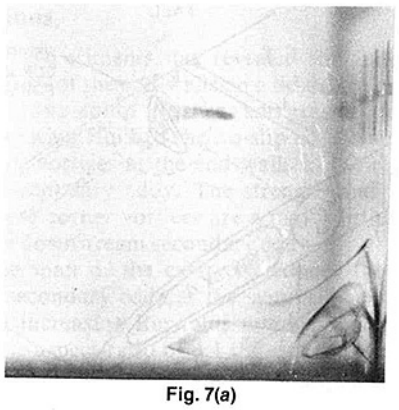

Fig. 7(*a*)

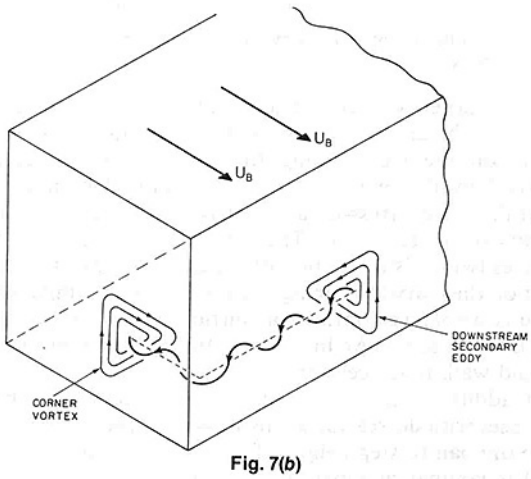

Fig. 7(*b*)

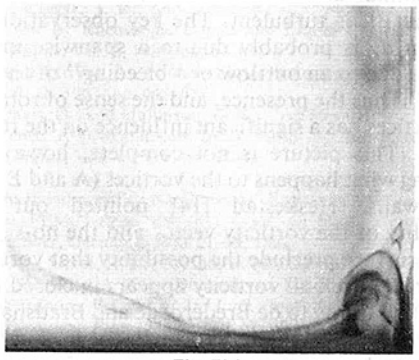

Fig. 7(*c*)

Fig. 7(*a*) Counter-clockwise spiral toward end-wall in DSE for Re = 5000, SAR = 3:1. (*b*) Schematic illustrates how outflow becomes part of corner vortex as shown in (*c*). (View A, Fig. 3, right-hand side only.)

3 Conceptual Views

3.1. Corner Vortex.

Concept. de Brederoede and Bradshaw [13] performed a set of experiments to illustrate the three-dimensional effects arising at the side walls which bound a "two-dimensional" separated flow. The flow, a rearward-facing step, is shown in schematic form in Fig. 8. They found structures in the region of the end-walls, around the zone of reseparation which they

Downloaded 02 Jun 2010 to 171.66.16.91. Redistribution subject to ASME license or copyright; see http://www.asme.org/terms/Terms_Use.cfm

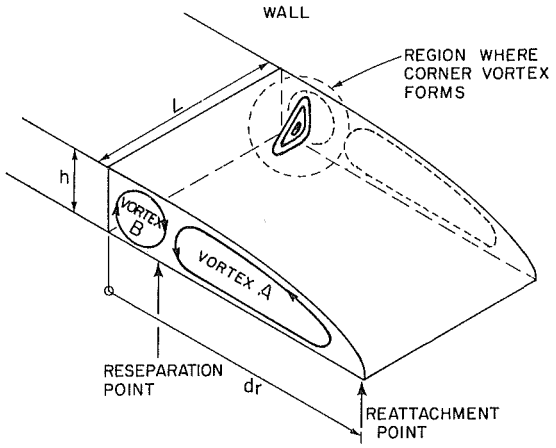

Fig. 8 Definition sketch of Rearward Facing Step (after de Brederoede and Bradshaw [13])

termed corner vortices. These vortices, they explain, are originated by an adjustment of the shear and pressure forces acting on the recirculating fluid to the no-slip condition imposed by the presence of physical lateral boundaries. In general, these stress-induced effects are confined to the vicinity of the end-walls. The sense of rotation of the corner vortices (which is a function of the character of the boundary layer on the rearward-facing step) seems to determine whether there is a spanwise inflow or outflow in vortex filaments A and B (see Fig. 8). (An inflow is defined as a net motion from the end-walls to the centerplane.)

In addition they found that the reattachment length d_r increases with decreasing spanwise-aspect-ratio (SAR $\equiv L/h$: ratio of span to step height) if the oncoming boundary layer (BL) is laminar at separation but decreases with decreasing SAR if the BL is turbulent. The key observation is that an increase in d_r is probably due to a spanwise inflow and a decrease is due to an outflow or "bleeding" of the separation "bubble." Thus the presence, and the sense of rotation, of the corner vortices has a significant influence on the reattachment length d_r. This picture is not complete, however, without considering what happens to the vortices (A and B in Fig. 8) at the end-walls. Heskestad [14] pointed out that "the solenoidality of the vorticity vector and the no-slip condition at a solid surface preclude the possibility that vortex lines end on the surface, i.e., all vorticity appears in closed loop." This condition according to de Brederoede and Bradshaw forces (*a*) part of the bubble main "vortex" (A in Fig. 8) to turn downstream close to the side-walls giving rise to a horseshoe-like vortex system and (*b*) the other part to close a loop with vortex filament B.

Application. The rationale behind the experimental finding of de Brederoede and Bradshaw [13] can be applied to the lid-driven cavity flow and especially to the region of the downstream secondary eddy. The cavity flow is similar to the rearward-facing step because both exhibit a secondary flow system as a result of separation and end-walls which influence the flow.

The spanwise spiralling motions of the fluid in the downstream secondary eddy (Fig. 7) are the result of the presence of corner vortices which drive the spanwise motions. The sense of rotation of these vortices is consistent with the spanwise outflow found in the visualization experiments. The process by which the dye streak showing the spiralling spanwise outflow (Fig. 7(*a*)) "becomes part" of the corner vortex (Fig. 7(*c*)) is driven by the corner vortex Fig. 7(*b*): the no-slip condition and vorticity vector solenoidality requirement forcing the eddy (at least the part shown by the dye) to turn downstream (relative to the local primary circulation direction).

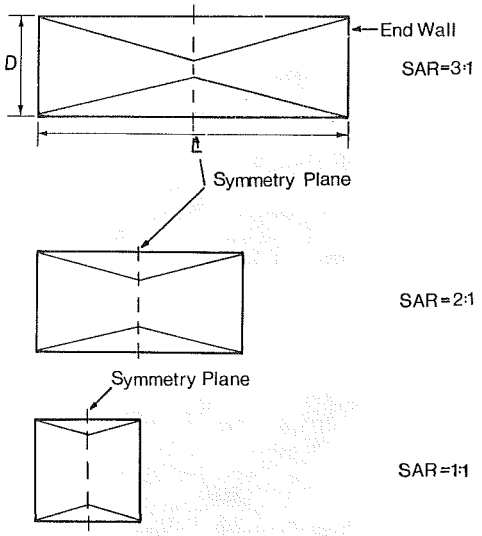

Fig. 9 Schematic model of end-wall effect at symmetry plane as a function of SAR

It is not clear, at this stage, whether, in the cavity flow, the secondary vortex "splits" as described by de Brederoede and Bradshaw [13]. If not all of the vortex turns downstream, then the presence of another spanwise vortex is required in this region to "close a loop." Moffat [15] showed analytically that an infinite series of "rapidly diminishing" counter-rotating vortices would be present in a corner flow. Thus one would expect such a series of vortices in the downstream secondary eddy corner. The two-dimensional numerical calculations of Ghia et al. [9], Gresho et al. [12], Schreiber and Keller [11], and Argarwal [10] show the presence of at least one eddy (tertiary) in addition to the secondary eddy in this corner at Re greater than 5000.

Our visualization studies have not shown the presence of the tertiary eddy and it is quite possible that the three-dimensional nature of the flow precludes the existence of this very "weak" eddy. According to Ghia et al. [9] the strength of this eddy is about 3 orders of magnitude less than that of the primary cell at a Re = 10,000. Therefore, we are led to believe that the secondary eddy does not "split" but rather turns downstream in its entirety and enters the corner vortex.

3.2. End-Wall Effects. The shear stress developed at the end-walls causes a local decrease in the mean kinetic energy resulting in weaker flow in the end-wall region. In general, the magnitude of this effect is a function of the roughness of the wall, the shear velocity at the wall, and the distance from the wall. The magnitude of this "kinetic-energy-sink-effect" increases as the roughness and shear velocity increase and distance from the wall decreases. Therefore, the nature of the flow at the symmetry plane (or any plane) is a function of the proximity of the end-wall to this plane, e.g., as represented by the spanwise-aspect-ratio (SAR).

Consider, therefore, the effect of the end-walls at the symmetry plane of the cavity as shown by the schematic model in Fig. 9. Because the wall is smooth in all of our experiments we plausibly assume that for a given Re the sink effect's magnitude is dependent only on distance from the wall. If (for the purposes of this argument only) the relationship is taken to be linear, the increased influence of the end-walls on the flow at the symmetry plane as the SAR reduces is quite dramatic (Fig. 9). Extending this point further, consider a case in which SAR is constant, but in which Re is varied. Since the shear velocity at the wall is a function of Re, the effect of the end-wall at any point some distance from the wall will increase with increasing Re. Thus, the effects of the end-walls at the symmetry plane are greater at Re = 10,000 than at Re = 1000.

Downloaded 02 Jun 2010 to 171.66.16.91. Redistribution subject to ASME license or copyright; see http://www.asme.org/terms/Terms_Use.cfm

The effect of the end-walls on the motion at the symmetry plane was demonstrated numerically by de Vahl Davis and Mallinson [4] and experimentally by Bogatyrev and Gorin [7]. de Vahl Davis and Mallinson compared the strength of the symmetry plane motion (in terms of the maximum value of the stream function ψ_{max}) as a function of SAR for two different Re. For a given Re, the value of ψ_{max} increased as the SAR increased. In addition this effect is enhanced by increased Re: for Re = 100, the ratio of ψ_{max} (SAR = 1:1) to ψ_{max} (SAR = ∞) is 0.88, whereas for Re = 400, the ratio is 0.66. Bogatyrev and Gorin [7] found that the effect of the end walls on the flow in a cavity of SAR = 2.5:1 is, on the whole, smaller than in a cavity of SAR = 1:1.

4 Hypothesis

In Section 2 we showed that the size of the DSE (D_D^*) increased with increasing Re for SAR = 3:1, and decreased with increasing Re for SAR = 2:1 and SAR = 1:1. In addition, spanwise spiralling motions were found in the DSE. It also appears that the size of the downstream secondary eddy (D_D^*) is influenced by the strength of the spanwise motion in the eddy. The strength of the motion itself is dependent on the strength of the corner vortices as well as their zone of influence. The available data suggest that the strength of the corner vortices is large enough at Re > 5000 to cause a significant outflow and consequently a reduction in D_D^* in the "one-third" plane region (see Fig. 2). (Bogatyrev and Gorin [7], in fact, attribute some of the observed variations in flow characteristics to the "three-dimensional nature of the secondary corner vortices."]

It was shown above that the end-walls influence the strength of the flow at the symmetry plane, the influence increasing with decreasing SAR. If we combine this concept with the corner-vortex-spanwise-motion idea then we have the essential ingredients for our hypothesis on the behavior of the DSE. The following scenario emerges.

1. As the SAR decreases, (i) the corner vortices are physically closer to the symmetry plane (and each other) so that their effect at the symmetry plane is greater and (ii) the "kinetic-energy-sink" effect of the end-walls at the symmetry plane is enhanced. (Because of this effect being greater at the symmetry plane at the smaller SAR's, the "effective" Re of the flow may be lower, i.e., the SAR = 3:1 Re = 5000 case may be "equivalent" to the SAR = 1:1 Re = 8000 case. On this basis alone one would expect D_D^* to be smaller at a similar Re for SAR = 1:1 than 3:1.)

2. As the Re increases, the corner vortices become stronger resulting in a more pronounced spanwise outflow in the region of the downstream secondary eddy. Therefore, the outflow induced by the stronger (and closer) corner vortices becomes more pronounced relative to the "weakened" symmetry plane motion, resulting in a shrinking downstream secondary eddy.

We end this subsection with two additional comments. First, the sizes, D_D^*, of the DSE in our experiments with SAR = 1:1 are similar in trend to those of Pan and Acrivos [3] but not in magnitude (see Fig. 4). This must be due to their use of a cylinder to drive the flow rather than a flat lid. The cylinder, which penetrated into the cavity to a maximum depth of about 10 percent of the cavity depth, produces significant differences in the flow and any comparisons between experiments should be made with discretion. Second, the 2-d numerical simulations of Nallasamy and Krishna Prasad [16] also show a trend in which D_D^* decreases with increasing Re. In their simulations the result is nonphysical and due to the effect of false diffusion resulting from use of an upwind difference scheme. The false diffusion is, then, the numerical equivalent of end-walls.

5 Conclusions

This set of experiments has revealed the following concerning the effect of the end-walls on a lid driven cavity flow:

(*a*) The adjustment of the shear and pressure forces acting on the recirculating fluid to the no-slip condition at the end walls produces vortices at the end walls in the region of the downstream secondary eddy. The strength and zone of influence of these corner vortices are a major influence on the size D_D^* of the downstream secondary eddy.

(*b*) As the span of the cavity is reduced the size of the downstream secondary eddy at the symmetry plane becomes smaller, with increasing Reynolds number, for Re > 2000. For a spanwise-aspect-ratio of 3:1 the size of the downstream secondary eddy at the "one-third" plane becomes smaller at Re > 5000. Thus, the size of this secondary eddy is not uniform over the span of the cavity, but becomes smaller toward the end-walls.

(*c*) The spanwise motions in the downstream secondary eddy suggest the presence of a circulation cell system perpendicular to the main cell system.

Acknowledgments

This work was performed in the Stanford University Environmental Fluid Mechanics Laboratory and was supported by National Science Foundation Grant CME-7921324 and by the Division of Engineering, Mathematical and Geosciences, Office of Basic Energy Sciences, Department of Energy Contract No. DOE-DE-AT03-81-ER-10867.

References

1 Koseff, J. R., and Street, R. L., "Visualization Studies of a Shear Driven Three-Dimensional Recirculating Flow," ASME JOURNAL OF FLUIDS ENGINEERING, Vol. 106, No. 1, 1984, pp. 21-29.

2 Rhee, H., Koseff, J. R., and Street, R. L., "Flow Visualization of a Recirculating Flow by Rheoscopic Liquid and Liquid Crystal Techniques," *Experiments in Fluids*, Vol. 2, 1984, pp. 57-64.

3 Pan, F., and Acrivos, A., "Steady Flows in Rectangular Cavities," *Jour. Fluid Mech.*, Vol. 28, 1967, pp. 643-655.

4 de Vahl Davis, G., and Mallinson, G. D., "An Evaluation of Upwind and Central Difference Approximations by a Study of Recirculating Flow," *Computers and Fluids*, Vol. 4, 1976, pp. 29-43.

5 Gresho, P. M., and Upson, C. D., "Current Progress in Solving the Time-Dependent Incompressible Navier-Stokes Equations in Three-Dimensions by (Almost) the FEM," *Proc. 4th Int'l Conf. on Finite Element in Water Resources*, Hannover, Germany, June 21-25, 1982.

6 Koseff, J. R., Street, R. L., Gresho, P. M., Upson, C. D., Humphrey, J. A. C., and To, W.-M., "A Three-Dimensional Lid-Driven Cavity Flow: Experiment and Simulation," *Proc. of 3rd Int'l. Conf. on Numerical Methods in Laminar and Turbulent Flow*, University of Washington, Seattle, Aug. 11, 1983, pp. 564-581.

7 Bogatyrev, V. Ya., and Gorin, A. V., "End Effects in Rectangular Cavities," *Fluid Mechanics—Soviet Research*, Vol. 7, No. 4, July-Aug, 1978, pp. 101-106.

8 Koseff, J. R., and Street, R. L., "The Lid-Driven Cavity Flow: a Synthesis of Qualitative and Quantitative Observations," ASME JOURNAL OF FLUIDS ENGINEERING, published in this issue, pp. 390-398.

9 Ghia, U., Ghia, K. N., and Shin, C. T., "Solution of Incompressible Navier-Stokes Equations by Coupled Strongly Implicit Multi-Grid Method," *J. Comp. Phys.*, Vol. 48, 1982, pp. 387-411.

10 Agarwal, R. K., "A Third-Order-Accurate Upwind Scheme for Navier-Stokes Solutions at High Reynolds Numbers," AIAA 19th Aerospace Sciences Meeting, St. Louis, Jan. 12-15, 1981.

11 Schreiber, R., and Keller, H. B., "Driven Cavity Flows by Efficient Numerical Techniques," *Jour. Comput. Physics*, Vol. 49, 1983, pp. 310-333.

12 Gresho, P. M., Chan, S. T., Upson, C. D., and Lee, R. L., "A Modified Finite Element Method for Solving the Time-Dependent, Incompressible Navier-Stokes Equations," submitted to *Jour. for Numerical Methods in Fluids*, 1983.

13 de Brederoede, V., and Bradshaw, P., "Three Dimensional Flow in Nominally Two-Dimensional Separation Bubbles I. Flow Behind a Rearward Facing Step," I. C. Aero Report 72-19, Aug. 1972.

14 Heskestad, G., "Remarks on Snow Cornice Theory and Related Experiments with Sink Flows," ASME Winter Meeting, Chicago, IL, Nov. 7-11, 1965.

15 Moffat, H. K., "Viscous and Resistive Eddies Near a Sharp Corner," *Jour. Fluid Mech.*, Vol. 18, 1964, pp. 1-18.

16 Nallasamy, M., and Krishna Prasad, K., "On Cavity Flow at High Reynolds Numbers," *Jour. Fluid Mech.*, Vol. 79, 1977, pp. 391-414.

Downloaded 02 Jun 2010 to 171.66.16.91. Redistribution subject to ASME license or copyright; see http://www.asme.org/terms/Terms_Use.cfm

The Lid-Driven Cavity Flow: A Synthesis of Qualitative and Quantitative Observations

J. R. Koseff
Assistant Professor.

R. L. Street
Professor of Fluid Mechanics and Applied Mathematics. Mem. ASME

Department of Civil Engineering, Stanford University, Stanford, CA 94305

A synthesis of observations of flow in a three-dimensional lid-driven cavity is presented through the use of flow visualization pictures and velocity and heat flux measurements. The ratio of the cavity depth to width used was 1:1 and the span to width ratio was 3:1. Flow visualization was accomplished using the thymol blue technique and by rheoscopic liquid illuminated by laser-light sheets. Velocity measurements were made using a two-component laser-Doppler-anemometer and the heat flux on the lower boundary of the cavity was measured using flush mounted sensors. The flow is three-dimensional and is weaker at the symmetry plane than that predicted by accurate two-dimensional numerical simulations. Local three-dimensional features, such as corner vortices in the end-wall regions and longitudinal Taylor-Görtler-like vortices, are significant influences on the flow. The flow is unsteady in the region of the downstream secondary eddy at higher Reynolds numbers (Re) and exhibits turbulent characteristics in this region at Re = 10,000.

1 Introduction

The lid-driven flow in a cavity has become a widely used vehicle for testing two and three-dimensional numerical simulation schemes. Its simple geometry and apparently straight-forward flow structure make the cavity flow an attractive test case. However, flow visualization studies performed in an isothermal, lid-driven flow in a cavity of depth to width ratio 1:1 and a span to width ratio 3:1 revealed an extremely complex flow which was rich in interesting phenomena.

Koseff and Street [1] showed that, for a Reynolds number (Re) range of 1000 to 10,000, the flow is somewhat three-dimensional and consists of one main circulation cell and three secondary eddies. (Here $\mathrm{Re} = U_B B/\nu$, where U_B is the lid speed, B is the width of the cavity, and ν is the kinematic viscosity of the water.) In addition, they found that the flow is turbulent in the region of the downstream secondary eddy (DSE) at a Re of about 8000, and that Taylor-Görtler-like (TGL) vortices and end-wall vortices are present in the flow. These vortices were examined more fully by Rhee et al. [2].

While these visualization studies proved invaluable in pinpointing the salient features of the flow, a quantitative picture of the above-mentioned phenomena is essential for a more complete understanding. This picture has been obtained through the use of laser-Doppler-anemometer (LDA) measurements and heat flux measurements. In this paper we provide insight into physics of the lid driven flow in a cavity and establish, in effect, a new baseline for evaluating numerical simulation codes by a synthesis of the flow visualization and the velocity and heat-flux measurement data.

Contributed by the Fluids Engineering Division for publication in the JOURNAL OF FLUIDS ENGINEERING. Manuscript received by the Fluids Engineering Division, October 17, 1983.

The next section of this paper describes the experimental apparatus, instrumentation and data acquisition methods used in this study. Then the observations are presented. The velocity measurements were made at Reynolds numbers of 3200 and 10,000 and were obtained in the form of profiles on the vertical and horizontal centerlines of the cavity and sectional "cuts" through the downstream secondary eddy (DSE). These results are subsequently discussed with respect to the overall three-dimensional picture of the flow and the existence of turbulence in the region of the DSE. The paper ends with conclusions.

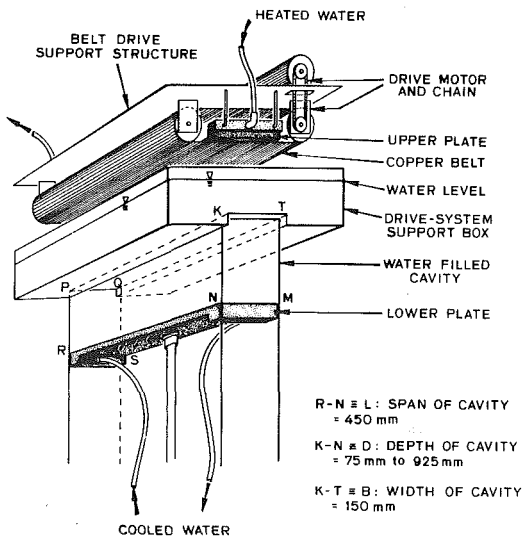

Fig. 1 Schematic of lid-driven cavity

Copyright © 1984 by ASME

Downloaded 02 Jun 2010 to 171.66.16.91. Redistribution subject to ASME license or copyright; see http://www.asme.org/terms/Terms_Use.cfm

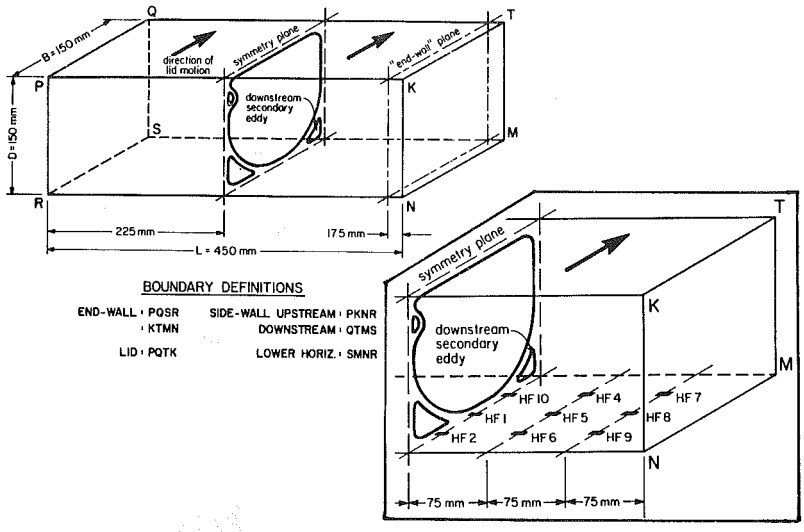

Fig. 2(*a*) Definitions for lid-driven cavity flow with position of heat-flux meters shown in the inset

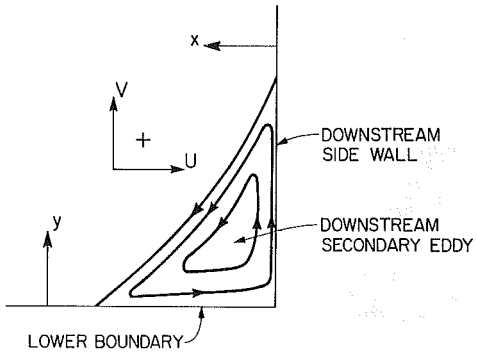

Fig. 2(*b*) Schematic of downstream secondary eddy

2 Experimental Facility and Instrumentation

2.1 Facility. The central component of the facility is a cavity upon which the system supplying the driving force rests (see Fig. 1). The facility is fabricated from 12.5 mm plexiglas. The cavity is bounded at the top and bottom by temperature-controlled plates. Shear is imparted to the cavity fluid by the lid, a 0.08 mm thick thermally conductive copper belt, supported on and driven by two rollers. According to the specifications for the belt-drive motor, the belt speed should be constant at a given setting within 2 percent. In fact, repeated measurements over the period of the experiments showed belt speed to be constant within a drift of 0.5 percent during any particular experiment. A key additional fact is that this small change is not a rapid or jerky fluctuation or unsteadiness in the belt motion, rather it is a true drift, i.e., a longterm, slow change. Thus, the belt motion is *not* a source of disturbances which might incite fluid instabilities of motions.

In the set of experiments described in this paper the ratio of the cavity depth D to cavity width B is 1:1 and that of the span L to width B is 3:1 (see Fig. 2(*a*)). A more complete description of the facility geometry, capabilities and belt arrangement is given in Koseff and Street [1].

2.2 Flow Visualization Techniques. Two flow visualization techniques were used viz., thymol blue and rheoscopic liquid. The thymol blue technique, as first described by Baker [3], is a pH-indicator technique based on producing a "dye" trace by inducing a local pH change in the flow [1]. The rheoscopic liquid technique [2] involves placing the substrate (containing crystalline micro-structures) in the flowfield in small, even concentrations, illuminating the flow with a sheet of light, and using time-exposure photography to obtain pathline patterns.

2.3 Velocity Measurements. Instantaneous velocity measurements, in two orthogonal directions in a vertical plane, were made using a two-component DISA 55X modular optical laser-Doppler-anemometer (LDA) system. The system is equipped with Bragg cell frequency shift and is capable of operating in both forward-scatter and backward-scatter modes. The data was sampled at a rate of 100 Hz by an HP 2100A data acquisition system. The absolute accuracy of the system is 0.1 percent of full scale. A more complete description of the LDA system, and the signal processing techniques employed, is given in Cheung and Koseff [4]. The uncertainty in the instantaneous velocity measurement was calculated using the root-sum-square addition technique of Kline and McClintock [5]. The uncertainty ranges from 10 percent at 1 mm/s to 1 percent at 30 mm/s. A list of the

Nomenclature

B = width of cavity
D = depth of cavity
DSE = downstream secondary eddy
L = span of cavity
LDA = laser-Doppler-anemometer
Q = instantaneous heat flux
Re = Reynolds number [$= U_B B/\nu$]
S = spectral density function
SAR = spanwise-aspect-ratio [$= L/B$]
TGL = Taylor-Görtler-like vortices
u' = horizontal fluctuating velocity component
$\bar{U}$ = mean horizontal velocity component
U = instantaneous horizontal velocity component
U_B = speed of cavity lid
v' = vertical fluctuating velocity component
$\bar{V}$ = mean vertical velocity component
V = instantaneous vertical velocity component
x = horizontal Cartesian coordinate in direction of lid motion
y = vertical Cartesian coordinate
ΔT = initial temperature difference
ϵ = energy dissipation rate
ν = average kinematic viscosity

Downloaded 02 Jun 2010 to 171.66.16.91. Redistribution subject to ASME license or copyright; see http://www.asme.org/terms/Terms_Use.cfm

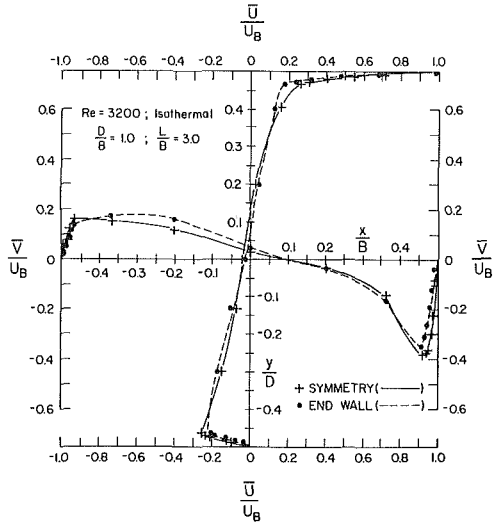

Fig. 3(*a*) Normalized mean velocity profiles at symmetry plane and at end-wall plane for Re = 3200

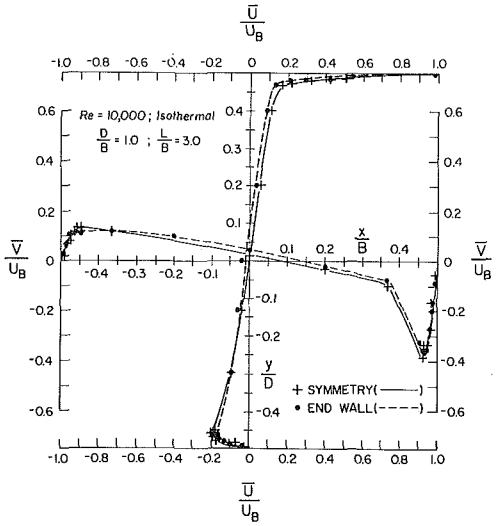

Fig. 3(*b*) Normalized mean velocity profiles at symmetry plane and at end-wall plane for Re = 10,000

uncertainties in the measured and calculated data is contained in Table 1.

2.4 Heat Flux Measurements. Nine RdF-type heat-flux meters are mounted on the lower thermal plate (see inset of Fig. 2(*a*). These meters, which are 0.08mm thick, are mounted flush with the surface to minimize their impact on the flow. The output of each meter is amplified by a factor of 80,000 (by specially constructed amplifiers) allowing for interface with the HP2100A data acquisition system. The amplitude response of the amplifiers decays to about 95 percent of the input at a frequency of 7Hz. This feature of the amplifiers results from the design goal of keeping the noise down to 0.5 percent of the real signal.

3 Experimental Observations

3.1 General. Figure 2(*a*) is a definition sketch for the cavity indicating the boundary nomenclature. The typical time-averaged flow structure on a central vertical plane (the symmetry plane) that is parallel to the direction of lid motion is sketched in this figure. The flow consists of one main circulation cell and three secondary eddies. A schematic of the downstream secondary eddy (DSE) is shown in Fig. 2(*b*). The local coordinate scheme used for referencing measurement locations in the region of the DSE is also shown in this figure.

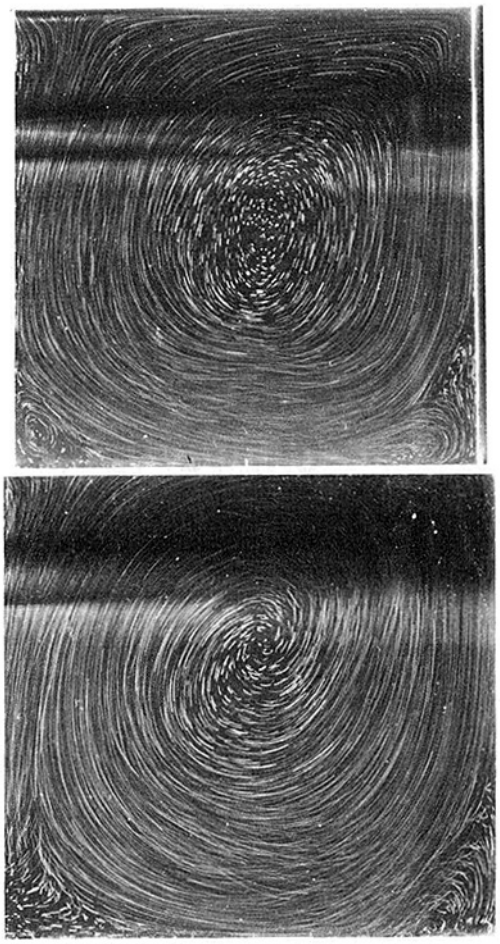

Fig. 4 Flow visualized using rheoscopic liquid at (*a*) symmetry plane and (*b*) plane 10 mm from end-wall for Re = 3300, SAR = 3:1 (View A)

Table 1 Uncertainty of measured and calculated data

MEASURED DATA

Measured	Instrument	Uncertainty	% Uncertainty
Instantaneous velocity	LDA	0.1 mm/s–0.15 mm/s	1–10%
Instantaneous heat flux	RdF meter		2%

SET-POINT STABILITY

Parameter	Uncertainty/Fluctuation
Belt speed	± 2%
Initial stratification	7% at 1.4°C; 2.3% at 4.2°C
LDA measuring volume position:	
– from Lower Boundary	0.25 mm
– from Side-Wall	0.25 mm
– from End-Wall	0.50 mm

CALCULATED DATA

Parameter	Uncertainty	Typical Uncertainty
Mean velocity ($\bar{U}$)	1–10%	1% at 10 mm/s
Root-mean-square velocity ($\sqrt{u'^2}$)	1–25%	2% at 5 mm/s
Stress correlation ($\overline{u'v'}$)	4–150%	10% at 1.8 mm^2/s^2

Velocity measurements were made for Reynolds numbers of 3200 and 10,000 on two vertical planes. These planes were the symmetry plane (see Fig. 2(*a*)) and a plane (referred to as the "end-wall" plane) parallel to it and 17.5 mm from the end-wall. Profiles were taken on the horizontal and vertical centerlines of both planes. The horizontal centerline is a line parallel to the lower boundary of the cavity and a height $D/2$ above it. The vertical centerline is parallel to the cavity side-walls and halfway between them. In addition, measurements in the form of sectional "cuts" were made through the shear layer separating the main circulation cell from the down-

Downloaded 02 Jun 2010 to 171.66.16.91. Redistribution subject to ASME license or copyright; see http://www.asme.org/terms/Terms_Use.cfm

stream secondary eddy (DSE). These "cuts" were made at heights "y" (see Fig. 2(b)) of 5 mm, 10 mm, 15 mm, 25 mm, and 40 mm above the lower boundary at both the symmetry and end-walls planes.

In general, the photographs shown in the paper are either of planes parallel to the symmetry plane (called View A herein) or of planes parallel to the downstream side-wall (View B) (see also Fig. 3, Koseff and Street [6], this issue). Heat flux measurements were made at discrete locations on the lower boundary as indicated in Fig. 2(a). The heat flux measurements were made for flow cases in which a temperature difference ΔT is established between the (hotter) upper boundary and the (cooler) lower boundary. These boundaries are maintained at constant temperatures throughout the experiment. In contrast, the side walls of the facility are insulated.

3.2 Overall Flow. Figures 3(a) and 3(b) show the normalized mean velocity profiles, on the vertical and horizontal centerlines, for Re = 3200 and Re = 10,000, respectively. The profiles were taken at the symmetry and end-wall planes as defined in Fig. 2(a). The profiles are generally similar at Re = 3200 (Fig. 3(a)) but with noticeable differences in the boundary regions near the top, bottom, and side walls. The shear layer below the lid is thicker at the symmetry plane; the velocity gradient is steeper at the end-wall plane. On the other three boundaries, particularly the downstream side-wall, the velocity gradient is steeper in the symmetry plane and the velocities are higher at corresponding positions in the symmetry plane than in the end-wall plane. Contrary to the above situation, there are differences in the profiles for Re = 10,000 but they are only in magnitude and not in shape (see Fig. 3(b)). In addition, the differences are not as significant as in the Re = 3200 case and are most noticeable in the lid and downstream-side-wall regions.

The difference in the circulation patterns between planes is illustrated visually by comparing the flows in Fig. 4 (View A). Figure 4(a) shows the flow in the symmetry plane for a Re = 3300 (spanwise aspect ratio, SAR = 3:1) case and Fig. 4(b) shows the same flow case but at a plant 10 mm from the end-wall. There are three obvious differences in the circulation patterns. First, near the end-wall the centroid of the main circulation cell is located in the upper right quadrant of the cavity, whereas in the symmetry plane it is located closer to the geometrical center of the cavity. The results of Ghia et al. [7] show that for lower Re flows (Re < 5000) the centroid of the main circulation cell is located in the upper right quadrant of the cavity and at higher Re it is close to the geometrical center of the cavity. This suggests then the flow is "weaker" (i.e., of lower effective Re) in the plane 10 mm from the end-wall than in the symmetry plane. Second, the circulation pattern is modified, particularly in the region near the upstream side-wall (see Fig. 2) in and above the upstream secondary eddy (cf. Fig. 3(a) in this region). Third, the sizes (and strengths) of the secondary eddies are not the same in each plane. This difference is particularly noticeable in the region of the upstream secondary eddy.

3.3 Downstream Secondary Eddy Region. Figure 5

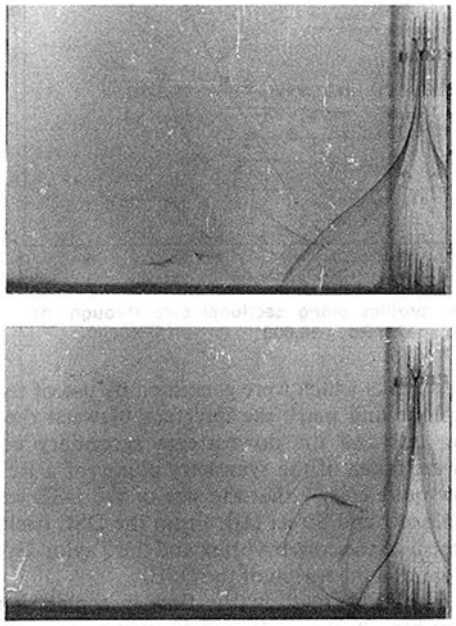

Fig. 5 Dye streaks indicating size of DSE at two instants in time for Re = 6000 (View A)

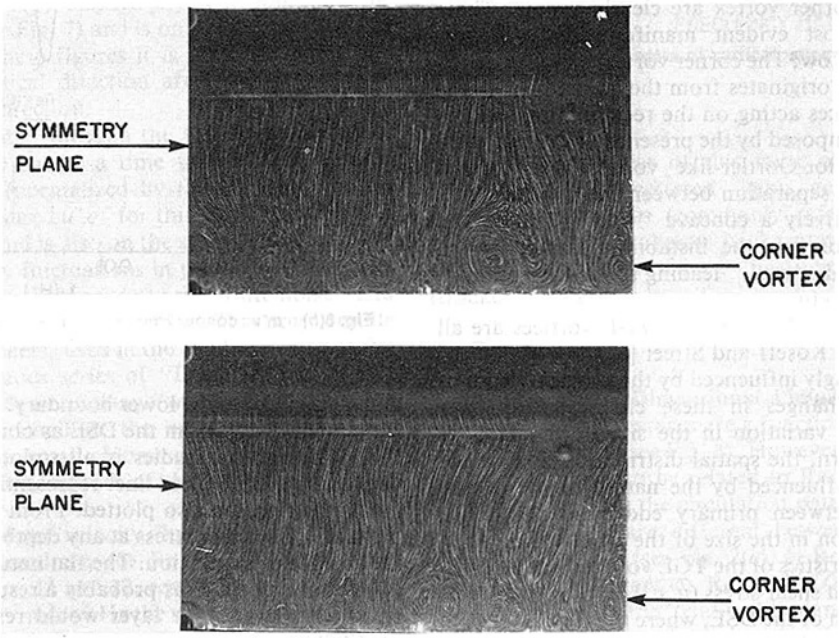

Fig. 6 Flow showing presence of corner vortex and Taylor-Görtlerlike vortices at two different times 30 s. apart for Re = 6000 (View B; plane 35 mm upstream of downstream side wall).

Downloaded 02 Jun 2010 to 171.66.16.91. Redistribution subject to ASME license or copyright; see http://www.asme.org/terms/Terms_Use.cfm

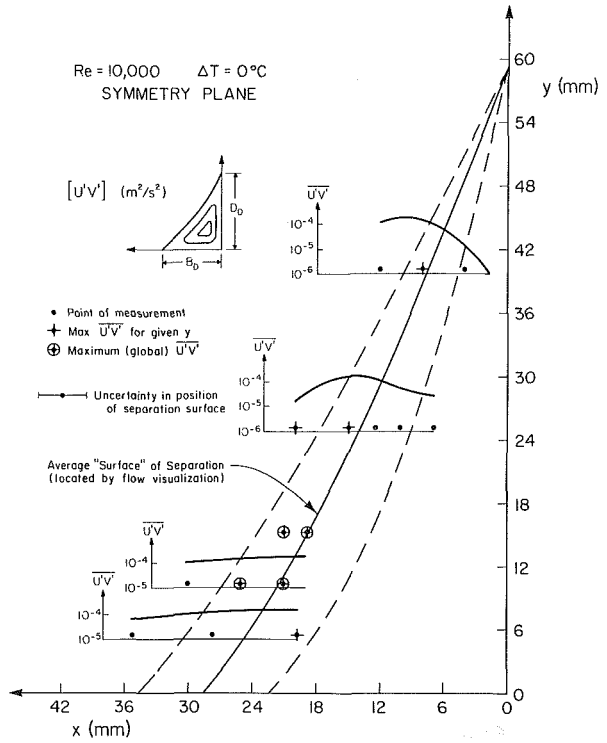

Fig. 7 $\overline{u'v'}$ profiles along sectional cuts through the DSE at the symmetry plane for Re = 10,000

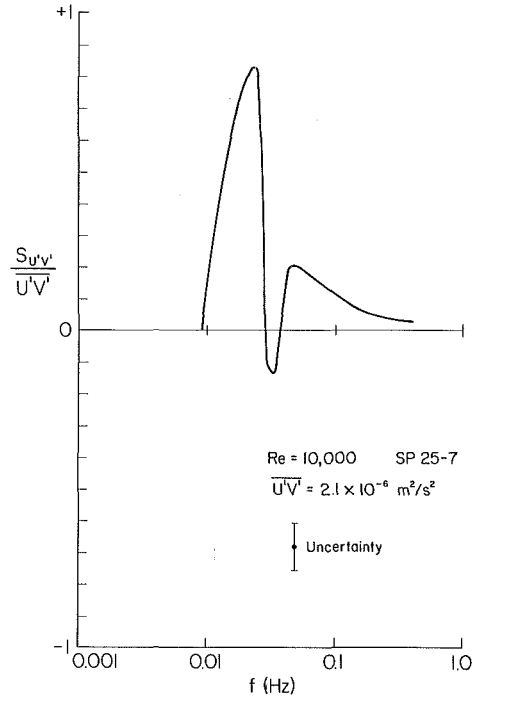

Fig. 8(*a*) $u'v'$ cospectrum at location SP25-7 for Re = 10,000

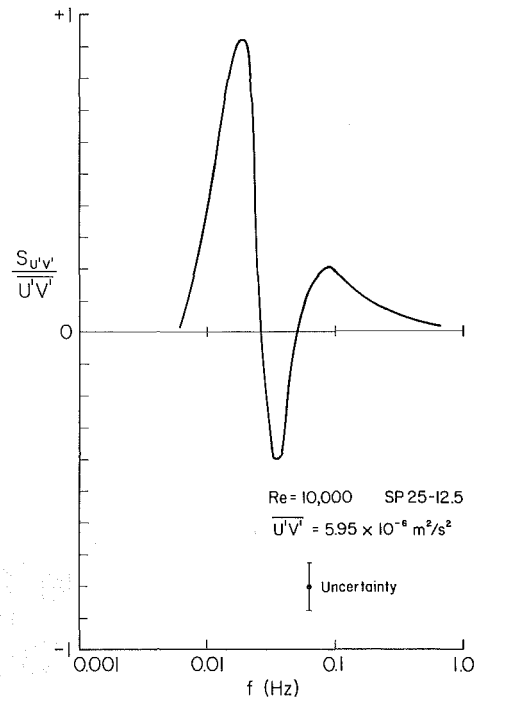

Fig. 8(*b*) $u'v'$ cospectrum at location SP25-12.5 for Re = 10,000

shows dye streaks which were generated by use of the thymol blue technique and mark the interface between the primary circulation cell and the downstream secondary eddy. The pictures were taken of the symmetry plane for a Re = 6000. They show quite clearly that the size of the DSE varies with time [see Koseff and Street [1]]. From the DSE itself we turn for a moment to the corner vortex and the Taylor-Görtler-like vortices found in the region of the DSE.

Figure 6(*a*) and 6(*b*) show the flow in a plane parallel to QTMS (see Fig. 2(*a*)) and 35 mm from it as visualized using rheoscopic liquid for Re = 6000. The pictures were taken about 30s apart. In both pictures the Taylor-Görtler-like (TGL) vortices and corner vortex are clearly visible. These structures are the most evident manifestation of three-dimensionality in this flow. The corner vortex, which is on the right edge of the flow, originates from the adjustment of the shear and pressure forces acting on the recirculating fluid to the no-slip condition imposed by the presence of the end-wall. The longitudinal Taylor-Görtler-like vortices are formed because the surface of separation between the primary eddy and the DSE is effectively a concave "wall." The curved separation surface promotes the instability caused by the centrifugal forces on this "wall," leading to the formation of Taylor-Görtler-like structures.

The corner vortex, the DSE, and the TGL vortices are all integrally inter-related. Koseff and Street [6] showed that the size of the DSE is strongly influenced by the characteristics of the corner vortex. Changes in these characteristics may produce the time-wise variation in the size of the DSE as shown in Fig. 5. In turn, the spatial distribution and size of the TGL vortices is influenced by the nature of the curved separation surface (between primary eddy and the DSE). Therefore, any variation in the size of the DSE will result in changes in the characteristics of the TGL vortices (see Fig. 6).

In Fig. 7 the turbulent shear stress ($\overline{u'v'}$) is plotted at various points in the region of the DSE, where the flow is thought to be most "turbulent." These stresses were calculated from velocity measurements made in the form of sectional "cuts" (see Fig. 2*b*) through the DSE at heights "y" of 5, 10, 15, 25, and 40 mm above the lower boundary. The surface separating the primary eddy from the DSE as obtained from the thymol blue visualization studies is also plotted. Because the DSE oscillates in size, dotted lines representing deviations from the mean position are also plotted. From Fig. 7 we observe that the maximum shear stress at any depth occurs in the region of the surface of separation. The flat nature of the these profiles (at the lower depths) is probably a result of the oscillation. A fixed (in space) shear layer would result in a more peaked profile.

Further quanitative evidence of unsteadiness in the size of the DSE is shown in Fig. 8 which shows $u'v'$ cospectra

Downloaded 02 Jun 2010 to 171.66.16.91. Redistribution subject to ASME license or copyright; see http://www.asme.org/terms/Terms_Use.cfm

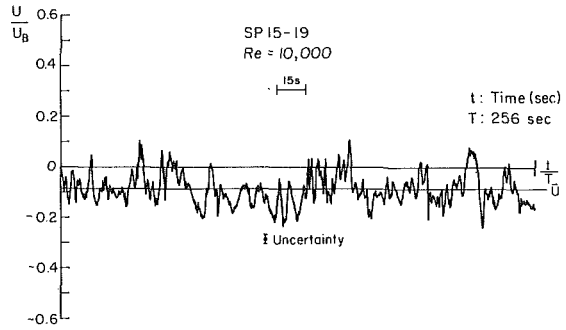

Fig. 9(*a*) Time trace of horizontal velocity at location SP15-19 for Re = 10,000

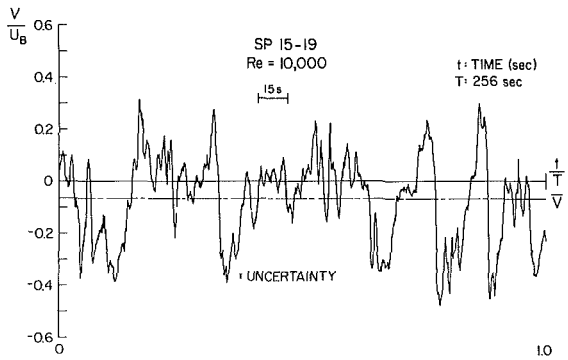

Fig. 9(*b*) Time trace of vertical velocity at location SP15-19 for Re = 10,000

(normalized by local $\overline{u'v'}$) at two different locations in the DSE at Re = 10,000 (SP denotes symmetry plane). Each cospectrum is characterized by a positve $u'v'$ peak at around 0.01 to 0.05 Hz. These spectra also have smaller negative peaks. The negative peaks occur because the separation surface (between the primary circulation cell and the DSE) is moving back and forth through the locations at which the spectra were measured. This is explained in more detail in Section 4.2.

Time traces of the instantaneous horizontal (U) and vertical (V) components of velocity (normalized by lid speed) at the point of maximum measured $\overline{u'v'}$ for a Re = 10,000 are shown in Figs. 9(*a*) and 9(*b*), respectively. The point is at the $y-x$ location 15–19 (see Fig. 7) and is on the symmetry plane (see Fig. 2(*a*)). From these figures it is quite clear that the fluctuations in the vertical direction are much larger than those in the horizontal direction.

Similar sectional "cuts" through the DSE were made for Re = 3200. Figure 10 shows a time trace of the vertical velocity component V (normalized by the lid speed) at the point of maximum measured $\overline{u'v'}$ for this Re. The point is at the y-x location 15–25 and is also on the symmetry plane. The apparent high frequency fluctuations in the Re = 3200 trace (shown in expanded form in the inset) are "white noise" and are not representative of the true velocity. This noise results from the frequency trackers, used in the LDA measurements, which require a continuous series of "Doppler bursts" and are, therefore, susceptible to tracking "white noise" when the signal-to-noise ratio is small or the number of "Doppler bursts" per unit time is small. However, this noise is contained with the uncertainty bounds of the signal as shown in Fig. 10.

The power spectra of the velocity fluctuations in the vertical and horizontal directions, for Re = 3200 and Re = 10,000 are shown in Figs. 11 and 12, respectively. At spectral density levels below 10^{-7} m^2/s^2-Hz the spectra are dominated by "white noise" which results in a tailing off or flattening of the spectra. This region is not shown in Fig. 11 (or Fig. 12) as it has no physical relevance. According to Cheung and Koseff

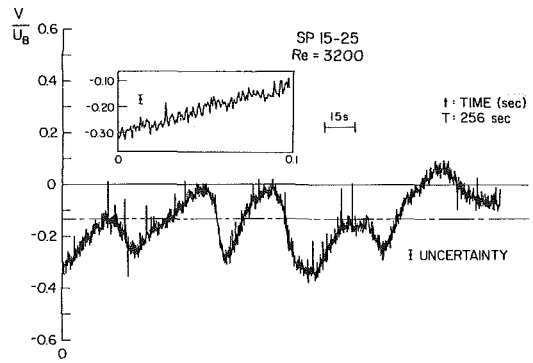

Fig. 10 Time trace of vertical velocity at location SP15-25 for Re = 3200

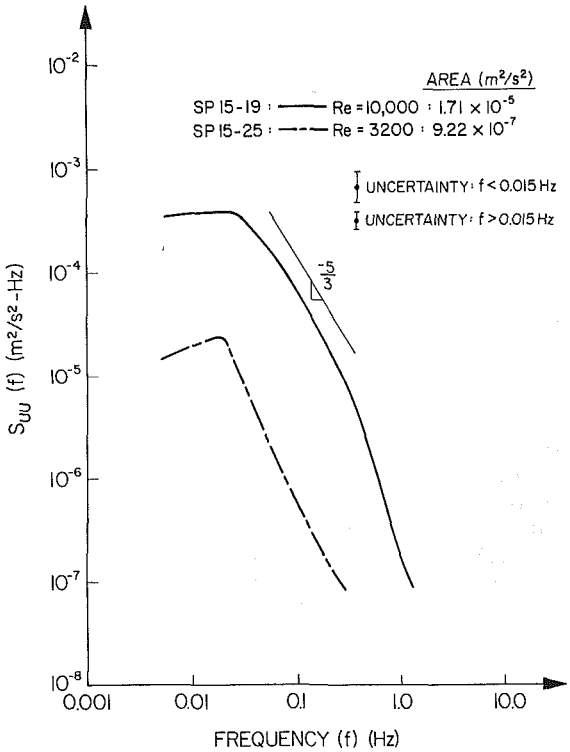

Fig. 11 Frequency spectra of vertical velocity fluctuations for Re = 3200 and 10,000

(4) the main sources of this noise are: (*a*) random phase fluctuations of scattered light generated by "signal-producing" particles (commonly referred to as ambiguity broadening); (*b*) incoherent background illumination; and (*c*) random noise generated by post-photodetector electronics (trackers, filters, etc.).

4 Discussion

4.1 The Three-Dimensional Picture. In section 3.2 we saw that the flow features are a function of position along the span of the cavity (see Fig. 4). However, the magnitude of the variations appear to be related to Re. Figures 3(*a*) and 3(*b*) show that, whereas the circulation patterns (as deduced from velocity profiles) are different between the symmetry and "end-wall" planes (see Fig. 2(*a*)) at Re = 3200, they are not significantly different at Re = 10,000. (The modified circulation pattern in the "end-wall" plane for Re = 3200 is best illustrated by the position of peak velocity in this horizontal centerline profile. It does not lie in the vicinity of the boundary, but rather closer to the cavity center.) There are two

Downloaded 02 Jun 2010 to 171.66.16.91. Redistribution subject to ASME license or copyright; see http://www.asme.org/terms/Terms_Use.cfm

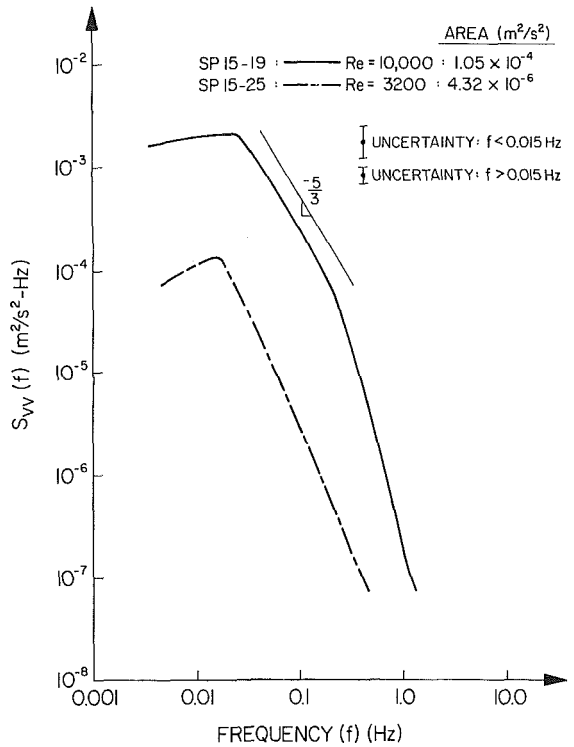

Fig. 12 Frequency spectra of horizontal velocity fluctuations for Re = 3200 and 10,000

plausible explanations for the fact that the profiles at the two planes are generally similar at Re = 10,000 but different at Re = 3200.

First, the flow may be in a different regime at the higher Re, having progressed from the purely laminar state at Re = 3200 to a state of transition with pockets of localized turbulence at Re = 10,000. If this were the case, then additional phenomena, such as strong diffusivity and vortictiy fluctuations, not present in a laminar flow, would be significant. these phenomena would increase the flux rates in the spanwise direction, "flattening" the spanwise velocity profile and resulting in similar profiles at both planes. (For example, turbulent flows over flat plates are characterized by steep near-wall gradients and flat free-stream profiles.)

Second, both the spatial extent and the magnitude of the influence of the end-walls are functions of Re (cf. Koseff and Street [6], in this issue). Thus, while the influence of the end-walls is felt strongly at both planes at Re = 10,000 resulting in similar profiles at the two planes, the reduced influence at the symmetry plane at Re = 3200 may be the reason for the more dissimilar profiles.

Unfortunately no three-dimensional numerical simulations at Reynolds numbers of 3200 and 10,000 exist to serve as a basis for comparison with the measured data. However, in view of the results shown in Figs. 3(*a*) and 3(*b*), one might expect that a very accurate two-dimensional simulation would compare favorably to data from the symmetry plane. This is not the case! The measured mean velocity profiles are significantly different from those produced by a two-dimensional numerical simulation at both Re = 3200 and 10,000. Figures 13(*a*) and 13(*b*) show the measured profiles and the profiles calculated by Ghia et al. [7] using a finite-difference mesh of 129 × 129 points for Re = 3200 and 257 × 257 for Re = 10,000. Agarwal [8], Schreiber and Keller [9], and Gresho et al. [10] performed similar calculations at, among others, Reynolds numbers of 10,000. Their results are not shown in Figs. 13(*a*) and 13(*b*) because they are essentially the same as those of Ghia et al. [7].

The most important result arising from this comparison is

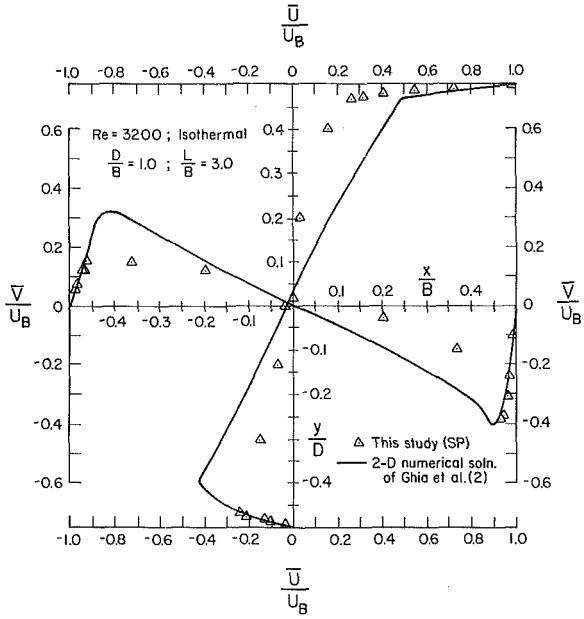

Fig. 13(*a*) Experimental data versus numerical simulation for normalized mean velocity profiles at symmetry plane for Re = 3200

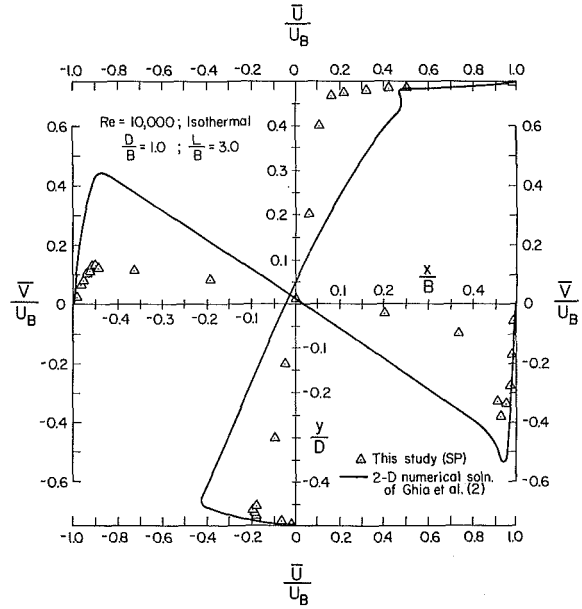

Fig. 13(*b*) Experimental data versus numerical simulation for normalized mean velocity profiles at symmetry plane for Re = 10,000

that both the absolute magnitude and profile shapes are different over most of the profiles. The point of slope discontinuity produced in the numerical solutions near the lid is not present in the measured data at either Re. This discontinuity appears in most two-dimensional numerical solutions; its absence in the data suggests that three-dimensional circulations wash it out. Unfortunately no velocity measurements have been made in the spanwise direction so the circulation patterns in this direction have not been fully defined. In addition the three-dimensional circulations are not adequately reflected in a comparison of the mean velocity profiles at the symmetry plane and end-wall plane due, for example, to the existence of Taylor-Görtler-like vortices and corner vortices. A comparison of the measurements (Figs. 13(*a*) and 13(*b*)) with a fine-grid, accurate two-dimensional numerical solution, however, effectively illustrates the three-dimensionality present. Two additional points arise from this comparison.

Downloaded 02 Jun 2010 to 171.66.16.91. Redistribution subject to ASME license or copyright; see http://www.asme.org/terms/Terms_Use.cfm

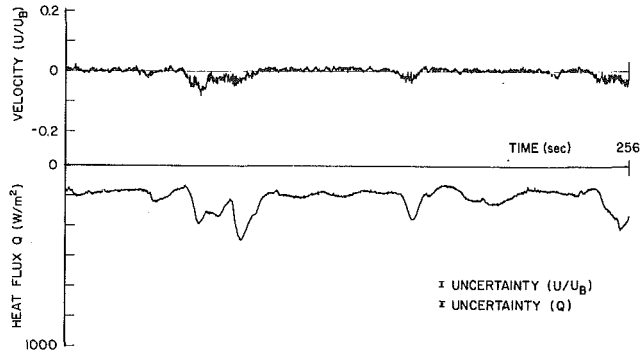

Fig. 14 Time history of heat-flux and horizontal velocity fluctuations at heat-flux meter HF5: Re = 10,000, ΔT = 4.2°C

First, the three-dimensionality of the flow appears to manifest itself in part as an adjustment of the flow to the shear gradients resulting from the presence of the end-walls, resulting in a weakened flow (compared to the pure two-dimensional flow). Second, the relative differences between the measurements and simulations are much greater at Re = 10,000 than at Re = 3200, confirming that the end-wall effect on the flow at the symmetry plane does increase with increasing Re for a given SAR as suggested in Section 3.2.

4.2 Flow Unsteadiness. In Section 3 we presented data which showed that, although the flow properties measured in vertical planes possessed distinct time averages, regions of the flow were clearly unsteady. One such region is the downstream secondary eddy region. In this sub-section we examine the unsteadiness in the DSE itself as well as in the Taylor-Görtler-like (TGL) vortices which originate in this region. Let us first consider the TGL vortices.

Taylor-Görtler-Like Vortices. Comparing Figs. 6(*a*) and 6(*b*), we use that the size and distribution of the TGL vortices is uneven and varies with time. Koseff [11] showed that this behavior was a function of Re; at lower Reynolds numbers the TGL vortices are more uniform in size and evenly distributed. Because the spanwise distribution of the vortices varies with time, we can deduce that the vortices meander in the spanwise direction. This is substantiated by the following evidence.

Figure 14 shows time history plots of heat flux and horizontal velocity fluctuations measured at location HF5 (see Fig. 2(*a*)) for a Re = 10,000, ΔT = 4.2°C case. The velocity measurements (by LDA) were made 1 mm above the heat-flux meters. There is a strong correlation between the major velocity and heat-transfer excursions. An increase in velocity is attributed to the motion of the outer layer of the TGL vortex pair as it passes through the measuring point. A corresponding increase in heat flux is also observed. From the time trace we can deduce, therefore, that the meander period of the vortex is about 80 s at this Re and that a local increase in heat transfer occurs when a TGL vortex pair sweeps the surface.

Downstream Secondary Eddy. In section 3.3 we showed that the size of the DSE varied with time using both flow visualization data (Fig. 5) and $u'v'$ cospectra (Fig. 8). It was stated that the presence of positive *and* negative peaks in these spectra was the key indicator of unsteadiness in the size of the DSE. Why is this so? Consider, for the moment, the shear stress term in the total production term of the turbulent energy budget equation, namely

$$P = -\frac{\overline{u_i' u_j'}}{2}\left(\frac{\partial \bar{U}_i}{\partial x_j} + \frac{\partial \bar{U}_j}{\partial x_i}\right)$$

The shear stress term is

$$-\frac{\overline{u'v'}}{2}\left(\frac{\partial \bar{U}}{\partial y} + \frac{\partial \bar{V}}{\partial x}\right)$$

in our notation. This term is positive (mean flow gives up energy to turbulence) and therefore a change in sign in the mean velocity gradients results in a change in sign in the mean shear stress $u'v'$.

Because the maximum local velocity occurs along the separation surface (between the primary circulation cell and the DSE) the signs of the velocity gradients on either side of this surface are opposite. Thus, if this surface were to move back and forth through a measurement point the sign of the calculated shear stress $u'v'$ would change accordingly. The flow visualization data shows that the surface (as denoted by a dye streak) does in fact shift significantly with time. This is reflected by the positive and negative peaks in the $u'v'$ cospectra at points SP25-7 and SP25-12.5.

4.3 Turbulence. Up to now in presenting the data we have assumed that the flow (in the DSE region) is indeed turbulent at Re = 10,000. According to Koseff and Street [1] the Re at which the flow changes from laminar to turbulent appears to be in the range from 6000 to 8000. This conclusion was reached on the basis of the nature of the streaks marking the interface between the primary circulation cell and the DSE. The technique used for this determination involves the observation of the waviness and instability of dye streaks, as was first described by Osborne Reynolds in 1883.

While the observation of the behavior of a dye streak is a time-honored method of determining whether or not a flow is turbulent, it is not the only means for such a determination. A more complete analysis of the flow in the DSE region in terms of the essential characteristics of a turbulent flow is appropriate.

Characteristics of Turbulence. What are these characteristics? According to Tennekes and Lumley [12] a turbulent flow is diffusive, irregular and random, dissipative, of high Re, and contains three-dimensional vorticity fluctuations. Kline [13] adds that shear flow turbulence is ". . .neither totally random nor totally coherent . . . shear flow turbulence is rather quasi-coherent, or if you prefer, quasi-random . . ." This certainly suggests that a turbulent flow may contain random motions superimposed on some organized structures or at least periods of coherence. Bradshaw [14] defines turbulence in terms of an energy cascade; turbulence is "a three-dimensional time dependent motion in which vortex stretching causes velocity fluctuations to spread to all wavelengths between a minimum determined by viscous forces and a maximum determined by the boundary conditions of the flow."

Combining the above definitions we arrive at the following:

1. A turbulent flow (*a*) contains three-dimensional vorticity fluctuations, (*b*) is irregular and generally random with some degree of coherence, and (*c*) is diffusive and dissipative.

2. The power spectra of turbulent fluctuations are typically broad and consist of an "energy-containing" range (low frequency and wavenumber), an "inertial sub-range," and a "dissipation" range (high frequency and wavenumber).

Turbulence or Laminar Unsteadiness. Based on the criteria presented above, then, is the flow in the region of the DSE turbulent at Reynolds numbers greater than 6000 to 8000? Let us consider first the time traces showing the vertical fluctuations of velocity for Re = 3200 (Fig. 10) and Re = 10,000 (Fig. 9(*b*)). There are two distinct differences between the two traces. First, the signal at Re = 3200 shows quasi-periodicity indicative of organized structures or coherence, whereas the Re = 10,000 signal is more irregular and random. Second, the amplitude of the fluctuations is much higher at Re = 10,000 than for Re = 3200. From these time traces it is clear that the flow at Re = 10,000 is not in the same regime as the flow at Re = 3200 which is laminar. The spectra of the velocity fluctuations substantiate this view.

There is about 25 times more energy contained in the

Downloaded 02 Jun 2010 to 171.66.16.91. Redistribution subject to ASME license or copyright; see http://www.asme.org/terms/Terms_Use.cfm

fluctuations at Re = 10,000 than at Re = 3200. The area referred to in Fig. 11 represents the area below the spectrum and is in fact the energy component in the vertical direction. The spectrum at Re = 10,000 has three distinct regions unlike the spectrum at Re = 3200 which, for example, does not have an inertial sub-range with its $-5/3$ slope. The inertial sub-range, which is a typical characteristic of a spectrum of a turbulent flow, spans about 1 frequency decade and 1.5 power decades for the Re = 10,000 case. The inertial sub-range in a fully turbulent spectrum is normally a little broader, suggesting that the present flow may not yet be fully turbulent in the DSE region. Low dominant frequencies are evident in the spectrum at Re = 10,000. An order of magnitude analysis reveals that the length scales implied by this frequency spectrum are compatible with these frequencies and the mean and rms velocities present. These scales vary from 20 cm (the diagonal length of the symmetry plane) to a Kolmogorov microscale of about 0.5 mm. The method of analysis and relevant equations are described in Tennekes and Lumley ([12], p. 67); the analysis hinges upon obtaining a good estimate of the dissipation rate ϵ.

Horizontal Versus Vertical Fluctuations. There is one further result from this set of measurements that deserves some attention. At both Re = 3200 and Re = 10,000 the velocity fluctuations generally are more energetic in the vertical direction than in the horizontal. The spectra of the horizontal velocity fluctuations at both Reynolds numbers are shown in Fig. 12. The areas below these spectra are almost an order of magnitude below those for the spectra of the vertical fluctuations shown in Fig. 11. What causes this? There are two phenomena which contribute.

The first is the unsteadiness in the size of the DSE as discussed in Section 4.2. Velocity measurements, made in the forms of sectional "cuts" (see Section 3.1), in the region of the DSE indicate that $\bar{U}$ is fairly constant along lines of constant depth (y). Contrastingly, the corresponding values of $\bar{V}$ vary quite noticeably from point to point indicating the presence of a well-defined shear zone which is characterized by a strong vertical velocity gradient in the x direction [$\partial \bar{V}/\partial x$; (see Fig. 2($b$)]. For example, at Re = 10,000 the ratio $\bar{U}/U_B$ equals 0.1 at SP15-19 and 0.11 at SP15-21, whereas the ratio $\bar{V}/U_B$ equals 0.07 at SP15-19 and 0.18 at SP15-21. Because the size of the DSE varies with time, as shown by flow visualization studies, the location of the shear zone relative to any measurement point also changes with time. Thus, as the shear zone moves back and forth through the sampling point the vertical velocity component measured at the point varies significantly more than the horizontal component which is quite uniform across the shear zone.

The second contributing factor is the existence of TGL vortices in the region of the DSE. These TGL structures meander back and forth at low frequency in the spanwise direction and are convected by the mean flow which is fairly uniform across the span. Thus, as a vortex moves across the lower boundary its velocity in the x direction is quite constant despite the spanwise meandering motion. This is shown by the velocity-time trace in Fig. 9(a). However, the vertical velocity component measured at any point is strongly dependent on the spanwise location of the vortex. When the measuring volume (MV) of the LDA is located near the center of the vortex the measured vertical velocity is small. As the vortex meanders in the spanwise direction the MV may be located at the edge of the vortex where the rotation-induced vertical velocity is high. Hence the large fluctuations in vertical velocity shown in Fig. 9(b).

At Re = 10,000 an additional factor, turbulence, comes into play. The effects of the turbulence are superimposed on the meandering TGL vortices. The presence of the TGL vortices, and their unsteady nature, however, has little or no effect on the fluctuations in the horizontal direction. This would account for the RMS v levels being higher than the rms u levels in this region.

5 Conclusions

In the light of the observations and analysis the following conclusions can be drawn:

1 The flow exhibits both global and local three-dimensional features. Globally, the three-dimensionality of the flow appears to manifest itself as an adjustment to the shear gradients resulting from the presence of end-walls, resulting in a weakened flow (compared to the pure two-dimensional flow). Locally, the flow contains Taylor-Görtler-like vortices in the region of the downstream secondary eddy and corner vortices along the end-walls.

(2) Two-dimensional numerical simulations produce significantly different mean velocity profiles from those measured on the symmetry plane in this study.

(3) The flow is unsteady in the region of the downstream secondary eddy at higher Reynolds numbers. This is shown by the oscillatory nature of the size of this eddy and the spanwise meandering of the Taylor-Görtler-like vortices.

(4) The flow in the region of the downstream secondary eddy exhibits some turbulent characteristics at Re = 10,000, but not at Re = 3200. In addition, the velocity fluctuations in the vertical direction are significantly higher than those in the horizontal direction. This is in part due to the presence of Taylor-Görtler-like vortices.

Acknowledgments

This work was performed in the Stanford University Environmental Fluid Mechanics Laboratory and was supported by National Science Foundation Grant CME-7921324 and by the Division of Engineering, Mathematical and Geosciences, Office of Basic Energy Sciences, Department of Energy Contract No. DOE-DE-AT03-81-ER-10867. The assistance of Hyop Rhee and Tak Kee Cheung in performing the experiments is gratefully acknowledged.

References

1 Koseff, J. R., and Street, R. L., "Visualization Studies of a Shear Driven Three-Dimensional Recirculating Flow," ASME JOURNAL OF FLUIDS ENGINEERING, Vol. 106, No. 1, 1984, pp. 21–29.

2 Rhee, H., Koseff, J. R., and Street, R. L., "Flow Visualization of a Recirculating Flow by Rheoscopic Liquid and Liquid Crystal Techniques," *Experiments in Fluids*, Vol. 2, 1984, pp. 57–64.

3 Baker, D. J., "A Technique for the Precise Measurement of Small Fluid Velocities," *Jour. Fluid Mech.*, Vol. 26, 1966, pp. 573–575.

4 Cheung, T. K., and Koseff, J. R., "Simultaneous Backward-Scatter Forward-Scatter Laser-Doppler Anemometer Measurements in an Open Channel Flow," *DISA Information*, Vol. 28, 1983, pp. 3–9. (Also ASCE EMD Specialty Conference on Measurement Techniques and Prediction Methods in Turbulent Flow, Purdue, May 23–25, 1983, pp. 1291–1294.

5 Kline, S. J., and McClintock, F. A., "Describing Uncertainties in Single Sample Experiments, "*Mech. Engrg.*, 1953, pp. 3–8.

6 Koseff, J. R., and Street, R. L., "On End Wall Effects in a Lid-Driven Cavity Flow," ASME JOURNAL OF FLUIDS ENGINEERING, published in this issue pp. 385–389.

7 Ghia, U., Ghia, K. N., and Shin, C. T., "Solution of Incompressible Navier-Stokes Equations by Coupled Strongly Implicit Multi-Grid Method," *J. Comp. Phys.*, Vol. 48, 1982, pp. 387–411.

8 Agarwal, R. K., "A Third-Order-Accurate Upwind Scheme for Navier-Stokes Solutions at High Reynolds Numbers," AIAA 19th Aerospace Sciences Meeting, St. Louis, Jan. 12–15, 1981.

9 Schreiber, R., and Keller, H. B., "Driven Cavity Flow by Efficient Numerical Techniques," *Jour. Comput. Physics*, Vol. 48, 1983, pp. 310–333.

10 Gresho, P. M., Chan, S. T., Upson, C. D., and Lee, R. L., "A Modified Finite Element Method for Solving the Time-Dependent, Incompressible Navier-Stokes Equations," submitted to *Jour. for Numerical Methods in Fluids*, 1983.

11 Koseff, J. R., "Momentum Transfer in a Complex Recirculating Flow," Ph.D. dissertation, Dept. of Civil Engineering, Stanford University, 1983.

12 Tennekes, H. and Lumley, J. L., *A First Course in Turbulence*, MIT Press, Cambridge, Mass., 1972.

13 Kline, S. J., "Universal or Zonal Modeling—The Road Ahead," *Proceedings of The 1980-81 AFOSR-HTTM-Stanford Conf. on Complex Turbulent Flows: Comparison of Computation and Experiment*, Stanford, CA, Vol. II, 1982, pp. 991–1015.

14 Bradshaw, P., *An Introduction to Turbulence and Its Measurement*, Pergamon Press, Oxford, England, 1975.

Downloaded 02 Jun 2010 to 171.66.16.91. Redistribution subject to ASME license or copyright; see http://www.asme.org/terms/Terms_Use.cfm

An Analysis of Jet Stripping of Liquid Coatings

C. H. Ellen
Research Manager,
Engineering & Physics.

C. V. Tu
Research Officer.

John Lysaght (Australia) Limited,
Research & Technology Centre,
Port Kembla, NSW 2505, Australia

This paper presents a new analysis of the jet stripping process, as used to control coating thicknesses in the paper, photographic and galvanizing industries, and demonstrates that the inclusion of a surface shear stress term, acting in conjunction with the pressure gradient on the coating, gives theoretical predictions of coating behavior quite different from those based on stripping which allows only for pressure gradient effect. An illustration is given of how jets operating close to, and further from, the strip during hot dip galvanizing have different effects on the molten coating even though the final coating mass might be the same. Measurements of coating mass, taken from galvanizing line trials, have shown good agreement with the revised theory.

1 Introduction

"Gas knife" or jet stripping has been used for many years to control liquid coating thicknesses in the paper and photographic industries, and metallic coatings on continuous galvanizing lines. The coating thickness obtained with jet stripping depends mainly on the properties of the coating liquid and other variables such as strip speed, jet supply pressure, and jet to strip distance. It is surprising that, in spite of the importance of the process, relatively few analytical studies have appeared in the literature.

Theoretical studies of both steady and unsteady draining (gravity stripping) have been published. Of the various theories proposed for steady-state gravity stripping, those which do not depend on the coating conditions created as the strip emerges from the bath appear to give the most accurate predictions of the final coating thickness of hot dip metallic coatings. This is illustrated by the comparisons shown in Fig. 1: it can be seen that the low capillary number/low Reynolds number theories of Landau and Levich [1] and Tallmadge and White [2], which match the lower meniscus region to the higher draining region and, therefore, involve the surface tension as a parameter, consistently under-estimate hot dip zinc coating surface masses on gravtiy-stripped material [3, 4] especially at higher strip speeds. The density of the molten metallic coating was taken to be 6540 kg/m^3. The shaded regions, characteristic of each theory, in Fig. 1 are associated with a range of viscosities from 2.5 to 3.5 mPas, and, for references [1] and [2], with a surface tension of 0.78 N/m. Although the values used for the viscosity are somewhat lower than the 4 mPas quoted for pure zinc [5], lower values appear to be associated with stripping and may be related to the effects of the small alloying additions used in zinc coatings. It should be noted that an excessively high viscosity would have to be used to shift the theories of references [1] and [2] closer to the measured experimental points. A realistic lowering of the surface tension also does not assist in raising the coating mass predictions of references [1] and [2] to give satisfactory agreement with the measured values. (Similar results could also be quoted for hot dip aluminum coatings.) In contrast, high capillary number/high Reynolds number theories which are independent of the bath exit conditions, through invoking a zero surface velocity [6, 7, 8] or a maximum flux condition [9, 10] exhibit closer agreement with measurements. Of the latter theories, both of which have the same parameter dependence, the "maximum flux" theory is far more acceptable from the fluid mechanics viewpoint, as will be shown in subsequent sections.

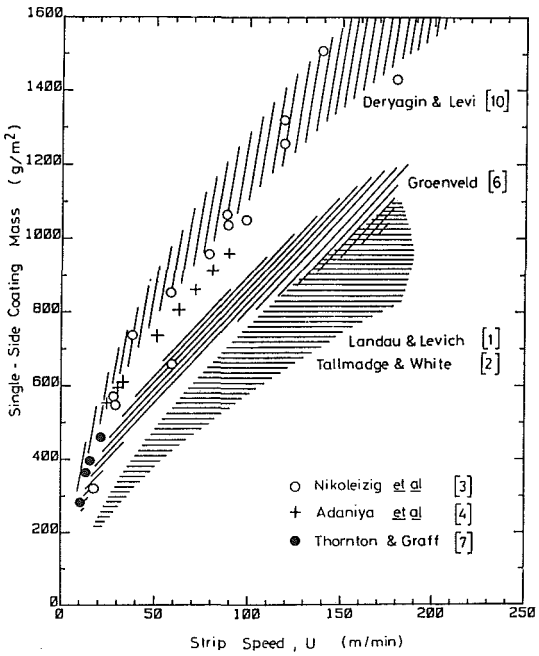

Fig. 1 A comparison of measured and theoretical coating masses of gravity-stripped hot dip zinc coatings. (Theoretical calculations use: surface tension = 0.78 N/m; liquid density = 6540 kg/m^3; viscosity range: 2.5 to 3.5 mPas.)

Contributed by the Fluids Engineering Division for publication in the JOURNAL OF FLUIDS ENGINEERING. Manuscript received by the Fluids Engineering Division, November 8, 1983.

Copyright © 1984 by ASME

Downloaded 02 Jun 2010 to 171.66.16.91. Redistribution subject to ASME license or copyright; see http://www.asme.org/terms/Terms_Use.cfm

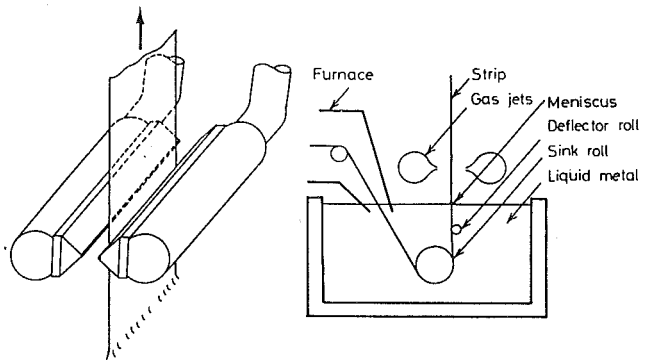

Fig. 2 Schematic of hot dip jet stripping

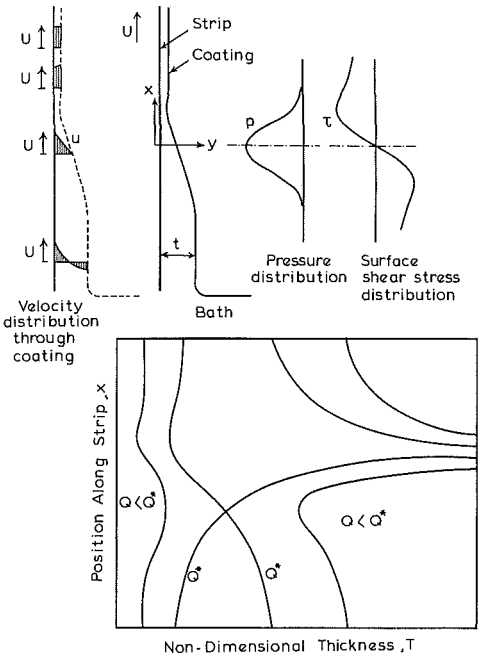

Fig. 3 Coating thickness behavior near the jet stripping zone

Observations of normal steady state draining of metallic coatings reveal, quite clearly, a draining action with the exposed surface "washing" back down into the bath. Under such circumstances, there appears to be justification in developing a theory which eliminates the direct effects of the bath, since there is no well-defined meniscus region, it being completely masked by liquid washing downwards and disturbing the surfaces of both coating and the bath. (It is not inconceivable that conditions for the stripping of other coatings may be such that the meniscus region plays a dominant role in controlling the final thickness and, in such circumstances, the low capillary number theories which are inapplicable to molten metal stripping may be more relevant.)

Jets, as shown in Fig. 2, are employed when gravity stripping alone, at the extraction speed required, would led to too large a coating thickness. Since the washing back of the excess coating material is even greater than in the gravity stripping situation, there is a substantial case for employing the large capillary number theories. Thorton and Graff [7] provide a theoretical coating mass prediction, based on the "maximum flux" theory, for jet stripping in which the jet effect is represented as a single additional body force, i.e., the gravity force is supplemented by a pressure gradient created by the jet. Thorton and Graff derive an expression for the maximum surface pressure gradient caused by the jet impingement but ignore the shearing effect of the jet on the coating. Although, at first sight, their theoretical predictions appear to be supported by measurements (Fig. 13 of [7]), one may observe, on closer inspection, that not only do the measurements cover a very small range of coating mass values, but that there is evidence of the measurements falling on a line with a different slope from that of the theory. It will be argued later that this latter feature is significant and can be explained in term of the jet shearing effects.

Although other simple theoretical derivations for the jet stripped coating mass may be found in the literature [8], and there is a number of regression analyses of measured jet stripping line data [3, 4, 8], there is no published evidence of any improvement being made to the jet stripping theory in order to account for jet shearing effects. It will be shown in the following sections that such an improvement leads to an improved correlation between theory and line data. The refinement, in addition, permits an assessment of whether jets, at lower pressure, close to the emerging strip are as effective as jets, at higher pressure, further from the strip. One cannot make such a distinction within the framework of the pressure gradient enhanced gravity stripping theory [7], but experienced operators are aware of subtle differences which can occur in the coating as a result of this type of change.

2 Jet Stripping Theory

The problem is defined as steady state vertical withdrawal of a flat plate from a viscous fluid bath. The formulation of the problem will be specifically directed towards the hot dip galvanizing application but, with minor modifications, could be applied to other processes involving jet stripping. Remote from the meniscus region, a variation of external pressure is imposed (say, by a two-dimensional jet impinging on the moving plate), as illustrated in Fig. 3. For a slowly varying film thickness, t (i.e., $|dt/dx| << 1$), and negligible surface tension, the Navier Stokes equations for a thin film on a plane surface reduce to

$$\mu d^2u/dy^2 - (\rho g + dp/dx) = 0, \tag{1}$$

where $u(y)$ is the fluid velocity parallel to the surface in the direction of plate motion which is vertically upwards (x direction), y is the coordinate normal to the surface, ρ and μ are the fluid density and viscosity, respectively, g is the acceleration due to gravity and dp/dx is the pressure gradient in the x direction which acts as an additional body force on the film. (In the case of gravity alone, $dp/dx = 0$.) It is worth noting that liquid metal films on moving strip solidfy far from the bath level and the assumption of constant viscosity in the stripping zone is acceptable since the viscosity of molten zinc or aluminum is relativley insensitive to temperature until the temperature falls within approximately 5°C of the freezing point.

The boundary conditions are:

$$u = U \text{ at } y = 0 \text{ (no slip)} \tag{2}$$

and $\mu du/dy = \tau$ at $y = t$,

where U is the plate velocity, the shear stress, τ, imposed by the external jet gas-fluid interface, is a slowly varying function of x. (It will be verified later that surface tension effects are insignificant in the striping zone.) In all previously published theories of jet stripping the surface shear stress, τ, has been ignored.

The solution of equation (1), subject to the given boundary conditions, equations (2), representing a combined Poiseuille-Couette flow, is

$$u/U = 1 - (GT^2/2)(y/t)(2 - y/t) + ST(y/t) \tag{3}$$

where T, S, and G are the nondimensional film thickness, shear stress and effective gravitational acceleration defined by

$$T = t(g/\nu U)^{1/2} \quad S = \tau(\mu\rho U g)^{-1/2} \quad G = 1 + (dp/dx)/\rho g. \tag{4}$$

The film thickness, t, has been nondimensionalized with, as

Downloaded 02 Jun 2010 to 171.66.16.91. Redistribution subject to ASME license or copyright; see http://www.asme.org/terms/Terms_Use.cfm

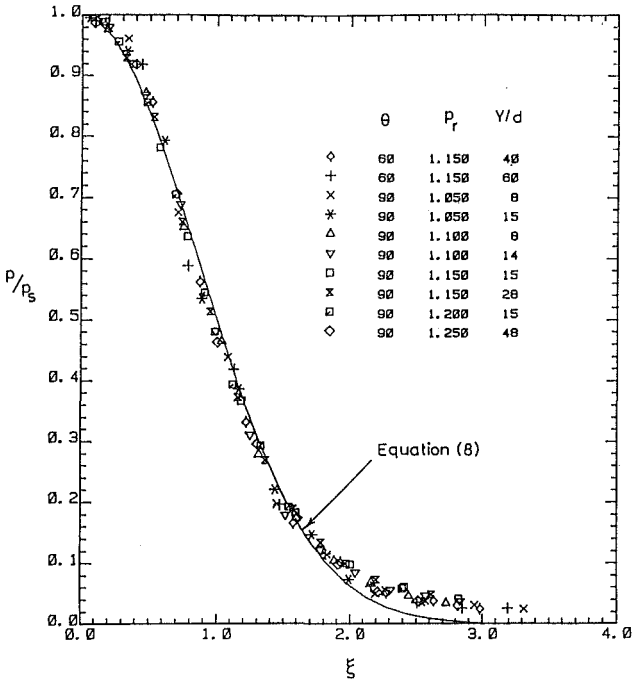

Fig. 4 Comparison of nondimensional plate pressure distributions for plane jet impingement. (Angle between jet direction and downward vertical direction, θ; ratio of jet supply pressure to ambient p_r; maximum impingement pressure, p_s; jet to plate distance/jet opening, Y/d. Uncertainty in $\theta = \pm 3$ deg, in $p_r = \pm 0.002$; in Y/d (8 to 15) $= \pm 1$ and Y/d (28 to 60) $= \pm 4$; in $p/p_s = \pm 0.005$, in $\xi = \pm 0.1$ at 20:1 odds.)

will become evident later, the thickness of a film subject to gravity stripping alone, or, alternatively, the transverse length scale associated with Poiseuille flow under a pressure gradient ρg and with a centerline velocity U. The shear stress, τ, has been nondimensionalized with a film shear stress associated with that generated at the boundaries of a Poiseuille flow. The body force term, $\rho g + dp/dx$, has been nondimensionalized with the gravity stripping force, ρg. These nondimensionalizations permit the straightforward examination of jet stripping when the extraction speed and the film properties remain constant while the jet characteristics are changed (by moving the jets closer to or farther from the strip).

Along the plate, at any position, G and S are known from a knowledge of the jet impingement pressures and the wall shear stresses on the plate.

The nondimensional withdrawal flux, Q, is given, on integration of equation (3), by

$$Q = T(1 - GT^2/3) + ST^2/2, \tag{5}$$

where

$$Q = (q/U)\,(g/\nu U)^{1/2} \tag{6}$$

and $q = \int_0^t u\,dy$, the nondimensionalization being with respect to the gravity stripping withdrawal flux. The final single-sided coating mass per unit area, M, is given by $M = \rho q/U$.

Under steady state conditions Q must be constant while T changes in response to a changing G and S caused by the stripping jet. The foregoing solution remains valid, however, since the "scales" associated with the changes in G and S are very much larger than the coating thickness. Consider the cubic function,

$$f(T) = GT^3/3 - ST^2/2 - T + Q, \tag{7}$$

which has either two or no positive real zeros. The loci of the zeros, as G and S change, describe the possible variations in coating thickness (as indicated in Fig. 3). It can be seen that the thicknesses will return to their original values unless a bifurcation point, $f'(T) = 0$, arises. This bifurcation point describes the only mechanism by which a net thicknees change can occur and also defines the maximum flux, Q^*, for a given C and S. (The solution which involves an increasing thickness through the jet stripping zone is unacceptable physically and can be shown to be unstable.) It may be noted that for gravity stripping: $G = 1$, $S = 0$, and the condition $f'(T) = 0$ tends to $T = 1$, the nondimensional value of the thickness of a gravity stripped coating.

It can be seen that, because the stripping action, and solution, depend on the variation of G and S along the plate, it is necessary to have details of them in order to obtain accurate predictions of the coating mass. Since the plate speed, U, is much smaller than the air velocity from the nozzle (typically 1 percent or less), it is unnecessary to correct the pressure distribution or shear stress for strip movement.

Various sources may be consulted for information on jet impingement [11–13]. As part of the investigation, however, flat plate jet impingement has been studied experimentally using various galvanizing line production jets with slot aspect ratios of 1000:1 to 6000:1, ratios of supply pressures to ambient, p_r, in the range of 1.05 to 1.25, and jet to plate distances, Y, varying between 8 and 48 times the jet opening, d. The jet Reynolds numbers, based on jet lip opening, were in the range 3×10^3 to 20×10^3. The data may be nondimensionalized and p/p_s plotted against $\xi = x/b$, where the pressure, p, has been nondimensionalized with the peak pressure, p_s (where $x = 0$), and $x = b$ is the point where $p = p_s/2$. Figure 4 confirms that the pressures remote from the edges of the plate, so plotted, closely fit a Gaussian distribution [12], both when jets are normal and when the jets are obliquely inclined to the plate,

$$p/p_s = f(\xi) = e^{-0.693\xi^2}. \tag{8}$$

The agreement is very good in the region where the maximum pressure gradient occurs but differences are evident when $|\xi| > 1.6$.

Although no shear stress measurements have been made during this investigation on production jets, previously established experimentally determined forms for the shear stress distribution [12] have been employed for calculations of withdrawal flux, i.e.

$$\tau = \tau_{\max}\{\operatorname{erf}(0.833\xi) - 0.2\,\xi f(\xi)\}, \tag{9}$$

where the maximum shear stress, $\tau_{\max}$, depends on the angle between the jet and the wall, and is given in reference [12].

It is of interest to note that the maximum pressure gradient occurs at $\xi = 0.849$, whereas, under most circumstances, the peak stripping condition with both the pressure gradient *and* the surface shear stress is indicated to occur for $1.0 < \xi < 1.4$.

Although the shear stress function, equation (9), is entirely adequate for determination of the stripping condition, it does not provide an accurate description of the jet induced surface shear stress of the wall jets which are formed either side of the impingement zone. In order to obtain a full description of the coating thickness variation as the plate moves through the stripping zone, it is necessary to extend the description of the surface shear stress beyond the impingement zone into the wall jet region in which the maximum flow velocity decreases as the inverse square root of the distance from the jet impingement point [12, 13]. An expression for the surface shear stress in this region can, therefore, be determined [12] showing a very slow decrease, from a value close to $\tau_{\max}$, for $\xi > 2.4$ (typically τ would reach half of $\tau_{\max}$ when $\xi = 10$ approximately).

In the application of the pressure and shear stress relationships to jet stripping, it is more appropriate to nondimensionalize the distance along the place with the jet lip opening, d, rather than b, so that the effect of varying the jet to plate distance may be readily examined without affecting the length scales along the plate.

Downloaded 02 Jun 2010 to 171.66.16.91. Redistribution subject to ASME license or copyright; see http://www.asme.org/terms/Terms_Use.cfm

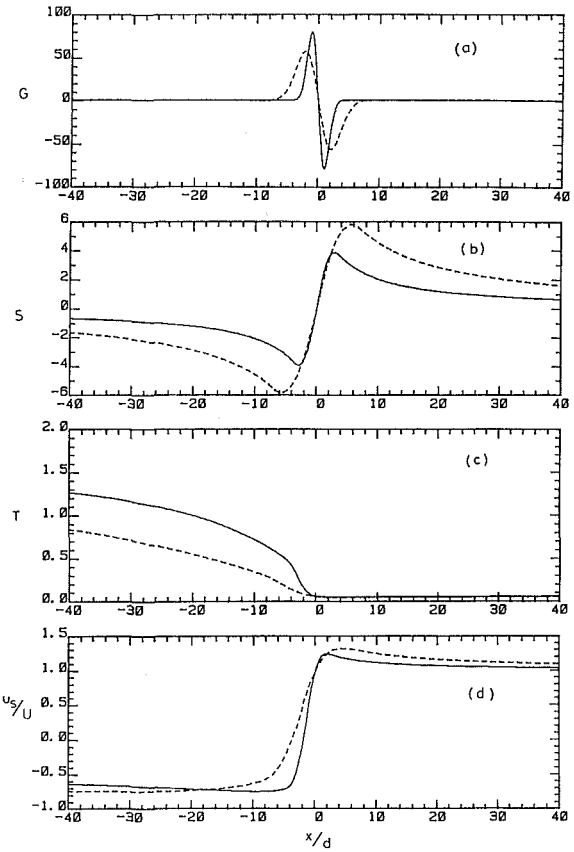

Fig. 5 Variation of G, S, T and u_s/U along the plate in the region of the stripping zone. (U = 100 m/min; d = 1.0 mm; μ = 2.5 mPas; ρ = 6540 kg/m^3; θ = 90 deg; and
——— p_r = 1.110 Y/d = 10;
------ p_r = 1.360 Y/d = 20.)

A computer program was written to calculate the variation in coating mass for a given jet. The program evaluated the local surface pressure gradient and shear, from equations (8) and (9), and then tracked the variation in T, from equation (7), such that the maximum flux condition was satisfied. The characteristics of the solutions thus obtained are discussed in the following section.

3 Theoretical Results

Figure 5 illustrates the results obtained from application of the theory for typical stripping conditions (a strip speed of 100 m/min and a single-sided coating mass of 100 g/m^2): Fig. 5(a) shows the variation of G; Fig. 5(b), the nondimensional surface shear stress, S; Fig. 5(c), the calculated nondimensional film thickness, T; and Fig. 5(d), the calculated nondimensional film surface velocity, u_s/U. In passing through the stripping zone the coating thickness decreases by a factor of 30; below the jets, the surface layers of the coating are travelling downwards whereas, above, the coating velocity distribution is unidirectional. The point at which the surface velocity is zero is just ahead of the jet stagnation point in the impingement zone. This may be explain why the zoro surface velocity condition was thought to be the criterion appropriate to jet stripping [8]. (The coating Reynolds number changes from several thousand below the jets to a value of 10 to 30 above the stripping zone.)

Figure 5 shows the difference between jets operating at normal incidence to the plate under two typical sets of conditions ((i) close to the plate: Y/d = 10, where Y is the jet to plate distance; ratio of supply pressure to ambient, p_r = 1.110, and (ii) far from the plate: Y/d = 20; p_r = 1.360), both of which are set to achieve the same final coating thickness.

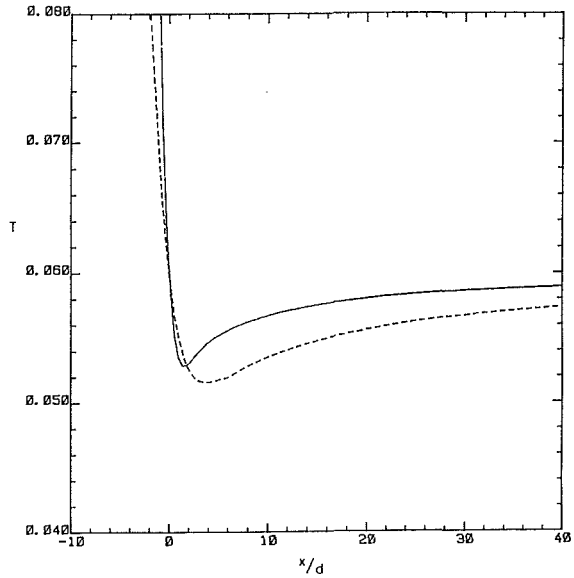

Fig. 6 Details of the coating thickness change in the region of the stripping zone. (Conditions as in Fig. 5.)

The greater the surface shear effects, the wider the transition zone over which the film changes. Figure 5 and Fig. 6, which is an enlargement of Fig. 5(c), indicate a more rapid change of thickness when the shear stress on the coating surface is less. This is not surprising since the shear force below the jet impingement stagnation point acts in the same direction as the draining surface layers whereas, above, the shear acts in the direction of strip motion.

It is also significant that the surface velocity of the film is relatively large for jets operating further from the plate: in the example given, the surface velocity of the film relative to the plate is over twice the value it is for jets operating close to the plate.

The greater surface shear is likely to induce a more rapid growth rate of 'wind driven' wave in the film. The liquid metal film, beyond the zone of influence of the jets, is an example of a gravitationally unstable film [14, 15] (although the growth rates can be shown to be very small for typical metallic coating film thicknesses), and, if the coating were not to solidify rapidly, the unstable waves would become readily visible. It is suggested that, when significant growth of shear induced instabilities occurs in the stripping zone, subsequent gravitational instabilities will build on the formed waves. On the basis of this hypothesis, at a given position beyond the jet stripping zone, the amplitude of the waves on the surface of the solidifying coating would be larger when an increased shear stress is induced by the stripping jet. (This theory, which is beyond the scope of the present paper, is currently under investigation.) It may be concluded, therefore, that jets should be operated close to the plate in order to avoid any tendency of the jets to create an uneven coating. The frozen wave patterns, known as "sag lines," which occur on galvanized surfaces, sometimes quite severely, are postulated, therefore, to be related to the effects of the jet induced surface shear effects.

Another characteristic of higher surface shears is the greater heat transfer rates; the jets operating further from the plate cool the coating faster than the jets operating close to the plate. The high rates of cooling are, nevertheless confined to a relatively narrow zone in the vicinity of the jet impingement point. It can be estimated, for example, that a 0.5 mm thick plate would cool by 3°C as it passed through the impingement zone of closely spaced jets and by three times as much when the jets are at twice the distance. These temperature changes are not an insignificant fraction of the coating bath to

Downloaded 02 Jun 2010 to 171.66.16.91. Redistribution subject to ASME license or copyright; see http://www.asme.org/terms/Terms_Use.cfm

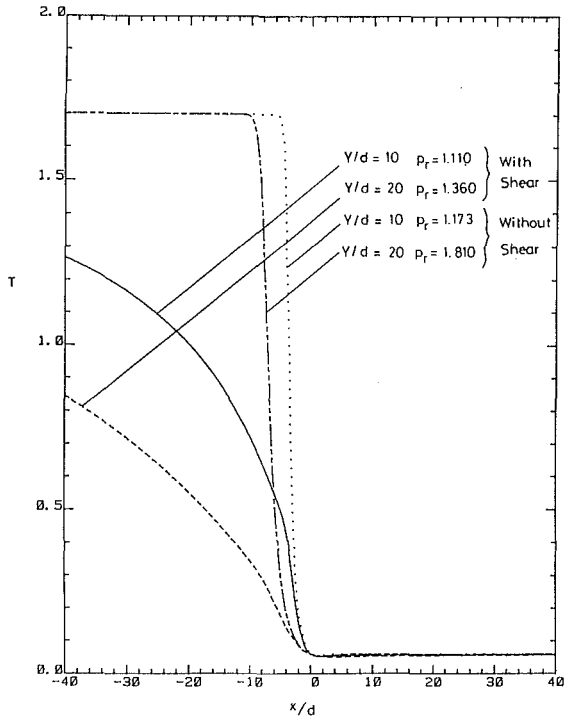

Fig. 7 Comparison of the theoretically predicted coating thickness variations with and without the shear stress term, the supply pressure being adjusted to give the same final coated thickness in each case.

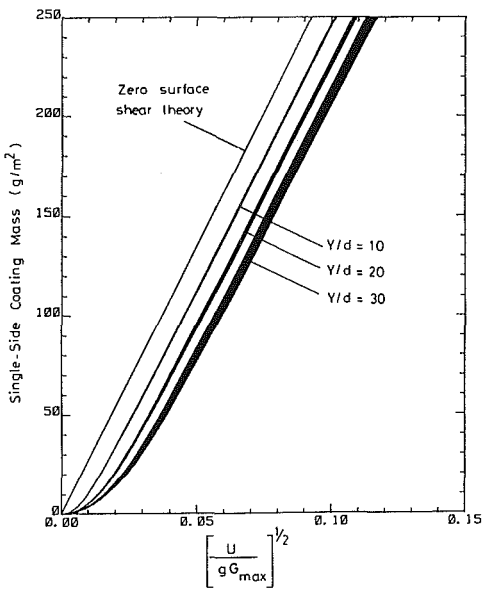

Fig. 8 Theoretical relationship between the coating mass and the parameter $\{U/(gG_{max})\}^{1/2}$ for various jet operating conditions. (Each band of results covers a relative supply pressure, p_r, range of 1.05 to 1.60; 0.5 mm $\leq d \leq$ 2.0 mm.)

solidification temperature difference. It may be concluded, therefore, that the wave generating feature of the higher shear jet conditions is accompanied by an enhanced cooling which would tend to reduce the growth period for surface instabilities. It is probably not good practice to rely on the enhanced cooling of high shear jets.

It can be checked, *a posteriori*, from the results obtained for the coating thickness variation, that is was justified to omit the surface tension effects from the theoretical formulation. Not only for the thickness variations given in Fig. 5 but for thickness changes caused by all other conditions investigated, the omission of surface tension was found to be valid. This does not, nevertheless, invalidate the argument that surface tension is important in controlling the growth rate of instabilities of the coating film beyond the stripping zone [14, 15].

Although Fig. 5 quite clearly establishes the importance of the stripping jet induced shear stress in controlling the coating thickness, it is of interest to elaborate on the errors which are caused by ignoring the shear term in equation (5). Figure 7 is a reproduction of the coating thickness variations shown in Fig. 5(*c*) for jets operating close to and far from the plate. Superimposed are the coating thickness curves predicted from pressure stripping alone, with the jet supply pressures adjusted to generate the same coating mass. The main feature of these curves is the much greater extent of the thickness transition zone when the jet shear effect is included. For the jet positioned close to the plate ($Y/d = 10$), the guage supply pressure must be increased by over 50 percent to achieve the same coating mass; for the jets further away ($Y/d = 20$), the pressure must be increased by 125 percent. An alternative interpretation is that if the jet pressures of the pressure stripping theory [7], are not changed from those of the surface shear theory, the coating masses are over-estimated by 20 percent (for $Y/d = 10$) and 40 percent ($Y/d = 20$).

The way in which the coating mass varies with the parameter $\{U/(gG_{max})\}^{1/2}$ is shown in Fig. 8. There is a single straight line through the origin for stripping theory which excludes the surface shearing effects. With the inclusion of surface shear the theory predicts a curve for each set of jet operating conditions. The coating mass is, however, more sensitive to the jet to plate distance than the other variables such as the jet supply pressure, as Fig. 8 indicates. Although these curves are based on a jet with a jet lip opening of 1.0 mm, it can also be shown that the coating mass, plotted in this way, is also quite insensitive to jet lip opening.

With such large differences evident between results from simple stripping theory and from the present theory which includes the shear stress, the use of the simple theory does not appear to be warranted. One might expect that the feed forward component of coating mass control systems might have limited capabilities if the control system were to utilize a model based on the simple theory of jet stripping.

An explanation of why experimentally measured data have not revealed the inadequacy of the simple theory may be in the paucity of data available for comparison and the limited knowledge of the values of some of the quantities such as the viscosity of alloys with small additions of other elements. These questions will be examined in the following section.

4 Comparison of Theory With Experiment

Data collected from a number of line trials were used for checking of the jet stripping theory with shear stress.

In practice, the strip position, relative to the jets, varies because of the strip shape and the other effects. The result is that the strip does not necessarily pass centrally through the jet stripping region. Since the jet to strip distance cannot be measured during trials, the coating masses on each surface of the strip were taken to be half the total coating mass and the jet to strip distances were calculated from the jet to jet distances and the strip thicknesses. The justification for using this procedure is that small perturbations should be linear and, therefore, when the strip moves closer to one jet and the coating mass on that surface decreases, the coating mass on the reverse surface (which has moved away from the opposing jet) increases by the same amount. This characteristic is observed in coating mass measurements taken from galvanizing lines.

The jet conditions for a number of experimental points were used as data for calculations of coating mass using the theory described in Section 2. A comparison was made by plotting the prediction of coating mass against 35 measured

Downloaded 02 Jun 2010 to 171.66.16.91. Redistribution subject to ASME license or copyright; see http://www.asme.org/terms/Terms_Use.cfm

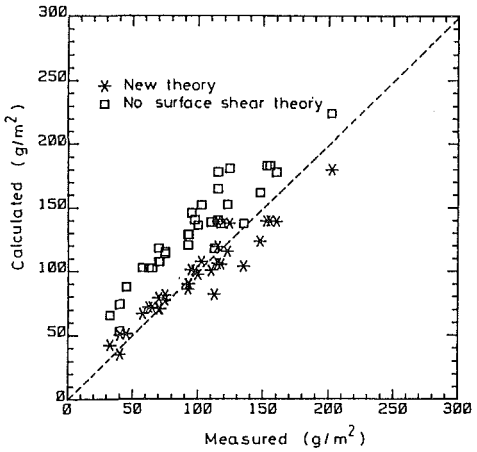

Fig. 9 Comparison of theoretical and measured coating masses. Uncertainty in measured coating mass = ± 5 g/m^2 and in calculated coating mass = ± 4 g/m^2 at 20:1 odds

values, taken from line trials for each point, as shown in Fig. 9. The comparison between measured values and the simple stripping theory ($\tau = 0$) has also been made in the figure. Analysis of the points plotted in Fig. 9 shows that the coating mass prediction from the new theory is within 10 percent of the measured points on average. This should be compared with the average of 60 percent for points given by the theory with zero surface shear stress in the stripping zone. These results indicate that the new theory, which includes the surface shear stress, gives significantly more accurate predictions of the final coating mass.

It should be noted that Fig. 13 in reference [7], for the limited data given, also appears to show an off-set which is indicative of the need to include the surface shear stress term in the theory of jet stripping.

6 Summary and Conclusions

An analysis of the jet stripping process with the surface shear stress term included has been presented. A comparison of galvanizing line measurements with theoretical predictions of coating masses has shown the new theory to be an improvement over other earlier theories.

Acknowledgment

The authors are indebted to the directors of John Lysaght (Australia) Limited for permission to publish the material contained in this paper.

References

1 Landau, L. D., and Levich, V. G., *Acta Physiochemica USSR*, Vol. 17, No. 41, 1942.

2 Tallmadge, J. A., and White, D. A., "Film Properties and Design Procedures in Cylinder Withdrawal," *I&EC Process Design and Development*, Vol. 7, No. 4, 1968, pp. 503–508.

3 Nikoleizig, A., Kootz, T., Weber, F., and Espenhahn, M., "Fundamentals of the Jet Process for Hot Dip Galvanizing," *Stahl u. Eisen*, Vol. 98, No. 7, 1978, pp. 336–342.

4 Adaniya, T., Abe, M., Shoji, M., and Yano, H., "Study on Gas Wiping Mechanism for Continuous Galvanizing Line" (in Japanese), *Iron and Steel*, Vol. 66, No. 7, 1980, pp. 835–844.

5 Thresh, H. R., White, D. W. G., Edwards, J. O., and Meier, J. W., "Properties of Molten Zinc and Zinc Alloys—Final Report," Physical Metallurgy Division Internal Report PM-R-64-26, 27, 28, Department of Mines and Technical Surveys, Ottawa, 1964.

6 Groenveld, P., "Laminar Withdrawal with Appreciable Inertia Forces," Chem. Eng. Sci., Vol. 25, 1970, pp. 1267–1273.

7 Thornton, J. A., and Graff, H. F., "Analytic Description of the Jet Finishing Process for Hot Dip Metallic Coatings on Strip," *Metallurgical Transactions B*, Vol. 7B, 1976, pp. 607–618.

8 Edwards, W. J., Carlton, A. J., Harvey, G. F., Evans, R. F. K., and McKerrow, P. J., "Coating Mass Control System Design for a Continuous Galvanizing Line," *Automatica*, Vol. 12, 1976, pp. 225–235.

9 Hrbek, A., "The Effect of Speed on the Thickness of the Coating Produced During Metallizing in Liquid Metals," *Metal Finishing J*, Vol. 7, No. 80, 1961, pp. 298–302.

10 Deryagin, B. V., and Levi S. M., *Film Coating Theory*, Focal Point Press, New York, 1964.

11 Hrycak, P., et al., "Experimental Flow Characteristics of a Single Turbulent Jet Impinging on a Flat Plate," NASA Technical Note TN D-5690, US National Aeronautics Administration, Washington, 1970.

12 Beltaos, S., "Oblique Impingement of Plane Turbulent Jets," *J. Hydraulics Division, Proc. ASCE*, Vol. 102, HY9, 1976, pp. 1177–1192.

13 Hwang, J. C., and Tsou, F. K., "Numerical Solutions for Flow and Heat Transfer of a Plane Turbulent Oblique Impinging Jet," *Proceedings of the Second National Symposium on Numerical Properties and Methodologies in Heat Transfer*, Sept. 1981, The University of Maryland, USA (Shih, T. M. (Ed.)), Hemisphere Pub. Corp., 1983, pp. 405–417.

14 Yih, C-S., "Stabilty of Liquid Flow Down an Inclined Plane," *Physics of Fluids*, Vol. 6, No. 3, 1963, pp. 321–328.

15 Lin, S. P., "Finite Amplitude Side-Band Stability of a Viscous Film," *J. Fluid Mech.*, Vol. 63, No. 3, 1974, pp. 417–429.

Downloaded 02 Jun 2010 to 171.66.16.91. Redistribution subject to ASME license or copyright; see http://www.asme.org/terms/Terms_Use.cfm

J. J. Stukel
Department of Civil Engineering and Department of Mechanical Engineering.

P. K. Hopke
Department of Civil Engineering, Institute for Environmental Studies, and Nuclear Engineering Program.

K. Nourmohammadi
Nuclear Engineering Program.

University of Illinois at Urbana-Champaign, Urbana, Ill. 61801

Turbulent Air Flow Over Rough Surfaces: Mean Flow Parameters

The objective of the study was to examine experimentally the turbulent flow structure near a repeated-rib geometry rough-walled surface as a function of the ratio of roughness height to pipe radius (K/R), the ratio of spacing between the elements to roughness height (P/K), and the axial position with the rib cycle. The centerline axial flow velocity was found to vary sinusoidally in the axial direction within a rib cycle for $P/K > 10$ for $K/R = 0.1437$ and $P/K > 13$ for $K/R = 0.100$. The roughness effect on the mean velocity profiles was characterized using a logarithmic equation which utilized an error in origin and a roughness function that was a function of the error in origin. The equation was found to be valid for P/K values of 7 or less for $K/R = 0.1437$ and 13 for $K/R = 0.1$ geometries.

Introduction

Turbulent flow over rough surfaces is an important phenomena and there have been many studies in this area. Various forms of rough surfaces have been used in the laboratory. A repeated rib geometry has been most often used in friction factor, heat, and mass transfer studies. The majority of the repeated rib rough wall flow studies have concentrated on the region of developing flow structures going from smooth to rough surfaces [1-6]. This transition region begins with the first roughness element and continues to the fully developed region where the mean flow is identical over every cycle. Morris [7] has proposed that different patterns of this geometry, from closely packed ribs to widely separated elements, cause the fluid flow to vary with several different identifiable flow regimes. Morris [8] claimed that the longitudinal spacing of the roughness was the only significant factor in determining the roughness effect.

Most of the previous workers have studied one or a limited number of roughness element spacing configurations, and, typically, data were taken at only one location within the rib cycle. No literature has been reported on the mean flow quantities, the turbulent intensities, Reynolds shear stresses, and the fluid turbulent eddy diffusivities for a range of roughness geometries. This paper will deal with the mean flow quantities.

The present work was an experimental study of turbulent flow over a repeated rib rough wall where roughness configurations were changed so that a large range of flows were studied. The axial variation of the mean velocity within each rib cycle and the system friction factor was measured for two pipe systems with different roughness height to pipe diameter ratios. All measurements were confined to the fully rough flow regime. Figure 1 is a schematic representation of the test configuration geometry and the flow characteristic parameters. As can be seen from the figure, the roughness elements are of the repeated rib type with spacing P and roughness height K. Various P/K geometries produce different flow regimes and flow structures [8]. Perry, Schofield, Joubert [9] categorized the flow regimes according to the length scale in the roughness function, velocity profiles, and the friction factor sensitivity with respect to K/R (roughness height ratio to the pipe radius). In the *"d"* type flow regime, small rotating eddies are trapped within the grooves of the roughness elements and do not affect the region away from the wall [8]. For this flow the friction factor does not depend on the relative scale of the roughness (K/R) and they proposed that the characteristic length for this flow was the pipe diameter. In the *"k"* type flow, eddies of the order of the roughness height scale are shed from the elements and penetrate through the bulk flow toward the pipe center. The friction factor does vary with K/R in this flow regime.

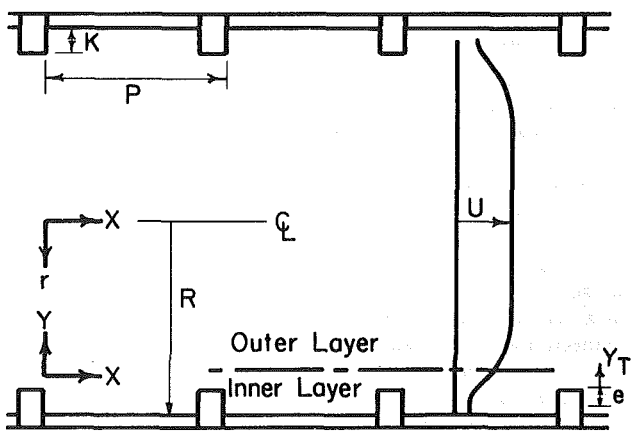

Fig. 1 Schematic diagram of experimental repeated rib configuration

Contributed by the Fluids Engineering Division and presented at the Winter Annual Meeting, New Orleans, La., December 9-14, 1984 of THE AMERICAN SOCIETY OF MECHANICAL ENGINEERS. Manuscript received by the Fluids Engineering Division November 8, 1982. Paper No. 84-WA/FE-5.

Copyright © 1984 by ASME

Downloaded 02 Jun 2010 to 171.66.16.91. Redistribution subject to ASME license or copyright; see http://www.asme.org/terms/Terms_Use.cfm

Flow Resistance and Mean Axial Velocity

The flow resistance was characterized utilizing the Fanning friction factor, f, based on the hydraulic diameter defined by [10]

$$D_h = \left[\frac{4V_L}{\pi L}\right]^{1/2} \tag{1}$$

where L and V_L are the axial length and volume within a single cycle of any geometry.

Following Perry et al. [9], the mean velocity profile is divided into an outer flow and an inner flow region. Away from the roughness elements, the flow is described by the velocity defect law. For the portion of the flow near the wall but outside of the roughness sublayer the velocity distribution is given by

$$U^+ = \frac{1}{k}\ln Y^+ + A - \Delta U^+ \tag{2}$$

where $U^+ (= U/U_s)$ is the mean axial velocity normalized with the shear velocity, Y^+ is the distance measured from a reference wall and normalized with the shear radius, ν/U_s, and ΔU^+ is the roughness function that determines the shift in the smooth wall logarithmic velocity profile caused by wall roughness ($\Delta U^+ = 0$. for smooth wall). A and k are generally constants for smooth pipe wall ($A = 5.0$, $k = 0.4$). Moore [11] and other workers [9, 12, 13] introduced a reference wall and noted a shift in origin of the mean velocity due to wall roughness. The "error in origin," e, of the mean velocity profile has been determined iteratively using the method of Perry and Joubert [14] and others [9, 13, 15]. In this approach, the slope is set at 2.5 (or $1/k$) and the value of e^+ is calculated to give the best fit of the mean axial velocity data, U^+, versus Y_I^+ in a semi-logarithmic plot. For the region $Y/R < 0.2$

$$U^+ = \frac{1}{k}\ln(Y_I^+ + e^+) + A - \Delta U^+ \tag{3}$$

Perry et al. [9] have shown that the roughness function is given by

$$\Delta U^+ = \frac{1}{k}\ln e^+ + C \tag{4}$$

where the constant C varies with roughness geometry. It was also shown that $e \propto K$ for k type roughness and $e \propto R$ for d type roughness.

It is important to note that equations (2) and (3) are valid if the inner and outer region blend along a line that has no periodic disturbances of wavelength P [9]. One would expect that as P/K increases, periodic disturbances would develop along the interface of these two regions. Therefore equations (2) and (3) are limited in their application to repeated rib systems.

Experiment

Two circular duct configurations were utilized to conduct the experimental measurements. In both systems, air was filtered at the bell-shaped inlet to the duct systems by a HEPA filter to provide particle-free air. The maximum attainable Reynolds number in the small and large diameter system was 150,000 and 170,000, respectively.

The small diameter system was constructed from 0.35 cm thick wall, 10.17 cm O.D. stainless steel pipe. The total length of the system was 8.53 m. The configuration was constructed of a series of 0.91 m and 0.45 m pipe sections that were connected with vacuum "O"-ring flanges. When in place, the effective roughness height of the small system was 0.635 cm. The inner radius for this configuration was 4.4175 cm. The various P/K geometries used in the small system were 2, 5, 7, 10, 13, 16, 19, 22, and 25.

The second pipe system, the large pipe system, was constructed from 0.305 cm thick wall, 20.3 cm O.D. stainless steel. The total length of this system was 13.41 m. Custom 0.305 cm thick aluminium angle iron was bent into rings that give roughness elements with dimensions of 1.27 cm wide and 1.27 cm high. When in place, the effective roughness height was 0.9525 cm. The inner radius for the large system was 9.53 cm. For static pressure measurements, two static pressure tubes were placed at the center of pipe to minimize the influence of velocity fluctuations. These static pressure measurements were used to find the friction factor f. Hot-film or hot-wire anemometry techniques were used to measure the turbulent mean flow characteristics.

To assure that the smooth wall pipe flow was fully developed, mean axial profiles were obtained at three different axial locations downstream of the inlet. In order to obtain a fully developed profile as rapidly as possible, roughness elements ($P/K = 2$) were placed upstream of the test section. Seventy and seventy-five diameters were sufficient for the small and large pipe systems, respectively, to achieve the fully-developed condition.

In the friction factor measurements, the flow rate was varied six to nine times for each P/K geometry, and in each case, the mean axial velocity profiles were measured within the rib cycle. For these measurements, four axial measurement locations were chosen for each geometry: $X1$ and $X4$ were measurement points at the same relative positions with respect to the upstream side of the roughness element for the ith and $i+l$th cycles, $X2$ was located one K downstream of the roughness element, and $X3$ was located at approximately the midpoint between the elements in the ith cycle. For $P/K = 2$, only one station was used since the cycle spacing was too narrow to permit additional positions within a cycle. For $P/K = 5$, three stations were employed since the spacing was sufficiently wide to permit a single mid-cycle location. For some of the very high P/K values, a fifth location beyond the midpoint of the rib cycle was also employed. Table 1 gives the axial measurement station locations for all geometries. Velocity measurements were made for three flow rates at each measurement position. Detailed mean velocity measurements at the center of the pipe within a rib cycle were also made for all geometries.

Results and Discussion

Flow Resistance. Figure 2 shows the friction factor as a function of P/K. The calculation of the friction factor requires the simultaneous measurement of dP/dL and U_b. The uncertainty in dP/dL was estimated to be a scale division on the micromanometer used in these experiments. The

Table 1 Axial location of measurement stations (X/K Values*)

	Station			
P/K	X1	X2	X3	X4
Small Pipe System			$K/R = 0.1437$	
2	0.5			
5	−1.5	1	3.5	
7	1	3	5.5	1
10	−1.5	1	5	8.5
13	−1.5	1	5	11.5
16	−1.5	1	8	14.5
19	−1.5	1	8	17.5
22	−1.5	1	11	20.5
25	−1.5	1	11	22.5
Large Pipe System			$K/R = 0.10$	
2	0.5			
13	−1.5	1	5	11.5
24	−1.5	1	11	22.5

*$X/K = 0$ is located at the downstream edge of the step.

Downloaded 02 Jun 2010 to 171.66.16.91. Redistribution subject to ASME license or copyright; see http://www.asme.org/terms/Terms_Use.cfm

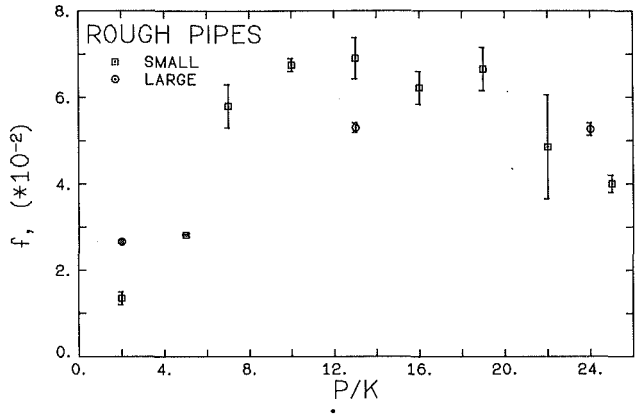

Fig. 2 Friction factor as a function of P/K ratio for large and small pipe systems. The error bars show the propagated uncertainties in the calculated values including the uncertainties in both the pressure gradient and the bulk flow measurements.

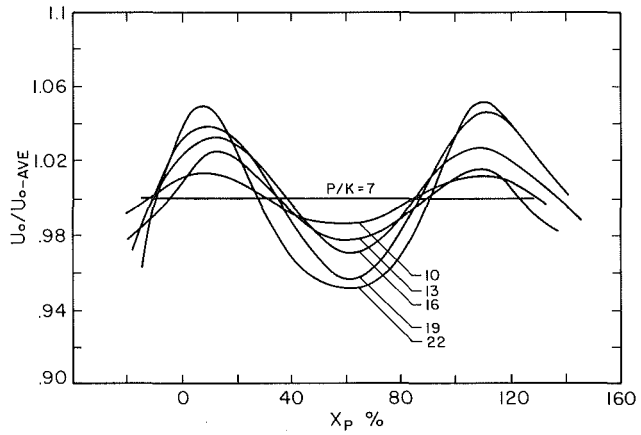

Fig. 3 Center of the pipe mean axial velocity as a function of the fraction of cycle length for K/R = 0.1437. The precision in the $U_0/U_{0\text{-ave}}$ values are ± 2 percent.

uncertainty in U_b was obtained from the noise level in the hot wire anemometer as shown by the strip chart recorder output. These errors were then propagated using standard formulae [16]. Friction factors varied from low values at low P/K to a maximum value near $P/K = 13$ and then decreased at high P/K. The friction factor increased for geometries with P/K values greater than 7 because of the increase in the form drag from each roughness element. A maximum occurred between P/K of 13 and 16. This trend agreed well with the results of Savage and Myers [17] and May [18]. The friction factor decreased as P/K was increased to 25. This result agreed with the supposition that in the extreme flow regimes, i.e., $P/K \to 0$ (quasi-smooth), and $P/K \to \infty$ (isolated roughness), the friction factors must approach the smooth pipe value.

The friction factor variation for the large system gave a similar trend to that of the small system although their values were not equal for the same P/K geometry. The difference was due to the difference in K/R ratio in the two configurations.

Mean Axial Velocity. At the center of the pipe, the mean axial velocity, U_0, was measured along the center axis at one flow rate for each geometry. In the small pipe system, the center line velocity was constant for geometries with P/K values less than 7. For the larger P/K values, the value of U_0 varied over a roughness length. In the larger system, this variation was only observed for P/K of 24 and not for the P/K of 13 geometries. For the small system, the centerline

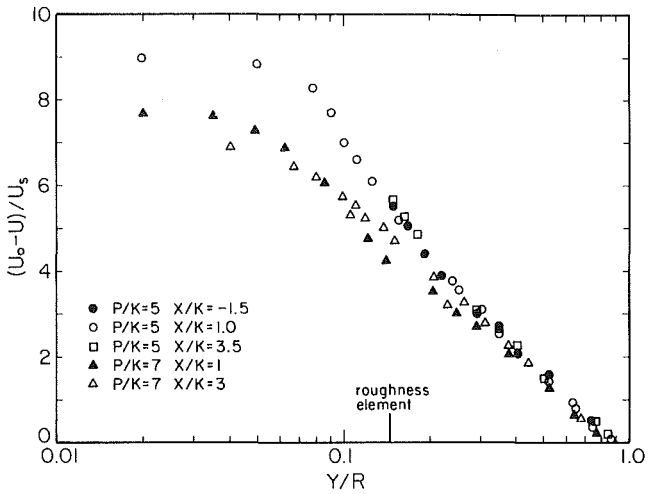

Fig. 4 Defect velocity profiles for P/K values of 5 and 7. The uncertainty in $(U_0 - U)/U_s$ ranges from ±5 percent at $Y/R = 1.0$ to ±15 percent at $Y/R = 0.05$.

velocities were normalized by dividing by the velocity averaged over one cycle and the axial distance expressed as a percentage of the cycle length, P, $X_P = (X/P)$, in order to compare the results from the range of P/K values studied. These normalized velocities, $U_0/(U_0)_{avg}$, are plotted against X_P in Fig. 3.

The amplitude of the velocity variations increased with increasing P/K. It was found that the curve could be fitted to

$$\frac{U_0}{(U_0)_{avg}} = B \sin [(X_P + 0.15)2\pi] + 1.0 \tag{6}$$

where B was a function of P/K. It was found that the effect of the increased spacing caused a variation in the centerline velocity that can be represented by

$$B = 0.0031 P/K - 0.019 \tag{7}$$

for $10 \le P/K \le 25$ with a correlation coefficient of 0.95.

The behavior of the mean axial velocity at the center of the pipe reflected the eddy characteristics of the various flow regime. For low P/K geometries, the fluid eddies were trapped within the elements and did not penetrate to the center of the pipe. For the other configurations fluid underwent sudden expansions and contractions as it encountered roughness elements so that for an incompressible fluid, the velocity varied systematically. The sinusoidal behavior of the core velocity (in equation (6)) resulted from the periodicity of the roughness elements. The increase in the amplitude, B, with the P/K was due to a change in the eddy structure associated with the various roughness configurations.

The centerline axial velocity variations could not be compared directly in the small and large systems because the K/D values were different. The amplitude of the oscillation in the large system was zero for $P/K = 13$ and 0.032 for $P/K = 24$. This value was equivalent to that of $P/K = 13$ in the small system. The oscillations were smaller in the large pipe system since the K/R ratios were smaller and thus the roughness elements comprise a smaller fraction of the pipe cross-sectional area.

Details of the mean axial velocity for all geometries and various axial stations are given in references [19] and [20]. Figure 4 shows the velocity defect profile for two geometries: $P/K = 5$ and $P/K = 7$. Examination of the $P/K = 5$ curves reveals that at all three measurement positions, $X1$, $X2$, and $X3$, the velocity profiles were identical. This suggests that the roughness elements are not causing a periodic disturbance in the velocity profile in the vicinity of the crest of the elements. For the $P/K = 7$ geometry however, a small velocity

Downloaded 02 Jun 2010 to 171.66.16.91. Redistribution subject to ASME license or copyright; see http://www.asme.org/terms/Terms_Use.cfm

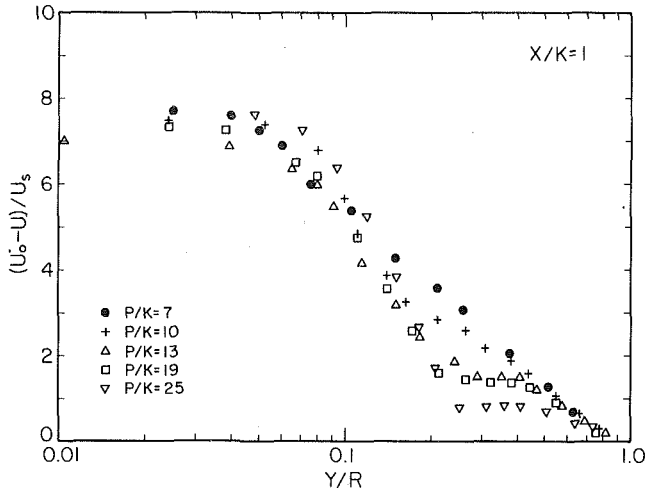

Fig. 5 Defect velocity profiles for P/K values of 7, 10, 13, 19, and 25 at the $X2$ ($X/K = 1$) axial position. The uncertainty in $(U_0 - U)/U_S$ ranges from ±5 percent $tY/R = 1.0$ to ±15 percent at $Y/R = 0.05$.

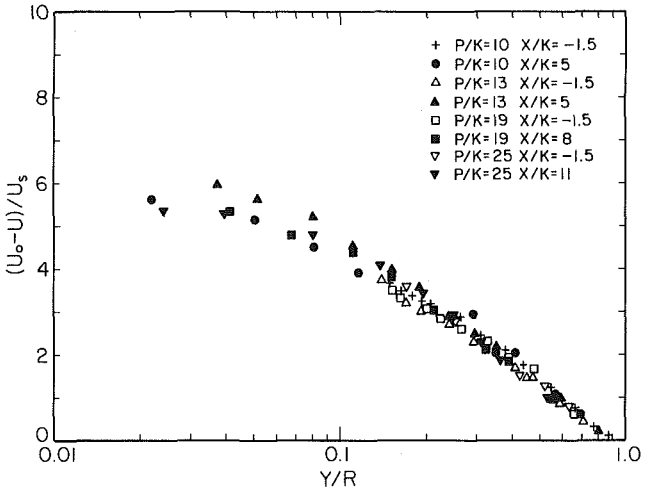

Fig. 6 Defect velocity profiles for P/K values of 10, 13, 19, and 25 at the $X1$ and $X3$ axial positions. The uncertainty in $(U_0 - U)/U_S$ ranges from ±5 percent at $Y/R = 1.0$ to ±15 percent at $Y/R = 0.05$.

deficiency associated with the flow behind the element exists at the measurement station, $X2$ ($X/K = 1$), directly downstream of the element. The separated region disappears at the $X/K = 3$ position. Figure 5 shows that this velocity deficiency continues to grow at the $X/K = 1$ position as the value of P/K increases. This suggests that the amplitude of the periodic flow in the vicinity of the crests increase as the value of P/K increases. A comparison of Figs. 3, 4, and 5 reveal that for P/K values of 7 or less in the small diameter system, a perturbation in the vicinity of the roughness element does not result in a perturbation of the centerline velocity. For P/K values greater than 7, the centerline velocity is affected. Therefore for values of P/K of 7 or less, a region exists in which the inner and outer region blend along a line with no periodic disturbance. Therefore, equations 2 and 3 are applicable [9]. For the large diameter system, equations (2) and (4) were found to be valid up to P/K values of 13. Figure 6 gives the velocity defect profiles at the $X1$ and $X3$ positions for P/K values greater than 7. Since the $X3$ measurement position was approximately at the midpoint of the element spacing, the X/K position of $X3$ measurement increased with increasing P/K configurations. It should be noted that the velocity profiles were identical at the $X1$ and $X4$ positions. Figure 6 shows that the flow recovers very rapidly from the "bubble" phenomena at $X/K = 1$.

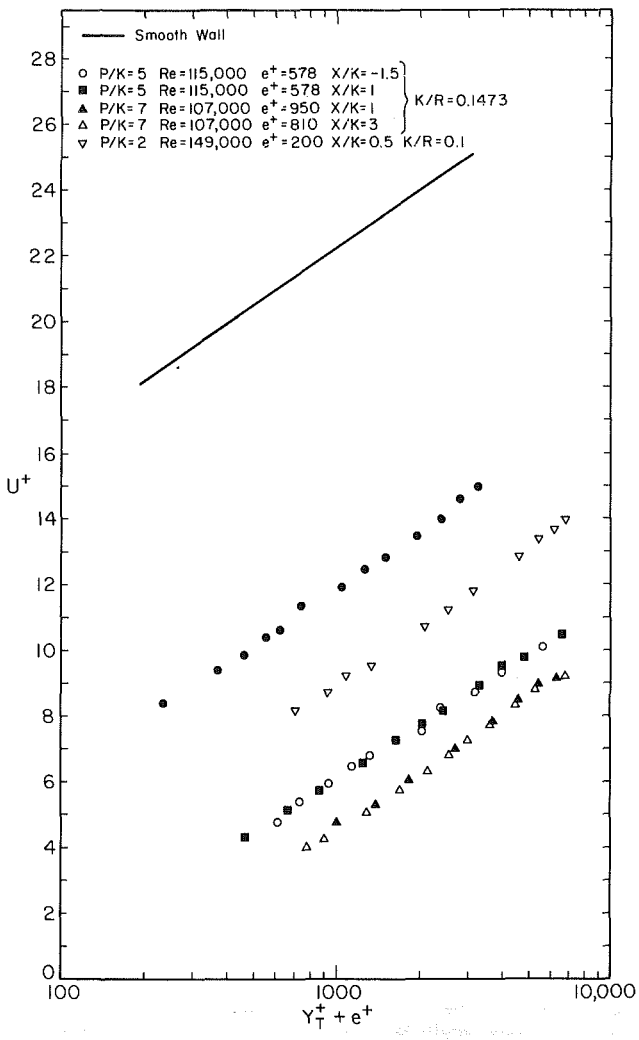

Fig. 7 Mean axial velocity distribution in the outer layer for P/K values of 2, 5, and 7. The uncertainty in U^+ ranges from ±2 percent at the pipe center to ±10 percent near the top of the roughness elements.

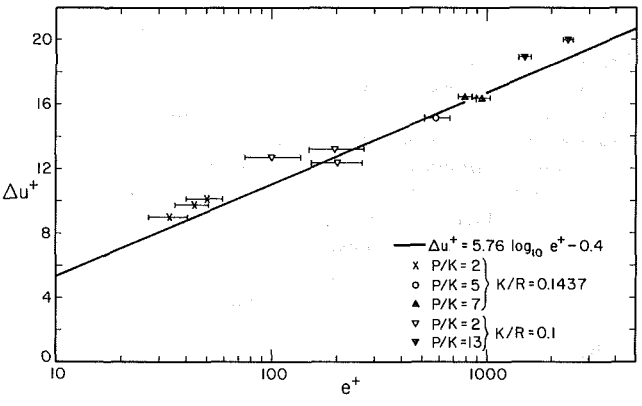

Fig. 8 Roughness function as a function of error in origin for P/K values of 2, 5, 7, and 13. The uncertainty in the roughness function is ±15 percent. The uncertainties in the e^+ values are displayed as horizontal error bars.

Figure 7 shows typical velocity profiles in the region above the roughness elements in the outer region for both experimental configurations. Of course, the vertical separation between the smooth and rough wall profiles is ΔU^+ the roughness functions. Figure 8 gives the variations of the roughness function and the error in origin for both systems.

Downloaded 02 Jun 2010 to 171.66.16.91. Redistribution subject to ASME license or copyright; see http://www.asme.org/terms/Terms_Use.cfm

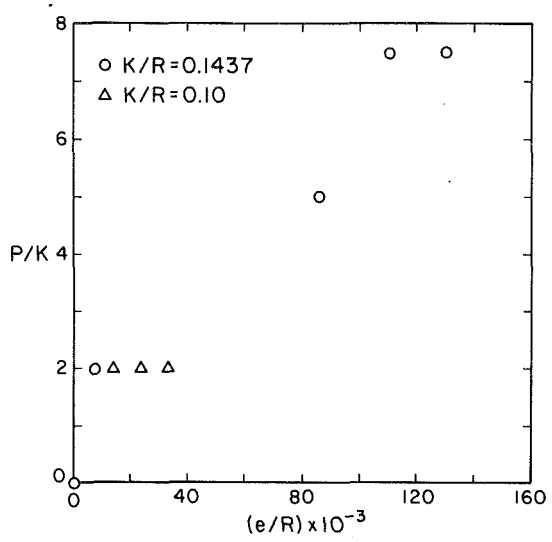

Fig. 9 Error in origin as a function of P/K. The uncertainty in the error in origin is approximately ±20 percent.

The results of this study compare favorably with those of Perry et al. [9] that state that the ΔU^+ and e^+ are related by the equation

$$\Delta U^+ = 5.76 \log_{10} e^+ - 0.4 \quad (8)$$

It should be noted, however, that the variation in e^+ for each pipe system in this study was solely due to variations in the element spacing, P, and not the element height, K, as in the other studies. Figure 9 gives the variation of the error in origin and P/K values for both systems.

Conclusions

1. Friction factors varied from low values at low P/K (2 and 5) to a maximum value at $P/K = 13$ and then decreased at high P/K.
2. For the small diameter rough wall system ($K/R = 0.1437$) the amplitude of the core velocity oscillations increased with increasing P/K. The equation for the core velocity variation was given by equations (6) and (7).
3. The validity of equation (2) is limited to P/K values of 7 or less for $K/R = 0.1437$ and 13 for $K/R = 0.1$.
4. The variation of ΔU^+ with e^+ due to the variation of the element spacing, P, alone can be characterized by equation (4) for P/K values up to 7 for $K/R = 0.1437$ and 13 for $K/R = 0.1$.

Acknowledgments

This work was conducted under contract H0292032 from the U.S. Bureau of Mines.

References

1 Islam, O., and Logan, E., "Channel Flow Over Smooth-to-Rough Surface Discontinuity with Zero Pressure Gradient," ASME JOURNAL OF FLUIDS ENGINEERING, Dec. 1976, pp. 626–634.

2 Logan, J. R. E., and Jones, J. B., "Flow in a Pipe Following an Abrupt Increase in Surface Roughness," ASME *Journal of Basic Engineering*, Vol. 85, 1963, pp. 35–40.

3 Antonia, R. A., and Luxton, R. E., "The Response of a Turbulent Boundary Layer to a Step in Surface in Surface Roughness, Part-1, Smooth to Rough," *Journal of Fluid Mechanics*, Vol. 48, 1971, pp. 721–761.

4 Siuru, W. D., and Logan, E., Jr., "Response of a Turbulent Pipe Flow to a Change in Roughness," ASME JOURNAL OF FLUIDS ENGINEERING, Vol. 99, 1977, pp. 548–555.

5 Siuru, W. D., "Response of a Turbulent Pipe Flow to a Change in Surface Roughness," Ph.D. dissertation, Arizona State University, 1975.

6 Antonia, R. A., and Luxton, R. E., "The Response of a Turbulent Boundary to an Upstanding Step Change in Surface Roughness," ASME *Journal of Basic Engineering*, Vol. 93, 1971, pp. 22–34.

7 Morris, H. M., "A New Concept of Flow in Rough Conduits," Ph.D. dissertation, University of Minnesota, 1950.

8 Morris, H. M., "Flow in Rough Conduit," *Trans. of ASCE*, Vol. 120, 1955, pp. 373–410.

9 Perry, A. E., Schofield, W. H., and Joubert, P. H., "Rough Wall Turbulent Boundary Layers," *Fluid Mechanics*, Vol. 37, 1969, pp. 383–413.

10 Kolar, V., "Heat Transfer in Turbulent Flow of Fluids Through Smooth and Rough Tubes," *International Heat Mass Transfer*, Vol. 8, 1965, pp. 639–653.

11 Moore, W. F., "An Experimental Investigation of the Boundary Layer Development Along a Rough Surface," Ph.D. dissertation, State University of Iowa, 1951.

12 Lawn, C. J., and Hamlin, M. J., "Velocity Measurements in Roughened Annulli," Central Electricity Generating Board, Berkeley. Report CEGB-RD/B/N1278, 1969.

13 Jackson, P. S., "On the Displacement Height in the Logarithmic Velocity Profile," *Journal of Fluid Mechanics*, Vol. 111, 1981, pp. 15–25.

14 Perry, A. E., and Joubert, P. N., "Rough Wall Turbulent Boundary Layers," *Journal of Fluid Mechanics*, Vol. 37, 1963, pp. 383–413.

15 Betterman, D., "Contribution a l'etude dela convection forcee turbulent le long de plaques rugueuses," *International Journal of Heat and Mass Transfer*, Vol. 9, 1966, pp. 153–164.

16 Bevington, P., *Data Reduction and Error Analysis for Physical Sciences*, McGraw-Hill, New York, NY, 1969.

17 Savage, D. W., and Myers, J. E., "The Effects of Artificial Surface Roughness on Heat and Momentum Transfer," *A.I.Ch.E. Journal*, Vol. 9, 1963, pp. 694–702.

18 May, J. C., Jr., "Laws of Turbulent Flow in Rough Pipes," Ph.D. dissertation, Virginia Polytechnic Institute, 1966.

19 Hopke, P. K., and Stukel, J. J., "Study of the Environmental Factors Affecting the Transport of Radon Daughters to Uranium Mine Surfaces," Third Annual Report of Progress on U.S. Bureau of Mines Contract H0292032. Institute for Environmental Studies, University of Illinois, Urbana, 1982.

20 Nourmohammadi, K., "Turbulent Flow over Rough Surfaces," Ph.D. dissertation, University of Illinois, Urbana, Ill., 1982.

Downloaded 02 Jun 2010 to 171.66.16.91. Redistribution subject to ASME license or copyright; see http://www.asme.org/terms/Terms_Use.cfm

Numerical Study of Turbulent Axisymmetric Jets Impinging on a Flat Plate and Flowing Into an Axisymmetric Cavity

R. S. Amano
Assistant Professor,
Department of Mechanical Engineering,
University of Wisconsin—Milwaukee,
Milwaukee, Wis. 53201
Mem. ASME

H. Brandt
Professor,
Department of Mechanical Engineering,
University of California at Davis,
Davis, Calif. 95616
Mem. ASME

A numerical study is made of the characteristics of turbulent submerged axisymmetric incompressible jets impinging on a flat plate and flowing into an axisymmetric cavity. The purpose of the study is to obtain a better understanding of the behavior of a fluid jet used to cut solid materials. In the computations a hybrid finite difference method is used to solve the full Navier-Stokes equations for an incompressible submerged jet with the $k \sim \epsilon$ turbulence model. All computed results are compared with experimental data reported in the literature. For the case of the jet impinging on a flat plate, the computations are made for nozzle-to-plate distances ranging from 2 to 40 nozzle diameters. For the jet flowing into an axisymmetric cavity, computations are made for cavity depths ranging from 0 to 60 nozzle diameters. The use of the $k \sim \epsilon$ turbulence model results in good predictions of the velocity, pressure, and skin friction distributions. The near-wall models for the kinetic energy and turbulent shear stress give good predictions of the skin friction coefficients.

1 Introduction

The objective of this study is to predict numerically the flow field of a turbulent submerged axisymmetric incompressible jet that either impinges on a flat plate or flows into a cavity. The problem is of interest to the field of jet cutting. In jet cutting, a high-velocity water jet is used to cut a variety of materials such as metals, rocks, and concrete. At lower velocities, jets impinging on flat plates are encountered in paint spraying, VTOL aircraft aerodynamics, arc welding with a shielding gas, and a number of heating and cooling applications.

In the jet cutting process, the jet initially impinges on a flat plate. After the cutting has progressed for some time, a cavity is formed. Initially, the cavity is small, but as time progresses the cavity becomes deeper and deeper, up to a maximum depth. Therefore, to better understand the jet cutting process, it is meaningful to study both the impingement of an axisymmetric jet on a flat plate and the flow of a jet into an axisymmetric cavity. Both flow regimes are analyzed numerically in this paper, and the numerical results for each case are compared with experimental data reported in the literature.

Several numerical studies have been made of a jet impinging on a flat plate [1–8]. Wolfshtein [5] solved the plane turbulent impinging jet by using a one-equation turbulence model, and he obtained good agreement with experiments of radial velocity, pressure, and skin friction along the wall. Bower et al. [6] used a one-equation turbulence model to study an axisymmetric jet impinging on a flat plate. They found that their one-equation turbulence model did not give satisfactory agreement with experimental data for small nozzle-to-plate distances. Spalding [7] and Gosman et al. [3] applied the one-equation model to recirculating flows and their results agree well with experiments. On the other hand, the one-equation models give inadequate results when used to predict the behavior of separated flows. More recently Agarwal and Bower [8] presented Navier-Stokes computations of a turbulent compressible planar jet by using the low-Reynolds number form of the $k \sim \epsilon$ model and showed that the $k \sim \epsilon$ model is superior to the simpler zero- or one-equation model of turbulence.

Unlike the study of impinging jets, few studies have been reported on the flow into a closed passage or cavity. Belov and Kogtev [9] obtained a closed form solution of a jet flowing into an axisymmetric cavity by dividing the flow field into two regions: a fully turbulent region and a flow region governed by the laws of an ideal fluid.

In this paper, the high-Reynolds number form of the $k \sim \epsilon$ turbulence model is adopted in all the computations presented by employing the near-wall turbulence model in which wall functions for the viscous sublayer and the overlapping layer are incorporated to evaluate the mean values of turbulence quantities.

Contributed by the Fluids Engineering Division and presented at the Winter Annual Meeting, New Orleans, La., December 9–14, 1984 of THE AMERICAN SOCIETY OF MECHANICAL ENGINEERS. Manuscript received by the Fluids Engineering Division, February 16, 1983. Paper No. 84-WA/FE-6.

Copyright © 1984 by ASME

Downloaded 02 Jun 2010 to 171.66.16.91. Redistribution subject to ASME license or copyright; see http://www.asme.org/terms/Terms_Use.cfm

Table 1 Summary of equations solved

Equation	ϕ	Γ_ϕ	S_ϕ
Continuity	1	0	0
x-Momentum	U	μ_{eff}	$-\frac{\partial p}{\partial x}+\frac{\partial}{\partial x}\left(\mu_{\text{eff}}\frac{\partial U}{\partial x}\right)+\frac{1}{r}\frac{\partial}{\partial r}\left(r\mu_{\text{eff}}\frac{\partial V}{\partial x}\right)$
r-Momentum	V	μ_{eff}	$-\frac{\partial p}{\partial r}+\frac{\partial}{\partial x}\left(\mu_{\text{eff}}\frac{\partial U}{\partial r}\right)+\frac{1}{r}\frac{\partial}{\partial r}\left(r\mu_{\text{eff}}\frac{\partial V}{\partial r}\right)-2\mu_{\text{eff}}V/r^2$
Turbulence Energy	k	$\mu+\frac{\mu_t}{\sigma_k}$	$\rho P-\rho\epsilon$
Energy Dissipation	ϵ	$\mu+\frac{\mu_t}{\sigma_\epsilon}$	$C_1\frac{\rho\epsilon}{k}P-C_2\frac{\rho\epsilon^2}{k}$

where $\mu_t=C_\mu\rho k^2/\epsilon$, $\mu_{\text{eff}}=\mu+\mu_t$

and $P=\nu_t\left[\left(\frac{\partial U}{\partial r}+\frac{\partial V}{\partial x}\right)^2+2\left(\frac{\partial U}{\partial x}\right)^2+2\left(\frac{\partial V}{\partial r}\right)^2+2\left(\frac{V}{r}\right)^2\right]$

C_μ	C_1	C_2	σ_k	σ_ϵ
0.09	1.44	1.92	1.0	1.3

2 Formulation of Numerical and Mathematical Models

2.1 Mathematical Formulation. The equations used for defining the mean velocity fields in statistically stationary, turbulent flow of an incompressible jet impinging on a flat plate and flowing into an axisymmetric cavity may be given in the general form as:

$$\text{div}(\rho U\phi)=\text{div}\ \Gamma_\phi\text{grad}\ \phi+S_\phi$$

or in axisymmetric cylindrical coordinates this can be written as

$$\frac{1}{r}\left[\frac{\partial}{\partial x}(r\rho U\phi)+\frac{\partial}{\partial r}(r\rho V\phi)\right]=\frac{1}{r}\left[\frac{\partial}{\partial x}\left(r\Gamma_\phi\frac{\partial\phi}{\partial x}\right)+\frac{\partial}{\partial r}\left(r\Gamma_\phi\frac{\partial\phi}{\partial r}\right)\right]+S_\phi \quad (1)$$

where ϕ stands for the dependent variables U, V, k, and ϵ, and S_ϕ is the corresponding source term. These equations are summarized in Table 1.

2.2 Boundary Conditions. The boundary conditions and typical numerical axisymmetrical grids used for the jet impinging on a flat plate and for the jet flowing into an axisymmetric cavity are shown in Fig. 1. For an impinging jet, a contracting grid system is used in the x-direction and an expanding grid system is adopted in the r-direction. In this way, finer grids near the wall are obtained. For a jet flowing into a cavity, a contracting grid system is used in the x-direction, a constant grid in the r-direction.

The boundaries CD and DE in Fig. 1(*a*) are both inflow and outflow boundaries, and the boundary DE in Fig. 1(*b*) is the outflow boundary. At these boundaries, the flow is assumed to be of the parabolic type. In particular, for the case of the impinging jet on a flat plate, a nozzle-to-plate distance greater than $5D_N$ is maintained so as to have negligible influence on the main flow.

For the evaluation of the wall effect, two methods have been proposed in the literature: a wall function model [10, 11] and a low-Reynolds number model [12, 13]. Taking into account that many cells are required in a low-Reynolds number model, the wall function model was employed in this study. The model used here is the one developed by Chieng and Launder [11]. In this model the turbulent kinetic energy is assumed to vary in a parabolic shape within the viscous sublayer which corresponds to the linear variation of a fluctuating velocity with distance from the wall and then varies linearly over the remainder of the cell. Unlike the

Nomenclature

C_μ, C_1, C_2 = constants used in turbulence models
D_N = nozzle diameter
D_T = diameter of a cavity
H = nozzle-to-plate distance
i = turbulence intensity (k/U_N^2)
k = turbulence kinetic energy
l_m = mixing length
L_T = cavity depth
p = pressure
P = generation rate of turbulence kinetic energy
r = coordinate in radial direction
r_N = nozzle radius
Re_D = nozzle Reynolds number
S_ϕ = source terms of ϕ-equation
U = mean velocity component in x-direction
U_N = nozzle exit velocity
V = mean velocity component in r-direction
x = coordinate in jet axial direction
y = distance from the wall
Γ_ϕ = diffusion coefficient of ϕ-equation
ϵ = turbulence energy dissipation rate
λ = length scale constant
μ = dynamic viscosity
μ_{eff} = effective viscosity ($\mu+\mu_t$)
μ_t = turbulent dynamic viscosity
ν_t = turbulent kinematic viscosity
ρ = density
$\sigma_k, \sigma_\epsilon$ = Prandtl numbers for turbulence kinetic energy and energy dissipation rate respectively
ϕ = dependent variables (U, V, k, and ϵ)

Subscripts

in = values pertaining to the inflow region of the solution domain
N = values pertaining to the nozzle exit

Downloaded 02 Jun 2010 to 171.66.16.91. Redistribution subject to ASME license or copyright; see http://www.asme.org/terms/Terms_Use.cfm

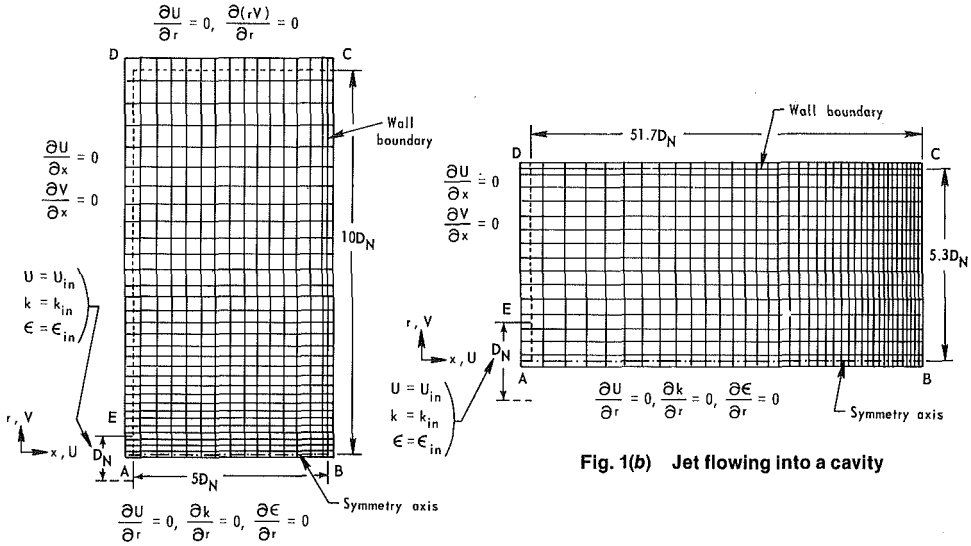

Fig. 1(*a*) Jet impinging on a flat plate

Fig. 1(*b*) Jet flowing into a cavity

Fig. 1 Typical numerical grids and boundary conditions for computation

turbulent kinetic energy, the shear stress is zero within the viscous sublayer and it undergoes an abrupt increase at the edge of the viscous sublayer and then varies linearly toward the outer region of the cell. In the model of Chieng and Launder [11] this treatment was applied only for the k-equation. In a new model by Amano and Jensen [14], the treatment of evaluating mean generation and destruction rates also are incorporated in the ϵ-equation. Amano and Jensen compared their model and the model of Chieng and Launder with the original one by Launder and Spalding [10] for turbulent jets impinging on a flat plate. It is shown in [14] that both models of Chieng and Launder and Amano and Jensen are superior to the model of Launder and Spalding [10] which dealt with a single approximation in the boundary layer.

The condition in the nozzle (boundaries EA in Fig. 1) is important in predicting the centerline velocity and shear stress. The velocity profile at the nozzle exit is affected by the nozzle design such as the length-to-diameter ratio, nozzle shape, and the presence or absence of a transition section upstream of the nozzle. In this paper, two nozzle velocity profiles were considered: a uniform velocity profile, and a 5.5 power velocity profile.

When the velocity profile at the nozzle exit is uniform, the conditions in the nozzle are given as

$$U = U_{in}$$
$$k = k_{in} = iU_{in}^2 \tag{2}$$
$$\epsilon = \epsilon_{in} = \frac{k_{in}^{3/2}}{\lambda r_N}$$

where i is the turbulence intensity, λ is the length-scale constant, and r_N is the radius of the nozzle.

When the velocity profile at the nozzle exit is nonuniform, the turbulent kinetic energy and the turbulent energy dissipation need to be calculated. On applying the near wall condition, such as negligible convection and diffusion of kinetic energy, we will obtain the following expressions [15] for both k and ϵ at the nozzle exit.

$$k = C_\mu^{-1/2} l_m^2 \left(\frac{\partial U}{\partial r}\right)^2. \tag{3}$$

$$\epsilon = C_\mu^{1/2} k \frac{\partial U}{\partial r} \tag{4}$$

From a specification of the velocity profile, and a knowledge of the mixing length, we can obtain k and ϵ from equations (3) and (4), respectively. The mixing length, l_m, may be determined from the smaller of either the Nikuradse formula,

$$\frac{l_m}{r_N} = 0.14 - 0.08\left(1 - \frac{y}{r_N}\right)^2 - 0.06\left(1 - \frac{y}{r_N}\right)^4, \tag{5}$$

or the mixing length computed from the wall region formula,

$$l_m = 0.41\, y, \tag{6}$$

where y is a distance from the wall. The procedure which incorporates the smaller of the two mixing lengths means that the wall mixing length formula is used near the wall and the Nikuradse formula at large distances from the wall.

Note that these formulations give zero values for k and ϵ at the center of the pipe which is not realistic. To compensate for possible unrealistic centerline values, a minimum value of the turbulent kinetic energy was given near the center of the pipe. The values of turbulent kinetic energy at the center of the nozzle were determined from the experimental setup considered by solving a separate pipe flow computer program [15]. For example, the turbulence intensity obtained for the conditions of Tani and Komatsu [16] and of Bradshaw and Love [17] are 0.005 and 0.004, respectively.

The 5.5 power velocity profile is expressed as

$$U = U_{\max}\left[1 - 0.3412\left(\frac{r}{r_N}\right)^{5.5}\right]. \tag{7}$$

The profile of (7) is a result of experimental measurements [17].

2.3 Numerical Procedure. The method adopted for solving equation (1) is the solution procedure for elliptic equations [18]. The value of each scalar quantity is associated with a grid node, although the vector quantities (velocity components) are displaced in space relative to the scalar quantities. In this study, a hybrid scheme is adopted in which a central-difference approximation is used when the cell Peclet number is less than 2, and an upwind-difference method with the combined effects of convection and diffusion is employed at the higher level of convection (when the cell Peclet number is greater than 2). Although the problem of false diffusion comes up by employing the hybrid method for large cell Peclet number flows, Leschziner [19] made tests of three different hybrid schemes and showed that artificial diffusion resulting from skewness is negligibly small when applied to the elliptic flows. In the present case the cell Peclet

Downloaded 02 Jun 2010 to 171.66.16.91. Redistribution subject to ASME license or copyright; see http://www.asme.org/terms/Terms_Use.cfm

numbers are small in the impingement region where the central-difference method is employed. Thus, the small skewness of the normal jet gives acceptable accuracy of the results. In the region outside the impingement region along the plate, the flow becomes mostly of the boundary layer type where the upwind-difference method would be used. In the boundary layer, the skewness becomes negligibly small. Hence, the error associated with the upwind difference method is minor as is discussed by Patankar [18]. Two problems associated with determining the pressure distribution and satisfying continuity are overcome by adjusting the pressure field [20].

For the present model the dependence of the results on the number of cells is relatively insensitive. For example, the variation in skin friction computed employing grids of 42 × 42 cells and 32 × 42 cells was within 3 percent. This variation is relatively small because the control volume approach and the near-wall model described in the preceding section permits rather complex local variations of turbulence quantities to be evaluated over each control volume. Thus the physical laws are satisfied over any group of numerical cells as well as over the whole solution domain.

3 Presentation and Discussion of Results

3.1 Axisymmetric Jet Impinging on a Flat Plate. Figure 2 shows the decay of the axial centerline velocity as a function of distance along the jet, and Fig. 3 shows the maximum radial velocity and pressure against radial distance from the stagnation point for both present computation and the measured results of Tani and Komatsu [16]. Referring to Fig. 2, we note agreement within 5 percent between the computed axial centerline velocity and the experimental results. When the nozzle-to-plate distance (H/D_N) is 4, the centerline velocity does not start to decrease until about 2.5 to 3 nozzle diameters from the nozzle. The centerline velocity then decreases rapidly to zero velocity at the stagnation point. When the nozzle-to-plate distance is large, the jet begins to take on the character of a free jet. The centerline velocity of the free jet was determined analytically by Kleinstein [21] who found an exponential expression for the decay. Kleinstein's expression shows a smooth transition of the axial centerline velocity decay between the potential core and developed regions of the jet. The angle at which the curves of axial centerline velocity at the stagnation point intersect the x axis increases from 90 to 98 degrees as H/D_N increases from 4 to 12.

Figure 3 shows both the maximum radial velocity and the pressure as a function of radial distance from the stagnation point. Starting from the stagnation point, the radial velocity along the wall increases with radial distance under the influence of a favorable pressure gradient and then decreases due to viscous dissipation. The maximum radial velocity occurs between 1 and 2 nozzle diameters from the stagnation point for nozzle-to-plate distances of 4 and 12, respectively. The pressure is at its maximum at the stagnation point and decreases to less than 10 percent of the stagnation pressure at a radial distance of about 1.1 nozzle diameters from the stagnation point for the case of $H/D_N = 4$. In the case of $H/D_N = 12$, the pressure decreases to less than 10 percent of the stagnation pressure at a radial distance of about 1.5 nozzle diameters. Thus, the impingement region increases as the nozzle-to-plate distance increases. This increase in the impingement region can also be found in the results in Fig. 2 as discussed earlier. We should also note that the normalized pressures are less than one for $H/D_N > 4$ because the impingement region is outside the potential core of the jet. In summary, the computations of axial and radial velocities are within 5 percent, and the pressure within 3 percent of experimental results.

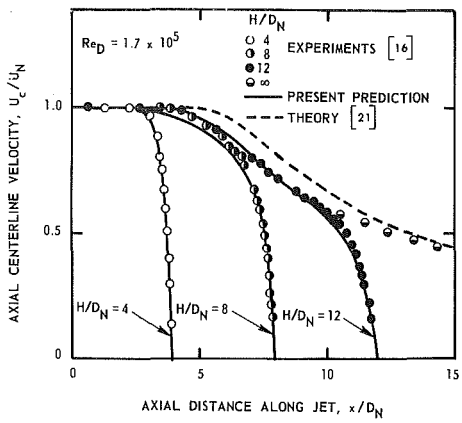

Fig. 2 Decay of axial centerline velocity for an axisymmetric jet impinging on a flat plate (uniform velocity profile at nozzle exit)

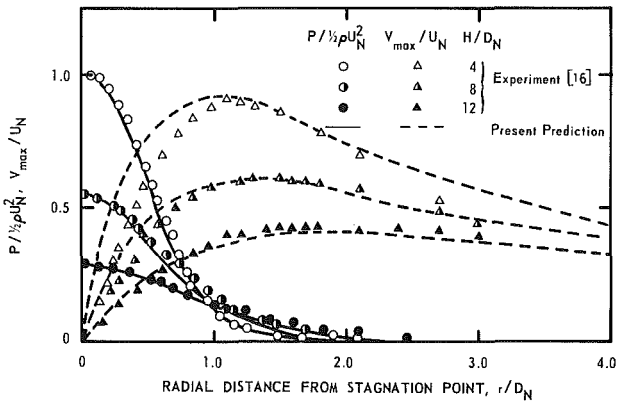

Fig. 3 Pressure and maximum radial velocity along the wall for an axisymmetric jet impinging on a flat plate

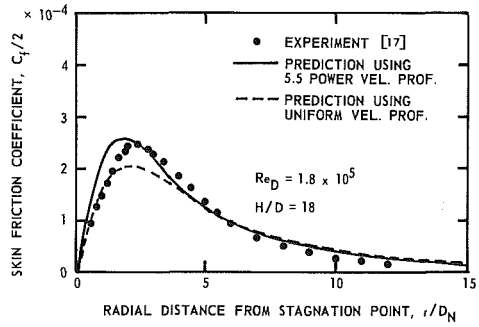

Fig. 4 Skin friction along the wall for an axisymmetric jet impinging on a flat plate

The variation of the skin friction coefficient ($C_f = \tau_w/\rho U_N^2$) along the wall was computed and compared with experimental data given by Bradshaw and Love [17] for $H/D_N = 18$ and Re $_D = 1.8 \times 10^5$, where U_N is the nozzle exit velocity (Fig. 4). The computations were performed for two different nozzle exit velocity conditions.

The nozzle used in the experiments by Bradshaw and Love [17] was 20 cm long and 2.5 cm in diameter with a bellshape entrance section. The turbulence intensity of the fluid flowing through this nozzle was not known. However, our assumption of a turbulence intensity of 0.004 gave the best overall agreement (25 percent) with the experimental data. This turbulence intensity was estimated by running a separate computer program [15] for their experimental setup of 8 nozzle diameter lengths. It is evident that the use of a 5.5 power velocity profile at the nozzle exit more closely approximates the experimental situation than a uniform velocity

Downloaded 02 Jun 2010 to 171.66.16.91. Redistribution subject to ASME license or copyright; see http://www.asme.org/terms/Terms_Use.cfm

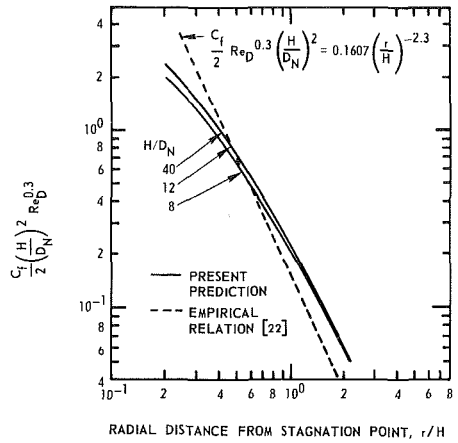

Fig. 5 Universal skin friction along the wall for an axisymmetric jet impinging on a flat plate (uniform velocity profile at nozzle exit)

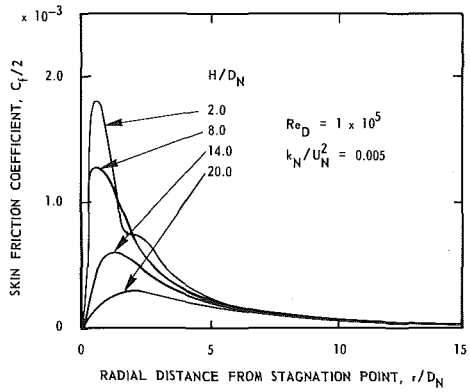

Fig. 6 Computed skin friction along the wall for different nozzle-to-plate distances of an axisymmetric jet impinging on a flat plate (uniform velocity profile at nozzle exit)

profile. In the case of the 5.5 power velocity profile, the turbulent kinetic energy is higher, especially at the edge of the jet. This higher turbulent kinetic energy results in a larger value for the maximum skin friction coefficient along the wall. However, at a radial distance greater than about 4 nozzle diameters from the stagnation point, the difference in the velocity conditions in the nozzle affects the behavior of the skin friction coefficient within 1 percent. It is also noted in Fig. 4 that the curve for the 5.5 power velocity profile has a sharper peak, particularly near the maximum value, than the cufve for the uniform velocity profile. The shape of the 5.5 power velocity profile curve displays actual situations more closely than the curve of the uniform velocity profile and fits experimental results more closely.

Figure 5 generalized the skin friction coefficient with nozzle-to-plate distance, H/D_N, and nozzle Reynolds number, Re_D. The results are compared to the empirical relation given by Poreh et al. [22]. Poreh et al. obtained the empirical relationship as a result of experiments with jets having H/D_N of 8, 12, and 40 and for Re_D ranging from 5×10^4 to 3×10^5. If we compare the computed results with the empirical relationship of Poreh et al., we note the similarity in the trends of the curves. The computed curves are based on a uniform velocity profile of the jet at the exit of the nozzle. Poreh et al. did not include a specification of either nozzle geometry nor turbulence intensity of the jets emerging from the nozzle. Hence, the use of a uniform velocity profile at the nozzle exit with a turbulence intensity of 0.005 was considered satisfactory and was found to give the best overall agreement between computed and empirical results. The discrepancy between the computation and the experimental results near

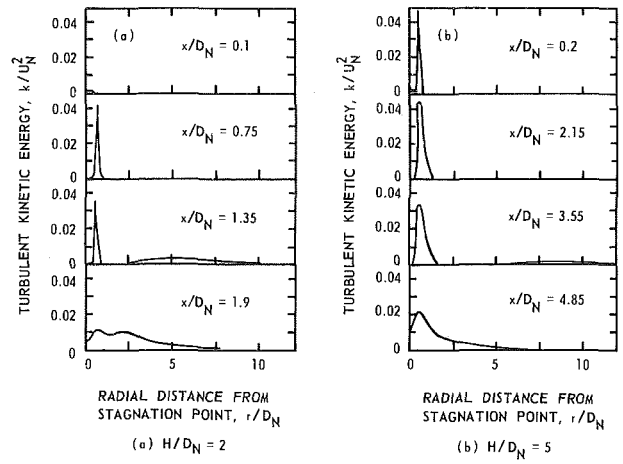

Fig. 7 Radial distributions of computed turbulent kinetic energy at different axial distances form nozzle for an axisymmetric jet impinging on a flat plate, $k_N/U_N^2 = 0.005$, $Re_D = 1 \times 10^5$ (uniform velocity profile at nozzle exit)

the stagnation point (where r/H is small) is attributed to the difference in the nozzle conditions of the computations and experimental setup.

Figure 6 shows the skin friction coefficients as a function of the radial distance from the stagnation point for H/D_N of 2 to 20. The computed skin friction coefficient curves show an interesting behavior when $H/D_N = 2$. For these conditions, the skin friction coefficient curve exhibits a different shape than that of the other curves at about 2 nozzle diameters from the stagnation point. If we move the nozzle away from the surface, keeping all other conditions fixed, the difference in the curve shape disappears. For ease of discussion, we shall call this difference a second maximum.

The second maximum was observed experimentally first by Gardon and Akfirat [23] in their measurements of the heat transfer coefficient of both plane and axisymmetric jets. Eleven years later, Baines and Keffer [24] also observed the second maximum in their skin friction coefficient measurements of plane impinging jets. Gardon and Akfirat explained the second maximum as a transition from laminar to turbulent flow. Their explanation, however, may not be correct because in their experiments they also observed that the relative magnitude of the second maximum became larger and the position of the second maximum moved regularly outward as the nozzle Reynolds number was increased. In fact, if this second maximum were to occur due to a transition from laminar to turbulent flow, the second maximum would move toward rather than away from the stagnation point.

To explain the second maximum analytically, the turbulent kinetic energy distributions in a radial direction are plotted in Fig. 7 for H/D_N of 2 and 5. In each figure the turbulent kinetic energy is shown at four positions from the nozzle. In Fig. 7, a peak kinetic energy is observed at the outer edge of the jet at an axial position (x/D_N) of 0.75 nozzle diameters downstream from the nozzle. At the outer edge of the jet, the kinetic energy generation rate is high due to high shearing action. This peak kinetic energy is convected away as a mixing of the jet continues (at $x/D_N = 1.35$). However, before the mixing zone reaches the axis of the jet, the plate impedes the convective action of the peak kinetic energy. Fluid particles with high kinetic energy cause a second disturbance in the turbulent kinetic energy spectrum as a function of radial distance (at $x/D_N = 1.9$). Since the shear stress is proportional to the square root of the turbulent kinetic energy near the wall region, the kinetic energy disturbance affects the skin friction coefficient. However, pressure and mean velocity are not affected by the kinetic energy disturbance in the near wall region and, therefore, no observable second maximum is

Downloaded 02 Jun 2010 to 171.66.16.91. Redistribution subject to ASME license or copyright; see http://www.asme.org/terms/Terms_Use.cfm

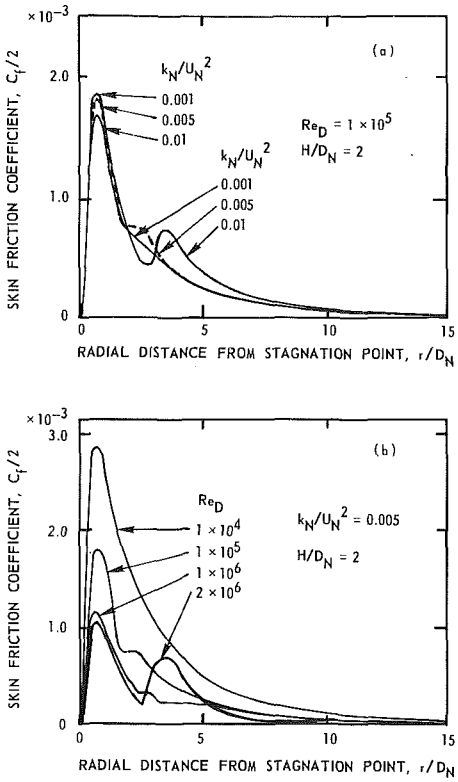

Fig. 8 Influence of turbulence intensity in the nozzle and nozzle Reynolds number on computed skin friction along the wall for an axisymmetric jet impinging on a flat plate (uniform velocity profile at nozzle exit)

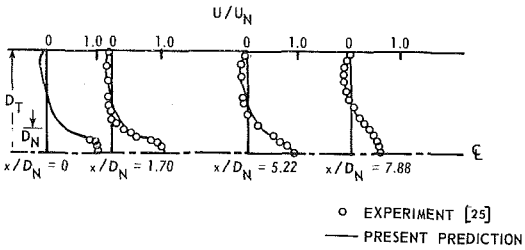

Fig. 9(a) Axial velocity profiles at different axial distances from nozzle, $k_N/U_N^2 = 0.005$ and $Re_D = 5 \times 10^5$

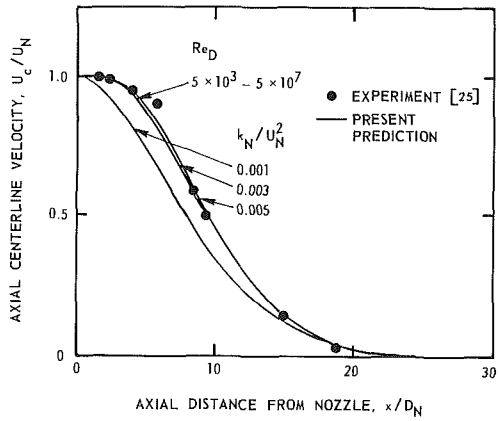

Fig. 9(b) Influence of turbulence intensity in the nozzle and nozzle Reynolds number on the decay of axial centerline velocity

Fig. 9 Axial velocities for an axisymmetric jet flowing into an axisymmetric cavity, $D_T/D_N = 5.3, L_T/D_N = 51.7$

found in the radial velocity distributions. However, as shown in Fig. 7(*b*), no second maximum in turbulent kinetic energy is observed for $H/D_N = 5$ because mixing of the jet is completed in a distance of less than 5 nozzle diameters.

In Fig. 8(*a*), skin friction coefficients are plotted for $H/D_N = 2$ for jets having different values of turbulence intensity (k_N/U_N^2) at the nozzle exit. When the turbulence intensity is small (0.001), the second maximum can barely be seen. However, when the turbulence intensity is increased to 0.005, a second maximum appears at a radial distance between 2 and 2.5 nozzle diameters. When the turbulence intensity is increased further to 0.01, the second maximum becomes a predominant feature at a radial distance of about 3.5 to 4 nozzle diameters.

In Fig. 8(*b*), the skin friction coefficient is plotted for jet flow with $H/D_N = 2$ for Re_D varying from 1×10^4 to 2×10^6. The turbulence intensity at the nozzle exit was held constant at 0.005. For the jet flow with lower Reynolds numbers, the second maximum is barely noticeable; however, at $Re_D = 1 \times 10^5$, the second maximum appears at a radial distance of about 2 to 2.5 nozzle diameters from the stagnation point and then it increases as Re_D becomes larger.

In both Figs. 8(*a*) and 8(*b*), the second maximum moves toward larger radial distances from the stagnation point when either the turbulence intensity or the nozzle Reynolds number is increased. In the case of Fig. 8(*a*), the increase in turbulence intensity causes an increase in the generation rate of turbulent kinetic energy at the outer boundary of the jet. This, in turn, causes an increase in the convection rate. In the case of Fig. 8(*b*), jet flows with a higher Reynolds number have a smaller length scale in the mixing region. As a result, the generation rate of turbulent kinetic energy is increased, which in turn increases the convection rate at the outer boundary of the jet. Thus, in both cases of Fig. 8, the convection rate of the jets is increased as the turbulence intensity and nozzle Reynolds number are increased. Furthermore, in both figures the second maximum moves toward larger radial distances from the stagnation point as turbulence intensity and nozzle Reynolds number are increased. This outward movement, therefore, is attributed to the increase in the convection rate at the outer boundaries of the jets.

3.2 Jet Flowing Into an Axisymmetric Cavity. Even though the technology of jet cutting has an extensive literature, only two investigators measured flow characteristics of jets flowing into an axisymmetric cavity. Rozenberg [25] studied the flow of an axisymmetric jet into an axisymmetric cavity. The outlet of the nozzle was located in the inlet plane of the cavity, and Leach and Walker [26] measured the variation in the stagnation pressure at the bottom of the cavity as a function of cavity depth. The results of the numerical computations are compared with the experimental measurements obtained by these investigators.

Figure 9 compares the results of the numerical calculations with the experiments by Rozenberg [25]. As is shown in the figure, the agreement between the computation and the experimental data is remarkable for both the axial velocity profile and the centerline velocity decay. In Fig. 9(*b*) the numerical computations were made for three turbulence intensities (k_N/U_N^2) ranging from 0.001 to 0.005 while the velocity profile in the nozzle was kept uniform. It is seen that the axial centerline velocity decay is affected less than 3 percent by the turbulence intensity if the turbulence intensity is greater than 0.003. However, for a jet with a turbulence intensity of 0.001, the axial centerline velocity decays more rapidly than centerline velocities of jets having higher turbulence intensities. The numerical computations indicate that the jets penetrate the cavity to a depth of about 20 to 25 nozzle diameters, but will not penetrate the cavity to any greater depth. The figure also shows centerline velocity decay as a function of axial distance from the nozzle for jets having nozzle Reynolds numbers ranging from 5×10^3 to 5×10^7. This figure indicates that the centerline velocity decay is

Downloaded 02 Jun 2010 to 171.66.16.91. Redistribution subject to ASME license or copyright; see http://www.asme.org/terms/Terms_Use.cfm

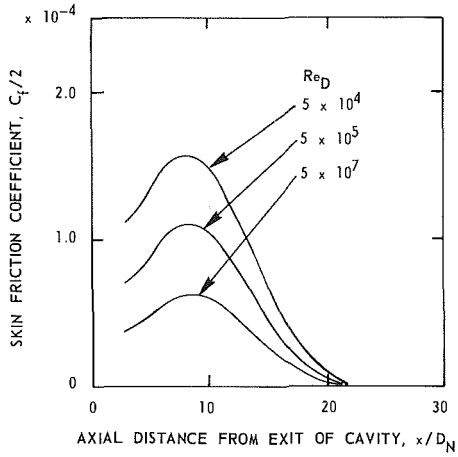

Fig. 10 Influence of nozzle Reynolds number on computed skin friction along the cavity wall for an axisymmetric jet flowing into an axisymmetric cavity, $D_T/D_N = 5.3, L_T/D_N = 51.7, k_N/U_N^2 = 0.004$

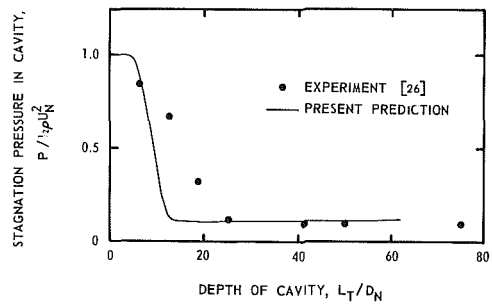

Fig. 11 Stagnation pressure in the cavity as a function of cavity depth for an axisymmetric jet flowing into an axisymmetric cavity, $Re_D = 1.7 \times 10^5, D_T/D_N = 5$

affected less than 0.5 percent by the nozzle Reynolds number. In spite of the large range of jet velocities, the jets again penetrate no further than about 22 to 25 nozzle diameters into the cavity.

Figure 10 shows the skin friction coefficient along the cavity wall. The maximum skin friction occurs at a depth of about 8 to 9 nozzle diameters. The skin friction approaches zero (less than 1/1000 of the initial value) at a depth of about 22 nozzle diameters. This depth is the same depth at which the centerline velocity decayed to zero. In other words, the jet flow from the nozzle penetrates the cavity to about 22 nozzle diameters and then turns around and flows back toward the cavity exit. Although not shown in the figures, it was found that a high generation of kinetic energy at the wall took place at a depth of about 18 to 20 nozzle diameters. The outward flow accelerates from its maximum depth and reaches its highest value at a depth of about 6 to 7 nozzle diameters. The maximum skin friction occurs between the depths of maximum outward velocity and maximum turbulent kinetic energy at the wall.

Figure 11 shows the stagnation pressure at the bottom of the cavity as a function of cavity depth. The results are compared with the data of Leach and Walker [26]. The cavity diameter, D_T, was 5 nozzle diameters, D_N, and the nozzle was located in the entry plane of the cavity. The stagnation pressure decreases with cavity depth for cavities having a depth less than 25 nozzle diameters (5 cavity diameters). For cavities with greater depth, the stagnation pressure remains approximately constant at 1/10th of the initial stagnation pressure of the jet. For cavities having a depth greater than 25 nozzle diameters, the numerical calculations agree within 1 percent with the stagnation pressure determined experimentally. For cavities with depths of less than 25 nozzle diameters, the computed stagnation pressures are as low as 24 percent of experimentally determined pressures. The discrepancy could be due to a lack of the information in the experimental condition on the jet. However, for a deeper cavity in which the impingement strength does not propagate to the cavity bottom, the variation of velocity profile in the jet has minor influence on the stagnation pressure.

4 Conclusions

The main conclusions of this study are:

Computational Model

(i) The use of the $k \sim \epsilon$ turbulence model results in a good prediction of the velocity distributions and pressure, within 5 percent of measured values.

(ii) The near-wall models for kinetic energy and turbulent shear stress at high Reynolds numbers give a prediction of the skin friction coefficient within 25 percent error of measured values.

Jet Impinging on a Flat Plate

(iii) The velocity profile and the turbulence intensity at the nozzle exit affect the magnitude of the maximum skin friction on the wall, but they have little (1 percent) effect on the remaining portions of the curve of skin friction versus distance from the stagnation point.

(iv) When the nozzle-to-plate distance is less than two nozzle diameters, a second maximum occurs in the distribution of skin friction coefficient versus radial distance from the stagnation point and its magnitude depends on the turbulence intensity in the nozzle, nozzle Reynolds number, and the nozzle-to-plate distance.

(v) The position of the second maximum moves in a direction away from the stagnation point as the turbulence intensity in the nozzle and the nozzle Reynolds number are increased. This is in accordance with the experimental observation by Gardon and Akfirat [23].

Jet Flowing Into an Axisymmetric Cavity

(vi) The decay of centerline velocity is insensitive (within 0.5 percent) to nozzle Reynolds number, but depends on turbulence intensity in the nozzle for a turbulence intensity of less than 0.005.

(vii) The maximum skin friction on the side wall inside the cavity occurs at a depth of about 8 to 9 nozzle diameters for $D_T/D_N = 5.3$ and $L_T/D_N = 51.7$, and the skin friction approaches zero (less than 1/1000 the initial value) at depths greater than 22 nozzle diameters.

(viii) The pressure at the bottom of the cavity decreases with cavity depth and remains constant at 1/10th of the initial stagnation value for cavities deeper than 5 cavity diameters.

Acknowledgments

All the computations were made on a CDC 6600 computer at the Lawrence Livermore National Laboratory, Livermore, California. Thanks are due to Ms. Karen Steldt who handled the production of the manuscript.

References

1 Welch, J. E., Harlow, F. H., Shannon, J. P., and Daly, B. J., *The MAC Method*, LASL Report No. LA-3424, Los Alamos Scientific Laboratory, Los Alamos, New Mexico, 1966.

Downloaded 02 Jun 2010 to 171.66.16.91. Redistribution subject to ASME license or copyright; see http://www.asme.org/terms/Terms_Use.cfm

2 Greenspan, D., "Numerical Studies of Prototype Cavity Flow Problems," *The Computer Journal*, Vol. 12, No. 1, 1969, pp. 88–93.

3 Gosman, A. D., Pun, W. M., Runchal, A. K., Spalding, D. B., and Wolfshtein, M., *Heat and Mass Transfer in Recirculating Flows*, Academic Press, 1969.

4 Amsden, A. A., and Harlow, F. H., *The SMAC Method: A Numerical Technique for Calculating Incompressible Fluid Flows*. LA-4370, Los Alamos Scientific Laboratory, Los Alamos, N.M., 1970.

5 Wolfshtein, M., "Some Solutions of the Plane Turbulent Impinging Jet," ASME *Journal of Basic Engineering*, 1970, pp. 915–922.

6 Bower, W. W., Kotansky, D. R., and Hoffman, G. H., "Computations and Measurements of Two-Dimensional Turbulent Jet Impingement Flowfields," *Proceedings of Symposium on Turbulent Shear Flows*. No. 3.1, 1977, Penn. State University.

7 Spalding, D. B., "Heat Transfer from Turbulent Separated Flows," *Journal of Fluid Mechanics*, Vol. 27, 1967, p. 97.

8 Agarwal, R. K., and Bower, W. W., "Navier-Stokes Computations of Turbulent Compressible Two-Dimensional Impinging Jet Field," *AIAA Journal*, Vol. 20, No. 5, 1982, pp. 577–584.

9 Belov, I. A., and Kogtev, R. N., "Flow of Gas in Axisymmetric Cavity," *Journal of Engineering Physics*, Vol. 12, No. 1, 1967, pp. 14–15.

10 Launder, B. E., and Spalding, D. B., "The Numerical Computation of Turbulent Flows," *Computer Methods in Applied Mechanics and Engineering*, Vol. 3, 1974, p. 269.

11 Chieng, C. C., and Launder, B. E., "On the Calculation of Turbulent Heat Transport Downstream from an Abrupt Pipe Expansion," *Numerical Heat Transfer*, Vol. 3, 1980, pp. 189–207.

12 Jones, W. P., and Launder, B. E., "The Prediction of Laminarization with a 2-Equation Model of Turbulence," *International Journal of Heat and Mass Transfer*, Vol. 15, 1972, p. 301.

13 Launder, B. E., and Sharma, B. I., "Application of the Energy-Dissipation Model of Turbulence to the Calculation of Flow Near a Spinning Disc," *Letters in Heat and Mass Transfer*, Vol. 2, 1974, p. 1.

14 Amano, R. S., and Jensen, M. K., "Turbulent Heat Transfer of Impinging Jet on a Flat Plate," ASME Paper No. 82-WA/HT-55, Winter Annual Meeting, Phoenix, 1982.

15 Amano, R. S., "Numerical Study of a Turbulent Jet Impinging on a Flat Plate and Flowing into an Axisymmetric Cavity," Ph.D. thesis, University of California, Davis, 1980.

16 Tani, I., and Komatsu, Y., "Impingement of a Round Jet on a Flat Surface," *The International Congress of Applied Mechanics*, 1966, pp. 672–676, Munich, Springer, Berlin.

17 Bradshaw, P., and Love, E. M., "The Normal Impingement of a Circular Air Jet on a Flat Surface," *ARC R. and M.* No. 3205, 1959.

18 Patankar, S. V., *Numerical Heat Transfer and Fluid Flow*, 1980, McGraw-Hill.

19 Leschziner, M. A., "Practical Evaluation of Three Finite Difference Schemes for the Computation of Steady-State Recirculating Flows," *Computer Methods in Applied Mechanics and Engineering*, Vol. 23, 1980, pp. 293–312.

20 Patankar, S. V., and Spalding, D. B., "A Calculation Procedure for Heat, Mass and Momentum Transfer in Three-Dimensional Parabolic Flows," *International Journal of Heat and Mass Transfer*, Vol. 15, 1972, p. 1787.

21 Kleinstein, G., "Mixing in Turbulent Axially Symmetric Free Jet," *Journal of Spacecraft*, Vol. 1, No. 4, 1964, pp. 403–408.

22 Poreh, M., Tsuei, Y. G., and Cermak, J. E., "Investigation of a Turbulent Radial Wall Jet," ASME *Journal of Applied Mechanics*, Vol. 89, 1967, pp. 457–463.

23 Gardon, R., and Akfirat, J. C., "The Role of Turbulence in Determining the Heat-Transfer Characteristics of Impinging Jets," *International Journal of Heat and Mass Transfer*, Vol. 8, 1965, pp. 1261–1272.

24 Baines, W. D., and Keffer, J. F., "Shear Stress and Heat Transfer at a Stagnation Point," *International Journal of Heat and Mass Transfer*, Vol. 19, 1976, pp. 21–26.

25 Rozenberg (Abramovich, G. N ., *Theory of Turbulent Jets*, MIT Press, 1963).

26 Leach, S. J., and Walker, G. L., "Some Aspects of Rock Cutting by High Speed Water Jets," *Phil. Trans. Roy. Soc. of London*, A260, 1966, pp. 295–308.

Downloaded 02 Jun 2010 to 171.66.16.91. Redistribution subject to ASME license or copyright; see http://www.asme.org/terms/Terms_Use.cfm

Some Effects of Upstream Turbulence on the Unsteady Lift Forces Imposed on Prismatic Two Dimensional Bodies

I. S. Gartshore
Department of Mechanical Engineering,
The University of British Columbia,
Vancouver, B.C. V6T 1W5

Measurements of fluctuating lift are reported from four fixed rectangular prisms and a fixed circular cylinder, for various intensities of turbulence in the oncoming stream. Variations of unsteady *lift with intensity of small scale turbulence are similar to present (and previous) measured variations of mean drag or base pressure. Reasons are suggested for these trends. Observations are also reported of the maximum (resonant) RMS amplitude of two cylinders, one square and the other circular in cross section, free to move in the cross stream direction. Small scale free stream turbulence provided by the wake of a small upstream rod increased the resonant amplitude of motion in both cases, the greater increase (and subsequent decrease) occurring for the square section. Two possible explanations for these observations are advanced.*

1 Introduction

The drag of a rectangular prism is surprisingly sensitive to the prism shape, as the experiments of Nakaguchi et al. [1] showed. Later measurements by Bearman and Trueman [2] and others have confirmed that a rectangular shape with a face of dimension h normal to the stream and dimension b parallel to the stream has a maximum drag (with low turbulence) when $b/h \simeq .62$, sections with larger or smaller values of this ratio having significantly lower drag and higher base pressure coefficients.

An explanation for this initially surprising behavior of the drag is that the minimum after body length needed to provide interference with the shear layers separating from the front of a prism is given by $b/h \simeq .62$. For shorter bodies little interaction occurs and increasing afterbody length, by progressively restricting the entrainment into the shear layer from the region next to the side wall, simply lowers the pressure there and behind the body, thereby raising the drag, provided $b/h < 0.62$. For longer bodies ($b/h > 0.62$), progressively greater interference with the shear layer and its position of roll-up causes an increasing pressure rise along the side walls and a higher base pressure or lower drag as b/h increases (see flow visualization of reference [2]).

The effects of free stream turbulence on the drag of these rectangular sections can be summarized for rectangular prisms at zero incidence by Fig. 1, adapted from the report by Laneville and Williams [3]. Drag is decreased by increasing the turbulence intensity for sections longer than the critical ($b/h \simeq 0.62$) whereas increasing and sometimes subsequently decreasing drag is found for $b/h < 0.62$. For very thin sections ($b/h \to 0$) very little effect is found.

An explanation for the effect of free stream turbulence in these cases is presented by Laneville et al. [4] where it is assumed that small scale turbulence increases entrainment into the shear layers separating from the front corners of the body and produces earlier interference between these shear layers and the back corner of the body. The effects of increasing free stream turbulence are therefore in many ways qualitatively like those of increasing after body length.

The effect of turbulence scale on prism drag is somewhat controversial, a few authors reporting appreciable effects (see for example Miyata and Miyazaki [5]). Most authors suggest however, that when blockage corrections are made, the mean forces are remarkably insensitive to turbulence scale over the range $0.2 < L_x/h < 18$, where L_x is the longitudinal integral scale of streamwise fluctuations in grid-produced turbulent flow (see Petty [6], Laneville and Williams [3]). A very dif-

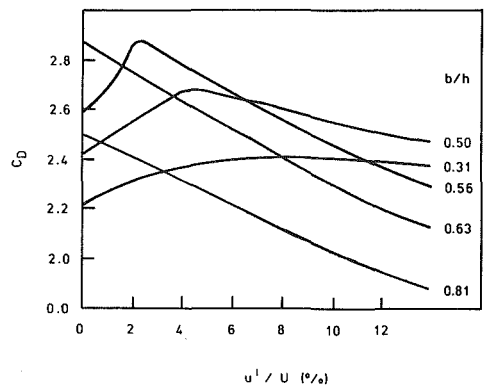

Fig. 1 Corrected drag coefficients for rectangular cylinders of various length/height ratio, from Laneville and Williams [3]

Contributed by the Fluids Engineering Division for publication in the JOURNAL OF FLUIDS ENGINEERING. Manuscript received by the Fluids Engineering Division, August 9, 1983.

Copyright © 1984 by ASME

Downloaded 02 Jun 2010 to 171.66.16.91. Redistribution subject to ASME license or copyright; see http://www.asme.org/terms/Terms_Use.cfm

ferent situation appears to exist for three dimensional bodies. Bearman [7] and Humphries and Vincent [8] report that disks and square plates normal to the flow are sensitive to both turbulence scale and intensity, whereas two-dimensional flat plates (again normal to the flow) appear to be sensitive to neither. Further studies are needed to investigate the effects of the shape and aspect ratio of flat plates subjected to turbulent streams.

As shown by Laneville et al. [4], effects on mean drag quantitatively similar to those of grid turbulence can be produced by placing a small round rod directly upstream of the front stagnation point of the prism and correlating results on the basis of the intensity of turbulence produced in the wake of the rod at the position occupied by the prism but in its absence. This confirms that turbulence near the front stagnation point is of primary importance, but it also suggests that the precise structure of the turbulence in the free stream is not critical in producing the observed effects on the separating shear layers, since the rod wake will contain turbulent structures not present in grid turbulence. The use of a rod to generate turbulence effects on a bluff body is used in the present work.

The effects of free stream turbulence on the forces induced by vortex shedding have not been investigated as completely as have the effects on the steady side force and drag (see review by Farell [9]). Body geometry is again important in assessing the effects of turbulence: for example, the measurements of Vickery [10] and Lee [11] show that large scale, grid-produced turbulence reduces the local fluctuating (rms) lift on a square prism at zero incidence ($\alpha = 0$ deg) but raises it (less dramatically) on the same prism at $\alpha = 45$ deg. High intensity large scale grid turbulence can lower the integrated fluctuating lift on a circular cylinder but the same turbulence can raise the fluctuating lift on a cylinder with strakes (Gartshore et al. [12]). It is widely believed that turbulence always reduces both the local and the integrated rms lift fluctuations occurring at frequencies near that of vortex shedding, by disturbing the regularity and spanwise correlation of shedding. The above examples demonstrate that this is not always so and a consideration of the response of the separating shear layer to turbulence is useful in explaining the results. Briefly, small scale turbulence which moves the oscillating shear layers closer to the side faces of the body from which they separate should increase the local fluctuating lift force on the body provided interference does not occur. Once such interference does occur, further turbulence additions should progressively reduce the local fluctuating lift on the body. This *fluctuating* lift can therefore be expected to vary with free stream turbulence in a similar way to that of the *mean* drag or base pressure magnitude. Measurements described in this report confirm the general picture. A related observation was made some years ago, without explanation, by Bishop and Hassan [13] in connection with the variation with Reynolds number of mean and oscillating forces on a circular cylinder. So and Savkar [14] have more recently confirmed these earlier conclusions.

There can be little doubt that turbulence scale can affect spanwise integrated lift simply because changes in spanwise correlation can be introduced by changes of turbulence scale. For moderately small scales of turbulence, those for which $L_x < h$, scale may not be of great importance however, considering that this has a very small effect on the mean forces. For very small scales, those approaching the limiting size in which dissipation becomes important, scale will again be significant, but overall it has been assumed in this report that intensity of turbulence is much more important than turbulence scale.

Some indication that local fluctuating lift can be markedly affected by turbulence is provided by the limited results of Ellis [15] in which the local rms lift coefficient was raised from 0.03 to 0.40 on a section of $b/h = .625$ when turbulence was added. Ellis' experiments were conducted on a prism of finite aspect ratio, complicating the effects, but his results demonstrate the importance of free stream turbulence for sections near the "critical" shape ($b/h \simeq 0.62$).

Blockage corrections for rectangular prism shapes have been discussed by Awbi [16], Courchesne and Laneville [17], and Petty [6]. These corrections vary with b/h and presumably with free stream turbulence intensity in some circumstances, since, as already mentioned, afterbody size and free stream turbulence create comparable effects. None of the data presented in this report has been corrected for blockage since absolute values are not as important as are the trends evident from the uncorrected values.

End effects may be particularly important in nominally two-dimensional tests on bluff bodies since a large separation region is easily altered by slight changes in pressure or cross flow far from the centre span. The end plates specified for circular cylinders by Stansby [18] cannot be cheerfully accepted for all geometries without further testing, particularly when boundary layers on the end walls confining the prism under test may be modified as the free stream turbulence is changed. Some of these problems are discussed by Lee [19] and most experimental studies report concern over the observed sensitivity to end effects of the flow around bluff bodies. Modest end plates were used in the present study without examining their effectiveness; in the present context absolute values are unlikely to be as important as trends.

2 Experimental Arrangements

Two different types of experiments were conducted during this investigation. In the first experiment the local fluctuating lift was measured on fixed rectangular and circular cylinders with various levels of free stream turbulence. In the second type of experiment the resonant motion of a cylinder free to move in the cross stream direction was measured as turbulence intensity was varied. Arrangements for the two experiments are described in the following paragraphs and all results are discussed together in Section 3.

The local instantaneous lift (not averaged along the span) on a fixed rectangular prism at zero incidence can be measured by a subtraction of the spatially averaged pressure on one side face from that on the opposite side face. These averaged pressures fluctuate predominantly at the vortex shedding frequency, with higher frequency pressure fluctuations presumably correlated over small areas and hence contributing little to the rms of the spatial average. High frequency response is therefore not required in the measurement. A measure of the spatial average of pressure on a face can be obtained by connecting many flush pressure taps on the face to a manifold of the type described by Surry and Stathopoulos [20]. The manifold provides a pressure at its output which is the average of the pressures at the input taps, although changes in amplitude and phase occur with frequency of input pressure fluctuation, due to resonance and damping effects. Two such spatially averaged pressures, each obtained through separate manifolds can be connected to either side of a pressure transducer diaphragm, automatically taking the difference between the two and giving an electrical voltage proportional to the required lift. This was the technique used in the first experiment.

Long (457 mm) thin (1 mm internal dia) tubing was used to connect the pressure taps to the manifold, producing a somewhat overdamped response but avoiding resonance peaks. Corrections for the response were made directly from a measured calibration curve by assuming that the signal was effectively at one frequency, that observed at the spectral peak of the transducer output, i.e., of the fluctuating lift. The spectra were almost always sharply peaked so that no dif-

Downloaded 02 Jun 2010 to 171.66.16.91. Redistribution subject to ASME license or copyright; see http://www.asme.org/terms/Terms_Use.cfm

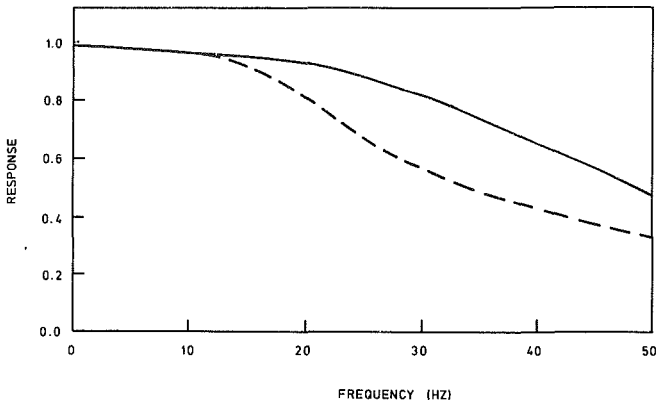

Fig. 2 Manifold, tubing and pressure tap frequency response; ___, 457 mm lengths of tubing; ------; 914 mm lengths of tubing. The former was used in the experiments reported here.

ficulty was found in determining the main vortex shedding frequency.

The manifold together with associated tubing was calibrated in a suitable manner, by subjecting it to fluctuating input pressures at various frequencies. The results are shown in Fig. 2.

Five nominally two-dimensional cylinder models were tested in the 0.457 m square suction wind tunnel (described by Britter et al. [21]) in Cambridge University (Department of Applied Mathematics and Theoretical Physics). Each model had a frontal dimension h of 38.1 mm so that blockage ratios were always 8.3 percent based on area. Models having b/h of 0.5, 0.667, 1 and 2 were used and a circular cylinder of diameter 38.1 mm was also tested. In each of the rectangular prisms, eight pressure taps were located on each side of the model and were uniformly spaced. In the circular cylinder the eight pressure taps were spaced at angular positions θ_n from the stagnationpoint such that

$$(1-\cos\theta_1)=\frac{\cos\theta_n-\cos\theta_{n+1}}{2}=\frac{1}{8}$$

and $n=1$ to 7. This spaced the taps equally across a diametrial line of the cylinder normal to the cross stream or lift direction, consistent with arrangements for the rectangular shapes. The use of eight taps to represent the spatially averaged pressure on each side was dictated by the model size.

End plates were used on all models. These were placed 38.1 mm from each end of the body and were 114.3 mm square, with a 25 mm radius on each corner. The assumption was made that these end plates would help to make the bodies under test less sensitive to end conditions and in particular to changes in the boundary layers on the tunnel walls. No gap was left at either end of the model in these tests.

To produce upstream turbulence effects a 6.4 mm diameter rod was traversed along the tunnel upstream of the model centre-line. It was convenient to place the model in various locations in the tunnel and to traverse the rod over a limited range directly upstream. Overall, it was possible to place the rod between about 20 d and 160 d (where d is the small rod diameter) from the front face of the prism. This produced relative longitudinal intensities in the rod wake between 12 and 2.5 percent and integral longitudinal turbulence scales, again on the rod centre-line, between 1.2 d and 2.9 d (or 0.2 h and 0.5 h). These estimates were obtained from the intensities measured in a previous study (Gartshore [22]) and from the measurements of turbulence scale in wakes made by Townsend [23]. With the rod closer to the prism than about 2 h, (where h is the frontal dimension of the prism), the rod often had a profound effect on the mean flow about the prism, markedly decreasing the prism drag and fluctuating lift. Flow visualization showed that the effect of the rod was, in such cases, to modify the mean flow pattern by creating relatively stable separation bubbles between the rod and the prism face. Similar effects in axisymmetric flow have been noted by Morel and Bohn [24] but the results, while interesting, are not relevant to the present study. With the rod even closer to, or in contact with, the front face of the prism, the rod had little or no effect on the flow, base pressure and fluctuating lift returning close to the values observed with no rod present. Some indication of these "two-body" effects is shown in the present results but the phenomenon is outside the scope of this work, and the effective limits on turbulence intensity are therefore $0<u'/U<.12$ and on scale $0.5>L_x/h>0.2$.

Lift coefficients used here are always based on the lateral projected dimension of the cylinder under test, that is, the local rms lift coefficient is:

$$C_L'\equiv\frac{L'}{\frac{1}{2}\rho U^2 b}$$

where L' is the local rms lift fluctuation per unit span, U is the mean free stream velocity, and b is the streamwise dimension of the body.

3 Results and Discussion

3.1 Local Fluctuating Lift and Mean Base Pressure on Fixed Cylinders. Fluctuating lift and mean base pressure were measured for various rod positions x upstream of the model face. The results were plotted first as local lift coefficients uncorrected for the frequency response of the manifolds, $(CL)_{unc}$, at various x/d where d is the rod diameter equal to $h/6$ for these experiments. At each x/d an effective turbulence intensity u'/U can be inferred, equal to the intensity on the rod wake centerline in the absence of other bodies. This varies slightly with the rod Reynolds number, an effect which has been taken into account (see Gartshore [22]). The values of u'/U so inferred are noted at each x/d of the abscissa in Fig. 4 which gives a typical result for $b/h=1/2$. For $x/d>10$, both CL_{unc} and $(-C_{pb})$ first rise and then fall with increasing x/d. For $x/d \lesssim 10$ (or $x/h \lesssim 2$) the effects observed are associated with gross changes in the mean flow pattern due to the interference between the rod and the prism, as mentioned in Section 2. The trends for small x/d are interesting and are dotted in to suggest expected results but are not of relevance to the present work on turbulence effects.

Results shown in Fig. 3 and similar results for four other prism shapes were cross-plotted against the associated free stream turbulence u'/U, after correction for the frequency response of the manifolds from the earlier calibration. In the cross plot and correction procedure, mean lines such as that shown in Fig. 3 were drawn through the data; values read from these mean lines at equal intervals of x/d were then corrected for frequency response of the manifolds.

The corrected data are plotted as a mean line in the summary graphs of Figs. 4(a) and (b), made for C_L' and C_{pb}, respectively.

It is clear from these graphs that the trend of C_L' with u'/U is the same as the trend for $(-C_{pb})$, for every shape tested, supporting the qualitative picture of turbulence effects given in Section 2. Not only are the shapes of the curves in Figs. 4(a) and (b) similar, their relative positions are also similar, those for $b/h=1/2$ and 2/3 being the highest in both cases.

The curves for $b/h=1/2$ and for the circular cylinder shape first rise then fall as intensity increases. In both these cases it appears that no strong interaction between separated shear layers and afterbody occurs at the lowest intensity so that

Downloaded 02 Jun 2010 to 171.66.16.91. Redistribution subject to ASME license or copyright; see http://www.asme.org/terms/Terms_Use.cfm

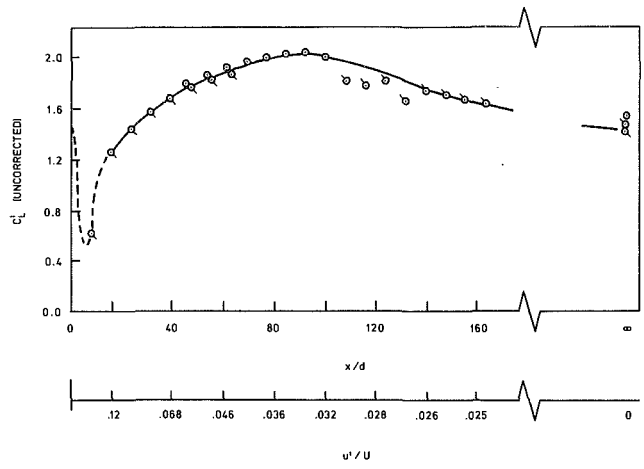

Fig. 3(*a*)

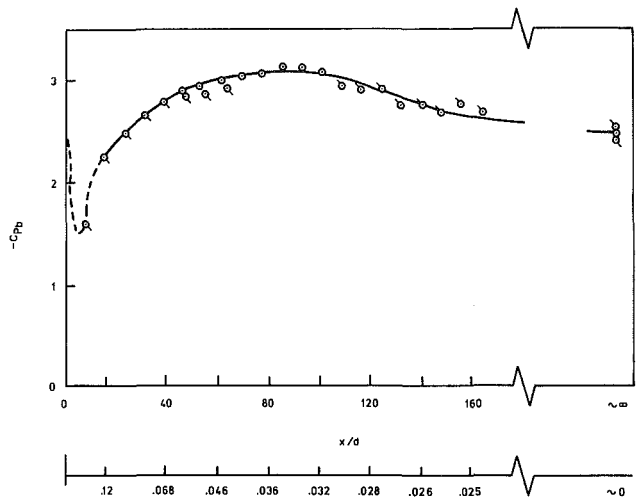

Fig. 3(*b*)

Fig. 3 Results for rectangular shape $b/h = ½$: (*a*) Lift coefficient (rms) uncorrected for manifold frequency response; (*b*) Base pressure coefficient.

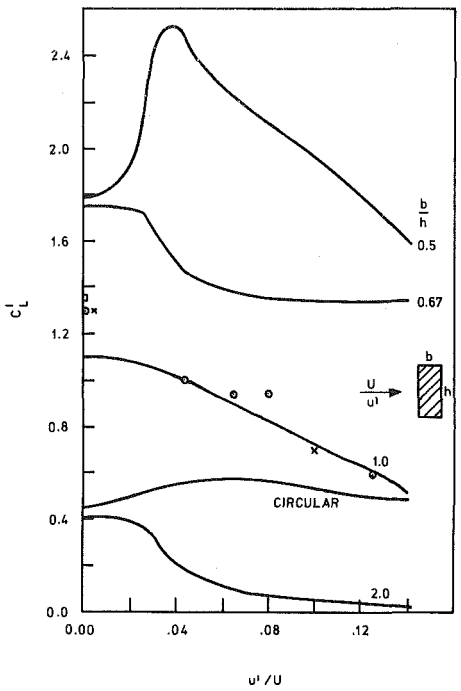

Fig. 4(*a*)

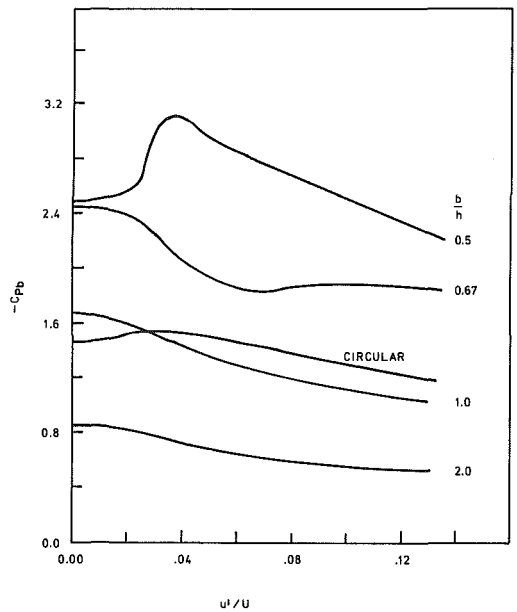

Fig. 4(*b*)

Fig. 4 Results for all cylinders tested in experiment 1: (*a*) Lift coefficient (rms). ⊙, Lee [11]; x, Vickery [10]; ⊡, Wilkinson [27]; for $b/h = 1$; (*b*) Base pressure coefficients.

increasing intensity initially draws the shear layer closer to the body and increases both the mean base suction and the amplitude of the pressure fluctuation.

An important observation made from the raw signals during the experiment was that the lift oscillation amplitude and the base pressure for the $b/h = 1/2$ prism were very irregular or unsteady at low turbulence levels but became very regular for higher intensities of turbulence. The same was true as well for $b/h = 2/3$ and $b/h = 1$, although this trend was less marked in these two cases. Apparently small scale turbulence actually makes the vortex shedding and shear layer reattachment (where this occurs) more regular and decreases random unsteadiness. This is in marked contrast to the usual view of turbulence as a "scrambling" effect, and may have important implications for integrated forces on long sections. (This is discussed in Section 3.2 below.)

It seems likely that, at large u'/U, the values of C_L', and $(-C_{pb})$ for the $b/h = 1/2$ prism fall with increasing intensity because of increasingly important interference between the separated shear layer and the afterbody of the prism. It is possible that by contrast similar trends observed at high u'/U for the circular shape are due to a progressive downstream shift in the mean separation point, an effect not possible for the sharp-edged prisms. This complication for the circular shape makes comparisons between the two somewhat risky and ambiguous. It is interesting, however, that for the circular shape, increasing Reynolds number with low turbulence finally produces a short separation bubble, i.e., laminar separation followed by turbulent reattachment. Transition in the separated laminar shear layer very near separation is much more important for the circular cylinder than for the rectangular prism because in the former case the shear layer lies so close to the body just downstream of separation. Perhaps this is why C_L' for the circular cylinder is so dependent on Reynolds number and turbulence in the range just preceding that for the formation of a separation bubble, as noted by Gerrard [26] and others.

The second type of experiment reported here involved motion of a square or circular cylinder in the wake of an

Downloaded 02 Jun 2010 to 171.66.16.91. Redistribution subject to ASME license or copyright; see http://www.asme.org/terms/Terms_Use.cfm

upstream rod. The effect of turbulence on the vortex-induced oscillation of a square bar can be obtained by measuring the amplitude of motion of the bar when it is allowed to move in the cross stream direction only (plunging motion). Such an experiment, done at the University of British Columbia, used suitable springs and air bearings in a 0.685 m by 0.914 m tunnel (see description of facility in the similar study by Laneville and Parkinson [25]). The structural damping of the motion was adjusted using electromagnetic dissipation and was set to a moderately high value ($\beta = 0.0036$ where β is the fraction of critical damping) to raise the onset speed for classical galloping to over twice the resonant speed. Blockage in this case was about 5.5 percent and the Reynolds number based on frontal dimension was close to 1.8×10^4. The aspect ratio of the bar was 13.5 between end plates. A round rod of diameter $d = 1/3\ h$ was mounted at various locations upstream of the bar centerline, as described above, to produce upstream turbulence. A resonant peak response was observed at a particular wind speed in every case and only maximum amplitudes of motion, at resonance, were noted. Measured rms values of oscillation at resonance varied from about .02 h with no turbulence to 0.07 h (maximum) with turbulence, so that quite small amplitudes were involved.

Another experiment similar to that for the square bar was performed, now using a circular cylinder. In this test, performed in the Cambridge University Engineering wind tunnel (which is 0.508 m square in section and of suction type) a bar of solid steel was cantilevered into the tunnel from a heavy rigid base. Strain gauges at the base of the bar were calibrated to allow instantaneous deflection of the free tip to be measured. A small base plate covered the hole in the tunnel floor through which the cylinder projected but no end plate was used at the free end. A gap was necessarily left between the free end and the tunnel roof and was of order 1 mm. The bar itself was 25.4 mm in diameter and its static stiffness was measured using weights and pulleys. The aspect ratio of the bar was approximately 20; blockage was about 5 percent.

Upstream turbulence was provided by the wake of a round rod of diameter 0.31 h (where h is bar diameter) mounted at various positions upstream of the cylinder centre-line. Only conditions at resonance were studied and Reynolds number based on h varied between 1.6×10^4 and 1.9×10^4. The damping, measured from the decay of oscillations without flow, was $\beta = 0.0008$ or 0.08 percent. No adjustment of this value was attempted. Motion was measured to be between 0.03 h and .04 h (rms values) at the free end of the bar. Only simple first-mode deflections were observed.

For prism shapes of $b/h > 2/3$, the curves for C_L' and $(-C_{pb})$ fall monotonically as u'/U increases. This trend is apparently due to progressively greater interference of the shear layers with the afterbody of the prisms as turbulence increases. On longer bodies such as $b/h = 1$ or 2, C_L' falls to very low values at high intensity since relatively permanent reattachment and relatively short separation regions can be produced at high turbulence levels.

In almost every measurement, the lift oscillations had an obvious central frequency, easily located by the use of a narrow band pass filter. This strongly supports the assumption made here, that the lift oscillations come from the shedding of vortices and are not a direct reflection of the upstream turbulence spectrum. In one case an obvious central frequency did not exist; the lift oscillations at the highest u'/U for the $b/h = 2$ prism were spread over a wide spectrum, probably because of reattachment of the shear layers in this case. The absence of a distinct shedding frequency made accurate frequency correction impossible but did not mask the trends apparent in this case. Corrections were made for manifold response at the last discernible vortex shedding frequency to provide the mean curve for $b/h = 2$ shown in Fig. 5(a). Overall, the C_L' data reported in this section are

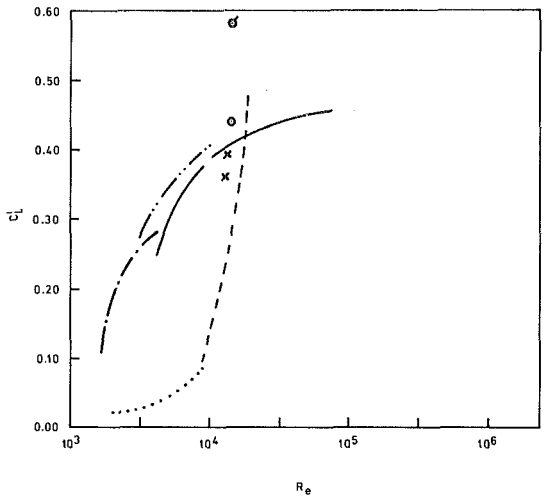

Fig. 5 Summary of fluctuating lift coefficients on a circular cylinder, after Vickery [28]. ..... Vickery, low turbulence; _._._._. , Vickery, high turbulence; -----, Gerard; _____, Keefe; _.._.._.._ , Bishop and Hassan; ⊙, ⊙, present results low turbulence and 8 percent turbulence respectively; x, Feng [29].

repeatable within ±5 percent, but because of the corrections for frequency response are only accurate to within about ±10 percent.

It is interesting to make comparisons between present results and previous measurements. Such comparisons are made difficult by the uncertain effects of turbulence scale and of blockage in various experiments and the interaction of blockage corrections with turbulence effects and end effects.

However, some comparisons can be made between the present measurements of C_L' and previous measurements. In particular, values for C_L' have been reported at various turbulence levels, on a square section, $b/h = 1$, by Lee [11], by Vickery [10], and by Wilkinson [27]. Their measurements are shown in Fig. 4(a) and agreement with present results and with each other are surprisingly good despite differences in blockage (Lee had 3.6 percent blockage, Vickery, 7.1 percent and Wilkinson, 10 percent) and differences in turbulence scale. This comparison suggests that present measurements, made with turbulence produced from a rod wake, and previous measurements, made using grids to produce turbulence are not essentially different. The largest differences appear at $u'/U = 0$ where end effects and tunnel disturbances may be expected to be most important and may account for the discrepancies.

Several previous measurements of C_L' have been made on the circular cylinder, and are summarized in Fig. 5, adapted from Vickery [28] and with added measurements of Feng [29] and Bishop and Hassan [13]. The present measurements, both that at $u'/U = 0$ and the maximum value of C_L' measured for $u'/U \simeq .08$ are also plotted at the experimental Reynolds number of 2.16×10^4. Again the present measurements are like previous values and give support to the techniques used. The changes in turbulence scale, end effects and blockage are additional variables not separable in the measurements reported to date but they presumably contribute to the scatter of all data shown in Fig. 5.

Several workers have made measurements of $(-C_{pb})$ for a square bar at various turbulence intensities and scales. The present value of $(-C_{pb})$ at $u'/U = 0$ ranges between 1.4 and 1.55 after correction, depending on the correction procedure used, and is in reasonable agreement with previous estimates. The measurements of Laneville and Williams [3] made with very large scale turbulence show significantly higher values of $(-C_{pb})$ than all other measurements, suggesting that their large scale turbulence does indeed have a lower effect on base

Downloaded 02 Jun 2010 to 171.66.16.91. Redistribution subject to ASME license or copyright; see http://www.asme.org/terms/Terms_Use.cfm

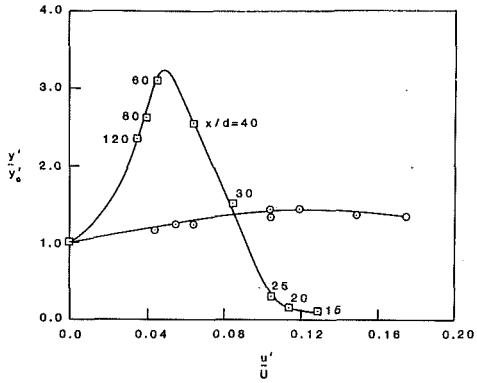

Fig. 6 Measured rms amplitudes of motion for resonant conditions: ⊙, circular cylinder; ⊡, square cylinder

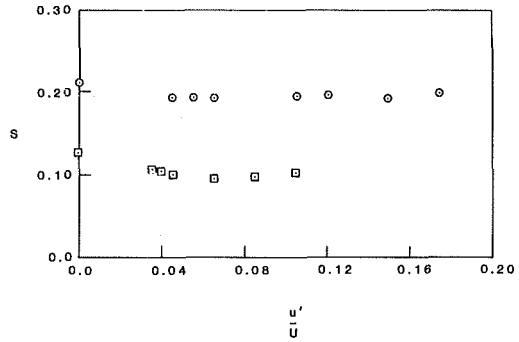

Fig. 7 Strouhal numbers: ⊙, circular cylinder; ⊡, square section

pressure than small scale turbulence of equal intensity. However, the trend of larger departures for lower L_x/h, within Laneville and Williams' values, does not support this conclusion and the influence of scale on the process must remain an open question, complicated by interactions with blockage and end effects. It seems safe to conclude that, for small scale turbulence ($L_x/h<1$) the intensity is the more important variable for nominally two-dimensional bodies.

3.2 Resonant Motion of A Square Bar and of a Circular Cylinder. Measurements of the maximum rms amplitude of motion (at resonance) were made for the square bar subjected to various intensities of turbulence produced by an upstream rod as described in Section 2. The results are plotted in Fig. 6, as rms amplitude, nondimensionalized with the average value observed in smooth flow (which was about $0.015h$, rms) against turbulent intensity inferred as usual from the upstream rod wake centre line. Repeatability was within ±10 percent in amplitude in these tests; long averaging periods were necessary at low turbulence levels because of the irregular nature of the motion there.

The measurements show a dramatic rise for intensities above 6 percent, peak values of amplitude reaching about three times the low turbulence values. At still higher intensities, the motion is progressively decreased, finally reaching very low values. The spectrum of the motion was not measured, but it was clear from the oscillation signal that the bar moved very erratically at low turbulence levels, sometimes with several cycles of regular motion and then with very little regularity or amplitude, but that it moved regularly at its maximum deflection ($u'/U \simeq .08$).

The position of the upstream rod, in terms of x/d (where d is the upstream rod diameter) is noted for each experimental point. For x/d of 80 and 120, the moving square bar needed an artificial initial displacement in order to reach the values shown on the graphs. In other cases the final large amplitudes of motion were sometimes reached after a sudden change from a lower amplitude, but without artificial displacement. These observations suggest that the phenomenon being observed is dependent on displacement, a possibility discussed below.

Values of observed Strouhal number are shown for the square bar in Fig. 7. The points correspond to the amplitudes of Fig. 6. Strouhal numbers show a decrease of about 25 percent over the range tested.

The range of x/d used is between 15 and 120 with the important points having larger values of x/d. In this range, at the Reynolds numbers used (about 0.3×10^4 based on small rod diameter) there will be no trace of the Karman vortex street shed by the front rod when the wake reaches the cylinder.

The observed amplitudes of motion at resonance of the circular cylinder are plotted in Fig. 6 as well. In this case, the rms motion at the free tip of the cantilevered cylinder at resonance, was about 0.03 h (where h is the frontal dimension, i.e., the diameter of the cylinder) in the absence of turbulence. Increases of about 45 percent are evident when the turbulence produced by the upstream rod reaches about 10 percent. Corresponding Strouhal numbers are again plotted in Fig. 7.

Two possible explanations can be advanced for the increased amplitudes of motion produced by the wake turbulence for these two cross-sectional shapes: either the effective oscillating force is increased by the turbulence in each case, or there is a displacement dependent effect which reaches a maximum at certain turbulence levels or at certain relative spacings between the upstream rod and the downstream cylinder. The first explanation is supported by the observation that the motion became much more regular when turbulence was added. This suggests a more sharply peaked spectrum of forces acting on the cylinder and possibly increased spanwise correlation of forces. Neither of these was measured directly.

The second explanation, that of displacement dependent effects, could not be related to classical galloping for the circular cylinder. The square section can gallop but this tendency occurs at a speed at least twice the resonant speed for the damping levels used in this experiment and produces continually rising amplitudes with increasing wind speeds, unlike the resonance observed here. For these reasons, classical galloping cannot be the cause of the present observations.

Another displacement-dependent effect is "wake-galloping" or "interference-galloping," observed as an interaction between two cylinders placed some distance apart (references [30, 31]). This oscillation can interact with vortex shedding for certain ranges of parameters [31], but before the onset velocity can be estimated, static lift forces must be made on the downstream cylinder for various offsets and for various longitudinal spacings between the cylinders. The variation of static force was not measured in the present experiments but it is certainly possible that the present observations are a manifestation of interference galloping coupled with vortex resonance. Further work will be necessary to explain and predict this phenomenon, but an explanation involving displacement-dependent effects appears to be quite possible. The turbulence from the wake of the upstream rod will play an essential role in this explanation.

4 Conclusions

Two important and practical conclusions can be drawn from this work: first, for fixed cylinders of prismatic shape and $b/h \gtrsim 0.6$, local values of C_L' can be increased by small scale turbulence; second, for cylinders of various cross-section, resonant amplitude of motion induced by vortex

Downloaded 02 Jun 2010 to 171.66.16.91. Redistribution subject to ASME license or copyright; see http://www.asme.org/terms/Terms_Use.cfm

shedding can be substantially increased by small scale turbulence produced by the wake of another, smaller cylinder placed upstream.

For the fixed bodies, small scale turbulence increases the entrainment into the shear layers separating from the leading edge of prismatic sectional shapes and hence produces trends in the oscillating lift force very like those on mean drag or base pressure. Sufficiently intense turbulence can drastically reduce C_L' on fixed bodies for which $b/h \lesssim 1$. The effect of the rod wake on a flexible body can be explained either as an effect of turbulence on the spectrum, spanwise correlation and relative phase angles of the vortex induced forces, or as an interference galloping phenomenon coupled with vortex shedding. Further work will be needed to distinguish clearly between the two explanations, but in either case it is again the effect of small scale turbulence on the shear layers of the large downstream cylinder which plays the essential role.

Acknowledgment

Much of this work was done while the author was on sabbatical leave at Cambridge University, and thanks are expressed to all concerned for this arrangement. Ingenious model construction was supervised by D. Cheesely. Financial support was received from the Killam Senior Fellowship and the Canadian NSERC Grant No. A-4308.

References

1 Nakaguchi, H., Hashimoto, K., Muto, S., "An Experimental Study on Aerodynamic Drag of Rectangular Cylinders," *Journ. of Japan. Soc. for Aero. and Space Sci.*, Vol. 16, 1968, pp. 1-5.

2 Bearman, P. W., "An Investigation of the Flow Around Rectangular Prisms," *Aero Quarterly*, Vol. 23, 1972, pp. 229-237.

3 Laneville, A., and Williams, C. D., "The Effect of Intensity and Large Scale Turbulence on the Mean Pressure and Drag Coefficients of Two Dimensional Rectangular Cylinders," *Proc. 5th Int. Conf. on Wind Engineering*, 1979, pp. 397-406.

4 Laneville, A., Gartshore, I. S., and Parkinson, G. V., "An Explanation of Some Effects of Turbulence on Bluff Bodies," *Proc. 4th Int. Conf. on Wind Effects on Structures*, 1975, pp. 333-340.

5 Miyata, T., Miyazaki, M., "Turbulence Effects on Aerodynamic Response of Rectangular Bluff Cylinders," *Proc. 5th Conf. on Wind Engineering*, 1979, pp. 631-642.

6 Petty, D. G., "The Effect of Turbulence Intensity and Scale on the Flow Past Square Prisms," *Journal Ind. Aero.*, Vol. 4, 1979, pp. 247-252.

7 Bearman, P. W., "An Investigation of the Forces on Flat Plates Normal to a Turbulent Flow," *J.F.M.*, Vol. 46, 1971, pp. 177-198.

8 Humphries and Vincent, "Experiments to Investigate Transport Processes in the Near Wakes of Discs in Turbulent Air Flow," *J.F.M.*, Vol. 75, 1976, pp. 737-749.

9 Farell, C., "Flow Around Fixed Circular Cylinders: Fluctuating Loads," *Journal of Engineering Mechanics A.S.C.E.*, Vol. 107, 1981, pp. 565-588.

10 Vickery, B. J., "Fluctuating Lift and Drag on a Long Cylinder of Square Cross Section in a Smooth and in a Turbulent Stream," *J.F.M.*, Vol. 25, 1966, pp. 481-494.

11 Lee, B. E., "The Effect of Turbulence on the Surface Pressure Distribution Field of a Square Prism," *J.F.M.*, Vol. 69, 1975, pp. 263-282.

12 Gartshore, I. S., Khanna, J., and Laccinole, S., "The Effectiveness of Vortex Spoilers on a Circular Cylinder in Smooth and Turbulent Flow," *Proc. 5th Int. Conf. on Wind Engineering*, 1979, pp. 1373-1379.

13 Bishop, R. E. D., and Hassan, A. Y., "The Lift and Drag Forces on a Circular Cylinder in a Flowing Fluid," *Proc. Roy. Soc.*, Series A-277, 1963, pp. 32-50.

14 So, R. M. C., Savcar, S. D., "Buffeting Forces on Rigid Circular Cylinders in Cross Flows," *J.F.M.*, Vol. 105, 1981, pp. 397-425.

15 Ellis, N., "A New Technique for Evaluating the Fluctuating Lift and Drag Force Distribution on Building Structures," *Proc. 4th Int. Conf. on Wind Effects on Structures*, 1975, pp. 527-536.

16 Awbi, H. B., "Wind Tunnel Wall Constraint on Two Dimensional Rectangular Section Prisms," *Journ. of Ind. Aero.*, Vol. 3, 1978, pp. 285-306.

17 Courchesne, J., and Laneville, A., "A Comparison of Correction Methods Used in the Evaluation of Drag Coefficient Measurements for Two-Dimensional Rectangular Cylinders," ASME JOURNAL OF FLUIDS ENGINEERING, Vol. 101, 1979, pp. 506-510.

18 Stansby, P. K., "The Effect of End Plates on the Base Pressure Coefficient of a Circular Cylinder," *Aero. Journ.*, 1974, pp. 36-37.

19 Lee, B. E., "The Susceptibility of Tests on Two-Dimensional Bluff Bodies to Incident Flow Variations," *Journal Ind. Aero.*, Vol. 2, pp. 133-148, 737-749.

20 Surrey, D., and Stathopoulos, T., "An Experimental Approach to the Economical Measurement of Spatially Averaged Wind Loads," *Journ. Ind. Aero.*, Vol. 2, 1977, pp. 385-397.

21 Britter, R. E., Hunt, J. C. R., and Mumford, J. C., "The Distortion of Turbulence by a Circular Cylinder," *J.F.M.*, Vol. 92, 1979, pp. 269-301.

22 Gartshore, I. S., "The Effects of Free Stream Turbulence on the Drag of Two-Dimensional Prisms," University of Western Ontario, Faculty of Engrg. Sci. Report BLWT 4-73.

23 Townsend, A. A., *The Structure of Turbulent Shear Flow* (first edition), Cambridge Univ. Press.

24 Morel, T., and Bohn, M., "Flow Over Two Circular Disks in Tandem," ASME JOURNAL OF FLUIDS ENGINEERING, Vol. 102, 1980, pp. 104-111.

25 Laneville, A., Parkinson, G. V., "Effects of Turbulence on Galloping of Bluff Cylinders," *Proc. 3rd Int. Conf. on Wind Effects on Structures*, 1971, pp. 789-797.

26 Gerrard, J. H., "A Disturbance-Sensitive Reynolds Number Range of the Flow Past a Circular Cylinder," *J.F.M.*, Vol. 22, 1965, pp. 187-196.

27 Wilkinson, R. H., "Fluctuating Pressures on an Oscillating Square Prism," Parts I and II, *Aero. Quarterly*, Vol. 32, 1981, pp. 97-125.

28 Vickery, B. J., "Wind Effects on Buildings and Structures: Critical Unresolved Problems," *Proc. Karlsruhe Symposium Practical Experience with Flow Induced Vibrations*, 1980, pp. 823-828.

29 Feng, C. C., "The Measurement of Vortex Induced Effects in Flow Past Stationary and Oscillating Circular and D-Section Cylinders," M.A.Sc. thesis, University of British Columbia, 1968.

30 Cooper, K. R., and Wardlaw, R. L., "Aeroelastic Instabilities in Wakes," *Proc. Third International Conference on Wind Effects on Buildings and Structures*, Tokyo, 1971, pp. 647-655.

31 Ruscheweyh, H., "Aeroelastic Interference Effects Between Slender Structures," *Proc. Sixth International Conference on Wind Engineering*, Gold Coast, Australia, *Journal of Wind Engineering*, Vol. 14, 1983, pp. 124 to 140.

Downloaded 02 Jun 2010 to 171.66.16.91. Redistribution subject to ASME license or copyright; see http://www.asme.org/terms/Terms_Use.cfm

E. Wacholder
Senior Lecturer,
Department of Nuclear Engineering.

J. Dayan
Associate Professor,
Faculty of Mechanical Engineering.

Technion—Israel Institute
of Technology,
Technion City,
Haifa 32000, Israel

Application of the Adjoint Sensitivity Method to the Analysis of a Supersonic Ejector

Although the concepts of various types of ejectors have been thoroughly discussed in the literature during the past sixty years, a rigorous sensitivity analysis of the ejector's performance has never been presented. In the present work a sensitivity analysis method, based on the use of adjoint functions, is introduced and applied to the one-dimensional model of a supersonic ejector. The advantage of the proposed method over all other possible techniques is that a single computer run can provide the response function sensitivities with respect to all input parameters. The usefulness of the sensitivity coefficients in predicting the ejector's performance and the uncertainty involved, as well as in the determination of manufacturing tolerances, is demonstrated and proven to be a powerful tool in the design.

Introduction and Problem Statement

As a first step of any sensitivity study, it is necessary to model the physical system and identify its parameters. It has been established [1-4] that the one-dimensional flow model of a supersonic ejector (Fig. 1) can accurately simulate its behavior over a wide range of operating conditions. In the following we deal with ejectors operating in the practical supersonic flow regime only (i.e., $0.3 < M_2 < 1$; $M_3 > 1$).

The governing equations for the ejector model, assuming [4] the steady, frictionless, adiabatic flow of an ideal gas with constant ratio of the specific heats, are obtained from applying the conservation laws to the fluids at stations 1, 2, and 3 of Fig. 1. Using conventional notation, the governing equations are written in a form amenable to sensitivity analysis as follows:

$$F_1 \equiv \dot{m}_1 + \dot{m}_2 - P_3 M_3 A_3 \left[\frac{\gamma_3 W_3}{\bar{R} T_{03}}\right]^{1/2} \left[1 + \frac{\gamma_3 - 1}{2} M_3^2\right]^{1/2} = 0 \tag{1}$$

$$F_2 \equiv J_1 + J_2 - A_3 P_3 [1 + \gamma_3 M_3^2] = 0 \tag{2}$$

$$F_3 \equiv P_{03} - P_3 \left[1 + \frac{\gamma_3 - 1}{2} M_3^2\right]^{\frac{\gamma_3}{\gamma_3 - 1}} = 0 \tag{3}$$

$$F_4 \equiv T_{03} - \frac{\gamma_3 - 1}{\gamma_3} \frac{W_1 W_2}{\dot{m}_1 W_2 + \dot{m}_2 W_1} \left[\frac{\gamma_1}{\gamma_1 - 1} \frac{\dot{m}_1}{W_1} T_{01} + \frac{\gamma_2}{\gamma_2 - 1} \frac{\dot{m}_2}{W_2} T_{02}\right] = 0 \tag{4}$$

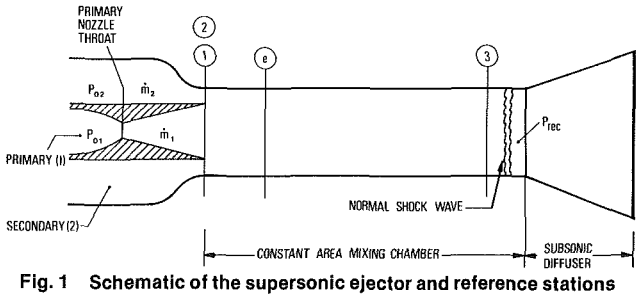

Fig. 1 Schematic of the supersonic ejector and reference stations

$$F_5 \equiv W_3 - \frac{(\dot{m}_1 + \dot{m}_2) W_1 W_2}{\dot{m}_1 W_2 + \dot{m}_2 W_1} = 0 \tag{5}$$

$$F_6 \equiv \gamma_3 - \frac{\frac{\gamma_1}{\gamma_1 - 1} \frac{\dot{m}_1}{W_1} + \frac{\gamma_2}{\gamma_2 - 1} \frac{\dot{m}_2}{W_2}}{\frac{1}{\gamma_1 - 1} \frac{\dot{m}_1}{W_1} + \frac{1}{\gamma_2 - 1} \frac{\dot{m}_2}{W_2}} = 0 \tag{6}$$

$$F_7 \equiv \dot{m}_1 - P_{01} A_{1,\text{throat}} \left[\gamma_1 \left(\frac{2}{\gamma_1 - 1}\right)^{\frac{\gamma_1 + 1}{\gamma_1 - 1}}\right]^{1/2} \left[\frac{W_1}{\bar{R} T_{01}}\right]^{1/2} = 0 \tag{7}$$

$$F_8 \equiv P_1 - P_{01} \left[1 + \frac{\gamma_1 - 1}{2} M_1^2\right]^{-\frac{\gamma_1}{\gamma_1 - 1}} = 0 \tag{8}$$

$$F_9 \equiv \frac{A_1}{A_{1,\text{throat}}} - \frac{1}{M_1} \left[\frac{2}{\gamma_1 + 1} \left(1 + \frac{\gamma_1 - 1}{2} M_1^2\right)\right]^{\frac{\gamma_1 - 1}{2(\gamma_1 - 1)}} = 0 \tag{9}$$

Contributed by the Fluids Engineering Division and presented at the Winter Annual Meeting, New Orleans, La., December 9-14, 1984, of THE AMERICAN SOCIETY OF MECHANICAL ENGINEERS. Manuscript received by the Fluids Engineering Division February 8, 1983. Paper No. 84-WA/FE-2.

Copyright © 1984 by ASME

Downloaded 02 Jun 2010 to 171.66.16.91. Redistribution subject to ASME license or copyright; see http://www.asme.org/terms/Terms_Use.cfm

Table 1 Definitions and numerical values for the independent variables, X, the dependent variables Y and the sensitivity coefficients near the design points X°, Y° and $P^{\circ}_{rec} = 1.02749 \times 10^5$ (N/m²)

j or i	X_j	X°_j	Y_i	Y°_i	$\left[\frac{dP_{rec}/P_{rec}}{dX_j/X_j}\right]_{(X^{\circ},Y^{\circ})}$
1	A_2	0.8244×10^{-1} (m²)	M_3	4.528 (−)	−.675402
2	P_{02}	0.170×10^{5} (N/m²)	P_3	0.051×10^{5} (N/m²)	$.950649\times10^{-1}$
3	T_{02}	500.0 (°K)	P_{03}	15.287×10^{5} (N/m²)	$-.255060\times10^{-2}$
4	M_2	0.409 (−)	T_{03}	314.55 (°K)	$-.103969\times10^{-2}$
5	γ_2	1.40 (−)	W_3	28.066 (kg/mol)	$.127869\times10^{-1}$
6	W_2	28.90 (kg/mol)	γ_3	1.40 (−)	$.255359\times10^{-2}$
7	P_{01}	60.820×10^{5} (N/m²)	$\dot{m}_1$	20.01 (kg/sec)	.904935
8	T_{01}	300.0 (°K)	P_1	0.200 (N/m²)	$.255053\times10^{-2}$
9	γ_1	1.4 (−)	M_1	4.54 (−)	−.535767
10	W_1	28.0 (kg/mol)	P_2	0.151×10^{5} (N/m²)	$-.255068\times10^{-2}$
11	$A_{1,throat}$	0.1432×10^{-2} (m²)	$\dot{m}_2$	1.62 (kg/sec)	.867148
12	A_1	0.2456×10^{-1} (m²)	J_1	1.467×10^{4} (N)	−.177825
13			J_2	0.154×10^{4} (N)	
14			A_3	0.107 (m²)	

$$F_{10} \equiv P_2 - P_{02}\left[1+\frac{\gamma_2-1}{2}M_2^2\right]^{-\frac{\gamma_2}{\gamma_2-1}} = 0 \tag{10}$$

$$F_{11} \equiv \dot{m}_2 - P_2 M_2 A_2\left[\frac{\gamma_2 W_2}{\bar{R}T_{02}}\right]^{1/2}\left[1+\frac{\gamma_2-1}{2}M_2^2\right]^{1/2} = 0 \tag{11}$$

$$F_{12} \equiv J_1 - A_1 P_1[1+\gamma_1 M_1^2] = 0 \tag{12}$$

$$F_{13} \equiv J_2 - A_2 P_2[1+\gamma_2 M_2^2] = 0 \tag{13}$$

$$F_{14} \equiv A_3 - A_1 - A_2 = 0 \tag{14}$$

Symbolically, equations (1)–(14) can be written as:

$$\mathbf{F(Y,X)} = 0 \tag{15}$$

where **F** is a column vector of order $N(N = 14)$ whose components, $F_1, \ldots, F_N$, represent the governing equations of the physical model. $\mathbf{Y} = \mathbf{Y(X)}$ is a column vector of order N representing the unknown dependent variables while **X** is an M order column vector representing the input parameters of the problem. The number of elements in **X** is independent of the number of equations, N.

In the formulation of the present sensitivity analysis problem, the geometry of the ejector, the fluids' properties (molecular weights and γ's), and the operating conditions (stagnation pressures and temperatures) at the injection plane are taken as the elements of **X**, while the properties and operating conditions at the ejection plane as well as the mass rate and static pressure of the inlet fluids are taken as elements of **Y**. The definitions of the elements of **X** and **Y**, along with their numerical values at the studied design point, are given in Table 1.

Assuming that the particular secondary gas properties, its stagnation pressure, P_{02}, its mass flow, $\dot{m}_2$, and the ambient pressure are given, the usual ejector design problem is the determination of its geometry and operating conditions for optimal performance. The optimal performance is defined as the use of the lowest possible primary gas flow rate, $\dot{m}_1$, for a given compression ratio P_{rec}/P_{02} or, alternatively, obtaining the highest compression ratio for a given mass flow ratio $\dot{m}_1/\dot{m}_2$. Therefore, the designer is mainly interested in the determination of the recovery pressure, P_{rec}, defined as the ejector's outlet stagnation pressure [1–3].

Nomenclature

A_i = flow area at station i
$A_{1,throat}$ = primary nozzle throat flow area
A = matrix defined in equation (20)
C = matrix defined in equation (19)
D_i = diameter of flow area i
F = the governing equations vector (equations (1–15))
J_i = impulse function at station i (equations (12, 13))
K = friction losses coefficient
M_i = Mach number at station i
$\dot{m}_i$ = mass flow rate at station i
N = number of dependent variables
P_i = static pressure at station i
P_{0i} = stagnation pressure at station i
P_{rec} = recovery pressure
P'_{rec} = first order approximation of P_{rec} according to equation (29)
P''_{rec} = exact P_{rec} due to perturbed parameters
R = response function
$\bar{R}$ = universal gas constant
S = the elementary sensitivity coefficients matrix
S* = the adjoint function vector
T_{0i} = stagnation temperature at station i
W_i = molecular weight at station i
X = input parameters vector
Y = dependent variables vector
γ_i = specific heats ratio at station i
σ^2 = variance of the response function
σ_j^2 = variance of input parameter j
η = ejector's overall efficiency

Superscripts

0 = conditions at design point
T = transpose

Downloaded 02 Jun 2010 to 171.66.16.91. Redistribution subject to ASME license or copyright; see http://www.asme.org/terms/Terms_Use.cfm

$$P_{rec} = KP_{03}\left[1+\frac{2\gamma_3}{\gamma_3+1}(M_3^2-1)\right]^{\frac{1}{\gamma_3-1}} \left[\frac{(\gamma_3+1)M_3^2}{2+(\gamma_3-1)M_3^2}\right]^{\frac{\gamma_3}{\gamma_3-1}} \tag{16}$$

The friction losses as well as other losses in the ejector and the diffuser are usually taken into account through an empirical coefficient, K. During experimental work conducted in conjunction with the present analysis it was found that the value of $K = 0.75$ fits the result best.

Based on several published optimization methods [4–6], a computer program [7] has been developed for the determination of the ejector's optimal design point, $(\mathbf{X}^\circ, \mathbf{Y}^\circ; P_{rec})$, subjected to given sets of input variables (Table 1) and constraints [7].

Once a design point $(\mathbf{X}^\circ, \mathbf{Y}^\circ)$ has been defined, a sensitivity analysis of the so called response function, $R(\mathbf{X}, \mathbf{Y})$, $(R = P_{rec}^\circ)$, around this point, is conducted. For the ejector's problem, the sensitivity coefficients $(dP_{rec}/d\mathbf{X})_{\mathbf{X}^\circ,\mathbf{Y}^\circ}$, which quantitize the sensitivity of P_{rec} to changes in the system's input parameters, $\mathbf{X}$, around $(\mathbf{X}^\circ, \mathbf{Y}^\circ)$, are evaluted.

Following the Linear Error Propagation Theory [8, 9], the sensitivity coefficients can subsequently be used to obtain the overall standard deviation (the uncertainty) of the particular response.

The Adjoint Sensitivity Method

Assuming that a continuous solution (in the input parameters domain) of the model equations $\mathbf{Y} = \mathbf{Y}(\mathbf{X})$ exists, the response R can then be differentiated with respect to $\mathbf{X}$

$$\frac{dR}{d\mathbf{X}_{(\mathbf{X}^\circ,\mathbf{Y}^\circ)}} = \frac{\partial R}{\partial \mathbf{X}} + \frac{\partial R}{\partial \mathbf{Y}}\frac{\partial \mathbf{Y}}{\partial \mathbf{X}} \tag{17}$$

where $dR/d\mathbf{X}$ and $\partial R/\partial \mathbf{Y}$ are row vectors of order M and N, respectively, and the expression $\partial \mathbf{Y}/\partial \mathbf{X}$ is a $(N \times M)$ matrix. $\partial R/\partial \mathbf{X}$ is called the "direct effect" of $\mathbf{X}$ on R while $(\partial R/\partial \mathbf{Y})(\partial \mathbf{Y}/\partial \mathbf{X})$ is called the "indirect effect" (implicitly through $\mathbf{Y}$) of $\mathbf{X}$ on R. The only unknown variables in equation (17) are the components of the matrix $\mathbf{S} \equiv \partial \mathbf{Y}/\partial \mathbf{X}$, referred to as the "elementary sensitivity coefficients" $(S_i^j \equiv \partial Y_i/\partial X_j)$.

In principle, the elementary sensitivity coefficients can be calculated directly from the "Forward Sensitivity Equations" obtained from the differentiation of the physical governing equations (1)–(14) with respect to the input parameters, $\mathbf{X}$

$$\frac{\partial \mathbf{F}}{\partial \mathbf{X}} + \frac{\partial \mathbf{F}}{\partial \mathbf{Y}}\frac{\partial \mathbf{Y}}{\partial \mathbf{X}} = 0 \tag{18}$$

Such an approach is usually denoted as the Sensitivity Direct Approach (SDA). As $\partial \mathbf{F}/\partial \mathbf{X}$ is explicitly dependent on the input parameter X_j, M systems of N equations must be repeatedly solved in order to obtain the whole elementary sensitivity coefficients matrix $\partial \mathbf{Y}/\partial \mathbf{X}$. Thus, a numerical solution by this method is an inefficient process. The Adjoint Sensitivity Method (ASM), however, overcomes this difficulty.

The earlier inception of adjoint-functions based approaches to sensitivity analysis was mainly in the field of nuclear reactor physics [10–12]. A generalized discussion of the adjoint sensitivity method for different cases of partial differential equations and response functions—not necessarily scalar—are given in recent papers by Cacuci [13]. The application of this method to the physical model of a supersonic ejector consisting of systems of algebraic equations is outlined below.

Define a new $(N \times M)$ matrix $\mathbf{C}$,

$$\mathbf{C} = -\frac{\partial \mathbf{F}}{\partial \mathbf{X}} = -\left(\frac{\partial \mathbf{F}}{\partial X_1}, \frac{\partial \mathbf{F}}{\partial X_2}, \ldots, \frac{\partial \mathbf{F}}{\partial X_M}\right) \tag{19}$$

and a new $(N \times N)$ matrix $\mathbf{A}$, of constant elements

$$\mathbf{A} = \frac{\partial \mathbf{F}}{\partial \mathbf{Y}}\Big|_{(\mathbf{X}^\circ,\mathbf{Y}^\circ)} = \begin{bmatrix} \frac{\partial F_1}{\partial Y_1} & & \frac{\partial F_1}{\partial Y_N} \\ \cdot & & \cdot \\ \cdot & & \cdot \\ \cdot & & \cdot \\ \cdot & & \cdot \\ \frac{\partial F_N}{\partial Y_1} & \cdots & \frac{\partial F_N}{\partial Y_N} \end{bmatrix} \tag{20}$$

Equation (18) can then be written in the following compact form

$$\mathbf{AS} = \mathbf{C} \tag{21}$$

A set of equations adjoint to equation (21) is selected according to

$$\mathbf{A}^*\mathbf{S}^* = \mathbf{C}^* \tag{22}$$

where $\mathbf{S}^*$ is the adjoint functions vector and $\mathbf{A}^*$ is the adjoint matrix defined by the inner product

$$(\mathbf{S}^*)^T\mathbf{AS} = (\mathbf{S})^T\mathbf{A}^*\mathbf{S}^* \tag{23}$$

From equation (23) one obtains

$$\mathbf{A}^* = \mathbf{A}^T \tag{24}$$

Selecting,

$$\mathbf{C}^* = \left(\frac{\partial R}{\partial \mathbf{Y}}\right)^T \tag{25}$$

and substituting equations (21), (22), (24), and (25) in equation (23) and transposing the result, the following is obtained:

$$(\mathbf{C})^T\mathbf{S}^* = \frac{\partial R}{\partial \mathbf{Y}}\mathbf{S} \tag{26}$$

The relations of equation (26) enable the exchange of the "indirect effect" term, $\partial R/\partial \mathbf{YS}$, in equation (17) by an equivalent term, $\mathbf{C}^T\mathbf{S}^*$, such that the sensitivity vector can now be calculated from

$$\frac{dR}{d\mathbf{X}}\Big|_{(\mathbf{X}^\circ,\mathbf{Y}^\circ)} = \frac{\partial R}{\partial \mathbf{X}} + (\mathbf{C})^T\mathbf{S}^* \tag{27}$$

$\mathbf{S}^*$ is obtained by solving the adjoint system of equations (22)

$$\mathbf{A}^T\mathbf{S}^* = \left(\frac{\partial R}{\partial \mathbf{Y}}\right)^T \tag{28}$$

Equations (27) and (28) are the most important results of the ASM. The adjoint system of equations (28) is independent of any differentiation with respect to $\mathbf{X}$, hence the vector $\mathbf{S}^*$ in equation (27) remains the same for all X_j's of the vector $\mathbf{X}$. Thus, once the design point is known, only a single computer run is needed in order to compute $dR/d\mathbf{X}$ for a specific R. However, in the case of several response functions, each R_k of interest requires a new calculation of the corresponding $\mathbf{S}^*$ from equation (28).

This property of the adjoint method reflects on the mutual relations between the ASM and the SDA. By the direct method one computer run can provide the sensitivity coefficients, $d\mathbf{R}/dX_j$ (differentiation of all responses $\mathbf{R}$ with respect to a single parameter X_j). On the other hand, with the ASM a single computer run yields all the sensitivity coefficients $dR_k/d\mathbf{X}$ (differentiation of a single response, R_k, with

Downloaded 02 Jun 2010 to 171.66.16.91. Redistribution subject to ASME license or copyright; see http://www.asme.org/terms/Terms_Use.cfm

respect to all the input parameters in $\mathbf{X}$). Thus, the use of the adjoint sensitivity method is recommended in problems with many input parameters, and only a few response functions that are of interest.

Sensitivity Analysis of P_{rec} and Its Engineering Benefits

A computer program [7] has been developed which solves the adjoint system of equations (equation (28)) and then computes the sensitivity coefficients vector $dP_{rec}/d\mathbf{X}$ (equation (27)). The input to this program are the numerical results of the design point, $\mathbf{X}^\circ$, $\mathbf{Y}^\circ$, and the response P°_{rec}. The analytical expressions and the numerical values for the components of $\mathbf{A}^T$, $\partial R/\partial \mathbf{Y}$ and $\mathbf{C}$, as well as the roots, S^*_i ($i = 1, 2, \ldots, 14$), of the adjoint system of equations (28) are given in Appendices A, B, and C of reference [7]. The numerical values of the nondimensional sensitivity coefficients,

$$\left(\frac{dP_{rec}}{dX_j}\cdot\frac{X_j}{P_{rec}}\right)_{(\mathbf{X}^\circ,\mathbf{Y}^\circ)},$$

which are the main product of the present method, are given in Table 1.

The reliability of the ASM results in calculating the sensitivity coefficients has been examined [7] by comparing the predicted new response function values, P'_{rec}, to the exact values, P''_{rec}.

The predicted new response functions, P'_{rec}, are obtained from a first order approximation of its Taylor series expansion

$$P'_{rec} = P^\circ_{rec} + \sum_{j=1}^{M}\left(\frac{dP_{rec}}{dx_j}\right)_{(\mathbf{X}^\circ,\mathbf{Y}^\circ)}\cdot\Delta X_j + 0(\Delta X_j^2) \tag{29}$$

while P''_{rec} is obtained by solving the original model equations with a perturbed parameter $X_j + \Delta X_j$. Good agreement between values of P'_{rec} and P''_{rec}, for perturbation, $\Delta X_j/X_j$, of 1 to 10 percent in the input parameters has been obtained [7] (deviations never exceed 1 percent).

Based on the computed sensitivity coefficients some physical and engineering conclusions can now be drawn. The results of Table 1 show that P_{rec} is influenced mainly by γ_1, A_2, P_{01}, and $A_{1,throat}$. Quantitative evaluation of the effect of changes in γ_1 on P_{rec} is usually quite difficult because of the complexity of the analytical relationship between them. However, with no additional effort, it is possible to evaluate this effect by the adjoint sensitivity method. From Table 1 and the value of P°_{rec}, reduction of 1 percent in γ_1 causes a 0.75 percent increase in the recovery pressure. Since a similar effect of γ_1 on P_{rec} has been obtained [7] at other design points, it suggests that the ejector's performance can be improved by selecting a primary fluid having the minimal possible γ_1 (close to unity).

The effect of the temperatures sensitivity coefficients can also be evaluated from Table 1. The sensitivity coefficients for perturbation in T_{01} and T_{02} are equal (to the fifth decimal digit) in absolute value and opposite direction. If the designer is asked to raise the recovery pressure in a certain amount while keeping the flow rates constant, he may consider either raising the temperature T_{01} (by preheating) or lowering T_{02} (by precooling). However, the mass flow rate of the primary gas is about ten times larger than the secondary gas flow rate and thus, cooling the secondary gas is, by far, more economical.

The sensitivity coefficients of the recovery pressure with respect to the main geometrical dimensions, A_1, $A_{1,throat}$ and A_2, can be exploited in determining the manufacturing tolerances (the latter are strongly affecting the manufacturing cost). Assuming for exampie that the allowed relative uncertainty in the recovery pressure is $\Delta P_{rec}/P_{rec} = \pm$ 1 percent. The relative cross-sections tolerances derived from this constraint (Table 1) are: $\Delta A_2/A_2 = \pm$ 1.5 percent, $\Delta A_1/A_1 = \pm$ 5.6 percent, $\Delta A_{1,throat}/A_{1,throat} = \pm$ 1.15 percent. The tolerances for the corresponding diameters are: $\Delta D_2/D_2 =$ 1.29 percent, $\Delta D_1/D_1 =$ 2.8 percent, $\Delta D_{1,throat}/D_{1,throat} =$ 0.575 percent.

The final determination of the above mentioned tolerances depends also on the overall efficiency of the ejector. Changes in $A_{1,throat}$, for instance, cause directly proportional changes in the primary flow rate, $\dot{m}_1$, resulting in a corresponding change in P_{rec} in the same direction. On the other hand, the overall efficiency of the ejector, $\eta = (P_{rec}/P_{02})/(\dot{m}_1/\dot{m}_2)$, (at the design point $\eta = 0.489$) changes in the opposite direction (η decreases when P_{rec} increases). For example, a change of $\Delta D_{1,throat} = +0.42$ mm in the diameter of the primary nozzle causes a change of $\Delta A_{1,throat}/A_{1,throat} = 1.0$ percent and, thus, an increase in the flow rate of $\Delta\dot{m}_1/\dot{m}_1 = 1.0$ percent, a corresponding increase in the recovery pressure of $\Delta P_{rec}/P_{rec} = 0.8671$ percent and a decrease of 0.13 percent in the efficiency. Thus, it is recommended to manufacture the primary nozzle throat with the smallest possible positive tolerance.

In many cases it is preferred to build the ejector with a wreath of 4–7 nozzles instead of a single central nozzle. This configuration usually contributes to the better mixing and higher compression ratio of the system. However, the required tolerance of each individual nozzle diameter in wreath reduces by a factor of n^{-1} (where n is the number of nozzles in the wreath) compared to the tolerance of a single nozzle. Thus, increase in performance is achieved only at the expense of lowering the tolerances and increasing the manufacturing cost.

The sensitivity coefficients enable the evaluation of the uncertainty (standard deviation) in the recovery pressure due to uncertainties in the input parameters [8, 9].

$$\sigma^2(P_{rec}) = \sum_{j=1}^{M}\left(\frac{dP_{rec}}{dX_j}\right)^2\sigma_j^2 \tag{30}$$

where σ_j^2 is the variance of an input parameter X_j. For a given [7] set of σ_j's values, the standard deviation of the recovery pressure is found to be $\sigma(P_{rec}) = \pm 0.0239 \times 10^5$ (N/m^2). This result ensures ejection to ambient pressure ($\sim 1.00 \times 10^5$ N/m^2) in 66 percent of the cases.

Summary and Conclusions

The applicability of the adjoint sensitivity methodology to supersonic ejector model has been demonstrated. The method yields accurate results and saves a substantial amount of computing time. It may, however, require considerable effort in the analytical differentiation of the model equations. The ASM provides the exact first-order derivatives of the response function with respect to changes in the input parameters (i.e., the sensitivity coefficients). Once the sensitivity coefficients have been evaluated, the variance of the response is calculated by means of the linear error propagation theory. Conclusions about the performance uncertainty are then readily available.

Analysis of several topics related to the physical and engineering aspects of the ejector operation and production, from sensitivity theory point of view, have been performed and the conclusions drawing process has been demonstrated. The analysis has shown that the recovery pressure, in the neighborhood of the investigated design-point, is most sensitive to changes in the secondary flow cross section area, A_2, the primary nozzle throat cross section area, $A_{1,throat}$, the primary fluid specific heats ratio, γ_1, and the primary fluid stagnation pressure, P_{01}. Thus, the ASM may prove to be an important tool in examining each design and evaluating its adequacy for the particular job.

Finally, it is suggested that the ASM, which has been

Downloaded 02 Jun 2010 to 171.66.16.91. Redistribution subject to ASME license or copyright; see http://www.asme.org/terms/Terms_Use.cfm

developed originally for problems associated with nuclear reactor physics [13], is, in fact, generally applicable to many different analytical models in different areas of pure and applied science and engineering.

References

1 Fabri, J., and Paulon, J., "Theory and Experiments on Supersonic Air-to-Air Ejectors," NACA TM 1410, 1958.

2 Keenan, J. H., Neumann, E. P., and Lustwerk, F., "An Investigation of Ejector Design by Analysis and Experiment," ASME *J. Appl. Mech.*, Vol. 17, Sept. 1950, pp. 299–309.

3 Nagaraja, K. S., and Hammond, D. L., "One Dimensional Compressible Ejectors Flows," AIAA Paper No. 73-1184, 1973.

4 Dutton, J. C., Mikkelson, C. D., and Addy, A. L., "A Theoretical and Experimental Investigation of the Constant Area Supersonic-Supersonic Ejector," AIAA Paper No. 81-0260, 1981. Also, *AIAA Journal*, Vol. 20, Oct. 1982, pp. 1392–1400.

5 Emanuel, G., "Optimum Performance for a Single-Stage Gaseous Ejector," AIAA Paper No. 76-341, 1976.

6 Ortwerth, P. J., "On the Rational Design of Compressible Flow Ejectors," AIAA Paper No. 78-1217, 1978.

7 Wacholder, E., and Dayan, J., "Application of the Adjoint Sensitivity Method to the Analysis of a Supersonic Ejector," Dept. of Mechanical Engineering, Technion, IIT, Haifa, Israel, EEC-130, June 1982.

8 Hahn, G. J., and Shapiro, S. S., *Statistical Models in Engineering*, Wiley, New York, 1967.

9 Brandt, S., *Statistical and Computational Methods in Data Analysis*, American Elsevier, New York, 1970.

10 Oblow, E. M., "Sensitivity Theory for Reactor Thermal-Hydraulics Problems," *Nuc. Sci. Eng.*, Vol. 68, 1978, pp. 322–330.

11 Cacuci, D. G., Weber, C. F., Oblow, E. M., and Marable, J. H., "Sensitivity Theory for General Systems of Nonlinear Equations," *Nuc. Sci. Eng.*, Vol. 75, 1980, pp. 88–110.

12 Weisbin, C. R., et al., "Sensitivity and Uncertainty Analysis of Reactor Performance Parameters," *Advances in Nuclear Science and Technology*, Vol. 14, Plenum Publishing Corporation, New York, 1981.

13 Cacuci, D. G., "Sensitivity Theory for Nonlinear Systems. I. Nonlinear Functional Analysis Approach, and II. Extensions to Additional Classes of Responses," *J. Math. Phys.*, Vol. 22, Dec. 1981, pp. 2794–2812.

Downloaded 02 Jun 2010 to 171.66.16.91. Redistribution subject to ASME license or copyright; see http://www.asme.org/terms/Terms_Use.cfm

R. B. Davis
Assistant Professor of Engineering,
Trinity College,
Hartford, Conn. 06106

D. J. Schneck
Professor of Engineering Science and Mechanics,
Chairman, Biomedical Engineering Program,
Virginia Polytechnic Institute and State University,
Blacksburg, Va.

W. H. Gutstein
Professor of Pathology,
New York Medical College,
Valhalla, New York
(supported in part by a Special Project for the Council for Tobacco Research U.S.A., Inc.)

Pulsatile Flow Through a Branching Tube With Collapsing Walls: Volumetric Flow Redistribution

A hydraulic collapse mechanism was incorporated into a recirculating pulsatile flow system to collapse an elastic branching tube in a controlled manner. Changes in volumetric flow rate into and out of the tube model as well as axial pressure drop were monitored during this process. It was found that the driven collapse of the tube acted as a pump, the effectiveness of which was dependent on upstream and downstream resistance. In addition, there was noted a difference in the volumetric flow curves representing fluid leaving the pre- and the post-collapsed model under the same inflow conditions.

Introduction

Fluid flow in collapsible elastic tubes has been of interest to investigators for many years. Studies of the arteries and veins of the human circulatory system, the large airways of the respiratory system, and certain types of flow in the urethra have addressed (i) tube wall behavior per se, i.e., structural stability; (ii) flow through tubes where the walls are displaced radially in response to changes in the internal flow (see [1] for a review); and (iii) flow through collapsed elastic tubes with a "fixed" noncircular cross-section.

Hecht [2] examined arterial collapse as a function of a number of variables, e.g., intraluminal pressure and the surface area of an externally applied pressure, and found that the primary factor influencing the nature of the collapse was the magnitude of the pre-constricted intraluminal pressure. In a recent analytical study by Wang [3], it was demonstrated that a linearly elastic, cylindrical tube (constrained radially by a series of circumferentially-located springs) remained circular as the external pressure was increased until some critical transmural pressure difference was reached. At this point, the tube wall buckled and the circular cross-section gave way first, to an elliptical shape, followed by a "dumb-bell" shape [3].

Much of the work addressing flow in collapsible elastic tubes has concentrated on fluid dynamic events associated with an already collapsed tube, e.g., a constant transmural pressure is applied to hold the tube in a pre-determined state of collapse. Employing this type of experimental technique, Conrad [4, 5] identified a flow regime in which an increasing volumetric flow rate was associated with a decreasing axial pressure drop (defined in that study as upstream pressure minus downstream pressure). Shimizu [6] examined a similar flow situation and concluded that Korotkoff sounds (heard during clinical blood pressure measurement) are generated by the sudden expansion of the vessel due to shock wave formation. In addition, steady, supercritical flow through a partially collapsed, thin-walled elastic tube has been studied in an effort to explain the wave-like shape of the tube wall which occurs under these conditions [7].

In this paper, the volumetric flow redistribution resulting from the forced collapse of an branching elastic tube in response to an externally applied driving pressure is described in order to more fully understand the fluid dynamic effects of the collapse of a human coronary artery (or coronary artery spasm [8]). Specifically, the resulting changes in volumetric flow and pressure during and after the collapse process are presented and discussed.

Experimental Arrangement

Based on a dimensional analysis of the human physiologic system, elastic models of the left main coronary artery (LMCA) as it branches into the left circumflex artery (LCA) and the left anterior descending artery (LAD) were molded from clear Dow Corning Sylgard 184 elastomer. The scaled-up internal diameters of the LMCA and LAD (both 3.175 cm) and the LCA (2.54 cm) yielded physiologically realistic [9–11] branch-to-LMCA area ratios of 1.0 for the LAD and 0.64 for the LCA and a wall thickness to LMCA radius ratio of 0.2. In addition, the length of the LMCA (21.6 cm) was selected based on flow development considerations (discussed later). Consistent with physiologic observations [9, 12, 13], the LAD was molded as a direct continuation of the LMCA with the branch angle between the LAD and LCA equal to 90 degrees.

The pulsatile component of the simulated coronary flow was superimposed on the steady volumetric flow (supplied by the constant head reservoir, Fig. 1) by a variable-speed, cam-driven lever mechanism which periodically varied the cross-sectional area of the inlet tube to the test section. In this

Contributed by the Fluids Engineering Division for publication in the JOURNAL OF FLUIDS ENGINEERING. Manuscript received by the Fluids Engineering Division, August 15, 1983.

Copyright © 1984 by ASME

Downloaded 02 Jun 2010 to 171.66.16.91. Redistribution subject to ASME license or copyright; see http://www.asme.org/terms/Terms_Use.cfm

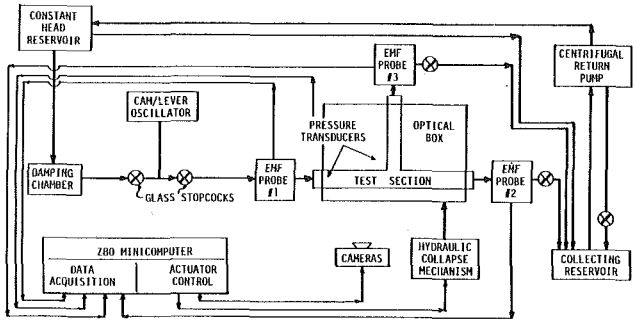

Fig. 1 Schematic diagram of the recirculating flow configuration

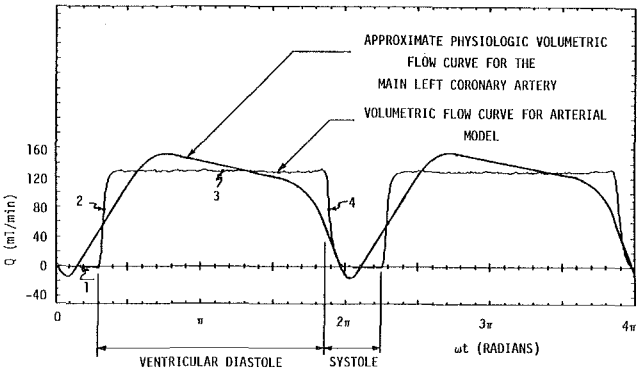

Fig. 2 Volumetric flow curves, physiologic and simulated

manner, the inlet tube was pinched between the moving lever and a fixed support, thus causing a time varying head loss across the cam/lever mechanism and a pulsatile volumetric flow. The resulting volumetric flow (Fig. 2) was monitored with electromagnetic flowmeter probes (Model 501D Carolina Medical flowmeter, calibrated with a graduated cylinder and stopwatch with an associated error of ±2 percent) interfaced with a minicomputer data acquisition system. In addition, the axial pressure drops in the LMCA, LAD, and LCA were calculated from measurements made with miniature strain gauge pressure transducers (Model 105, Precision Measurement Company). Calibration of these probes indicated a relative static pressure error and relative dynamic frequency response of ±1.5 percent and ±0.5 percent, respectively. The test fluid was a saline solution (2 percent sodium chloride by weight) with a kinematic viscosity, ν, of 0.01055 cm^2/s at 26 C which was calculated from measurements made with a cone-in-plate viscometer (Brookfield Engineering Laboratories, Inc.) and a hydrometer.

The branching model was enclosed in a transparent acrylic chamber (or optical box), within which the pressure could be varied so as to collapse the model at a controlled rate to a predetermined degree of occlusion. This collapse pressure was generated by the stroke of a gravity-powered hydraulic piston, i.e., the stroke velocity dictated the collapse rate and the magnitude of piston displacement specified the degree of occlusion. The elasticity of the tube model allowed the controlled radial displacement of the tube wall by an increasing external pressure loading. The usual contribution of an elastic wall to unsteady fluid dynamics, e.g., as an energy storage mechanism was minimized here because the tube wall was not allowed to expand freely in the radial direction, i.e., the incompressible fluid surrounding the model constrained the model. Under these conditions, the model was considered a "rigid" tube with a radially driven boundary.

A dimensional analysis of the collapsing tube [14] based on the Buckingham pi theorem defined the dimensionless parameters required to model the collapse process as,

collapse parameter: fT;

mean Reynolds number: $\mathrm{Re} = \dfrac{UR}{\nu}$;

unsteady Reynolds number: $\alpha = R\sqrt{\dfrac{2\pi f}{\nu}}$;

degree of occlusion: $\%A$;

Equating the physiologic and model collapse parameters with an assumed physiologic collapse period, T, of approximately 0.1 seconds resulted in a model collapse period equal to 8.5 seconds. Similarly, the Reynolds number and unsteady Reynolds number (physiologically equal to approximately 32 and 5, respectively [9–11]) specified a time-averaged volumetric flow rate of 101.1 ml/min and frequency of flow oscillation, f, of 0.0158 cycles /min in the model. The degree of occlusion, $\%A$, of the collapse was defined to be the maximum percent reduction in tube cross-sectional area caused by the increased transmural pressure. The 75 percent degree of occlusion of the model (an approximate mid-range value between the observed physiologic values of 40 and 100 percent) was calculated from measurements recorded from photographs of the collapsed LCA as viewed from the branch site.

While it was realized that the flow within the human coronary system is seldom fully developed (due to a continuously varying vessel geometry), in this study, a fully developed flow at the branch site at the time of collapse iniation facilitated the analysis of the results. Consequently, the length of the LMCA (21.6 cm) was selected to allow fully developed flow (Atabek's criteria [15] specified a minimum length of 13.4 cm) at the branch site. For the same reasons, the flow prior to collapse was adjusted so as to be evenly divided between the two branches of the test section, i.e., 50 percent of the LMCA volumetric flow went into each branch.

The discussion which follows describes the collapse of the model at four particular points in the pulsatile flow cycle (Fig. 2). These four points characterize the types of flow situations found in the coronary system, that is, a "zero" volumetric flow rate (Point 1), a rapidly increasing flow rate (Point 2), a quasi-steady flow rate (Point 3) and a rapidly decreasing flow rate (Point 4).

Nomenclature

$\%A$ = degree of occlusion, percent change in tube cross-sectional area during the collapse process
R = unstretched left main coronary artery radius
Re = Reynolds number, UR/ν
T = period of collapse
U = mean axial fluid velocity
f = frequency of flow oscillation
fT = dimensionless collapse parameter
p_i = axial pressure within the model where $i = 1, 2, \ldots 6$
Δp = downstream pressure minus upstream pressure
t = time
α = unsteady Reynolds number, $R\sqrt{2\pi f/\nu}$
ν = kinematic viscosity of the fluid
π = pi, approximately 3.1416
ω = circular frequency, $2\pi f$

Downloaded 02 Jun 2010 to 171.66.16.91. Redistribution subject to ASME license or copyright; see http://www.asme.org/terms/Terms_Use.cfm

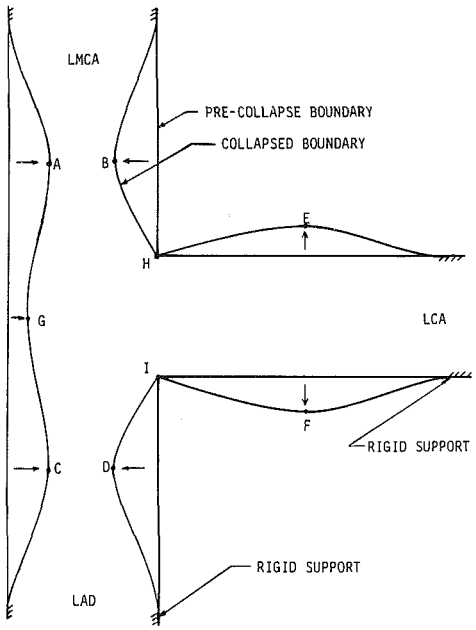

Fig. 3 Collapse mode shape of the model

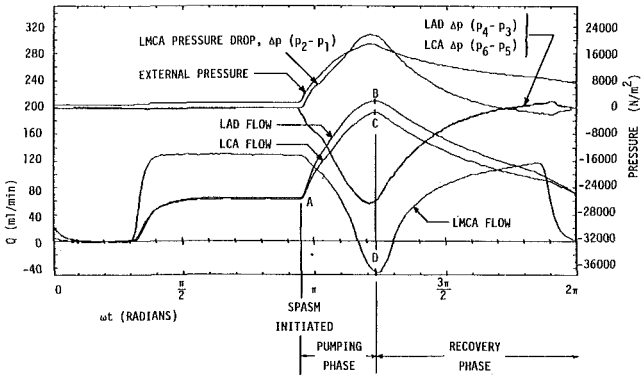

Fig. 4 Point 3 collapse results illustrating the pumping and recovery phases

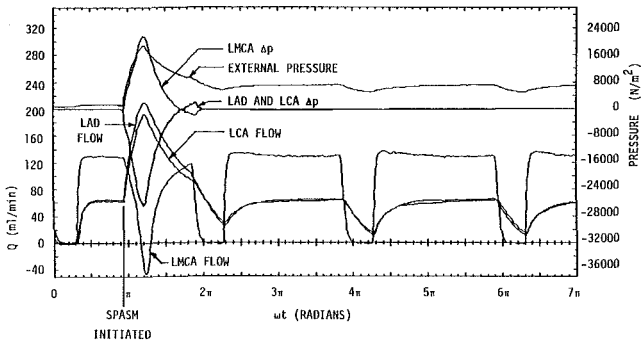

Fig. 5 Point 3 collapse results showing partial flow recovery while the collapse is maintained

Results and Discussion

A Qualitative Description of the Collapse Process. When the hydraulic collapse mechanism drove fluid into the pressure chamber, the segments of the model away from the branch site began to collapse first. When viewed from above (Fig. 3), the LMCA and LAD appeared to grow narrower, and the LCA seemed to expand. When viewed in the horizontal plane, the LMCA and the LAD segments grew wider and the LCA became narrower. This relative tube wall displacement resulted in a double-lobed collapsed model cross-sectional shape throughout. Point G began to move radially inward *after* the other segments (points A and B, points C and D, and points E and F) began to deform, and completed its inward displacement *before* these other points. This suggested a pulse wave transmission similar to that described by Kamm [16]. The propogation of the collapse from the segments downstream and upstream of the branch site toward the branch site was related, in this case, to the structural discontinuity represented by the branch configuration. It was expected that the downstream branches would collapse before the LMCA (due to the lower downstream pressure relative to the upstream pressure), but this was not observed. The fluid dynamic consequences of this wave propogation are discussed further in a future communication [17]. The corners of the test section, points H and I, did not translate, presumably held in place by the axial tension (both residual from the undeformed model and the increase due to the collapse deformation).

The double-lobed cross-section described above may not represent the physiologic case where the artery cross-section is more likely to remain essentially circular during the spasm collapse. However, the results presented below which describe the volumetric flow redistribution during the collapse process are thought to be more of a function of the final degree of occlusion generated during the collapse than the actual shape of the collapsed cross-section.

Volumetric Flow Results and Discussion. After the hydraulic collapse mechanism was released, a specific sequence of fluid dynamic events took place. This sequence was essentially independent of the point in the flow cycle where the collapse was initiated, in that it progressed through two basic phases:

(i) Pumping Phase: The test section began to collapse. This resulted in the rapid downstream pumping of fluid out of each branch, together with a corresponding tendency to pump fluid upstream out of the test section. The actual pumping of fluid upstream, i.e., the generation of a net mean volumetric backflow depended upon the final degree of occlusion of the test section and the upstream resistance to flow encountered by the fluid. That is, a substantial degree of occlusion, corresponding to an equally large pumping action, increased the likelihood of volumetric backflow in the LMCA given favorable upstream flow resistance conditions.

(ii) Recovery Phase: After the hydraulic piston had stopped pumping fluid into the optical/pressure chamber, the model continued to collapse (somewhat more slowly than in the pumping phase) while the flow and pressure within the various model segments began to recover their respective precollapse values. This recovery period was completed in approximately one flow cycle after collapse initiation, but the flow out of the test section continued to reflect the increased resistance to flow offered by the now collapsed test section.

While the results reported by Kamm [16] are similar to these, a direct comparison is difficult because of fundamental differences in the two experimental arrangements, e.g., a thin-walled, straight tube was used in the Kamm study with no (precollapse) volumetric flow through the model (in the reported results) and compressed air was used to drive the collapse of the tube. However, a rapid increase in the volumetric flow out of the collapsing model in the downstream direction (pumping phase) was reported and after the flow peaks (approximately coincident with the cessation of an increasing collapse pressure), it then subsided to the initial zero flow rate (recovery phase). Both of these observations are consistent with the results described in the next section.

Point 3 Collapse. The point 3 collapse sequence (refer to Figs. 4 and 5) was triggered at $\omega t = 2.98$ radians ($\omega = 2\pi f$, $t = 30.1$ seconds) in the flow cycle and the pumping phase thus

Downloaded 02 Jun 2010 to 171.66.16.91. Redistribution subject to ASME license or copyright; see http://www.asme.org/terms/Terms_Use.cfm

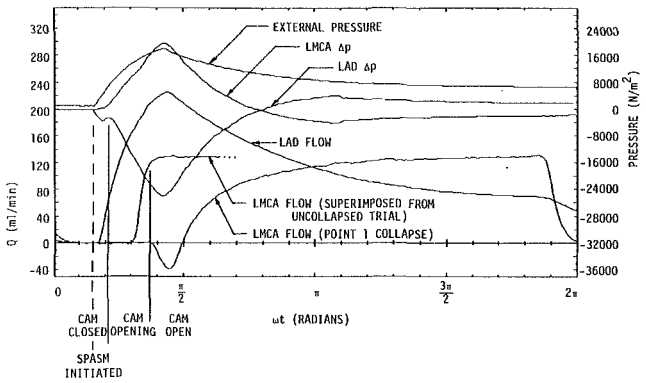

Fig. 6 Point 1 collapse results

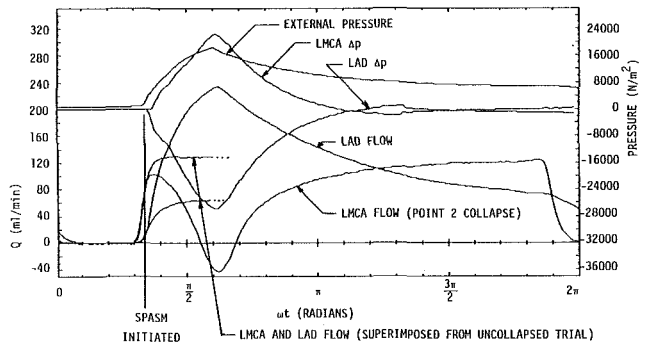

Fig. 7 Point 2 collapse results

began at point A in Fig. 4. As the transmural pressure (external pressure minus intraluminal pressure) rose, there was observed a rapid increase in the flow exiting the branches. The pumping phase was complete in approximately 8.6 seconds (ωt = 0.85 radians) when the flow and pressure curves reached either maximum or minimum values, points B, C and D in Fig. 4. The axial pressure drop along each segment reflected these changes in volumetric flow rate, i.e., when downstream pressure was less than upstream pressure, the pressure drop was negative, which favored downstream flow, and vice versa. Thus, the falling volumetric flow rate in the LMCA corresponded to a rising LMCA pressure drop (see Fig. 4 where p_1 and p_2 refer to the pressure at two axial locations in the LMCA). For the time scales involved here, the small phase shift between the beginning of the rise in external pressure and the associated flow response were attributed to the slight compressibility of the elastomer, i.e., the magnitude of the phase difference (ωt = 0.06 radians) was small, as was the compressibility of the elastomer.

During the recovery phase, the flow into the LMCA returned to the pre-collapse value even before the conclusion of the flow cycle (see Fig. 4). However, the flow rates out of the test section did not completely recover pre-collapsed values until the next flow cycle (see Fig. 5). The extent to which the curves representing flow into and out of the collapsed test section were changed because of the new shape of the test section (e.g., noncircular cross-section and curved walls) is addressed later.

Point 1, Point 2 and Point 4 Collapses. In general, volumetric flow rate and pressure responses to a point 3 collapse of the test section were similar to those seen with the collapse initiated at points 1, 2, and 4 in the flow cycle (see Fig. 2). The primary difference was related to the resistance to flow into LMCA at the time of collapse, offered by the cam/lever mechanism. Recall, the upstream resistance to flow offered by the cam/lever mechanism during a point 3 collapse sequence was essentially negligible.

With the collapse initiated at point 1 (ωt = 0.53 radians) in the flow cycle (Fig. 6), the cam/lever mechanism had closed the inlet tube to the point where flow into the LMCA had essentially ceased. As the cam began to open (0.65 ≤ ωt ≤ 1.16 radians) flow in the LMCA remained at approximately zero because, although inlet tube pressure was rising due to the cam opening and LMCA pressure was rising due to the tube collapsing, the throttling effect of the cam offered more resistance to flow than could be overcome by either pressure. Consequently, the drop in volumetric flow rate into the LMCA which previously occurred during the pumping phase (Fig. 4), was delayed (see Fig. 6). It was not until the rising pressure in the LMCA (due to the increasing transmural pressure) became large enough, and the cam/lever mechanism resistance became small enough, that volumetric backflow out of the test section resulted. The recovery phase described earlier for the point 3 collapse sequence was observed for the point 1 collapse. A similar LCA volumetric flow response (as described for the point 3 collapse) was seen during this collapse process, but was not presented in Fig. 6 to avoid cluttering the figure.

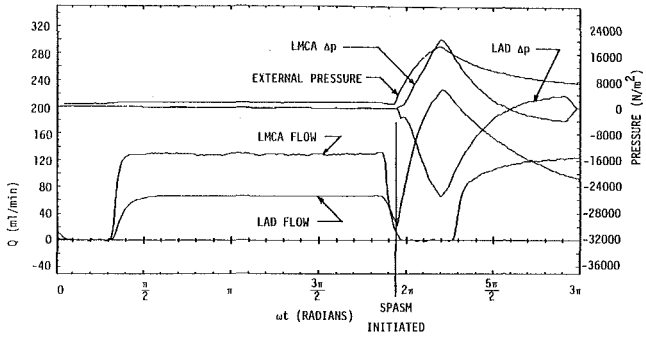

Fig. 8 Point 4 collapse results

When the collapse of the test section was initiated at point 2 in the flow cycle (ωt = 1.1 radians), the cam/lever throttling effect was dropping to a minimum, but had not yet reached that minimum (see Fig. 7). The flow into the LMCA did not begin to decrease immediately due to the fact that the downstream pressure in the LMCA was not sufficient to overcome the upstream resistance offered by the cam/lever mechanism. The pumping and recovery phases were completed as described above.

Collapse was also initiated at ωt = 6.09 radians (Point 4 in the flow cycle, see Fig. 8). The flow into the LMCA continued on its normal course to approximately zero, although somewhat faster than would have been the case without the collapse being initiated. No volumetric backflow was observed in the LMCA because of the throttling effect of the cam/lever mechanism which never allowed pressure within the LMCA (which was increasing during this time interval) to exceed the constant hydrostatic back pressure. In all other respects, flow out of both branches, all axial pressure drops and the external pressure behaved as previously described during both the pumping phase and the recovery phase.

Effect of the Degree of Occlusion. The extent to which the model was collapsed dictated, through the rise in the internal model pressure, the amount of fluid which was pumped out of each branch. Coupled with the time in the flow cycle at which the spasm began, this rise in pressure also determined the probability of generating volumetric backflow out of the entrance to the test section. For example, when the model was collapsed at Point 3 to a maximum 65 percent occlusion (as opposed to 75 percent) the resulting changes in volumetric flow rate in any of the model segments reflected this smaller degree of occlusion. Moreover, no volumetric backflow out of the LMCA was observed due to this diminished pumping action.

Downloaded 02 Jun 2010 to 171.66.16.91. Redistribution subject to ASME license or copyright; see http://www.asme.org/terms/Terms_Use.cfm

Flow Through the Collapsed Models. As shown in Fig. 5, the curve representing LMCA flow entering the model recovered its precollapse appearance, both in magnitude and form, after approximately one flow cycle. The LAD and LCA curves of the flow leaving the collapsed test section did not, however, recover fully, i.e., the quasi-steady magnitude of approximately 65 ml/min was apparent, but the form of the curves were significantly different. These flow curves lack the distinctive "on/off" pattern which was evident prior to collapse. This was due to energy-dissipating events which were occuring within the collapsed model segments, but which did not take place in the uncollapsed model. For example, the changes observed in the branch flow curves could arise due to energy losses associated with the local branch site fluid dynamics, e.g., unsteady flow separation (examined in a future communication [17]). In addition, the collapsed shape of the test section may have allowed the elastic walls to more effectively act as an energy-storage mechanism. In Fig. 5, the indication of flow continuation out of the model after the flow into the LMCA had ceased, suggests that the fluid in the test section was being driven by stored (in the walls) elastic energy.

Summary and Conclusions

A summary of the results obtained in this investigation showed that:

(i) The local collapse of an elastic tube provided energy to the system that tended to pump fluid both upstream and downstream away from the collapsing region. A direct mechanical analog of the phenomenon is the positive displacement pump, i.e., the energy required to move the fluid is provided by the work done in the displacement process.

(ii) The effectiveness of the pumping action depended on the upstream and downstream conditions (e.g., resistance) encountered by the fluid attempting to move away from the collapsing region. This, in turn, depended also on *when* in the flow cycle the collapse began and to what *degree of occlusion* the test section collapsed (all other variables being kept constant).

(iii) The collapse (or pumping phase) was followed by a period of recovery that was complete in the LMCA, but not in the LAD and LCA. That is, collapse throttled the flow by generating a new tube shape (curved-walls and noncircular). Due to the pulse wave nature of this effect, it was believed to be related to the elasticity of the model wall. While the flow exiting the collapsed model was effected by the collapsed shape, the flow was not diminished. This latter result appeared to contradict physiologic evidence that coronary artery spasm is directly related to ischemia of the heart [8], or a reduced supply of blood to the heart. In response to this observation, it was concluded that just as the 75 percent occlusion more effectively redistributed flow through the model (when compared to the 65% occlusion), an 85% or 90% occlusion would have a still greater effect. Much more remains to be learned about this phenomenon.

References

1 Kuchar, N. R., and Ostrach, S., "Unsteady Entrance Flows in Elastc Tubes with Application to the Vascular System," Case Western Reserve University Technical Report FTAS/TR-67-25, 1967.

2 Hecht, A. M., Yeh, H., and Chung, S. M. K., "Collapse of Arteries Subjected to an External Band of Pressure," ASME *Journal of Biomechanical Engineering*, Vol. 102, 1980, p.8.

3 Wang, C. Y., Watson, L. T., and Kamat, M. P., "Buckling, Postbuckling, and Flow Through a Tethered Elastic Cylinder Under External Pressure," ASME *Journal of Applied Mechanics*, Vol. 50, 1983, p. 13.

4 Conrad, W. A., "Pressure-Flow Relationships in Collapsible Tubes," *IEEE Transactions on Biomedical Engineering*, Vol. 16, 1969, p. 284.

5 Conrad, W. A., McQueen, D. M., and Yelin, E. L., "Steady Pressure Flow Relations in Compressed Arteries: Possible Origins of Korotkof Sounds," *Medical and Biological Engineering and Computing*, Vol. 18, 1980, p. 419.

6 Shimizu, M., and Tanida, Y., "On the Mechanism of Korotkoff Sound Generation at Diastole," *Journal of Fluid Mechanics*, Vol. 127, 1983, p. 315.

7 Kececioglu, I., McClurken, M. E., Kamm, R. D., and Shapiro, A. H., "Steady, Supercritical Flow in Collapsible Tubes. Part 1: Experimental Observations," *Journal of Fluid Mechanics*, Vol. 109, 1981, p. 367.

8 Schneck, D. J., and Davis, R. B., "Ischaemia in the Heart due to Atherosclerotic Mechanisms, Flow Anomalies and Vascular Spasm," in *Heart Perfusion: Energetics and Ischemia*, Plenum Press, New York, 1983, pp. 229–274.

9 James, T. N., *Anatomy of the Coronary Arteries*, Paul B. Hoeber, Inc., New York, 1961, pp. 12–37.

10 Baroldi, G. and Scomazzoni, G., *Coronary Circulation in the Normal and Pathologic Heart*, Office of the Surgeon General, Department of the Army, Washington, D.C., 1967, pp. 5–19.

11 Schneck, D. J., and Ostrach, S., "Pulsatile Blood Flow in a Diverging Circular Channel," Case Western Reserve University Technical Report FTAS/TR-73-86, 1973.

12 James, T. N., Sherf, L., Schlant, R. C., and Silverman, M. E., "Anatomy of the Heart," in *The Heart: Arteries and Veins*, McGraw-Hill, New York, 1982, pp. 22–74.

13 Farrer-Brown, G., "Normal and Diseased Patterns of the Myocardium of the Human Heart: I. Normal Pattern in the Left Ventricular Free Wall," *British Heart Journal*, Vol. 30, 1968, p. 527.

14 Davis, R. B., and Schneck, D. J., "An Examination of Flow Characteristics in Collapsing Elastic Tubes," Virginia Polytechnic Institute and State University Technical Report VPI-E-83-36, 1983. Available through NTIS (PB-83/259 457).

15 Atabek, H. B., Chang, C. C., and Fingerson, L. M., "Measurement of Laminar Oscillatory Flow in the Inlet Length of a Circular Tube," *Physics in Medicine and Biology*, Vol. 9, 1964, p. 219.

16 Kamm, R. D., and Shapiro, A. H., "Unsteady Flow in a Collapsible Tube Subjected to External Pressure or Body Forces," *Journal of Fluid Mechanics*, Vol. 95, 1979, p. 1.

17 Davis, R. B., Schneck, D. J., and Gustein, W. H., "Pulsatile Flow Through a Branching Tube with Collapsing Walls: Visualization of Streakline Patterns," ASME JOURNAL OF FLUIDS ENGINEERING (submitted for publication).

Downloaded 02 Jun 2010 to 171.66.16.91. Redistribution subject to ASME license or copyright; see http://www.asme.org/terms/Terms_Use.cfm

Experimental Study of the Diversion Crossflow Caused by Subchannel Blockages.

Part I: Experimental Procedures and Mass Flow Rates in the Channels[1]

S. Gencay
Institute for Nuclear Energy,
Technical University of Istanbul,
Istanbul, Turkey

A. Tapucu

N. Troche

Institut de genie nucleaire,
Ecole Polytechnique de Montreal,
Montreal, Canada

M. Merilo
Electric Power Research Institute,
Palo Alto, Calif.

In this research, the hydrodynamic behavior of two laterally interconnected channels with blockages in one of them has been studied experimentally. For blockages of different shapes and severities, the mass flow rates as well as the pressures in the channels upstream and downstream of the blockage were determined. The experiments were conducted on a test sections which consists of two-square channels separated by an intermediate plate with slots of different geometric parameters. Two types of blockages have been considered: plate and smooth. The shape of the smooth blockage was a cosine. In the region upstream of the blockage, the diversion cross-flow takes place over a relatively short distance. Downstream of the blockage, the recovery of the diverted flow by the blocked channel is a slow process and the rate of this recovery worsens with increasing blockage severity. For a given blockage rate, the diversion crossflow caused by a smooth blockage is smaller than that of a plate blockage.

1 Introduction

Investigation of the consequences of coolant flow area blockages in fuel assemblies is of great importance for both thermal and fast breeder reactor safety. In pressurized water reactors, during the refilling and reflooding phases of a hypothetical loss-of-coolant accident, the temperature of the zircaloy fuel cladding may reach very high values. These high temperatures coupled with high internal pressures, brought about by gaseous fission products, may trigger a ductile or brittle failure of the cladding. The ductile failure may result in a ballooning of the fuel rod while with brittle failure, the rod may burst open. In both cases, the flow area of a given subchannel or a group of subchannels could be reduced. The grid spacers and, especially in CANDU reactors, the end plates may also perturb the emergency core cooling fluid flow significantly.

One of the consequences of the blockage of a subchannel or a group of subchannels is to divert, depending on the severity of the blockage, some or all of the flow into neighboring unblocked ones. The flow recovery downstream of the blockage is a slow process and it may take many hydraulic diameters before the flow is restored to its far upstream value. Therefore, immediately downstream of the blockage, higher enthalpies will prevail in the blocked subchannels than in the unblocked subchannels, and the heat transfer in these regions may be impaired. An adequate prediction of the enthalpies and heat transfer conditions in the downstream region requires detailed information on the flow redistribution caused by the blockage.

The objective of this research is to study the hydrodynamic behavior of two laterally interconnected channels when one of them is partially or completely blocked. Two main parameters, pressures and mass flow rates in the channels upstream and downstream of the blockage, were measured. The present paper deals only with experimental procedures and mass flow rates. The results on the pressure distribution in the channels along with the comparison of the COBRA-III-C predictions with the data will be the subject of a companion paper.

2 Literature Survey

When a blockage occurs in a rod bundle, its local and long range effects on the coolant flow should be determined. The local effects include the separation of the flow from the fuel surface, the reattachment of the flow to the surface in the downstream region and the recirculating zones which develop both upstream and, mainly, downstream of the blockage. Long range effects include the flow diversion out of the blocked subchannel and the recovery of this diverted flow downstream of the blockage. Knowledge of the irrecoverable pressure loss caused by the blockage is also essential in the

[1]The work reported herein was funded by the Electric Power Research Institute, Palo Alto, U.S.A.

Contributed by the Fluids Engineering Division for publication in the JOURNAL OF FLUIDS ENGINEERING. Manuscript received by the Fluids Engineering Division, November 11, 1983.

Copyright © 1984 by ASME

Downloaded 02 Jun 2010 to 171.66.16.91. Redistribution subject to ASME license or copyright; see http://www.asme.org/terms/Terms_Use.cfm

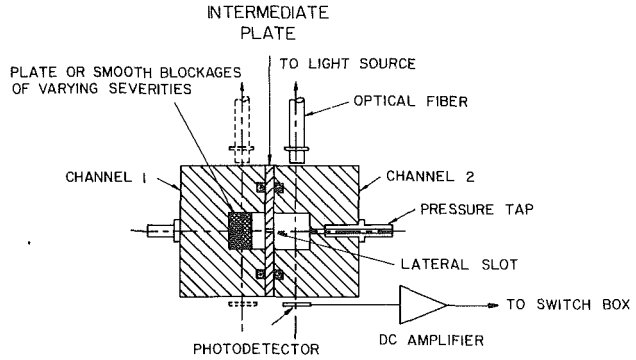

Fig. 1 Cross-sectional view of the square channel test section and the photodetector-light source system

determination of the hydraulic behavior of the blocked channel.

Good and Joubert [1] showed that the length of the upstream recirculation zone is of the same order as the plate height, and about 60 % of the front face of the blockage is exposed to the separated flow. Experiments indicate that the downstream recirculation zone could be quite long [1-3]. Bishop et al. [4] compiled the length of the recirculation zone for local blockages of different geometry and boundary conditions obtained by different investigators and found that the ratio of the wake length to the height of the plate varies between 3 and 17.

Experiments on rod bundles [5] have also shown that a distinct recirculation zone, qualitatively comparable to that behind a circular disk normal to a turbulent flow in a tube, develops downstream of an impermeable or nearly impermeable blockage. The length of the recirculation zone is influenced mainly by the bulk velocity of the flow and by the magnitude of the blockage, and it increases with increasing velocities [6, 7] and blockage rates [8, 9].

Irrecoverable pressure losses caused by flow blockages are deduced from the variation of the static pressure upstream and downstream of the blockages. A dimensionless representation of the blockage-related irrecoverable pressure loss Δp_b is given by:

$$K_b = \frac{\Delta p_b}{\frac{1}{2}\rho v^2} \tag{1}$$

where "v" is the average velocity of the undisturbed flow. The dependence of this coefficient on the extent of the blockage and on the Reynolds number have been investigated by Sparrow [9] and Lafay [10].

Experiments on interconnected subchannels, when one of them is partly or fully blocked, to the best of the author's knowledge, have been carried out only in single phase flow by Stiefel [11, 12] and Stiefel and Nöthiger [13]. The experimental results can be summarized as follows:

1. The upstream influence of the blockage on pressures and mass flow rate could only be detected over a distance of about 8 hydraulic diameters.

2. There is a substantial pressure difference between subchannels in the region of high crossflow velocities.

3. Downstream of the disturbance, a very gradual readjustment of the mass-flow distribution takes place.

The experiments of Rowe et al. [14] were conducted on a more complex test section consisting of six half rods arranged in two rows to represent two full and two half subchannels in a square-square rod bundle array. Subchannel blockages up to approximately 90 percent area reduction were considered to be of the swelling and plate type. The experimental results indicate that the introduction of a flow blockage causes a significant redistribution of flow, and that the flow reduction observed behind the blockage persists well downstream. The plate blockage caused a larger flow reduction in the blocked subchannels, and the flow recovery behind this blockage was also considerably slower than for the sleeve blockage. Because of the limitations of measurement techniques, experiments on rod bundles are very limited. The investigation has usually been limited to single phase flow conditions and mainly flow velocities in the blocked subchannels and the neighboring unblocked subchannels have been measured [15, 16, 17]. A special effort has also been devoted to the study of the behavior of the recirculation zone which develops behind the blockage [18].

3 Experimental Apparatus

The blockage experiments were conducted in a test section consisting of two square channels separated by an intermediate plate in which slots were machined with different geometric parameters (Fig. 1). The test section was machined from transparent acrylic blocks, which were chosen to allow average flow velocity measurements by cross-correlating the fluctuating signals from two successive photodetector-light source systems when a dye is injected into the channels. The relevant geometric parameters of the test section are given in Table 1. Plate and smooth blockages of varying severities were placed in channel 1 at a distance of approximately 26 hydraulic diameters downstream of the beginning of the interconnected region. Water at 20° was used as working fluid.

Pressure along the unblocked channel and pressure differences between the blocked and unblocked channels are measured with pressure transducers every 19.05 mm in the vicinity of the blockage and every 38.1 mm or 76.2 mm far from the blockage. Figure 2 shows the locations at which the pressures were measured.

The flow velocities were measured by cross-correlating the fluctuating signals from two successive photodetector-light systems spaced 38.1 mm apart. The positions of the photodetector and light systems are also given in Fig. 2. The photodetectors, 12 mm long and 9 mm wide, were mounted on the same board as their associated DC amplifiers. Ten such units were assembled in a plastic casing (detector holder) which could be moved from one position to another to measure the velocities upstream and downstream of the blockage in both channels. The sensitive surface of the photodetectors were protected with an opaque plate on which slots 1.6 mm wide, equal in number to that of the detectors

Nomenclature

K_b = irrecoverable pressure drop coefficient
Q = flow rate, m^3/h
d_h = hydraulic diameter, m
f_0 = the ratio v_{tr}/v_{fm}
l' = length of the diversion crossflow region upstream of the blockage, m
m = mass flow rate, kg/s
s = gap clearance, m
t = time, s
v = velocity, m/s
v_{fm} = average velocity given by a turbine flow meter, m/s
v_{tr} = transit velocity of the fluctuations, m/s
z = distance, m
z^- = regions upstream of the blockage, m
z^+ = regions downstream of the blockage, m
Δp_b = irrecoverable pressure drop caused by the blockage, N/m^2
ρ = specific mass, kg/m^3

Downloaded 02 Jun 2010 to 171.66.16.91. Redistribution subject to ASME license or copyright; see http://www.asme.org/terms/Terms_Use.cfm

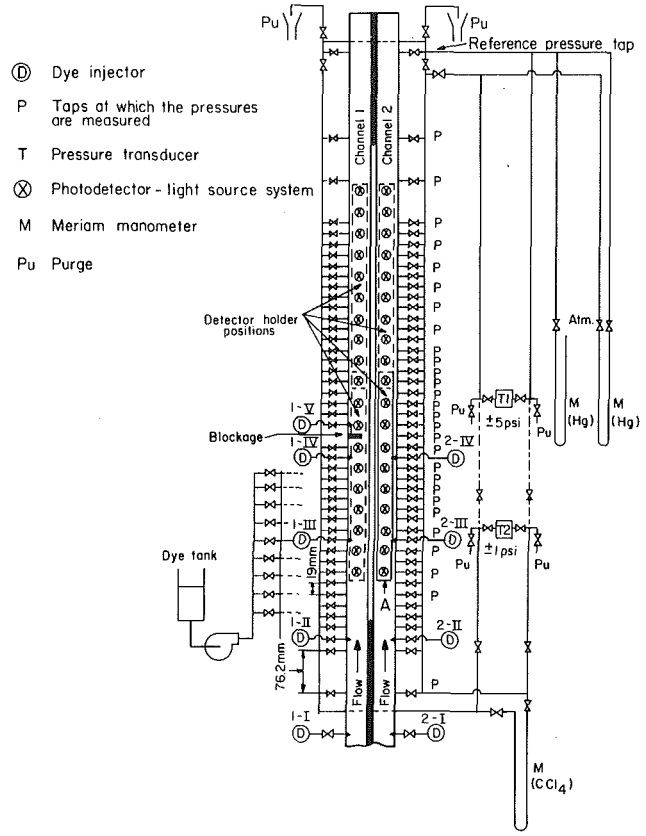

Fig. 2 Location of pressure taps, photodetector-light source systems and dye injection

were machined. Each photodetector is equipped with its individual excitation light which is brought from a common light source by optical fibers. Special care has been taken to align the excitation lights and the slots mounted on the opposite side of the channel. The dye ($KMn0_4$ solution) was injected into the flow through needles mounted on the test section using a variable speed pump (Fig. 2) to generate fluctuations for cross-correlation measurements. The details of the experimental apparatus are given in reference [19].

Two blockage geometries were studied in this investigation: plate and smooth. The shape of the latter blockage was a cosine defined by the function $y = h \cos(\pi z/L)$. The plate blockage was always mounted on the wall opposite to the interconnection gap. Two situations were considered in the case of smooth blockage; single piece and two-piece blockages. The single piece blockage was fixed on the wall opposite to the interconnection gap, while for the two-piece blockage, the pieces were fixed on the side walls. Table 2 gives the geometric parameters of the blockages.

4 Experimental Procedures

As already pointed out, the average velocities in the channels upstream and downstream of the blockage were measured by cross-correlating the fluctuating signals from two successive photodetector-light source systems when a dye is injected into the flow. The location of the maximum of the cross-correlation function gives the average transit time of the fluctuations, Δt, between the photodetectors, and the average transit velocity is calculated from $v_{tr} = \Delta z/\Delta t$. Δz is the distance between two successive photodector-light source systems.

Obviously, such a system should be calibrated for the channel geometry in which the velocities have to be measured. For calibration purposes, the channels were isolated from

Table 1 Geometric parameters of the test section

- Gap clearances (s), mm		1.52 ± 0.05 3.04 ± 0.05
- Gap thickness, mm		3.17 ± 0.05
- Hydraulic diameter of the channels*, mm		
s = 1.52 mm	CH1	12.6 ± 0.05
	CH2	12.5 ± 0.05
s = 3.04 mm	CH1	13.1 ± 0.05
	CH2	13.1 ± 0.05
- Cross-sectional area of the channels*, mm^2		
s = 1.52 mm	CH1	166.2 ± 1.3
	CH2	165.0 ± 1.3
s = 3.04 mm	CH1	168.6 ± 1.3
	CH2	167.4 ± 1.3
- Length of the interconnection, mm		847.0 ± 1

*Including half of the interconnecting gap.

Table 2 Interconnected channel experiments

Square Channel Test Section

Plate Blockage

% Area Reduction*				
Gap Clearance 1.5 mm	29.8 ±0.4	59.2 ±0.5	88.8 ±0.5	98.5
Gap Clearance 3.0 mm	--	58.4 ±0.5	87.6 ±0.5	--
Thickness (L), mm	3.22±0.02	3.22±0.02	3.22±0.02	3.22±0.02
Height (h), mm	3.82±0.05	7.60±0.05	11.40±0.05	12.65±0.05

Smooth Blockage $y = h \cos \frac{\pi z}{L}$

% Area Reduction*	58.6±0.5, One-piece	64.2±0.5, Two-pieces
Length (L), mm	50.±0.1	48.3±0.1
Height (h), mm	7.52±0.05	2x4.12±0.05

*Flow section includes the half of the interconnection region.

each other by a blank intermediate plate. The calibration of a successive pair of photodetector-light source systems consisted of measuring the average transit time with the cross-correlation technique (i.e., average transit velocity (v_{tr}) of the fluctuation between the photodetectors) and plotting the ratio of this velocity to the true average flow velocity (v_{fm}) in the channel as a function of the transit velocity. The volume flow rates in the channels, i.e., true average velocities, were determined with a turbine flowmeter with an accuracy better than 1 percent of the reading (specified by the manufacturer).

The above calibration was conducted for each successive pair of photodetector-light source systems in all four positions of the detector holder (Fig. 2). As a typical example, Fig. 3 gives the calibration curve for photodetector-light source system 3-4 in Position A (Fig. 2). The flow rate of the dye injection which was used to generate fluctuation was always a small fraction of the flow rate in the channel (0.1 percent or less).

Two parameters were measured in the interconnected channel experiments: pressures and average flow velocities upstream and downstream of the blockage. The flow velocities in the channels upstream and downstream of the blockage are determined by using the information on the transit velocity of the fluctuations between two successive photodetectors in conjunction with the corresponding calibration curve. In Fig. 3, the knowledge of the transit velocity determines the value of f_0 ($= v_{tr}/v_{fm}$) which, in turn, gives the average velocity over the interval under study. The basic assumption made in this procedure is that the calibration curve obtained under single channel flow con-

Downloaded 02 Jun 2010 to 171.66.16.91. Redistribution subject to ASME license or copyright; see http://www.asme.org/terms/Terms_Use.cfm

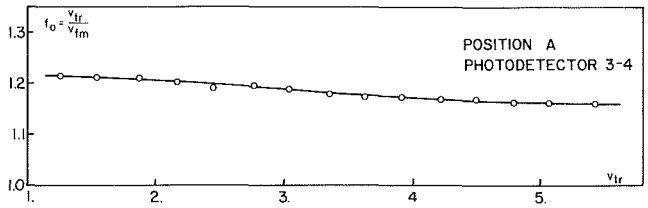

Fig. 3 Calibration curve for square channel. (Standard error in f = ± 1.4 %, in v_{tr} = ± 1%)

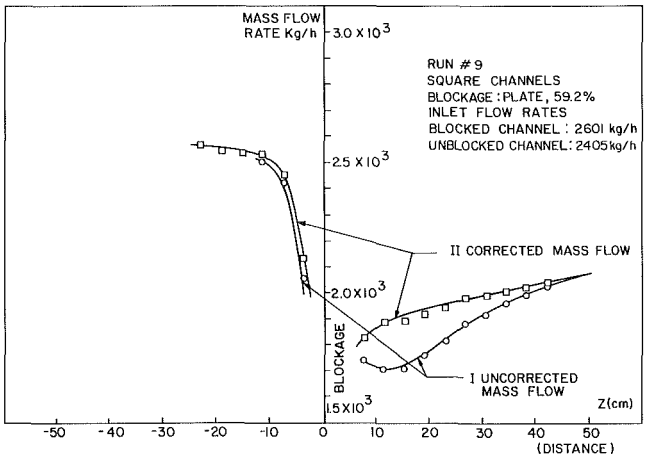

Fig. 4 Mass flow rates in the blocked channel. (Standard error in the corrected mass flow rates: ± 2%)

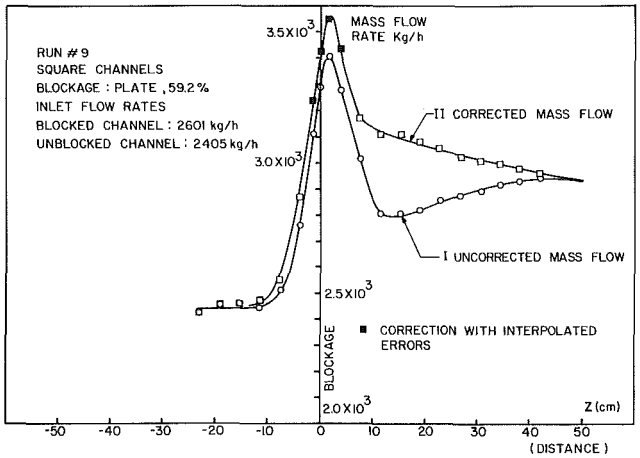

Fig. 5 Mass flow rates in the unblocked channel. (Standard error in the corrected mass flow rates: ± 2%)

ditions holds true for two laterally interconnected channels when there is substantial lateral inflow or outflow. As will be seen in the presentation of the experimental results this assumption is not completely true and a correction scheme is required to obtain the true average velocity.

5 Experimental Results on Mass Flow Rates

Curve I in Figs. 4 and 5 give the mass flow rates (i.e., average axial velocities) in the blocked and unblocked channels for a typical run as determined using the information on the transit time of the dye fluctuations. A sudden drop in the flow rate in the blocked channel (concurrently a sudden rise in the unblocked channel) has been observed immediately upstream of the blockage. In the region downstream of the blockage, the variations of the flow rates in the channels were inconsistent: in the unblocked channel, the flow first decreased quite rapidly then increased while in the blocked channel after a slight decrease, it also increased. Obviously, flow rates in both channels cannot be expected to increase simultaneously. When the sum of the flow rates in the channels, m_c, obtained with the present method was compared with the total flow rate, m_0, at the inlet of the test section, measured by the turbine flowmeters, a mass balance error defined as:

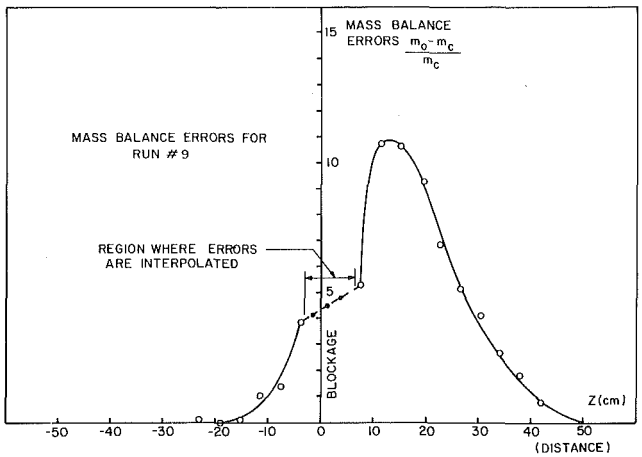

Fig. 6 Mass balance errors

$$\frac{m_0 - m_c}{m_c}$$

has been observed. This error varied with the distance from the blockage in the upstream and downstream regions as shown in Fig. 7.

This error is a consequence of the difference in radial velocity profile which exists between the single channel flow conditions where the velocity calibration curves were obtained and the interconnected channel flow conditions where substantial lateral inflow and outflow exist.

To determine the error caused by the variation of the radial velocity profile under the influence of lateral flow and to find out how this error can be corrected, a set of special experiments was conducted on two channels interconnected by a short slot of length 38.1 mm. These experiments showed that the mass flow rates in the channels determined by the cross correlation technique may be corrected by the mass balance error defined above to obtain the true mass flow rates. The details on the short slot experiments and the justification for the proposed correction are detailed in reference [19].

Based on the above observation, the raw data obtained on the mass flow rates in the channels have been corrected with the mass balance errors $(m_0 - m_c)/m_c$ given in Fig. 6, and the resulting variations are shown with Curve II in Figs. 4 and 5. This correction yielded a more consistent variation of mass flow rates in the channels downstream of the blockage. The standard error in the mass flow rates in the channels after the mass balance error correction is evaluated at ±2 percent. The details of this evaluation are also given in reference [19].

Since no cross-correlation function could be obtained in the blocked channel immediately upstream and downstream of the blockage, no information on the mass flow rates, i.e., no information on the mass balance errors, could be obtained in these regions. In order to circumvent this difficulty, the errors in these regions have been obtained by interpolation between the last measurement point upstream of the blockage and first measurement point downstream of the blockage in Fig. 6 and the resulting mass flow rates are indicated by shaded symbols in Fig. 5.

Figures 7 through 9 give the mass flow rates in the unblocked channel upstream and downstream of the blockage for typical runs. In these figures also, the shaded symbols show the mass flow rates obtained by interpolation of the errors. The data on the mass flow rates in the channel for all runs are given in reference [19].

In the upstream region, the diversion cross-flow induced by the blockage takes place over a relatively short distance. The

Downloaded 02 Jun 2010 to 171.66.16.91. Redistribution subject to ASME license or copyright; see http://www.asme.org/terms/Terms_Use.cfm

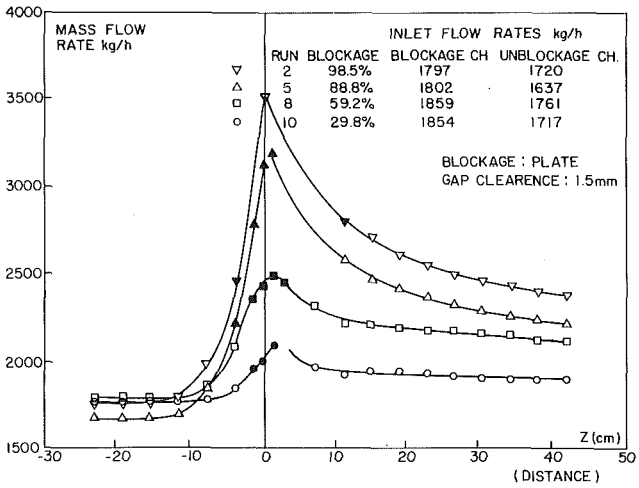

Fig. 7 Mass flow rates in the unblocked channel. (Standard error in the mass flow rate: ± 2%)

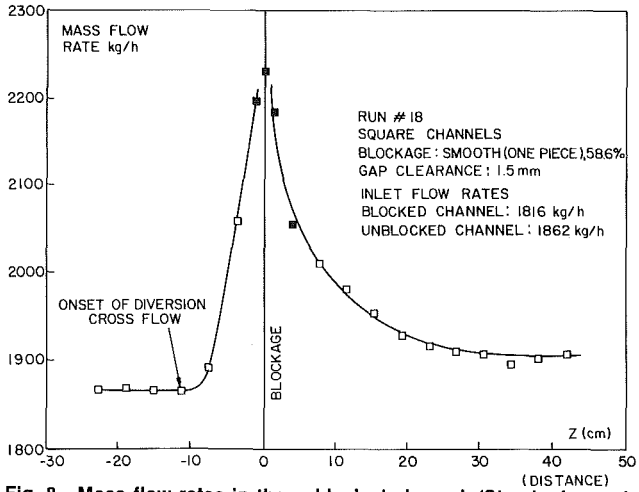

Fig. 8 Mass flow rates in the unblocked channel. (Standard error in the mass flow rate: ± 2%)

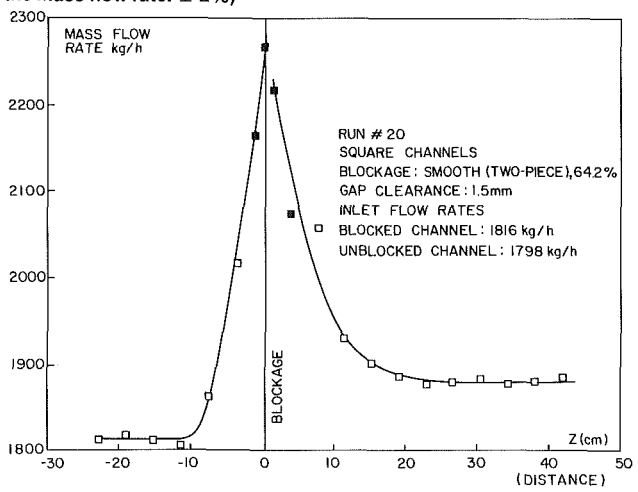

Fig. 9 Mass flow rates in the unblocked channel. (Standard error in the mass flow rate: ± 2%)

length l' of the upstream diversion cross-flow region, defined as the distance between the point of onset of diversion crossflow and the beginning of the blockage, depends on the severity of the blockage, and increases with increasing blockage fraction. This length also depends on the gap clearance of the interconnection and the shape of the blockage: it decreases with increasing gap clearance or when the plate blockage is replaced with a smooth blockage of the same blockage fraction. The dependence of the length of the diversion crossflow region on the above parameters is shown

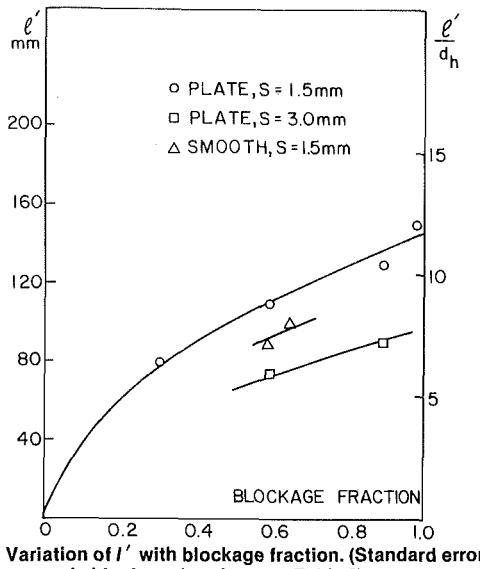

Fig. 10 Variation of l' with blockage fraction. (Standard error in l' = ±3%, for errors in blockage fraction, see Table 2)

in Fig. 10. The point of onset of diversion crossflow, as shown in Fig. 8, is taken as the point where the mass flow rate in the unblocked channel (or the pressure difference between the blocked and unblocked channel) departs significantly from their far upstream constant values.

The situation in the region downstream of the blockage is quite different. The recovery of the diverted flow by the blocked channel is quite a slow process. Indicating by z^- and z^+ the regions upstream and downstream of the blockage respectively and Q_{z-} and Q_{z+} the flow rates in these regions, Fig. 11, give the variation of the ratio Q_{z+}/Q_{z-} in the blocked channel with the blockage fraction for $z^- = l' + L/2$ (L: length of the blockage), and $z^+ = 12\,d_h$ (/152 mm), and for $z^- = l' + L/2$ and $z^+ = 33\,d_h$ (419 mm)[1]. In both cases, this ratio is less than 1 and decreases with increasing blockage fraction. Therefore, the recovery of the diverted flow by the blocked channel worsens with increasing blockage fraction. The length of the interconnected region in the present test section was not sufficient to reach the point where the ratio Q_{z+}/Q_{z-} becomes 1; it is expected that several tens of hydraulic diameters are needed before the flow is equally divided between the channels. The Q_{z+}/Q_{z-} ratio is also affected by the shape of the blockage. For 58.6 percent smooth blockage, the ratio $Q_{z+} = 12d_h/Q_{z-}$ was approximately 0.96 which is much higher than that for plate blockage with the same blockage fraction. Comparison of Figs. 8 and 9 with 7 shows that, for the same blockage fraction, the diversion cross-flow caused by a smooth blockage is smaller than that caused by a plate blockage and the flow recovery downstream of a smooth blockage is a fairly rapid process.

The effect of gap clearance is also illustrated in Fig. 11. For regions close to the blockage, increasing the gap clearance seems to favor the flow recovery for 88.8 percent-plate blockage. The opposite happens for 59.2 percent-plate blockage. However, for regions far from the blockage, the recovery for the above blockage fractions seems to improve with increasing gap clearance.

Because of the close resemblance between the test sections used in the present research and the Stiefel [11, 12], and Stiefel and Nöthiger [13] experiments, a comparison of mass flow rates data obtained in the two cases could prove very useful. In the Stiefel and Nöthiger experiments, air was used as the working fluid. The comparison will be limited to the data obtained for a gap clearance of 2 mm in the Stiefel experiments and 1.5 mm in the present research.

[1] Last flow rate measurement point.

Downloaded 02 Jun 2010 to 171.66.16.91. Redistribution subject to ASME license or copyright; see http://www.asme.org/terms/Terms_Use.cfm

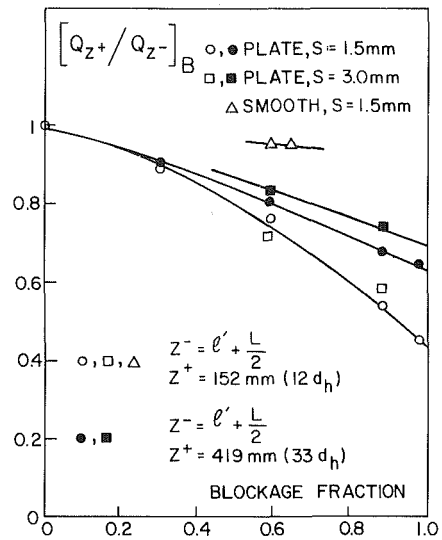

Fig. 11 Variation of the Ratio Q_{z+}/Q_{z-} with blockage fraction. (Standard error in $Q_z/Q_z = \pm 2.8\%$, for errors in blockage fraction, see Table 2)

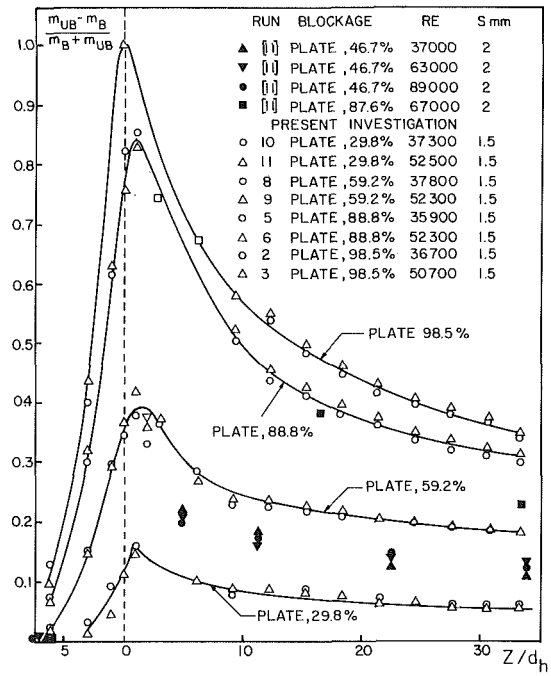

Fig. 12 Comparison of the difference of mass flow rates in the channels. (Standard error in each data point for the present investigation: ±5.8%)

Figure 12 gives the comparison of $(m_{UB}-m_B)/(m_{UB}+m_B)$ (m_{UB} and m_B are the mass flow rates in the unblocked and blocked channels, respectively) obtained on 98.5, 88.8, 59.2, and 29.8 percent blockages in the present research with that on 46.7 and 87.6 percent blockages in the Stiefel-Nöthiger experiments. The agreement between the data is quite satisfactory: the data for 46.7 percent blockage in the Stiefel-Nöthiger experiments fall between the data for 29.8 and 59.2 percent blockages in the present experiments, and the data on 88 percent blockage in both experiments agree reasonably well.

6 Conclusions

In this research, the hydrodynamic behavior of two laterally interconnected channels with blockages in one of them has been studied experimentally. For blockages of different shapes and severities, the flow rates in the channels upstream and downstream of the blockage were determined. The experiments were conducted on a test section which consists of two-square channels separated by an intermediate plate in which slots are machined with different geometric parameters. Two types of blockages have been considered: plate and smooth. The shape of the smooth blockage was a cosine. The following conclusions can be drawn from the investigation.

1. In the upstream region, the diversion cross-flow induced by the blockage takes place over a relatively short distance.
2. The length of the upstream diversion cross-flow region, l', depends on the severity of the blockage and increases with blockage fraction.
3. This length also depends on the gap clearance of the interconnection and the shape of the blockage: it decreases with increasing gap clearance or when the plate blockage is replaced with a smooth blockage of the same severity.
4. Downstream of the blockage, the recovery of the diverted flow by the blocked channel is a slow process.
5. The recovery distance of the diverted flow increases with increasing blockage fraction.
6. For the same blockage fraction, the diversion crossflow caused by a smooth blockage is smaller than that of a plate blockage.
7. The flow recovery is faster for smooth blockages than for plate blockages.
8. For the region close to plate blockages, increasing the gap clearance favors the flow recovery for high blockage fraction. The opposite is true at low blockage fraction. For regions far from the blockage, the recovery seems to improve with increasing gap clearance.

References

1 Good, M. C., and Joubert, P. N., *J. Fluid Mech.*, Vol. 31, 1968, pp. 547–582.

2 Arie, M., and Rouse, J., *J. Fluid Mech.*, Vol. 1, 1956, pp. 129–141.

3 Leutheusser, J. L., and Baines, W. D., *J. of the Hydraulic Division ASCE*, Vol. 93, HY 3, 1967, pp. 35–49.

4 Bishop, A. A., et al., *Trans. Amer. Nucl. Soc.*, Vol. 14, No. 2, 1971, pp. 748–749.

5 Basmer, P., et al., *Atomwirtschaft*, Vol. 17, No. 8, 1972, pp. 416–418.

6 Robinson, D. P., and Smith, R. A. K., "Water Modeling Studies of the Hydrodynamic Characteristics of Impermeable Blockages in an 11-Pin Geometry," 1977, AEE-M 1471.

7 Fontana, M. H., et al., "Thermal-Hydraulic Effects of Partial Blockages in Simulated LMFBR Fuel Assemblies with Applications to the CRBR," ORNL-TM-4479.

8 Kirsch, D., *Nucl. Eng. and Design*, Vol. 31, 1974, pp. 266–279.

9 Sparrow, E. M., et al., *Trans. ASME*, Vol. 101, 1979, pp. 200–206.

10 Lafay, J., and Picut, M., "Thermo-hydraulique d'un élément de combustible situé au centre d'un canal annulaire localement perturbé par un bouchage partial," Report CEA-1774, 1974.

11 Stiefel, U., "Comparison of Measured and Calculated Mass Flow Distribution in Partially Blocked Parallel Flow Channels," EIR Report TM-IN-481, 1971.

12 Stiefel, U., "Berechnung nd Messung des Massequerstromes Zwischem Parallelen Teilkanälen," Reaktor Tagung, Deutsches Atomforum (Bonn), Paper 136, 1972.

13 Stiefel, U., and Nöthiger, H., "Cross-Flow between Subchannels. Results of Measurements Carried Out in the MEGAFRE-Rig," EIR Internal Report TM-IN-408, 1969.

14 Rowe, D. S., et al., "An Experimental Study of Flow and Pressure, in Rod Bundle Subchannels Containing Blockages," BNWL-1771, 1971.

15 Creer, J. M., et al., *Nucl. Eng. and Design*, Vol. 52, 1979, pp. 15–33.

16 Vegter, B. J., et al., "Measurement of Velocities Downstream of a Blocked Subchannel in a Model Reactor Rod Bundle," Westinghouse Research Laboratories, Report No. 74-8E9-RODS-R1, 1974.

17 Trippe, G., and Weinberg, D., "Investigation of Turbulent Velocity and Mass Flow Distribution in Rod Bundles with Grid-Type Spacers," NUREG-CP-0014, Vol. III, 1980, pp. 2189–2203.

18 Hochreiter, L. E., et al., "PWR Flecht Seaset 21-Rod Bundle Flow Blockage Task, Task Plan Report," NUREG-CR-1370, 1980.

19 Tapucu, A., Gençay, S., and Troche, N., "Experimental Study of the Diversion Cross-Flow Caused by Subchannel Blockages, Part I: Single Phase Flow," EPRI NP-3459, Vol. 1, 1984.

Downloaded 02 Jun 2010 to 171.66.16.91. Redistribution subject to ASME license or copyright; see http://www.asme.org/terms/Terms_Use.cfm

Experimental Study of the Diversion Crossflow Caused by Subchannel Blockages.

Part II: Pressures in the Channels and the Comparison of the COBRA III-C Predictions With Experimental Data[1]

A. Tapucu
Institut de génie nucléaire,
Ecole Polytechique de Montreal,
Montreal, Canada

S. Gençay
Institute for Nuclear Energy,
Technical University of Istanbul,
Istanbul, Turkey

N. Troche
Institut de génie nucléaire,
Ecole Polytechnique de Montreal,
Montreal, Canada

M. Merilo
Electric Power Research,
Institute, Palo Alto, Calif.

In this research, the hydrodynamic behavior of two laterally interconnected channels with blockages in one of them has been studied experimentally. For blockages of different shapes and severities, the mass flow rates as well as the pressures in the channels upstream and downstream of the blockage were determined. The experiments were conducted on two square channels separated by an intermediate plate with slots of different geometric parameters. Two types of blockages have been considered: plate and smooth. The shape of the smooth blockage was a cosine. The experimental data on the mass flow rates and pressures in the channels have been compared with the predictions of the subchannel code COBRA-III-C. It is observed that COBRA-III-C may not be adequate to describe the hydrodynamic behavior of two-interconnected channels with plate type blockages much higher than 30 percent severity in one of the channels. The limit of applicability of the code in the case of smooth blockages can be safely extended up to 60 percent severity.

1 Introduction

The purpose of the present research is to investigate the diversion crossflow between two laterally interconnected square channels when one of them was partially or completely blocked. The experimental apparatus, the experimental procedures as well as the experimental results obtained on the mass flow rates in the unblocked channel upstream and downstream of the blockage have been reported in the previous paper [1]. Experiments were conducted under adiabatic conditions and water at 20°C was used for working fluid. In the present paper, the experimental results on the pressures in the channels are presented and the predictions of the subchannel code COBRA-III-C are compared with the data on mass flow rates and pressures.

2 Experimental Results on Pressures

The way in which the axial pressures in the channels and the pressure difference between them are measured is outlined in reference [1]. As typical examples, Figs. 1(*a*) and 2(*a*) give the axial pressures in the blocked and unblocked channels for plate blockages with different severities. The corresponding mass flow rates in the unblocked channel can be found in reference [1]. Other examples on the axial pressures are also given in the section where the COBRA-III-C predictions are compared with experimental data. In turn, Figs. 1(*b*) and 2(*b*) show the pressure differences between the channels upstream and downstream of the blockage. According to the manufacturer specifications, the accuracy of the pressure transducers used in the present research is ±2 percent of the reading. All data related to the pressures are given in reference [2].

The pressures upstream of the blockage in the blocked and unblocked channels are equal and decrease linearly up to the point of onset of diversion cross-flow caused by the blockage. Starting from this point, the pressure increases in the blocked channel and decreases substantially in the unblocked channel due to the strong diversion cross-flow from the blocked channel to the unblocked channel. Immediately downstream of the blockage, the pressure in the blocked channel assumes its lowest value; in the unblocked channel, in general, it continues to drop slightly. Depending on the blockage fraction, the pressure recovery in the blocked channel is accomplished over a distance between 3 cm and 18 cm downstream of the blockage. Longer recovery distances are requried with increasing blockage severity. The pressure recovery in the blocked channel is usually substantial. Some pressure recovery has also been observed in the unblocked

[1]The work reported herein was funded by the Electric Power Research Institute, Palo Alto, Calif.

Contributed by the Fluids Engineering Division for publication in the JOURNAL OF FLUIDS ENGINEERING. Manuscript received by the Fluids Engineering Division, November 11, 1983.

Copyright © 1984 by ASME

Downloaded 02 Jun 2010 to 171.66.16.91. Redistribution subject to ASME license or copyright; see http://www.asme.org/terms/Terms_Use.cfm

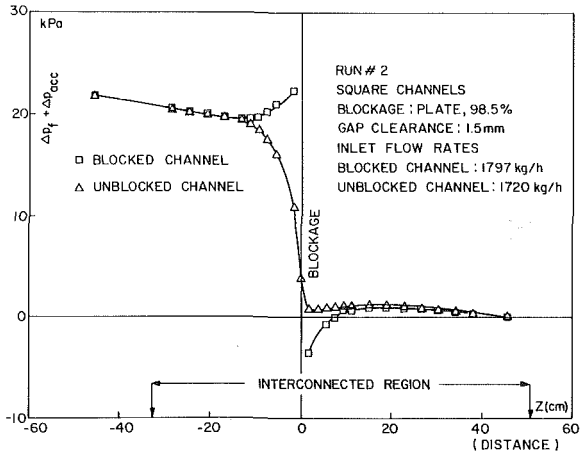

Fig. 1(*a*) Axial pressures in the blocked and unblocked channel. (Standard error in the pressures: ±2%)

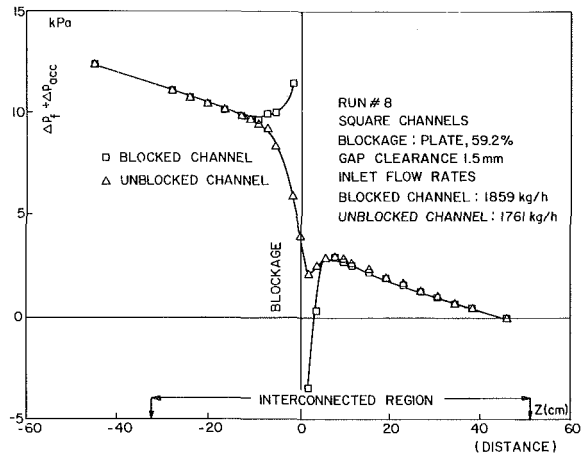

Fig. 2(*a*) Axial pressures in the blocked and unblocked channel. (Standard error in the pressures: ±2%)

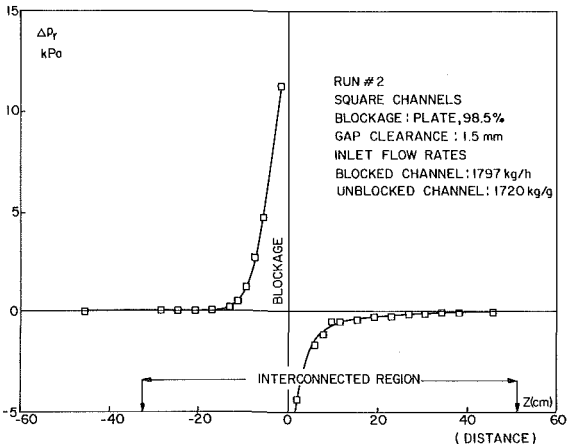

Fig. 1(*b*) Pressure differences between the blocked and unblocked channels. (Standard error in the pressures: ±2%)

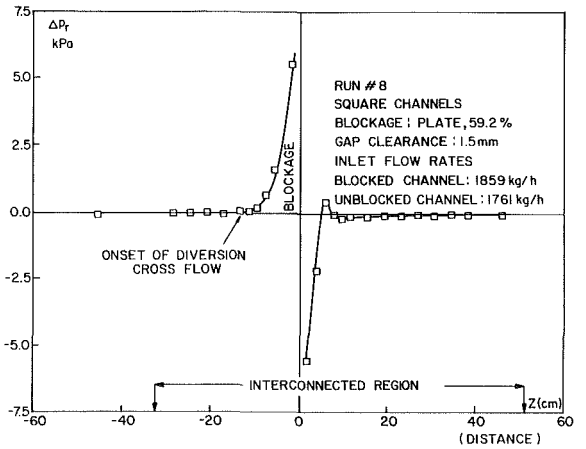

Fig. 2(*b*) Pressure differences between the blocked and unblocked channels. (Standard error in the pressures: ±2%)

channel. Pressure equalization between the two channels is a fairly rapid process, except for high blockage rates. At the point where the pressures in the channels are very close to each other, the mass flow rates in the channels are substantially different. Since the driving force of the diversion crossflow is the pressure difference between the channels, under the present conditions, this flow is quite small and low radial velocities prevail in the gap region. This is the reason why the recovery of the diverted flow by the blocked channel is quite a slow process as pointed out in reference [1].

In the upstream region, far from the blockage, the pressure difference between the channels is practically zero. Starting from the point of onset of diversion crossflow (Fig. 2(*b*)), the pressure difference between the channels increase rapidly in favor of the blocked channel driving some or all of the flow to the unblocked channel, depending on the blockage severity.

Nomenclature

A, a = flow area, m^2
C = thermal conduction coefficient, kJ/ms°K
D, d_h = hydraulic diameter, m
F = friction and form pressure loss due to crossflow, $F = [K|w|w/2s^2\rho]s/l$
K = spacer loss coefficient
K_{ij} = crossflow resistance coefficient
T = temperature, °C
Z = distance from blockage, m or cm
f = friction factor
f_r = turbulent momentum factor
g = acceleration of gravity, m/s^2
h = enthalpy, kJ/kg
h^* = enthalpy carried by diversion crossflow, kJ/kg
l = distance between subchannels, m
m = mass flow rate, kg/s
p = pressure, N/m^2
q' = heat addition per unit length, Watt/m
s = rod spacing or gap clearance, m
t = time, s
u = effective momentum velocity, m/s
u^* = effective velocity carried by diversion crosflow, m/s
v = specific volume, m^3/kg
v' = effective specific volume for momentum $(1 - x)^2/\rho_f (1 - \alpha) + x^2/\rho_g \alpha$, m^3/kg
w = diversion crossflow, kg/ms
w' = turbulent crossflow between adjacent subchannels, kg/ms
ϕ = two-phase multiplier
ψ = slip correction for energy transport, kg/m^3
ρ = specific mass, kg/m^3
Δp_f = frictional pressure loss, N/m^2
Δp_{acc} = acceleration pressure loss, N/m^2

Downloaded 02 Jun 2010 to 171.66.16.91. Redistribution subject to ASME license or copyright; see http://www.asme.org/terms/Terms_Use.cfm

Downstream of the blockage, this trend reverses and high pressures prevail in the unblocked channel gradually driving the diverted flow back to the blocked channel. A rapid drop in the pressure difference between the channels is observed immediately downstream of the blockage. This drop is followed by a gradual approach to zero for high blockages fractions (Fig. 1(*b*)) or by a pressure overshoot for blockages of 60 percent or less. During the overshoot, the pressure in the blocked channel becomes high over a short distance; subsequently, the pressure difference between the channels gradually approaches zero (Fig. 2(*b*)).

3 Comparison of COBRA-III-C Predictions With Experimental Data

In the recent years, a great deal of effort has been devoted to the suchannel type of computer codes which give more detailed information on the thermal-hydraulic behavior of the rod bundle than the bundle average approach. In these codes, as their name indicates, the cross-sectional area of the rod bundle is divided into smaller sections called "subchannels." Using, generally, a lumped parameter approach, the equations of mass, momentum and energy are written for each channel and solved numerically taking into account interchannel interactions such as mixing and diversion cross-flow. The end product is a map of pressures, mass flow rates, enthalpies, etc., throughout the rod bundle. Several subchannel codes have been quoted in the open literature [3–10]. However, only a limited number are easily acessible. Once the subchannel codes are developed, they should be checked against experimental data. In this section, the experimental data obtained on two laterally interconnected subchannels with blockages in one of them will be compared with the predictions of the COBRA subchannel code. Among the versions of COBRA codes, COBRA-III-C [3] has been chosen for comparison purposes. COBRA-III-C is similar to COBRA-IV [4] except that the latter can handle a wider range of thermal-hydraulic problems.

The COBRA-III-C and COBRA-IV computer programs compute the flow and enthalpy in the subchannels of a nuclear fuel rod bundle during both steady and transient conditions; they can also handle the situation where one or several subchannels are partially blocked. In these programs, the cross-section of the rod bundle is divided into discrete flow subchannels. The equations of continuity, momentum and energy are then derived for each subchannel by taking into account the cross-flow and turbulent mixing. These equations for COBRA-III-C have the following form.

Continuity equation:

$$A_i \frac{\partial \rho_i}{\partial t} + \frac{\partial m_i}{\partial x} = -\sum_{j=1}^{N} w_{ij}; \quad i = 1,2, \ldots N \tag{7}$$

Energy equation:

$$\frac{1}{u_i''}\frac{\partial h_i}{\partial t} + \frac{\partial h_i}{\partial x} = \frac{q_i'}{m_i} - \sum_{j=1}^{N} (T_i - T_j)\frac{C_{ij}}{m_i} - \sum_{j=1}^{N} (h_i - h_j)\frac{w_{ij}'}{m_i} + \sum_{j=1}^{N} (h_i - h^*)\frac{w_{ij}}{m_i} \tag{8}$$

where an effective enthalpy transport velocity is defined as:

$$u_i'' = \frac{m}{A\left[\rho - h_{fg} - \frac{\psi}{h}\right]}$$

For single phase flow and for homogeneous flow, $u''_i = u_i$.

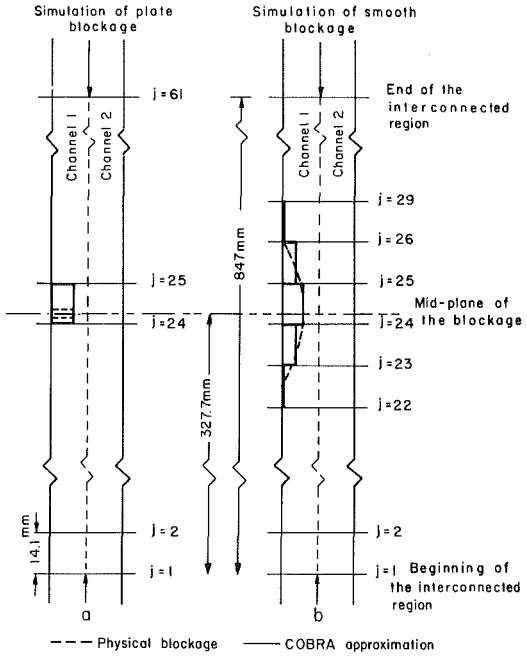

Fig. 3 Subchannel area reduction to model blockages

Axial momentum equation:

$$\frac{1}{A_i}\frac{\partial m_i}{\partial t} - 2u_i\frac{\partial \rho_i}{\partial t} + \frac{\partial P_i}{\partial x} = -\left(\frac{m_i}{A_i}\right)^2\left[\frac{v_i f_i \phi_i}{2D_i} + \frac{K_i v_i'}{2\Delta x} + A_i\frac{\partial}{\partial x}\left(\frac{v_i'}{A_i}\right)\right] - f_T\sum_{j=1}^{N}(u_i - u_j)\frac{w_{ij}'}{A_i} + \sum_{j=1}^{N}(2u_i - u^*)\frac{w_{ij}}{A_i} - g\rho_i\cos\theta \tag{9}$$

Transverse momentum equation:

$$\frac{\partial w_{ij}}{\partial t} + \frac{\partial (u^* w_{ij})}{\partial x} = \frac{s}{l}(p_i - p_j) - F_{ij} \tag{10}$$

The assumptions made in the formulation of these equations are summarized in [11], and their derivation can be found in [3]. One of the major deficiencies of equation (10) is the lack of a term representing the convective contribution of the transverse momentum due to the transverse velocity. A good review of transverse momentum equations used in various computer programs is given by Sha [9]. This same author also pointed out that in subchannel analysis, the transverse momenum equation cannot be treated with the same rigor as the axial momentum equation, because of the subchannel arrangement. Furthermore, approximations must be used to interface information between two different control volumes, i.e. one for the transverse momentum equation and another for the axial momentum equation., These basic limitations are inherent; therefore, the validity of subchannel analysis in situations with large flow disturbances poses serious concern. The following comparison should give a good idea of the limits of applicability of COBRA-III-C to flow blockages.

To solve the above system of equations, the constitutive equations for the axial friction factor and for the turbulent mixing should be specified. In addition to these constitutive equations, the cross-flow resistance (K_{ij}), the crossflow momentum parameter (s/l: s is the gap clearance of the interconnected region and l is the distance between the subchannels over which the lateral acceleration occurs; l is usually taken equal to the centroid-to-centroid distance of the subchannels) and finally, the blockage pressure loss coefficient (K) are to be specified. Also, the method of assigning the axial

Downloaded 02 Jun 2010 to 171.66.16.91. Redistribution subject to ASME license or copyright; see http://www.asme.org/terms/Terms_Use.cfm

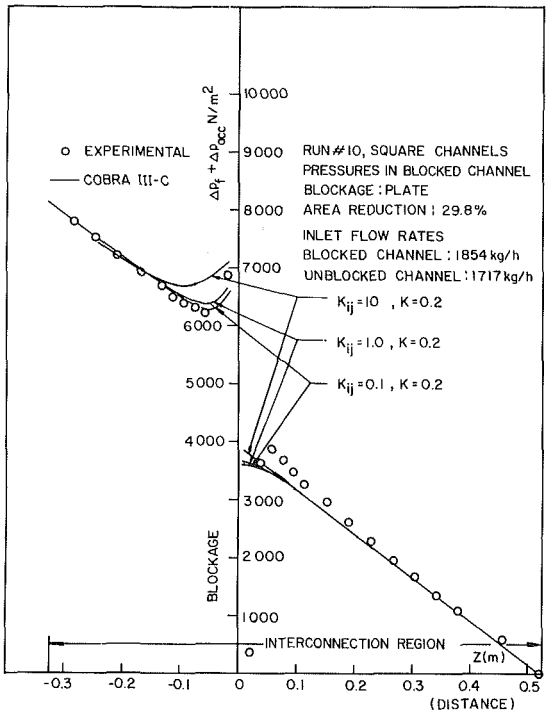

Fig. 4(*a*) Comparison of COBRA-III-C predictions with experimental data. (Standard error in each data point: ±2%)

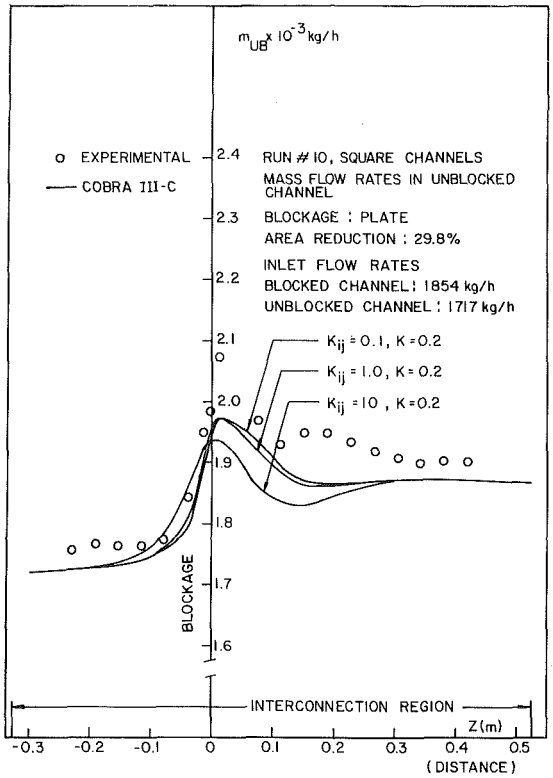

Fig. 4(*c*) Comparison of COBRA-III-C predictions with experimental data. (Standard error in each data point: ±2%)

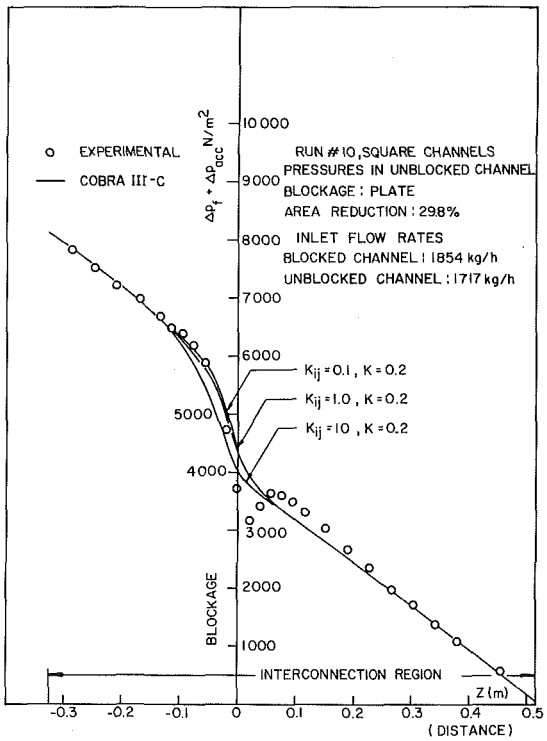

Fig. 4(*b*) Comparison of COBRA-III-C predictions with experimental data. (Standard error in each data point: ±2%)

velocity component of the crossflow must be decided. In the present comparison, the effective axial velocity (u^*) of the crossflow is taken equal to the arithmetic mean of the velocities in the interconnected channels (i.e., $u^* = (u_i + u_j)/2$).

Both the plate and smooth blockages were modeled using a combination of area reduction and pressure loss coefficients. The approximations of the physical blockages are shown in Fig. 3. The interconnected region is divided into 60 nodes starting from the beginning of this region. The length of each node is 14.1 mm. The plate blockage falls into the 24th node and its thickness (3.22 mm) is less than the length of the node (Fig. 3(*a*)). In the COBRA code, the thickness of the blockage should be set at least equal to the length of one node; this means that for modeling purposes, the plate blockage 3.22 mm thick would be replaced by a blockage 14.1 mm thick. In order to get close to the real thickness of the blockage, the node number has been increased three fold. Slight changes have been observed in the calculated pressures. However, for large node numbers, the calculated mass flow rates in the unblocked channel were less satisfactory than those calculated with a small number of nodes. Consequently, in the comparison of COBRA predictions with experimental data, the number of nodes has been fixed at 60. As sketched in Fig. 3(*b*), the smooth blockage occupies several nodes and its mid-plane which falls within 24th node does not coincide with the mid-plane of this node. In each interval, the continuously varying blockage fraction is replaced by an average step blockage. Therefore for code modeling purposes, the smooth blockage is represented by successive step changes as illustrated in Fig. 3(*b*).

For selected runs, Figs. 4(*a*), (*b*), (*c*) through 6(*a*), (*b*), (*c*) give the comparison of COBRA-III-C predictions with experimental data on pressures in the blocked and unblocked channels and mass flow rates in the unblocked channel. Three main code parameters which have been considered in the comparison are: the transverse momentum factor (s/l), the diversion cross-flow resistance, (K_{ij}), and the irrecoverable pressure loss coefficient of the blockage (K). As reported by Tapucu and Troche [12], a sensitivity test conducted on s/l, for a constant K_{ij}, has shown that the results of the COBRA calculations are quite insensitive to variations in this factor. Consequently, in the present comparison, a single value of s/l

Downloaded 02 Jun 2010 to 171.66.16.91. Redistribution subject to ASME license or copyright; see http://www.asme.org/terms/Terms_Use.cfm

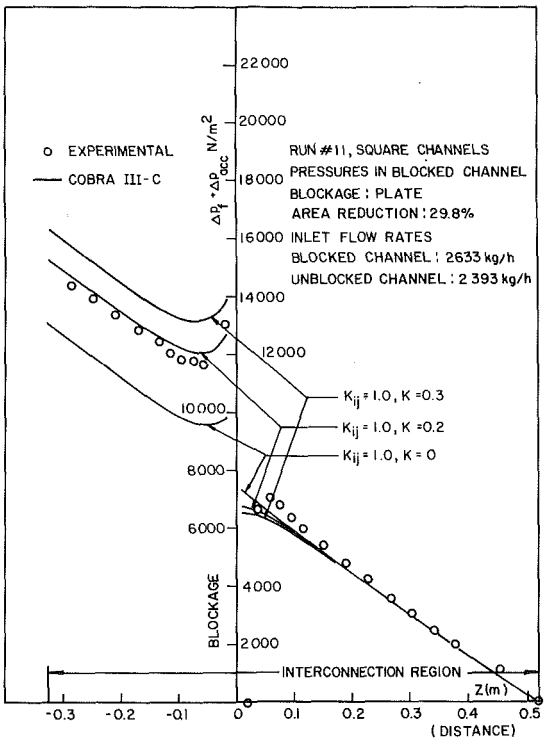

Fig. 5(*a*) Comparison of COBRA-III-C predictions with experimental data. (Standard error in each data point: ±2%)

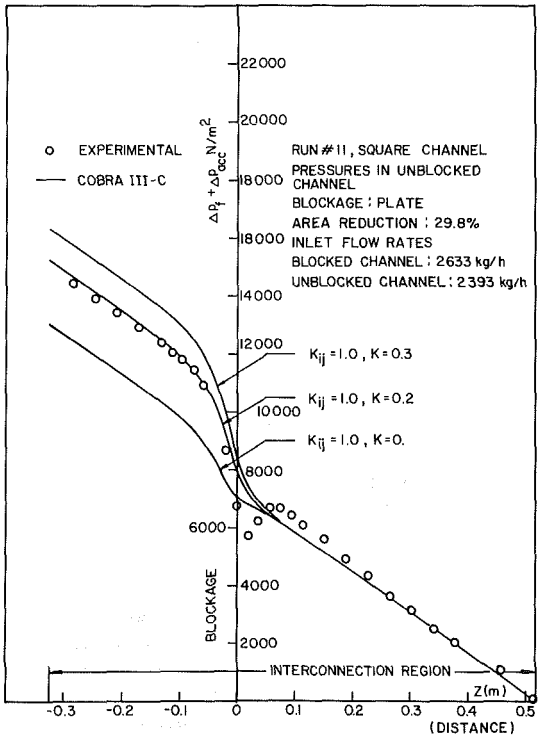

Fig. 5(*b*) Comparison of COBRA-III-C predictions with experimental data. (Standard error in each data point: ±2%)

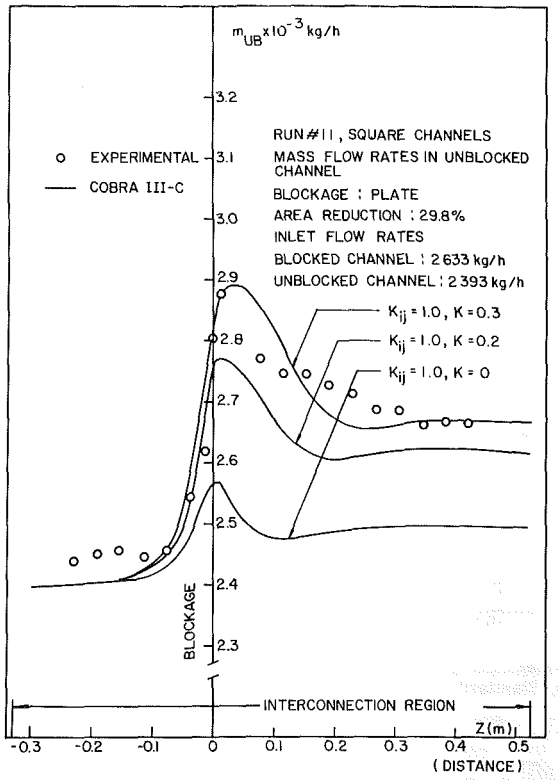

Fig. 5(c) Comparison of COBRA-III-C predictions with experimental data. (Standard error in each data point: ±2%)

(= 0.1) obtained by dividing the gap clearance by the centroid-to-centroid distance between the channels has been used.

Figures 4(*a*), (*b*), (*c*) compares the COBRA predictions with experimental data for 29.8 percent plate blockage. In this comparison, the pressure loss coefficient of the blockage was taken as 0.2 and the transverse resistance coefficient was given values of 0.1, 1 and 10. For pressures, the effect of varying K_{ij} from 0.1 to 10 was felt only in the vicinity of the blockage (~ 10 cm upstream, ~ 5 cm downstream). Increasing K_{ij} from 0.1 to 1 does not affect either the prediction of pressures nor the prediction of mass flow rates in the channels. Some effect on mass flow rates has been observed when K_{ij} went from 1 to 10. With a K_{ij} between 0.1 and 1, the prediction of pressures in the region upstream of the blockage is quite satisfactory. However, a good agreement between the predictions and the data has only been obtained for downstream regions farther than 20 cm from the blockage. This is quite understandable: first of all, immediately downstream of the blockage the assumption of small cross flows in the transverse direction made in the formulation of the COBRA code is no longer valid. Secondly, the same code does not take into consideration the recirculating zone which develops downstream of the blockage. For regions farther than 20 cm, the lateral flows are quite small and the flow conditions in the channels are close to those for which the COBRA code was written. Consequently, better agreement has resulted between the pressure data and COBRA predictions. In conclusion, with K_{ij} = 0.1 (or 1) and K = 0.2, the agreement between the predictions and the data is satisfactory. In Figs. 5(*a*), (*b*), (*c*) for the same blockage fraction but different interconnected region inlet flow rates, the effect of varying the pressure loss coefficient (for a constant value of K_{ij} (= 1)) is illustrated. As one would expect, the code is very sensitive to variations in the K-coefficient. The best prediction of pressures is achieved for K = 0.2. However, the best prediction for mass flow rates is obtained for K = 0.3. These values compare very well with those determined experimentally in reference [2]: 0.18 ± 0.006 under single channel flow conditions and 0.30 ± 0.011 under two interconnected channel flow conditions. The predictions of COBRA-III-C for plate blockages of 60 percent or higher were not satisfactory.

Figures 6(*a*, *b*, *c*) illustrate the comparison of the COBRA-prediction with the experimental data obtained on 58.6

Downloaded 02 Jun 2010 to 171.66.16.91. Redistribution subject to ASME license or copyright; see http://www.asme.org/terms/Terms_Use.cfm

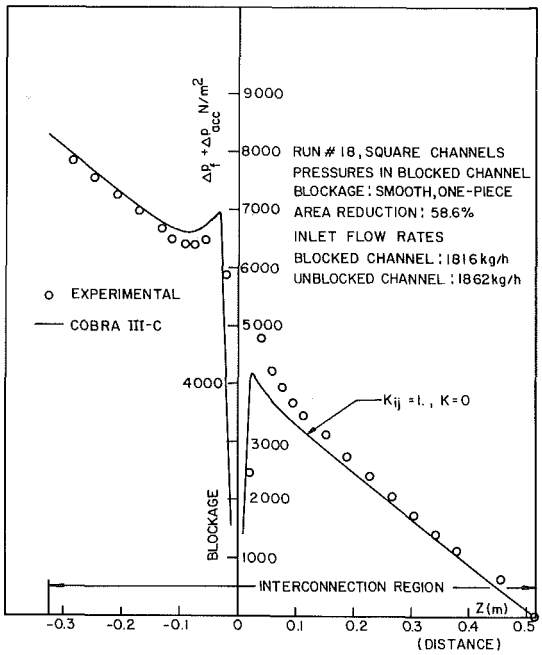

Fig. 6(a) Comparison of COBRA-III-C predictions with experimental data. (Standard error in each data point: ±2%)

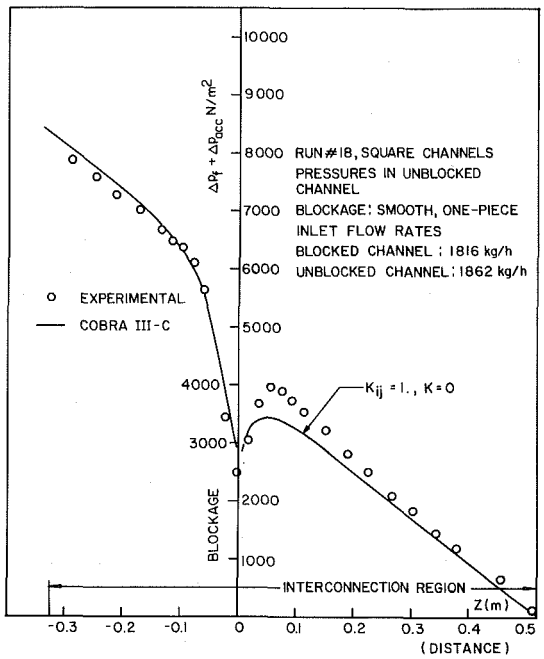

Fig. 6(b) Comparison of COBRA-III-C predictions with experimental data. (Standard error in each data point: ±2%)

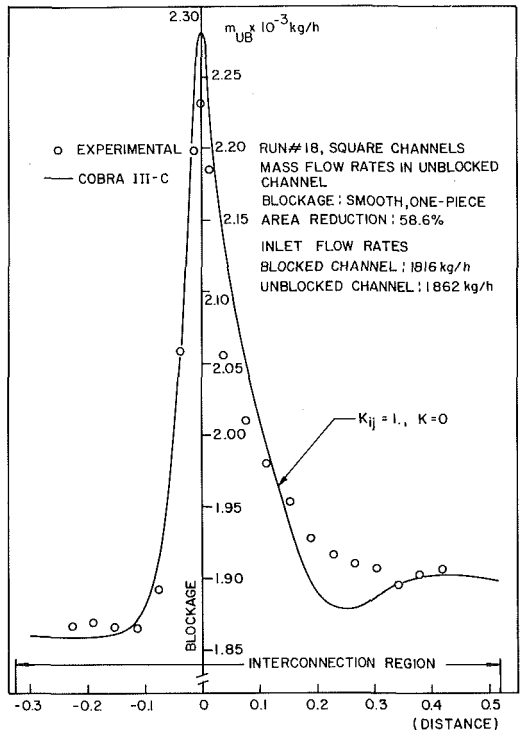

Fig. 6(c) Comparison of COBRA-III-C predictions with experimental data. (Standard error in each data point: ±2%)

percent one-piece smooth blockage. Very reasonable agreement has been observed between the predictions and experimental data for $K_{ij} = 1$ and $K = 0$. As a matter of fact, the K-coefficients determined experimentally under the single and two channel flow conditions are also very close to zero: 0.03 and 0.08, respectively (reference [2]). It may be concluded that the use of COBRA-III-C in the case of smooth blockages can be safely extended up to blockages of 60 percent.

5 Conclusions

In this research, the hydrodynamic behavior of two laterally interconnected channels with blockages in one of them has been studied experimentally. For blockages of different shapes and severities, the mass flow rates as well as the pressures in the channels upstream and downstream of the blockage were determined. The experiments were conducted on two-square channels separated by an intermediate plate in which slots are machined with different geometric parameters. Two types of blockages have been considered: plate and smooth. The shape of the smooth blockage was a cosine. The experimental data have been compared with the predictions of the subchannel code COBRA-III-C to ascertain how well they can be predicted. The following conclusions can be drawn from the investigation.

1. Except for high blockage fractions, the pressure equalization of the channels is a fairly rapid process.
2. For plate blockages, at the point where the pressures in the channels become almost equal, the mass flow rates are substantially different.
3. Since the driving force of the diversion cross-flow is the pressure difference between the channels, it follows from conclusion 1 that the lateral flow is quite small. This is the reason why the recovery of the diverted flow by the blocked channel is a slow process.
4. The COBRA-III-C subchannel code predicts the data on 30 percent – plate blockage fairly well. However, it fails to predict the data on plate blockage of 60 percent or higher severity. For 60 percent – smooth blockage, very reasonable agreement is obtained between COBRA predictions and experimental data.
5. From the above observation, it may be concluded that COBRA-III-C may not be adequate to describe the hydrodynamic behavior of two-interconnected channels with plate type blockages much higher than 30 percent severity in one of the channels. The limit of applicability in the case of smooth blockages can be extended up to 60 percent severity.
6. Improvement of the transverse momentum equation by adding the terms representing the convective contribution of the transverse momentum due to transverse velocity and the shear stress generated by the axial gradient of the transverse

Downloaded 02 Jun 2010 to 171.66.16.91. Redistribution subject to ASME license or copyright; see http://www.asme.org/terms/Terms_Use.cfm

velocity, and appropriate modeling of the recirculating zone behind the blockage should improve predictions of the subchannel codes and extend their range of applicability.

References

1 Gençay, S., Tapucu, A., Troche, N. and Merilo, M., "Experimental Study of the Diversion Cross-Flow Caused by Subchannel Blockages—Part I: Experimental Procedures and Mass Flow Rates in the Channel," published in this issue pp. 435–440.

2 Tapucu, A., Gençay, S., and Troche, N., "Experimental Study of the Diversion Cross-Flow Caused by Subchannel Blockages—Part I: Single Phase Flow," EPRI NP-3459, Vol. 1, 1984.

3 Rowe, D. W., "A Digital Computer Program for Steady State and Transient Thermal Analyiss of Rod Bundle Nuclear Fuel Elements," BNWL-1695, 1973.

4 Stewart, C. W., et al., "COBRA-IV: The Model and the Method," BNWL-2214, 1977.

5 Fajeau, M., "Etude thermodynamique d'un reacteur ou d'une boucle thermique," CEA-R-3716, 1969.

6 Bowring, R. W., "HAMBO: A Computer Program of the Subchannel Analysis of the Hydraulic and Burnout Characteristics of Rod Cluster—Part 1: General Description," AEEEW-R254, 1967. "Part 2: The Equations," AEEW-R582, 1968, UKAEA, Winfrith.

7 Sha, W. T., Schmitt, R. C., and Lin, E. I. H., "THI 3D-1: A Computer Program for Steady-State Thermal-Hydraulic Multichannel Analysis," ANL-77-15, 1977.

8 Hirad, S., and Nakao, N., "DIANA—A Fast and High Capacity Computer Code for Interchannel Coolant Mixing in Rod Array," *Nucl. Eng. Design*, Vol. 30, 1974, pp. 214–222.

9 Sha, W. T., *Nucl. Eng. Design*, Vol. 62, 1980, pp. 214–222.

10 Aly, A. M., and Ahmad, S. Y., "SAGA-II: A Computer Program for Subchannel Analysis of Two-Phase Flow in Two Interconnected Channels," ASME, 79-QA/HT-64, 1980.

11 Wheeler, C. L., et al., "COBRA-IV: An Interim Version of COBRA for Thermal-Hydraulic Analysis of Rod Bundle Nuclear Fuel Elements and Cores," BNWL-1962, 1976.

12 Tapucu, A., and Troche, N., "Comparison of Subchannel Code COBRA-III-C with Experimental Data Obtained on Two Laterally Interconnected Flows," *Proceeding of the Ninth Simulation Symposium on Reactor Dynamics and Plant Control*, AECL-TDAI-295, April, 1982.

Downloaded 02 Jun 2010 to 171.66.16.91. Redistribution subject to ASME license or copyright; see http://www.asme.org/terms/Terms_Use.cfm

C. P. Liou
Senior Staff Engineer,
Stoner Associates, Inc.
Carlisle, Pa. 17013

E. B. Wylie
Professor,
Civil Engineering Department,
The University of Michigan,
Ann Arbor, MI 48109
Fellow ASME

One Dimensional Gas Flow With Internal Heating

This paper presents a comparison of two solutions, a numerical and an analytic, to an idealized problem of frictionless transient gas flow driven by internal heating. The purpose of such a comparison is to provide a check on a general method for transient gas flow in pipelines with friction and heat transfer. The numerical solution to this problem is formulated based on the method of characteristics with specified time intervals. To avoid interpolation for integration along the characteristics, a multiplier is introduced to the acceleration term in the equation of motion. Favorable comparisons of pressure and density time histories are obtained.

Introduction

This paper presents a comparison of a numerical solution and an analytical solution to the following transient gas flow problem. Consider a horizontal frictionless pipe with one end closed and one end open to atmosphere. Initially, the gas inside the pipe is at rest. How do the pressure, velocity, and mass density of the gas at various locations respond to a sudden uniform internal heating?

The purpose of such a comparison is to provide an initial check for a numerical method by Wylie and Streeter [1] for transient gas flows in pipelines with friction and heat transfer.

The basic equations for this idealized problem are developed and transformed into the characteristics form for numerical integration. A favorable comparison between the numerical solution and the analytical solution is obtained.

Basic Equations

The continuity equation, the equation of motion, and the energy equation govern the transient flow in the problem under consideration. They are [1]

$$\frac{D\rho}{Dt}+\rho\frac{\partial V}{\partial x}=0 \tag{1}$$

$$\rho\frac{DV}{Dt}+\frac{\partial P}{\partial x}=0 \tag{2}$$

and

$$\rho C_P\frac{DT}{Dt}-\frac{DP}{Dt}-\rho q=0. \tag{3}$$

All symbols are defined in the nomenclature. The total derivative of a variable following the fluid is given by $D(\ )/Dt$.

In order for an analytical solution to be found, the heat generation rate per unit mass, q, in equation (3) is specified such that

$$\frac{q}{\rho\dfrac{\partial h}{\partial\rho}}=a \tag{4}$$

where a is a constant with a value of $-1\ \mathrm{s}^{-1}$.

Assuming ideal gas, the equation of state is

$$P=\rho RT. \tag{5}$$

Using equations (4) and (5), it can be shown that

$$q=-aC_PT \tag{6}$$

and thus, the energy equation assumes the following form for the present problem

$$\rho C_P\frac{DT}{Dt}-\frac{DP}{Dt}+a\rho C_PT=0. \tag{7}$$

In the numerical solution procedure, pressure, velocity, and temperature are chosen to be the dependent variables. The mass density derivative in equation (1) can be replaced by pressure and temperature derivatives via the equation of state as

$$\frac{DT}{Dt}-\frac{T}{P}\frac{DP}{Dt}-T\frac{\partial V}{\partial x}=0. \tag{8}$$

One can eliminate the temperature derivative terms in equations (7) and (8) to obtain

$$\frac{DP}{Dt}+\rho C^2\frac{\partial V}{\partial x}+a\rho C^2=0 \tag{9}$$

in which

$$C^2=\frac{1}{\dfrac{\rho}{P}-\dfrac{1}{TC_P}}. \tag{10}$$

It can easily be shown that for ideal gas

$$C^2=\frac{\gamma P}{\rho} \tag{11}$$

which is the square of the isentropic acoustic wavespeed.

Contributed by the Fluids Engineering Division of THE AMERICAN SOCIETY OF MECHANICAL ENGINEERS *and presented at the Fluids Engineering Conference, Houston, Texas, June 1983. Manuscript received by the Fluids Engineering Division, July 21, 1983.*

Copyright © 1984 by ASME

Downloaded 02 Jun 2010 to 171.66.16.91. Redistribution subject to ASME license or copyright; see http://www.asme.org/terms/Terms_Use.cfm

It is observed that equations (2) and (9) form a set of hyperbolic equations with variable coefficients. They describe wave propagation in a fluid with temperature and pressure dependent properties.

Method of Characteristics

The characteristics method is based on the physical fact that disturbances to the fluid propagate only in discrete directions in a distance versus time, or x-t plane. Along these directions in the x-t plane, called characteristics, the solution to the partial differential equation is reduced to integrating a set of ordinary differential equations. There are two common ways to implement the characteristics method: the characteristic grid method and the method of specified time intervals [2]. The latter, with a slight modification, is used for the present problem.

The method of specified time intervals involves interpolations when the coefficients in the partial differential equations are variable. To avoid such interpolations, a multiplier α^2 is introduced to the acceleration term in the equation of motion [1].

$$\rho\alpha^2 \frac{DV}{Dt} + \frac{\partial P}{\partial x} = 0. \tag{12}$$

Yow [3] first used such a multiplier and established the relationship between α and error bound in pressure based on steady oscillatory gas flow in a horizontal pipe. Yow's motive in using α was to increase the size of the timestep in the explicit solution procedure as well as to avoid interpolation.

Multiplying equation (12) by an unknown number λ and adding it to equation (9), one can write

$$\frac{\partial P}{\partial t} + \left(V + \frac{\lambda}{\rho\alpha^2}\right)\frac{\partial P}{\partial x} + \lambda\left[\frac{\partial V}{\partial t} + \left(V + \frac{\rho C^2}{\lambda}\right)\frac{\partial V}{\partial x}\right] + a\rho C^2 = 0. \tag{13}$$

Two distinct real values of λ can be found by requiring $\lambda/(\rho\alpha^2) = \rho C^2/\lambda$ to obtain

$$\lambda = \pm \rho C\alpha.$$

Equation (13) can now be written as a pair of total differential equations

$$\frac{dP}{dt} \pm \rho C\alpha \frac{dV}{dt} + a\rho C^2 = 0 \tag{14}$$

with the total derivatives defined along the two characteristic directions in the x-t plane

$$\frac{dx}{dt} = V \pm \frac{C}{\alpha} \tag{15}$$

Equation (15) represents C^+ and C^- characteristics along which the compatibility equations defined by equation (14) hold.

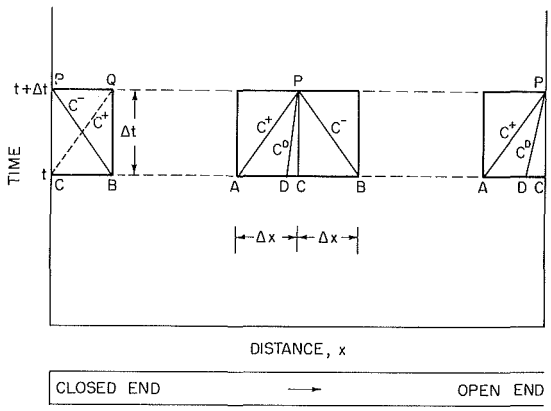

Fig. 1 Integration along the characteristics in the interior and at the boundaries

Numerical Integration

It was found more convenient to use P^2 and mass flux Q instead of P and V in the integration. Thus, along the C^+ characteristics, one can multiply the compatability equation by $2P$ and note that

$$dV = \frac{1}{\rho A}\left(dQ - \frac{Q}{\rho}d\rho\right) \tag{16}$$

to obtain

$$\frac{dP^2}{dt} + \frac{2PC\alpha}{A}\left(\frac{dQ}{dt} - \frac{Q}{\rho}\frac{d\rho}{dt}\right) + 2aP\rho C^2 = 0. \tag{17}$$

Similarly, along the C^- characteristics

$$\frac{dP^2}{dt} - \frac{2PC\alpha}{A}\left(\frac{dQ}{dt} - \frac{Q}{\rho}\frac{d\rho}{dt}\right) + 2aP\rho C^2 = 0. \tag{18}$$

Referring to Fig. 1, equations (17) and (18) are integrated along the C^+ and C^- characteristics as follows

$$C^+ : P_P{}^2 - P_A{}^2 + \frac{2C_{AP}\alpha}{A}\left(\frac{P_P + P_A}{2}\right)\left(Q_P - Q_A - \frac{Q_P + Q_A}{2}\ln\frac{\rho_P}{\rho_A}\right) + 2a\left(\frac{P_P + P_A}{2}\right)\rho_{AP}C^2{}_{AP}\Delta t = 0 \tag{19}$$

and

$$C^- : P_P{}^2 - P_B{}^2 - \frac{2C_{BP}\alpha}{A}\left(\frac{P_P + P_B}{2}\right)\left(Q_P - Q_B - \frac{Q_P + Q_B}{2}\ln\frac{\rho_P}{\rho_B}\right) + 2a\left(\frac{P_P + P_B}{2}\right)\rho_{BP}C^2{}_{BP}\Delta t = 0 \tag{20}$$

Nomenclature

a = a constant, s^{-1}
A = cross sectional area of pipe, ft^2
C = acoustic wavespeed, ft/s
C_p = specific heat at constant pressure, ft-lbf/slug-R
h = specific enthalpy of gas, ft-lb/slug
L = length of pipe, ft
q = heat generation rate per unit mass, ft-lbf/slug-s
P = pressure, psf
R = universal gas constant ft-lbf/lb mole R
T = temperature, R
t = time, s
V = velocity, ft/s
x = distance, ft
α = inertia multiplier, dimensionless
γ = specific heat ratio, dimensionless
Δt = timestep size, s
Δx = length of computational reach, ft
λ = multiplier, dimensionless
ρ = mass density, slugs/ft^3

Subscripts

0 = initial value
A,B,C,D,P,Q = positions shown in Fig. 1

Downloaded 02 Jun 2010 to 171.66.16.91. Redistribution subject to ASME license or copyright; see http://www.asme.org/terms/Terms_Use.cfm

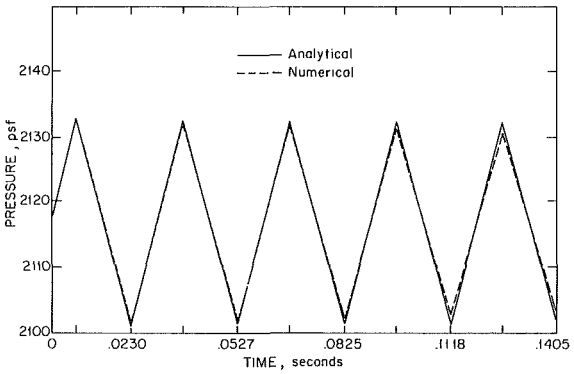

Fig. 2 Comparison of pressure at the closed end

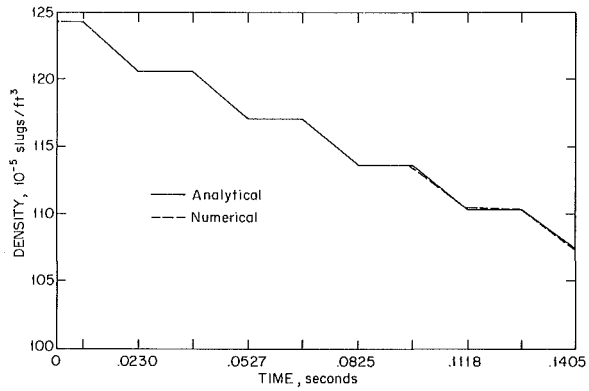

Fig. 3 Comparison of mass density at the closed end

where ρ_{AP}, ρ_{BP}, C_{AP} and C_{BP} are density and wavespeed evaluated based on reach average pressure and temperature.

The energy equation, equation (7) needs no transformation since it only involves total derives along the gas particle path line. Referring to Fig. 1, one can integrate it numerically as

$$C_P(T_P - T_D) - \frac{1}{\rho_{DP}}(P_P - P_D) + aC_P\left(\frac{T_P + T_D}{2}\right)\Delta t = 0. \quad (21)$$

Equations (19), (20), and (21) are solved simultaneously for P, Q, and T by the Newton Raphson method. All variables appearing in the coefficients are temporarily held constant during the Newton Raphson procedure but are subsequently iterated to convergence.

At the closed end of the pipe, Q_p equals zero since there is no flow. One can employ equations (20) and (21) to solve for pressure and temperature. At the open end where the pressure P_P is held at the constant ambient pressure P_0, one can use equations (19) and (21) to obtain flow and temperature.

The use of the multiplier α is best explained by referring to Fig. 1. At each time level, a timestep size is calculated according to the average velocity and acoustic wavespeed along the C^+ characteristics in the first reach connecting points C and Q

$$\Delta t = \frac{\Delta x}{V_{CQ} + C_{CQ}} \quad (22)$$

With the Δt so established, the parameter α is calculated for each of the C^+ and the C^- characteristics in all the reaches by

$$C^+ : \alpha = \frac{C_{AP}}{\frac{\Delta x}{\Delta t} - V_{AP}} \quad (23)$$

$$C^- : \alpha = \frac{C_{BP}}{\frac{\Delta x}{\Delta t} + V_{BP}} \quad (24)$$

It is seen that the slope of the characteristics is adjusted by α such that all characteristics intersect grid points. No interpolation is used in evaluating the compatibility equations along C^+ and C^-. At the same time, the CFL stability criterion is always satisfied.

Linear interpolation is used to obtain flow conditions at D for integrating the energy equation along the path line.

Analytical Solution

Spencer [4] presented an analytical solution to a symmetrical problem of the same internal heating but with constant pressure maintained at both ends. Due to symmetry, the velocity is zero at the middle section of the conduit and the flow condition in either half of the conduit is identical to that of the present problem.

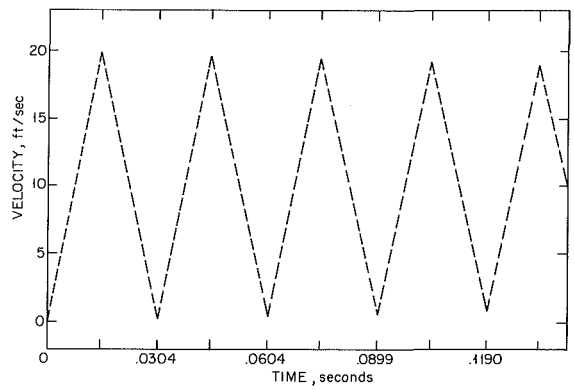

Fig. 4 Calculated velocity at the open end from the numerical method

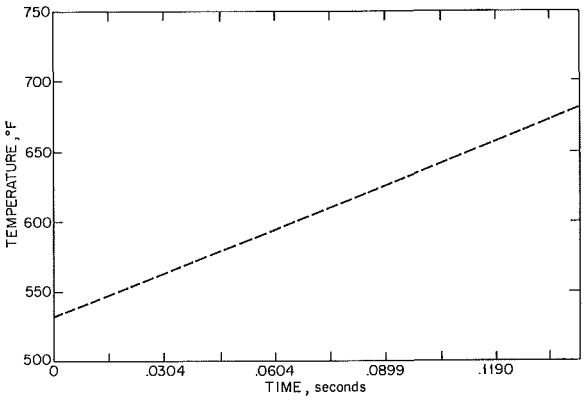

Fig. 5 Calculated temperature at the closed end from the numerical method

The expression for pressure and density are

$$P(x,t) = P_0 e^{y(x,t)} \quad (25)$$

and

$$\rho(x,t) = \frac{P(x,t)}{C_0^2} e^{-t} \quad (26)$$

where

$$y(x,t) = \frac{-2L}{\pi^2 C_0} \sum_{n=1}^{\infty}$$

Downloaded 02 Jun 2010 to 171.66.16.91. Redistribution subject to ASME license or copyright; see http://www.asme.org/terms/Terms_Use.cfm

$$\frac{[1-(-1)^n][Y_0(Z_0)J_0(Z)-J_0(Z_0)Y_0(Z)]}{n^2[Y_0(Z_0)J_1(Z_0)-Y_1(Z_0)J_0(Z_0)]}\sin\frac{n\pi x}{L}$$

$$Z=\frac{2n\pi}{L}C_0e^{t/2}$$

$$Z_0=\frac{2n\pi}{L}C_0$$

In the above, C_0 is the initial acoustic wavespeed, and J and Y are Bessel's functions of the first and the second kind. Convective acceleration is neglected in obtaining the analytical solution.

Comparison

The numerical solution is compared with the analytical solution for the case in which L = 10 ft (3.05 m), P_0 = 2116.8 psf absolute (101.35 KPa) and ρ_0 = 0.04 lbm/ft^3 (0.641 Kg/m^3). In the numerical solution, the pipe was divided into 20 reaches resulting in a Δx = 0.5 ft (0.15 m). In evaluating the analytical expression for pressure, one hundred terms were used for the infinite series for accuracy.

The calculated time history of pressure and density at the closed end are compared in Figs. 2 and 3. The timing of the pressure peaks compare well, while slight attenuation in magnitude can be noticed. The mass density comparison is satisfactory.

The velocity at the open end and the temperature at the closed end from the numerical solution are shown in Figs. 4 and 5. The same two parameters from the analytical solution are not directly available without numerical integration, and thus are not presented.

Conclusion

A comparison of the numerical and the analytical solutions to an idealized problem of transient frictionless gas flows due to internal heating is presented. The equations that describe the idealized problem represent a simplification of the more general dynamic equations that describe unsteady natural gas flow with friction and heat transfer. The numerical method for both problems is essentially the same, however. Therefore, it is postulated that the favorable comparison to the internal heating problem shown herein provides a valid, although indirect, check, of the numerical method utilized in the more general application [1], which analyzes transient gas flows including friction and heat transfer.

References

1 Wylie, E. B., and Streeter, V. L., "Computer Program to Simulate Natural Gas Flow in the Alaska Gas Pipeline," Final Report to Stoner Associates, Inc., Carlisle, Pennsylvania, Oct. 1978.

2 Wylie, E. B., and Streeter, V. L., *Fluid Transients*, FEB Press, Ann Arbor, MI, 1983, pp. 55–58.

3 Yow, W., "Numerical Error in Natural Gas Transient Calculations," ASME *Journal of Basic Engineering*, Vol. 94, No. 2, June, 1972, pp. 422–428.

4 Spencer, A. C., "Method of Characteristics For Solving Two-Dimensional Reactor Core Flows," Proc. ANS Top'l Mtg. Mathematical Models and Computational Techniques for Analysis of Nuclear Systems, Ann Arbor, Mich., April 9–11, 1973.

Downloaded 02 Jun 2010 to 171.66.16.91. Redistribution subject to ASME license or copyright; see http://www.asme.org/terms/Terms_Use.cfm

Critical Conditions and the Choking Mass Flow Rate in Nonequilibrium Wet Steam Flows

J. B. Young
Lecturer in Engineering,
Whittle Laboratory,
University of Cambridge,
Cambridge, England

A theoretical analysis of choking in steady, one-dimensional, nonequilibrium, wet steam flows is presented. It is shown that such a flow becomes choked when the vapor phase velocity attains the frozen speed of sound somewhere in the system. The upstream flow pattern cannot then be altered by small adjustments of the back pressure and the mass flow rate is close to, although not necessarily identical to, its maximum value. The equilibrium speed of sound has no physical relevance in such flows. In a choked converging nozzle the critical conditions always occur in the exit plane of the nozzle. In a converging-diverging nozzle, however, the shape of the diverging section influences the throat conditions and throughput. Comparison of the theory with the few experiments reported in the literature shows excellent agreement.

Introduction

The accurate calculation of the choking mass flow rate passed by a nozzle operating with wet steam of high quality is important in the design of steam turbines and in a variety of flow metering applications.

It is well known that when a wet steam mixture expands rapidly through a significant pressure ratio, departures from equilibrium occur [1]. *Thermal nonequilibrium* effects are characterized by the development of a temperature difference between the liquid and vapor phases, while *inertial nonequilibrium* manifests itself by the development of an interphase slip velocity. Both these phenomena affect the mass flowrate passed by a choked nozzle, but are generally ignored due to a lack of understanding of the physical processes involved. A further difficulty is the specification of the *critical conditions*. In single phase flow the velocity at the nozzle throat is equal to the local speed of sound, but in wet steam the equivalent is not obvious as the sound speed varies from an equilibrium to a frozen value depending on the frequency of the wave transmitted.

This paper addresses itself to the underlying physical principles of choked, nonequilibrium, wet-steam flows. The analysis is restricted to cases where the steam is wet at inlet to the nozzle and nucleation does not occur. Nucleating flows are more difficult to analyze and may involve unsteady effects if the nucleation occurs in the transonic region.

Few direct references to the subject can be found in the open literature. The passage of plane harmonic small disturbances through wet steam mixtures of high quality has been studied theoretically by Deich [2], Konorski [3] and Petr [4] and the latter has also considered the transmission of finite amplitude waves in both one and two dimensions [5]. The problem of extending this analysis to the case of choking in steady flows has been tackled by Konorski [6, 7], but his results are not presented in a form suitable for practical calculation and do not illuminate the physical principles involved. Bakhtar and Young [8] discuss the effect of nozzle angle of divergence on the throat velocity, but their results are completely numerical and there is no attempt to generalize the analysis.

In common with most wet steam work, experimental measurements are virtually nonexistent due to the difficulty of obtaining low velocity, spontaneously nucleated steam in the laboratory. Consequently the only measurements of mass flowrate in wet steam nozzles are those reported in [9] and [10].

Governing Equations

Wet steam is assumed to be a homogeneous mixture of vapor at pressure p and temperature T_g, and spherical water droplets of radius r. It is assumed that the liquid phase is monodispersed, but the analysis can easily be extended to polydispersed flows by employing suitable average values as described in [1].

Let there be n droplets per unit mass of mixture, each of mass m. The wetness fraction y is given by

$$y = nm \tag{1}$$

and, neglecting the volume of the liquid phase, the mixture density is

$$\rho = \frac{\rho_g}{x} \tag{2}$$

where ρ_g is the vapor density and $x = 1 - y$ is the dryness fraction.

Equations governing non-nucleating, wet-steam flows have

Contributed by the Fluids Engineering Division and presented at the Winter Annual Meeting, New Orleans, La., December 9–14, 1984 of THE AMERICAN SOCIETY OF MECHANICAL ENGINEERS. Manuscript received by the Fluids Engineering Division, November 29, 1982. Paper No. 84-WA/FE-12.

Copyright © 1984 by ASME

Downloaded 02 Jun 2010 to 171.66.16.91. Redistribution subject to ASME license or copyright; see http://www.asme.org/terms/Terms_Use.cfm

been derived elsewhere [11] and are presented below for the case of steady, inviscid, adiabatic, one-dimensional flow with area change.

The conservation of droplets is expressed by

$$\frac{d}{dz}(n\rho A V_l) = 0 \tag{3}$$

where A is the flow cross-sectional area and z is the distance measured in the flow direction.

The combined liquid and vapor continuity, momentum and energy equations can be written:

$$\frac{d}{dz}(W_g + W_l) = 0 \tag{4}$$

$$A\frac{dp}{dz} + \frac{d}{dz}(W_g V_g + W_l V_l) = 0 \tag{5}$$

$$\frac{d}{dz}\left[W_g\left(h_g + \frac{V_g^2}{2}\right) + W_l\left(h_l + \frac{V_l^2}{2}\right)\right] = 0 \tag{6}$$

where V is the velocity, h is the specific enthalpy and subscripts g and l refer to the vapor and liquid phases, respectively. W_g and W_l are the individual vapor and liquid mass flowrates given by

$$W_g = x\rho A V_g \tag{7}$$

$$W_l = y\rho A V_l \tag{8}$$

Neglecting the partial pressure of the droplets, the equation of state of the vapor phase can be expressed quite generally by

$$\frac{1}{\rho_g}\frac{d\rho_g}{dz} = \beta\frac{dp}{dz} - \alpha\frac{dT_g}{dz} \tag{9}$$

where α is the coefficient of thermal expansion and β is the isothermal compressibility. For a perfect gas (αT_g) and (βp) both equal unity, but any other convenient equation of state can be employed. That used for the calculations presented below is a truncated virial series which represents steam properties accurately for pressures below 100 bars. A description can be found in [12].

The transfer of mass, energy, and momentum between the phases has been discussed by many authorities and derivations of suitable equations describing these processes can be found in [11] and [12]. A reliable equation for the droplet growth rate (mass and energy transfer) is that due to Gyarmathy [11], which can be written

$$(h_g - h_l)nV_l\frac{dm}{dz} = \frac{xc_{pg}\Delta T}{\tau_T} \tag{10}$$

where c_{pg} is the isobaric specific heat capacity of the vapor and ΔT is the vapor supercooling $(T_s - T_g)$, T_s being the saturation temperature at the local pressure p. τ_T is the thermal relaxation time defined by

$$\tau_T = \frac{xc_{pg}r^2\rho_l(1 + 3.78\,\mathrm{Kn}/\mathrm{Pr}_g)}{3y\lambda_g}$$

where λ_g and Pr_g are the vapor phase thermal conductivity and Prandtl number, respectively, and Kn is the Knudsen number based on the droplet diameter. According to Gyarmathy, equation (10) is valid for pressures below 100 bar and for all values of Kn from the continuum to the free molecular regime. Note that the capillary supercooling of the droplet has been neglected, implying that the droplet temperature is equal to the local saturation value. This is a permissible approximation for $r > 0.01\ \mu$m.

The equation of motion for a droplet (momentum transfer) can be written

$$V_l\frac{dV_l}{dz} = \frac{\Delta V}{\tau_I} \tag{12}$$

where ΔV is the slip velocity $(V_g - V_l)$ and τ_I is an inertial relaxation time defined by

$$\tau_I = \frac{2r^2\rho_l[c(\mathrm{Re}) + 2.76\,\mathrm{Kn}]}{9\mu_g}$$

where μ_g is the dynamic viscosity of the vapor and c(Re) is a correction factor based on the slip Reynolds number. The form of this correction together with the assumptions underlying the derivation of (12) are discussed in [11].

Definition of the Critical Condition in Wet Steam

As shown in any text on elementary gas dynamics, an inviscid, adiabatic, one-dimensional compressible flow is considered to be choked when the flow velocity equals the speed of sound at the nozzle throat. The flow in the converging section is then insensitive to changes downstream of the throat and the mass flowrate remains fixed at a constant, maximum value. A physical explanation is that small disturbances propagate at the speed of sound and hence cannot pass upstream through the throat of the nozzle.

In translating these ideas to two-phase flow, various problems arise because the speed of a sound wave varies with the dispersion of the liquid phase and also with the frequency of the wave itself. As shown by Petr [4] two limiting cases can be identified. Very high frequency waves moving through a medium containing large droplets propagate at the *frozen* speed of sound,

$$a_f = (k_f p/\rho_g)^{1/2}, \tag{14}$$

where k_f is the isentropic exponent of the vapor phase alone. On the other hand, very low frequency waves moving through a medium containing small droplets propagate at the *equilibrium* speed of sound

$$a_e = (k_e p/\rho)^{1/2} \tag{15}$$

where k_e is the isentropic exponent for the mixture at

Nomenclature

A = flow cross-sectional area
a = speed of sound
c = specific heat capacity
h = specific enthalpy
k = isentropic exponent
L = latent enthalpy
M = Mach number
m = mass of a droplet
$\dot{m}$ = mass flowrate
n = number of droplets per unit mass of steam
p = pressure
r = droplet radius
s = specific entropy
T = temperature
ΔT = supercooling
V = velocity
ΔV = slip velocity
x = dryness fraction
y = wetness fraction
z = distance in flow direction
α = coefficient of thermal expansion
β = isothermal compressibility
ϕ = mass flow coefficient
λ = thermal conductivity
μ = dynamic viscosity
ρ = density
τ = relaxation time

Subscripts

e = equilibrium
f = frozen
g = vapor phase
l = liquid phase
s = saturation
0 = stagnation
$*$ = critical

Downloaded 02 Jun 2010 to 171.66.16.91. Redistribution subject to ASME license or copyright; see http://www.asme.org/terms/Terms_Use.cfm

equilibrium. For low pressure steam, typical values of k_f and k_e are 1.32 and 1.12 respectively. The equilibrium speed a_e depends on the wetness fraction and the ratio a_e/a_f is usually close to 0.9.

The question now arises as to how to define the critical velocity in a wet steam flow and whether this can be related to the frequency dependent speed of sound. Konorski [6, 7] suggested that the most suitable choice is to define the critical velocity as equal to the velocity at the nozzle throat, but unfortunately this leads to a number of difficulties. In particular, the extension to two-and three-dimensional flows is not straightforward because the throat velocity is a function of the nozzle geometry rather than of the medium properties alone.

A better definition of the critical velocity is that flow velocity which is equal to the local *frozen* speed of sound. The reason for this choice hinges on the fact that, as shown by Petr [5], the leading tip of any wave system in wet steam travels with the frozen speed of sound, although other wave points may well propagate at lower velocities. Thus, unless the flow velocity is supersonic with respect to a_f, information about downstream pressure changes can propagate upstream and can affect the flow development.

This result can easily be demonstrated mathematically by combining equations (4)–(9) to give

$$(1-\mathrm{M}_f^2)\frac{d(\ln V_g)}{dz} = -\frac{d(\ln A)}{dz} + \frac{y}{x}\left(\frac{V_l}{V_g}\right)^2 \mathrm{M}_f^2 \frac{d(\ln V_l)}{dz}$$

$$\frac{y}{x}\left(\frac{V_l}{V_g}\right)\left(\frac{\alpha L}{c_{pg}} - 1\right)\frac{d(\ln m)}{dz} \qquad (16)$$

where $\mathrm{M}_f = V_g/a_f$ is the Mach number based on the vapor velocity and the frozen speed of sound and

$$L = \left(h_g + \frac{V_g^2}{2}\right) - \left(h_l + \frac{V_l^2}{2}\right) \cong (h_g - h_l)$$

Equations (10) and (12) now show that dV_l/dz and dm/dz depend on ΔV and ΔT, respectively, and *not on the gradients of the flow variables.* Substituting into (16) gives

$$(1-\mathrm{M}_f^2)\frac{d(\ln V_g)}{dz} = -\frac{d(\ln A)}{dz} + \frac{y}{x}\frac{\mathrm{M}_f^2}{V_g \tau_I}\left(\frac{\Delta V}{V_g}\right)$$

$$+ \frac{(\alpha T_g - c_{pg} T_g/L)}{V_g \tau_T}\left(\frac{\Delta T}{T_g}\right) \qquad (17)$$

Equation (17) is singular when $\mathrm{M}_f = 1$. In order for dV_g/dz to remain finite, this must occur at the point in the nozzle where

$$\frac{d(\ln A)}{dz} = \frac{(\alpha T_g - c_{pg} T_g/L)}{V_g \tau_T}\left(\frac{\Delta T}{T_g}\right) + \frac{y}{x}\frac{1}{V_g \tau_I}\left(\frac{\Delta V}{V_g}\right) \qquad (18)$$

The value of dA/dz satisfying (18) depends on the local values of ΔT and ΔV and these in turn depend on the liquid dispersion and flow history. For a continually expanding flow, ΔT and ΔV both remain positive and, as $\alpha T_g > c_{pg} T_g/L$, dA/dz must also be positive where $\mathrm{M}_f = 1$. In steady flow, therefore, the critical condition can never occur in the converging section of the nozzle.

Estimation of the Supercooling and Wetness Fraction

So far in the analysis departures from both thermal and inertial equilibrium have been considered. For most wet steam flows formed as a result of spontaneous nucleation, however, thermal effects dominate over inertial ones. For the present, therefore, the slip velocity will be assumed to be zero.

In order to apply equation (18) it is necessary to estimate the supercooling at the critical condition and this obviously depends on the expansion rate in the converging section of the nozzle together with the droplet size and number density. The calculation of departures from thermal equilibrium are considered at length in [1], where it is shown that the supercooling obeys an equation of the form

$$\frac{d}{dt}(\Delta T) + \frac{\Delta T}{\tau_T} = F\dot{p} \qquad (19)$$

where $\dot{p} = d(\ln p)/dt$ (the rate of expansion) and the differentiation is with respect to time following a fluid particle. F is a weak function of pressure given by

$$F = \frac{p}{c_{pg}\rho_s}\left[\frac{(xc_{pg} + yc_l)T_s}{xL} - (\alpha T_g)\frac{\rho_s}{\rho_g}\right] \qquad (20)$$

where ρ_s is the vapor density at p and T_s.

Equation (19) is derived by combining the energy and momentum equations with the droplet growth and Clausius-Clapeyron equations. Given the variation of the rate of expansion, it can be integrated to give the supercooling at the critical condition. The corresponding wetness fraction can then be obtained by integrating equation (10).

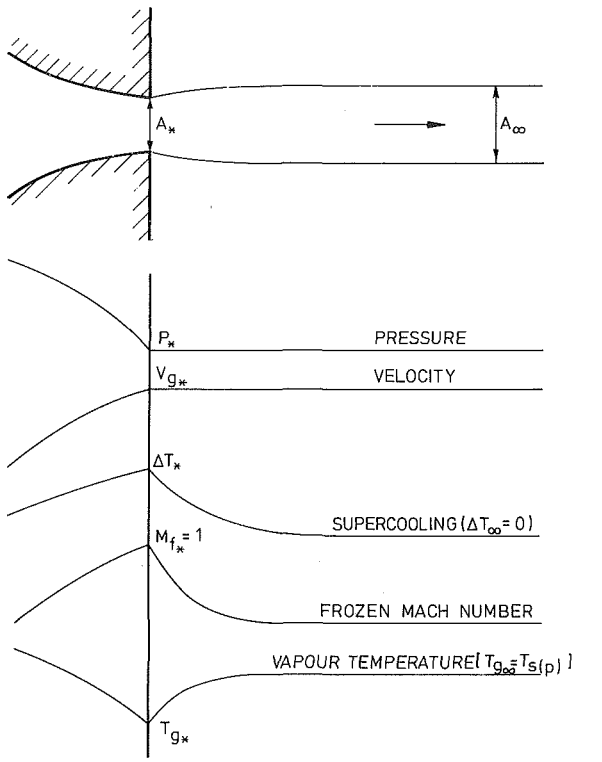

Fig. 1 Schematic diagram showing the variation of flow parameters in a wet steam jet emerging from a choked converging nozzle

Choking in Converging Nozzles

The simplest case of choking occurs in a converging nozzle having the minimum cross-sectional area in the exit plane, the jet emerging into an infinite region of constant static pressure.

Initially, with the nozzle unchoked, a lowering of the back pressure causes an increase in flow velocity. However, unlike a single-phase flow where the emerging jet is straight and parallel (neglecting three-dimensional and shear layer effects), the cross-sectional area of a wet steam jet actually increases downstream of the nozzle exit plane due to thermal relaxation effects. The mathematical analysis can be found in the Appendix where it is also shown that, although the flow velocity remains constant in the jet, M_f decreases downstream of the exit plane. These results are shown schematically in Fig. 1 and lead to the important conclusion that, for *any* operating condition, *the maximum value of* M_f *occurs at the nozzle throat.*

Downloaded 02 Jun 2010 to 171.66.16.91. Redistribution subject to ASME license or copyright; see http://www.asme.org/terms/Terms_Use.cfm

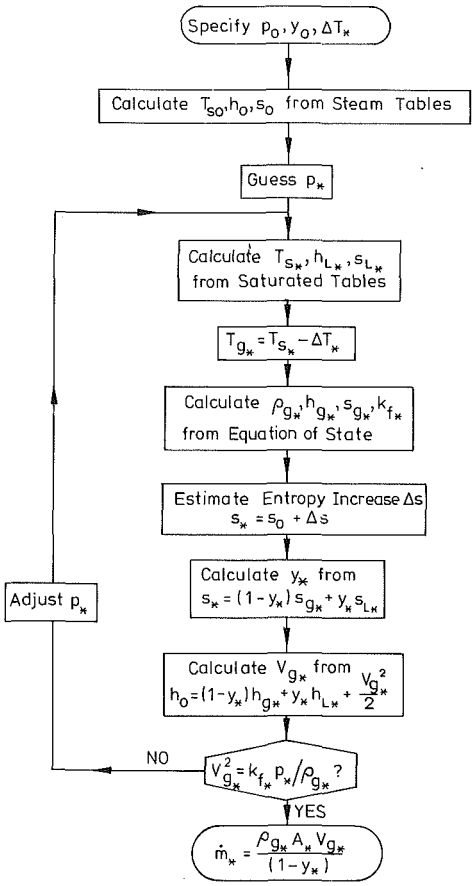

Fig. 2 Flow chart for calculating the choking mass flowrate in a converging nozzle

Eventually a stage is reached when a further reduction in back pressure has no effect on the flow pattern in the nozzle. A frozen Mach number of unity must therefore exist somewhere in the system and, because the maximum Mach number occurs in the exit plane, this must correspond to the critical condition, $M_f = 1$.

The critical pressure ratio p_*/p_0 and choking mass flowrate $\dot{m}$ can now be evaluated for any given inlet stagnation pressure p_0 and wetness fraction y_0, it being assumed that the steam enters the nozzle in equilibrium. In practice the critical supercooling ΔT_* would be estimated by integrating equation (19), but for the present purposes it is specified as input data. Inertial equilibrium is assumed to prevail throughout the expansion.

An iterative calculation procedure is required and a flowchart of the method is shown in Fig. 2. This should be self-explanatory with the exception of the step involving the estimation of the entropy increase Δs during the expansion to the critical condition. This calculation replaces the integration of equation (10) and is much more convenient as experience has shown that the choking mass flowrate is almost completely independent of the value of Δs. Using the expression for the thermodynamic entropy increase derived in (12), it is possible to show that Δs is bounded by

$$0 < \Delta s < L\Delta T_*(y_* - y_0)/T_s^2$$

Mass flowrates calculated using first the lower and then the upper bound differ by less than 1 percent, thus demonstrating that the critical flow condition is effectively a function of the critical supercooling only (for a given inlet condition) and is almost independent of the path by which this is attained.

Figure 3 shows the critical pressure ratio as a function of ΔT_* for an inlet stagnation pressure of 1 bar and various inlet wetness fractions. $\Delta T_* = 0$ corresponds to equilibrium at the

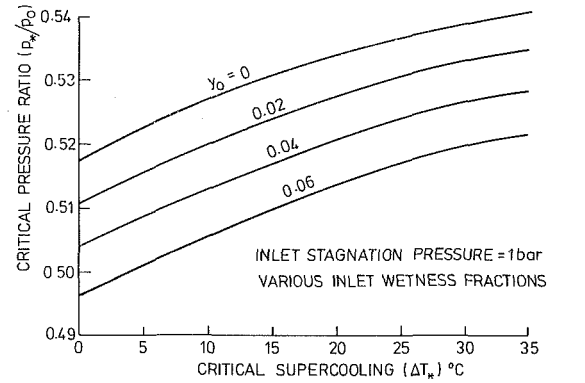

Fig. 3 Critical pressure ratio as a function of critical supercooling

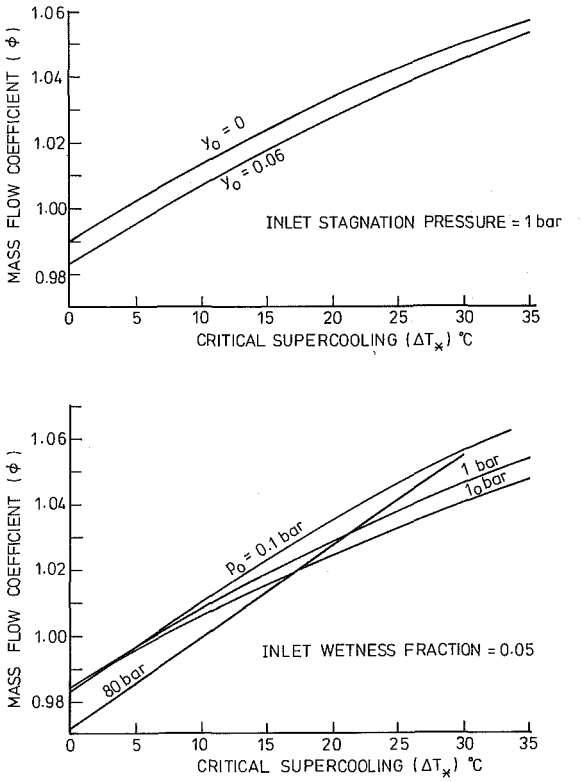

Fig. 4 Mass flow coefficient for a choked converging nozzle

throat, while $\Delta T_* = 35$K corresponds approximately to a thermally frozen flow from the inlet (assuming a secondary nucleation does not occur).

Usual practice for estimating the critical pressure ratio in wet steam flows is to assume equilibrium flow to the nozzle throat and a critical velocity equal to the equilibrium speed of sound (15). The value of this *equilibrium critical pressure ratio* is approximately 0.58 and is almost independent of the inlet stagnation conditions, even at high pressure. Figure 3 shows that the true critical pressure ratio is always significantly less than this, because the throat velocity corresponds to the frozen rather than the equilibrium speed of sound. This even applies when the flow within the nozzle deviates only infinitesimally from equilibrium.

Figure 4 presents the choking mass flowrate passed by a converging nozzle normalized with respect to the equilibrium choking mass flowrate (which is the flowrate based on the equilibrium critical pressure ratio). This is known as the *choked mass flow coefficient* and is denoted here by the symbol ϕ. For large deviations from thermal equilibrium the swallowing capacity of a converging nozzle is increased by

Downloaded 02 Jun 2010 to 171.66.16.91. Redistribution subject to ASME license or copyright; see http://www.asme.org/terms/Terms_Use.cfm

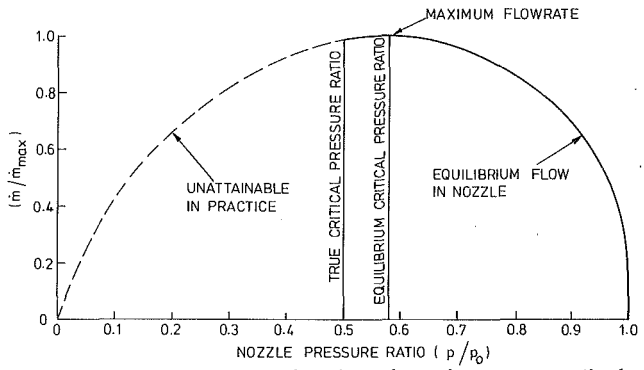

Fig. 5 Mass flow rate as a function of nozzle pressure ratio for equilibrium flow in a converging nozzle

some 6 percent over and above that suggested by equilibrium theory. Somewhat surprisingly, however, values of ϕ less than unity are obtained for near-equilibrium flows. The explanation is to be found in Fig. 5 which shows the mass flowrate as a function of nozzle pressure ratio for an equilibrium flow of steam. Because the critical condition is controlled by the frozen rather than the equilibrium speed of sound, a small portion of the descending part of the curve to the left of the maximum is theoretically attainable. Hence, in two-phase flows of this type, although a choked nozzle implies the existence of critical conditions, it does not necessarily imply the maximum possible flowrate. Unfortunately this intriguing phenomenon would be difficult to demonstrate in practice, because the effect in wet steam is very slight.

Choking in Converging-Diverging Nozzles

Choking in converging-diverging nozzles is more complicated, because the swallowing capacity may be limited by the nozzle geometry downstream of the throat [8]. This is easily appreciated by reference to Fig. 1, where it is clear that any diverging section added to the nozzle must diverge at such an angle so as not to restrict the jet in any way. If this is not the case, the critical condition will be established downstream in the diverging section and the frozen Mach number at the throat will be less than unity.

It is simple to derive a condition for the angle of divergence θ_* of a plane nozzle which will ensure that the critical velocity occurs at the throat. The nozzle must be shaped as shown in Fig. 6A and equation (18) shows that

$$\tan\theta_* \geq \left(\alpha T_g - \frac{c_{pg} T_g}{L}\right)\left(\frac{w_*}{V_{g*T}}\right)\left(\frac{\Delta T_*}{T_{g*}}\right) + \left(\frac{y_*}{x_*}\right)\left(\frac{w_*}{V_{g*}\tau_I}\right)\left(\frac{\Delta V_*}{V_{g*}}\right), \quad (21)$$

where w_* is the throat width. If (21) is satisfied, the calculation of the choking conditions is identical to that for a converging nozzle. If, on the other hand, the slope of the nozzle wall is continuous, Fig. 6B, the throat velocity will be subcritical and the choking mass flowrate reduced. A lower limiting case is the long, frictionless parallel duct fed by a converging nozzle shown in Fig. 6C. Although the complete system can be classed as a converging nozzle in its own right, it also represents the limiting case of a converging-diverging nozzle with zero angle of divergence. As such, the throat is deemed to occur at the start rather than the end of the parallel section.

Consider first the case shown in Fig. 7, curves A, when the back pressure is higher than the critical value and the exit Mach number is well below one. As the flow enters the parallel section, the heat released during the return to equilibrium causes a slight acceleration and fall in static pressure. However, once the reversion is complete, all the flow variables remain constant to the nozzle exit plane.

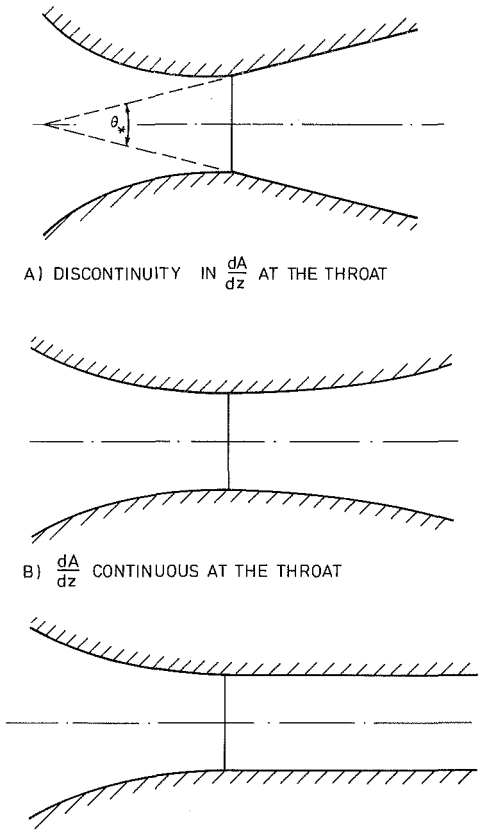

Fig. 6 Different types of converging-diverging nozzle

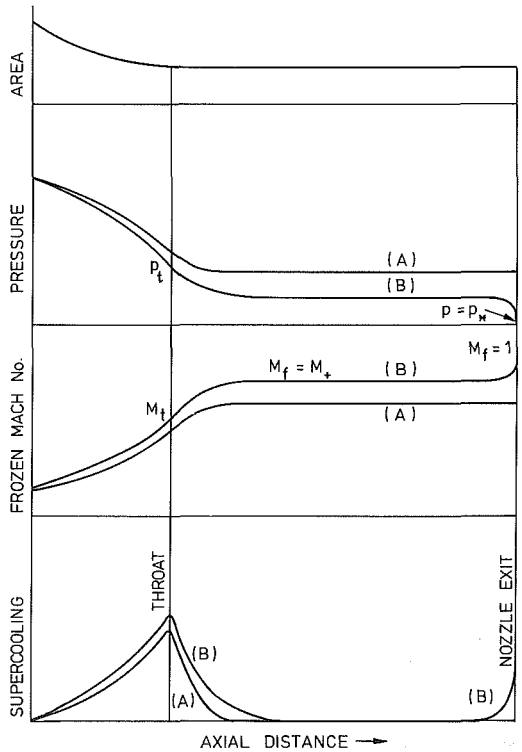

Fig. 7 Flow behavior in a parallel duct fed by a converging nozzle

On lowering the back pressure one might imagine that this type of behavior is repeated qualitatively until the frozen Mach number in the parallel duct reaches a value of unity. Bakhtar and Young [8] showed, however, that this is not the case due to a type of instability which develops at Mach

Downloaded 02 Jun 2010 to 171.66.16.91. Redistribution subject to ASME license or copyright; see http://www.asme.org/terms/Terms_Use.cfm

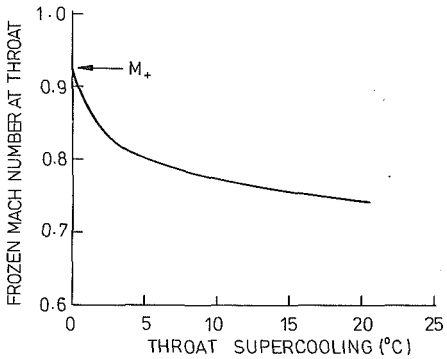

Fig. 8 Throat Mach number in the converging nozzle – parallel duct system

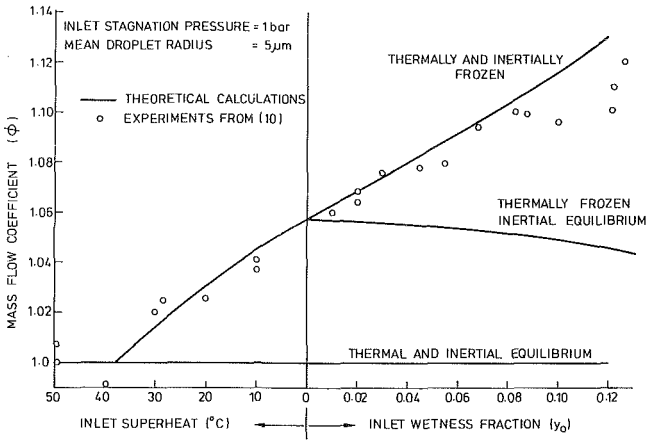

Fig. 9 Comparison of theoretical calculations with experimental measurements from [10]

numbers close to one. Normally, in the absence of external influences such as area change, the effect of condensation is to decrease the supercooling as the system reverts to equilibrium. However, for a narrow range of Mach numbers the supercooling actually increases, thus causing a further deviation from equilibrium.

By combining equations (4)–(9) with the Clausius-Clapeyron equation, it is possible to obtain an expression for the change in supercooling. A simplified form is derived in [8], but a more complete version is

$$(1-M_f^2)\alpha\frac{d(\Delta T)}{dz}=M_f^2(1-k_f\psi)\frac{d(\ln A)}{dz}$$

$$-\frac{y}{x}\left(\frac{V_l}{V_g}\right)^2 M_f^2(1-k_f\psi)\frac{d(\ln V_l)}{dz}$$

$$+\frac{y}{x}\left(\frac{V_l}{V_g}\right)\left[M_f^2\left[1+k_f\psi\left(\frac{\alpha L}{C_{pg}}-1\right)\right]-\frac{\alpha L}{c_{pg}}\right]\frac{d(\ln m)}{dz} \quad (22)$$

where

$$\psi=\left[(\beta p)-(\alpha T_s)\frac{p}{L\rho_s}\right] \quad (23)$$

Neglecting the drag force of the steam on the droplets, it follows that, in a constant area duct, the effect of condensation is to increase the supercooling for $M_+ < M_f < 1$, where

$$M_+^2=\frac{\alpha L/c_{pg}}{1+k_f\psi(\alpha L/c_{pg}-1)} \quad (24)$$

The behavior of the flow variables when the nozzle and parallel duct system becomes choked is shown in curves B of Fig. 7. The throat pressure and velocity are such that equilibrium is established in the parallel duct at a frozen Mach number equal to M_+. The final (and invariably nonequilibrium) expansion to the exit plane is accomplished over a very short distance due to the intrinsic instability of the flow in this region. Equation (24) shows that, although M_+ is a function of pressure, the dependence is weak and $M_+ = 0.92 \pm 0.01$ over a wide range of conditions.

The corresponding mass flow coefficient can be calculated by a similar procedure to that shown in Fig. 2, except that the criterion for successful convergence of the iterative sequence is that $M_f = M_+$ at $\Delta T = 0$. The results show that, for inlet-pressures up to 100 bars, $\Phi \cong 1.0$. In other words, the choking mass flowrate is almost exactly equal to the value obtained using equilibrium theory! This agreement, however, is fortuitous and is due to the fact that the pressure ratio associated with M_+ is always close to the equilibrium critical pressure ratio.

Once the mass flowrate has been determined, the flow variables at the throat can be calculated by the application of the continuity equation. The results are shown in Fig. 8 for an inlet stagnation pressure of 1 bar and an inlet wetness of 5 percent. For large departures from equilibrium the throat Mach number can be as low as 0.74, the system remaining choked.

As the angle of divergence of the nozzle is increased, so the value of the throat Mach number increases to a value of unity at the angle given by equation (21). Similarly the mass flow coefficient changes from unity to the values given in Fig. 4. Due the infinite variety of nozzle shapes available, no simple analytical theory can be formulated to describe these cases. Indeed a simplified theory would be of little value, because computer programs are available which solve the governing equations numerically for any specified geometry. Some typical examples can be found in [8].

Experimental Evidence

Although there are few experimental measurements available to test the theory proposed in the previous sections, the work by Bratuta, Shatilov and Pyasik [10] does substantiate some of the points.

Bratuta and his colleagues measured the throughput of a turbine cascade for both superheated and wet steam. The wetness was obtained from water sprays and measurements indicated the average droplet radius to be 5 μm, which, at a pressure of 1 bar, corresponds to thermal and inertial relaxation times of 10 ms and 500 μs, respectively. Although few geometrical details of the cascade were supplied, it appears that the blade chord was about 40 mm giving a flow transit time of about 150 μs. This implies that the flow was effectively frozen, both thermally and inertially.

Of the large number of tests presented in [10], those with a cascade pressure ratio of 0.4 are particularly relevant because the flow is choked under these circumstances. The results are reproduced in Fig. 9, which shows the measured value of ϕ as a function of cascade inlet conditions. The experimental values have been corrected for boundary layer effects by assuming a discharge coefficient of 0.99. This value was estimated from the curves presented in [10] for highly superheated flow.

Theoretical values of ϕ were calculated by a procedure similar to that shown in Fig. 2. The only modification required was to the energy equation where, because of the high inertial relaxation time of the droplets, it was assumed that there was no acceleration of the liquid phase during the expansion. As the blades were of the converging nozzle type, it was also assumed that the critical flow area corresponded to the throat area at the trailing edge, any further expansion or reversion process being accommodated by a Prandtl-Meyer expansion downstream of the throat.

The results of the calculations are compared with the ex-

Downloaded 02 Jun 2010 to 171.66.16.91. Redistribution subject to ASME license or copyright; see http://www.asme.org/terms/Terms_Use.cfm

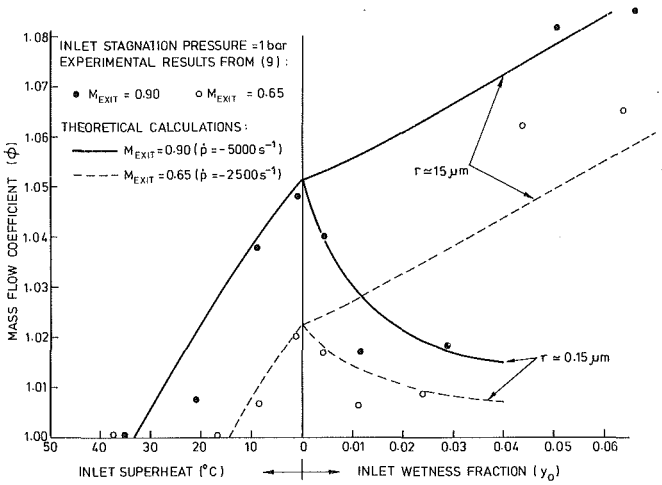

Fig. 10 Comparison of theoretical calculations with experimental measurements from [9]

periments in Fig. 9 and the agreement is obviously excellent. Included also is a curve showing the effect of neglecting the velocity slip between the phases. The difference is considerable and illustrates the importance of including this effect when the inertial relaxation time is large.

Experimental measurements of mass flowrate in a turbine cascade were also made by Filippov, Povarov, and Nicholsky [9]. They emlployed two different methods of generating the wetness giving rise to droplets of average radii 0.15 μm and 15 μm, respectively. The former are of considerable interest because both thermal and inertial relaxation effects play dominating roles. Curves of mass flow coefficient as a function of cascade inlet conditions were presented for a range of exit Mach numbers up to 0.9, but the case of fully choked flow was, unfortunately, not included.

In order to make theoretical comparisons it was necessary to estimate the supercooling at the cascade exit. For droplets of radius 15μm the relaxation times are so high that the flow is effectively frozen for both thermal and inertial effects. For droplets of radius 0.15 μm, inertial equilibrium may be assumed, but the supercooling must be estimated by integrating equation (19). Although few geometrical details are given in [9], it was possible to deduce approximately the rate of expansion near the blade throat from calculations on similar shaped blades. As before, a discharge coefficient to allow for boundary layer effects was estimated from the fully superheated tests.

A comparison between theory and experiment is presented in Fig. 10 where it can be seen that the agreement is generally very good. Obviously further experimental work is required to confirm all the details of the theoretical analysis, but it is gratifying that the evidence available to date corresponds so well with the theoretical predictions.

References

1 Young, J. B., "The Fluid Mechanics of Non-Nucleating Wet Steam Flows," Whittle Laboratory Report No. TR 111, University of Cambridge, 1982.

2 Deich, M. E., "Sound Velocity and Decrement of Wave Attenuation in Two-Phase Media" (in Russian), *Trans. Inst. Fluid Flow Machinery* (Poland), Vols. 29–31, 1966.

3 Konorski, A., "Propagation of Small Disturbances in Two-Phase Media" (in Polish), *Trans. Inst. Fluid Flow Machinery* (Poland), Vol. 57, 1971.

4 Petr, V., "Variation of Sound Velocity in Wet Steam," Inst. Mech, Engnrs., *Wet Steam 4*, Paper C24/73, 1973, p. 17.

5 Petr, V., "Non-Linear Wave Phenomena in Wet Steam," Proc. 7th Conference on Steam Turbines of Large Output," Plzen, May 1979, p. 248.

6 Konorski, A., "Critical Flow Conditions of Non-Equilibrium Two-Phase Media" (in Polish), *Trans. Inst. Fluid Flow Machinery* (Poland), Vol. 65, 1974, p. 3.

7 Konorski, A., "Critical Flow Conditions and Choking Flowrates of Wet Steam Flows," *Proc. 7th Conference on 'Steam Turbines of Large Output'*, Plzĕn, May 1979, p. 228.

8 Bakhtar, F., and Young, J. B., "A Study of Choking Conditions in the Flow of Wet Steam," *Proc. Instn. Mech. Engnrs.*, Vol. 192, 1978, p. 237.

9 Filippov, G. A., Povarov, O. A., and Nickolsky, A. J., "The Steam Flow Discharge Coefficient and Losses in Nozzles of a Steam Turbine Stage Operating in the Low Steam Wetness Zone," *Aero-Thermodynamics of Steam Turbines*, Edited by Steltz, W. E., and Donaldson, A. M., ASME, Winter Annual Meeting, Washington, Nov. 1981, p. 117.

10 Bratuta, E. G., Shatilov, S. P., and Pyasik, D. N., "A Comparison of the Throughput Capacities of the TS-1A and TS-1AV Blade Cascades with Flows of Superheated and Wet Steam," *Teploenergetika* (English Translation), Vol. 20, 1973, p. 117.

11 Moore, M. J., and Sieverding, K. H. (Editors), *Two-Phase Steam Flow in Turbines and Separators*, McGraw-Hill, 1976.

12 Young, J. B., "The Spontaneous Condensation of Steam in Supersonic Nozzles," *Physico-Chemical Hydrodynamics*, Vol. 3, 1982, p. 57.

APPENDIX

Relaxation in a Constant Pressure Jet

Assume that the jet emerges from a converging nozzle into an infinite region of constant static pressure and neglect effects due to inertial nonequilibrium. Conditions in the exit plane are assumed to be critical and are denoted by subscript $*$.

Equation (5) shows that the jet velocity remains constant at the critical value V_{g*} and, according to (19), the supercooling decays exponentially,

$$\Delta T = \Delta T_* \exp(-t/\tau_T) \tag{25}$$

where $t = z/V_{g*}$ is the time for a fluid particle to traverse a distance z downstream of the nozzle exit plane.

The jet cross-sectional area can be obtained from the continuity requirement.

$$\frac{A}{A_*} = \frac{x\rho_{g*}}{x_*\rho_g} \tag{26}$$

The energy equation (6) applied between the throat and a downstream point becomes

$$x_*(h_{g*} - h_{l*}) = x(h_g - h_l) \tag{27}$$

and $h_l = h_{l*}$ because p (and hence T_s) is constant. To a good approximation $(h_g - h_{l*}) = L$ and $(h_{g*} - h_g) = c_{pg}(\Delta T - \Delta T_*)$, so that

$$\frac{x}{x_*} \cong 1 - c_{pg}\frac{(\Delta T_* - \Delta T)}{L} \tag{28}$$

Assuming, for convenience, perfect gas behavior of the vapor phase,

$$\frac{\rho_{g*}}{\rho_g} = \frac{T_g}{T_{g*}} = 1 + \frac{(\Delta T_* - \Delta T)}{T_{g*}} \cong \left[1 + \frac{(\Delta T_* - \Delta T)}{T_s}\right] \tag{29}$$

Substituting (28) and (29) in (26),

$$\frac{A}{A_*} \cong \left[1 - c_{pg}\frac{(\Delta T_* - \Delta T}{L}\right]\left[1 + \frac{(\Delta T_* - \Delta T)}{T_s}\right] \tag{30}$$

Far downstream equilibrium is established and $\Delta T \to 0$. The jet becomes parallel with cross-sectional area A_∞ given by

$$\frac{A_\infty}{A_*} \cong \left[1 - c_{pg}\frac{\Delta T_*}{L}\right]\left[1 + \frac{\Delta T_*}{T_s}\right] \cong 1 + \frac{\Delta T_*}{T_s}\left[1 - \frac{c_{pg}T_s}{L}\right] \tag{31}$$

As the critical supercooling rarely exceeds 35°C, $A_\infty/A_* < 1.07$, representing a comparatively modest area increase.

Note finally that, as the jet velocity remains constant and the vapor temperature rises, the frozen Mach number decreases downstream of the nozzle exit plane.

Downloaded 02 Jun 2010 to 171.66.16.91. Redistribution subject to ASME license or copyright; see http://www.asme.org/terms/Terms_Use.cfm

The Utilization of Specially Tailored Air Bubbles as Static Pressure Sensors in a Jet

K. K. Ooi
Able Corporation,
Anaheim, Calif.

A. J. Acosta
California Institute of Technology,
Pasadena, Calif.

It is shown that air bubbles of a certain size may be used to measure the fluctuating pressure in a liquid jet. The conditions under which these bubbles accurately reflect the local static pressures are described in detail; the volume shape of the bubbles was determined by holography for a 3.17 mm jet and the change in volume is interpreted as a result of the fluctuating pressure. The experimental results revealed that at any one instant, a wide spectrum of static pressure fluctuation intensities exist in the jet. It was also found that the probability distribution of these intensities has a slightly skewed bell shape distribution and that the fluctuating static pressure peaked at a higher positive value than a negative one.

Introduction

A complete knowledge of the local static pressure is required for a clear understanding of the many phenomenon associated with fluid flows, for example, aerodynamic noise and cavitation. While such pressure measurements on the surface of a body are relatively easy to achieve, the same cannot be said for similar measurements in a free shear layer, such as a jet. This is because one would require a probe whose reading is independent of yaw in any direction and of the dynamic pressure. It is also necessary to use a probe that will not create a substantial flow disturbance when it is in the flow. Although fast response condenser microphones and piezoelectric pressure transducers have been widely used in the past to measure the fluctuating pressure spectrum, as reported in [1], [8], and [10], the measurements obtained were not accurate reflections of the local static pressures. The inaccuracies were due in part to the induced flow disturbance by the probe and partly as a result of spatial averaging over the probes relatively large sensing area. In view of these considerations, it is fairly obvious that the measurement of the local static pressure in a jet is not trivial and continues to present a problem to investigators.

The primary purpose of this paper is to introduce a new concept in the measurement of the instantaneous local static pressure. This concept, as will be demonstrated, will lead to a measurement technique that does not have the many setbacks of the conventional methods described earlier. Some experimental results are also presented as evidences that this new technique is feasible. The current method relied on specially tailored air bubbles as instantaneous pressure indicators. The conditions under which these bubbles could be employed is considered next.

Contributed by the Fluids Engineering Division of THE AMERICAN SOCIETY OF MECHANICAL ENGINEERS and presented at the Fluids Engineering Conference, Houston, Texas, June 20–22, 1983. Manuscript received by the Fluids Engineering Division, August 24, 1983. Paper No. 83-FE-34.

Theoretical Analysis

The motion of a spherical bubble in a fluid is governed by the familiar Rayleigh-Plesset equation viz:

$$\rho(R\ddot{R}+3\dot{R}^2/2)=P_g(T)+P_v(T)-P_\infty(t)-\frac{4\nu\rho\dot{R}}{R}-\frac{2\sigma}{R} \tag{1}$$

where the symbols are as defined in the nomenclature. In theory, if a complete history of the motion of the bubble is known, then the local static pressure at any instant in time as seen by the bubble can be calculated from the equation above. This is undeniably an involved procedure which will require a continuous monitoring of the bubbles trajectory. It is indeed a difficult task since the bubble is often very small in size, is moving at a high speed and its path is not usually known a priori. Fortunately, this whole analysis can be greatly simplified, as is shown below.

Order of Magnitude Analysis. If the dominant pressure fluctuation in a free shear flow is at a circular frequency of ω, then it is to be expected that the radius of a bubble in the flow field will change at the same frequency. Consequently, the instantaneous bubble radius, $R(t)$, is described by the equation:

$$R(t)=R_0+\epsilon e^{j\omega t} \tag{2}$$

where R_0 is the reference bubble radius and ϵ is the amplitude of the oscillation about the mean radius. In general, the amplitude of this oscillation is not small and could be of the same order as R_0. By referring all linear dimensions to R_0 and the circular frequency of fluctuation to the resonant frequency of the bubble, ω_0, it follows that:

$$\dot{R}^2\sim\left(\frac{\epsilon}{R_0}\right)^2\left(\frac{\omega}{\omega_0}\right)^2$$

$$R\ddot{R}\sim\left(\frac{\epsilon}{R_0}\right)\left(\frac{R}{R_0}\right)\left(\frac{\omega}{\omega_0}\right)^2$$

$$\text{pressure term}\sim\frac{1}{\rho u_0{}^2}\ (\text{where } u_0=R_0\omega_0) \tag{3}$$

Copyright © 1984 by ASME

Downloaded 02 Jun 2010 to 171.66.16.91. Redistribution subject to ASME license or copyright; see http://www.asme.org/terms/Terms_Use.cfm

$$\text{viscous term} \sim \left(\frac{\epsilon}{R_0}\right)\left(\frac{\omega}{\omega_0}\right)\Big/\left(\frac{R}{R_0}\right)$$

$$\text{surface tension term} \sim \frac{1}{\text{We}}$$

Furthermore the following ratios are defined as:

$$\frac{R}{R_0} = 0(1)$$

$$\frac{\epsilon}{R_0} = 0(1) \tag{4}$$

and

$$\frac{\omega}{\omega_0} = 0(\delta) \text{ where } \delta << 1$$

From equations (3) and (4) it can be shown that the left hand terms of equation (1) are of the order δ^2 and the viscous term is of the order δ. Therefore these terms can be dropped from equation (1). As a consequence, the equation simplifies to:

$$P_\infty(t) = P_g(T) + P_v(T) - \frac{2\sigma}{R} \tag{5}$$

Since attention will be focused on the local static pressure, it will be more apropriate to rewrite equation (5) with a subscript x yielding:

$$P_{\infty_x}(t) = P_{g_x}(T) + P_{v_x}(T) - \frac{2\sigma}{R_x} \tag{6}$$

The terms with the subscript refer to the corresponding local values. In addition, the partial pressure of the gas is given by:

$$P_{g_x}(T) = P_{g_0}(T)\left(\frac{R_0}{R_x}\right)^{3\gamma} \tag{7}$$

By substituting equation (7) into (6), the following is obtained:

$$P_{\infty_x}(t) = P_{g_0}(T)\left(\frac{R_0}{R_x}\right)^{3\gamma} + P_{v_x}(T) - \frac{2\sigma}{R_x} \tag{8}$$

It is now necessary to devise an experimental technique whereby equation (8) above can be used to compute the local static pressure as sensed by the bubble.

Practical Considerations

It is apparent from equation (8) that the radii of the bubble at position x and at some reference position should be measured before the local pressure could be calculated. An immediate tendency would be to inject a single bubble into the jet, then photographing it at the location of injection and again at position x, a short time later. Although this is a realizable method, it will involve a great deal of picture taking before the entire pressure field in the jet is mapped out. Instead of doing this, a continuous stream of bubbles could be introduced into the jet at a reference point. The instantaneous bubble sizes at the various positions in the jet could then be revealed in a single photograph. Furthermore if it is ensured that the size of the bubble at the point of injection is always the same, then any observed change in the size of the bubble from this reference position could be regarded as a direct result of the pressure fluctuations in the flow. Here again, it should be stressed that the above interpretations are only true provided the conditions stipulated by equation (4) are satisfied. It will be demonstrated that by careful design, the selected bubbles can be made to meet the stated requirements.

Experimental Verification

An axisymmetric jet exiting from a 3.17mm nozzle was chosen as the subject for investigation. Since the jet was to discharge into a stationary medium at a static pressure of only 1.1 atmospheres, it was necessary to restrict the exit velocity of the jet to 12.2 m/s, to avoid cavitation. It has been reported in [1], [8], and [10] that the normalized power spectrum of pressure fluctuations in a jet peaked at a Strouhal number ($=fD/V_j$) of 0.45 and on either side of this value, the spectrum dropped rapidly to insignificant values. Therefore under the present flow conditions, the dominant frequency of the pressure fluctuations would be approximately 1.7 kHz, or a time scale of the order of a millisecond. It follows then the bubble to be used in this jet has to have a response time of at least a tenth of a millisecond if it is to be a good instantaneous pressure indicator. Theoretically, as can be seen from equation (9) below, an infinitely small bubble would easily meet this condition. However the need to be able to measure any change in the size of the bubble easily and accurately require a bubble of finite size. Another requirement is that the bubble has to be sufficiently small to sense the local "point" pressures. It is known from bubble dynamics that the resonant circular frequency of a spherical bubble in an incompressible medium is governed in general by:

$$\omega_0^2 = \frac{3}{\rho R_0^2}\left[\gamma(P_0 - P_v) + 2\frac{(3\gamma - 1)}{3R_0}\sigma\right] \tag{9}$$

and

$$\omega_0^2 = \frac{3}{\rho R_0^2}\left[(P_0 - P_v) + \frac{4\sigma}{3R_0}\right] \text{ for } \gamma = 1$$

It can easily be shown from equation (9) that the response

Nomenclature

D = diameter of the jet at exit
f = frequency of the pressure fluctuation
f_0 = resonant frequency of the bubble
m = number of data points
$P_{g_0}(T)$ = partial pressure of the gas in the bubble at the reference location.
$P_g(T)$ = partial pressure of the gas in the bubble
$P'(t)$ = fluctuating pressure at any instant ($=P_\infty(t)$-P_0)
$P_\infty(t)$ = instantaneous static pressure
P_0 = mean ambient static pressure
$R(t)$ = instantaneous bubble radius
$\dot{R}(t)$ = instantaneous radial velocity of the bubble
$\ddot{R}(t)$ = instantaneous radial acceleration
R_m = geometric mean radius of the injected bubble
R_0 = reference bubble radius
T = temperature
t = time
u_0 = peripheral velocity of the bubble
V_j = velocity of the jet at exit
We = Weber number
β = damping constant
γ = polytropic index
δ = a quantity of the order much less than unity
ϵ = amplitude of oscillation about the mean bubble radius
ν = kinematic viscosity of water
ρ = density of water
σ = surface tension
ω = circular frequency of the pressure fluctuation
ω_0 = resonant circular frequency of the bubble

Downloaded 02 Jun 2010 to 171.66.16.91. Redistribution subject to ASME license or copyright; see http://www.asme.org/terms/Terms_Use.cfm

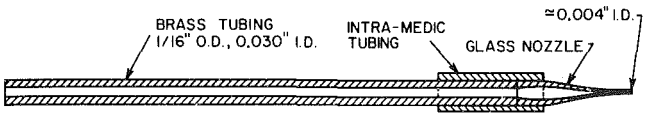

Fig. 1 Diagram showing the geometrical details of the bubble injector

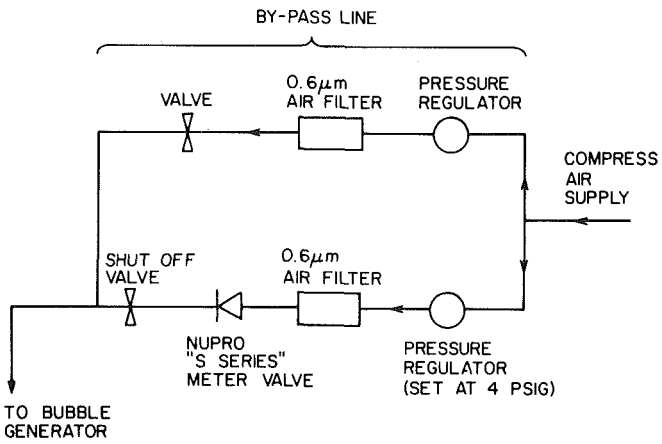

Fig. 2 Diagram of the air bubble injection system

time of a bubble in the size range of 50μm to 100μm is at least an order and a half faster than the time scale of the pressure fluctuation. Any change in volume in a bubble this size due to the fluctuation of pressure could also be easily detectable. Consequently it became the choice for the present work.

Description of Test Apparatus. The required bubble size was generated by a bubble injector which was made up of a glass nozzle drawn from a 1.6 mm outer diameter tubing. The inner diameter of the nozzle at exit was approximately 100μm. This nozzle was attached to a short length of brass tubing as shown in Fig. 1. Bubbles were generated by passing dry compressed air, filtered and regulated to 1.27 atmospheres, through the glass nozzle. The whole injection system is depicted diagramatically in Fig. 2. A meter valve located downstream of the air filter allowed the very small air flow rate (approximately 3×10^{-8} m^3/s) to be finely adjusted.

The primary component of the flow apparatus was the flow assembly which comprised of several sections, as shown in Fig. 3. The jet was created by discharging a column of water from a pressurized vessel through the 3.17 mm nozzle into a stationary water tunnel, the jet being submerged. Flow visualization was accomplished with a holocamera, a description of which is found in [9] and [11]. A general layout of the test apparatus is shown in Fig. 4

Test Procedures. The bubble injector was introduced into the nozzle assembly through a hole in the vaned elbow. The tip of injector was positioned on the jet centerline and at four diameters upstream of the nozzle lip. With the water jet running, the air flow through the injection system was carefully adjusted until a steady stream of individual bubbles was seen exiting from the nozzle lip under stroboscopic lighting. A hologram of the flow field was then taken. A whole series of holograms was obtained this way. In all the tests, the water in the jet and that of the surroundings was kept at a dissolved air content of 11 p.p.m. (approximately 75 percent saturated with air).

Data Reduction. The bubble size as a function of jet position was obtained from the reconstructed images of the holograms. Prior to calculating the static pressure in the jet from equation (8), it was necessary to establish that the rate at which the injected bubbles was dissolving into the jet water was small and that these bubbles acquired steady state soon

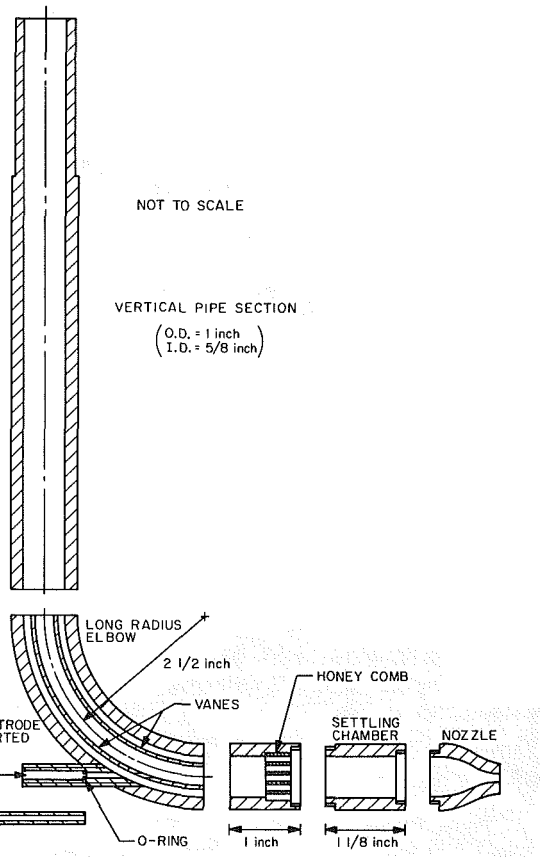

Fig. 3 Diagram showing the geometrical details of the nozzle assembly

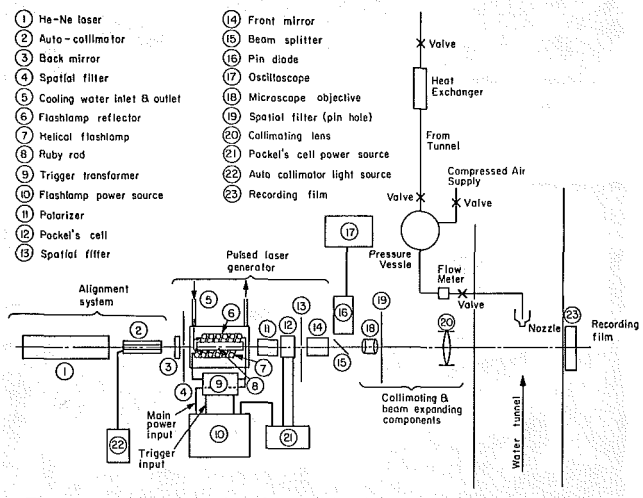

Fig. 4 Diagram showing the layout of the experimental apparatus

after exiting from the flow nozzle. These conditions have to be satisfied if the recorded sizes of the bubble downstream of the jet are to be indicative of the local instantaneous static pressures. Both these effects were found to be negligible under the present test conditions as is demonstrated below.

As the bubbles were accelerated through the flow nozzle, they were set into oscillations. The amplitude of the oscillation with time was reported in [7] as:

$$\epsilon(t) = \epsilon_0 e^{-\beta f_0 t} \cos(2\pi f_0) t \tag{10}$$

where $f_0 = \omega_0/2\pi$. The damping constant for a 65μm bubble (the size of the bubble that was used in the present work) was estimated to be 0.11 by [4] and [5]. By defining steady state as the instant the amplitude of the oscillation was 5 percent or

Downloaded 02 Jun 2010 to 171.66.16.91. Redistribution subject to ASME license or copyright; see http://www.asme.org/terms/Terms_Use.cfm

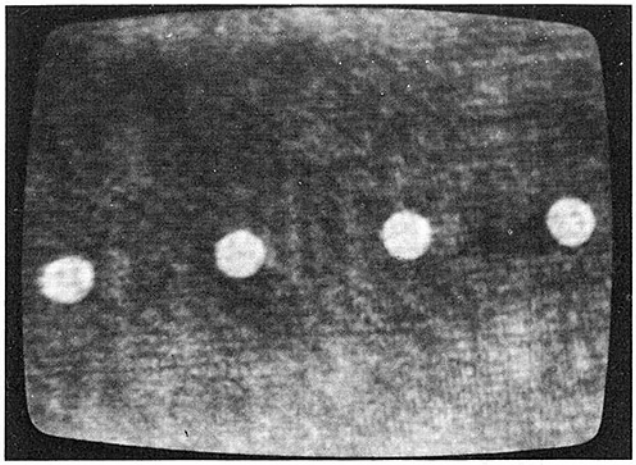

Fig. 5 Photograph of the reconstructed image of a string of injected bubbles in the potential core of the jet, near the nozzle exit. The bubbles are 128μm in diameter.

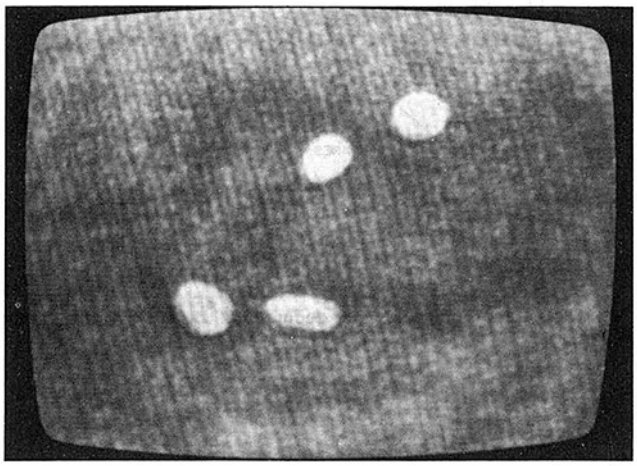

Fig. 6 Photograph of the reconstructed image of ellipsoidal bubbles in the transition region of the jet.

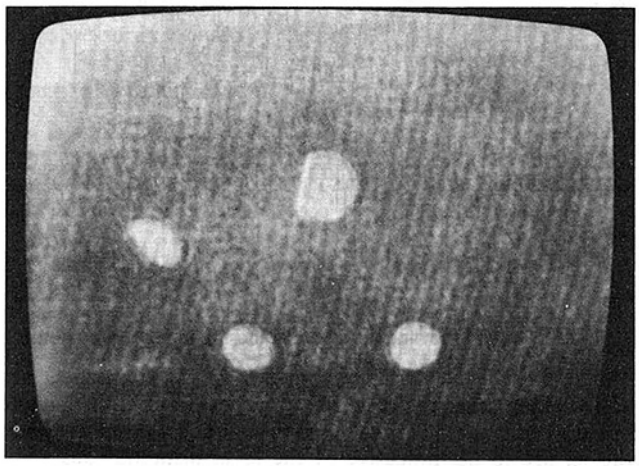

Fig. 7 Photograph of the reconstructed image of a badly sheared bubble in the transition region of the jet

less of the initial amplitude, it followed from equation (10) that the elapsed time was given by:

$$e^{-\beta f_0 t} = 0.05 \tag{11}$$

or $t = 6.2 \times 10^{-4}$s (for a 65μm bubble). This implied that at a jet velocity of 12.2 m/s, the injected bubble acquired steady state at 7.5 mm beyond the nozzle lip. In fact, flow visualization has revealed that equilibrium was reached as near as 5 mm downstream of the nozzle exit. A photographic evidence of this is shown in Fig. 5. As to the rate at which the injected bubbles were going into solution, this problem has been studied in some detail and reported in [6]. Based on this work, it has been estimated that it will take approximately 400 seconds for the present bubbles to completely dissolve in water that is 75 percent saturated. Since the traverse time of the bubbles in the current investigation was of the order of milliseconds, it was inferred that the dissolved volumes of the bubbles were negligibly small. Hence it was concluded that the recorded bubble sizes on the holograms were true reflections of the local instantaneous static pressures.

Equation (8) was further simplified by dropping the vapor pressure term. The justification for doing this lies in the fact that dry air was used in the injector and no significant evaporation was expected to occur in the extremely short traverse time through the region under scrutiny. It could also be readily shown that the initial gas pressure, P_{g_0}, could be obtained from the reduced Rayleigh-Plesset equation, that is

$$P_{g_0} = P_0 + \frac{2\sigma}{R_0} \tag{12}$$

On substitution of P_{g_0}, equation (8) becomes

$$P_{\infty_x}(t) = \left(P_0 + \frac{2\sigma}{R_0}\right)\left(\frac{R_0}{R_x}\right)^{3\gamma} - \frac{2\sigma}{R_x} \tag{13}$$

Observations of the reconstructed images of the holograms showed that in the transition region of the jet, some of the injected bubbles did not retain their spherical form but were ellipsoidal in shape. An example of this situation is shown in Fig. 6. The immediate concern then was whether these ellipsoidal bubbles could still be regarded as good pressure sensors. In reference [13], it was reported that the natural frequency of an ellipsoidal bubble could be very accurately approximated by the response time of a spherical bubble with the same volume. The report also pointed out that the frequency of an ellipsoidal bubble was only slightly dependent on the ratio of the major to the minor axis of the bubble if that ratio was less than four. In the present measurements, the largest change in volume detected was about 3.5 times the original. This translated into an increase of about 50 percent in the radius of the bubble. It follows from equation (9) that a bubble of this size still has a relatively short response time. Hence, all the bubbles in the flow field remained as good indicators of the instantaneous static pressure.

There was however a problem associated with these ellipsoidal bubbles. This problem was the correct determination of the respective volumes. It arose because out of the three minor and major axes of the ellipsoid required for the computation of the volume, only two could be measured from the reconstructed image. It was hoped that the third dimension could somehow be theoretically determined but it has been pointed out in [3] that such a problem is far too complex to solve. Therefore to circumvent this problem, it was assumed that the third axes was given by the geometric mean of the other two measured radii. This meant that the volume of the ellipsoidal bubble was proportional to the cube of the geometric mean radius. Hence an equivalent expression of equation (13) for the ellipsoidal bubbles is:

$$P_{\infty_x}(t) = \left(P_0 + \frac{2\sigma}{R_m}\right)\left(\frac{R_0}{R_m}\right)^{3\gamma} - \frac{2\sigma}{R_m} \tag{14}$$

It is worth pointing out that at present the radius of the bubble could be measured to within 2μm.

One interesting observation is that in all the holograms that were analyzied (17 in all), no fragmentation of the bubbles was ever detected. However, in a number of instances, a few badly sheared bubbles were seen. Such a case is shown in Fig. 7. The volumes of these bubbles were difficult to determine accurately and consequently these bubbles were omitted in the

Downloaded 02 Jun 2010 to 171.66.16.91. Redistribution subject to ASME license or copyright; see http://www.asme.org/terms/Terms_Use.cfm

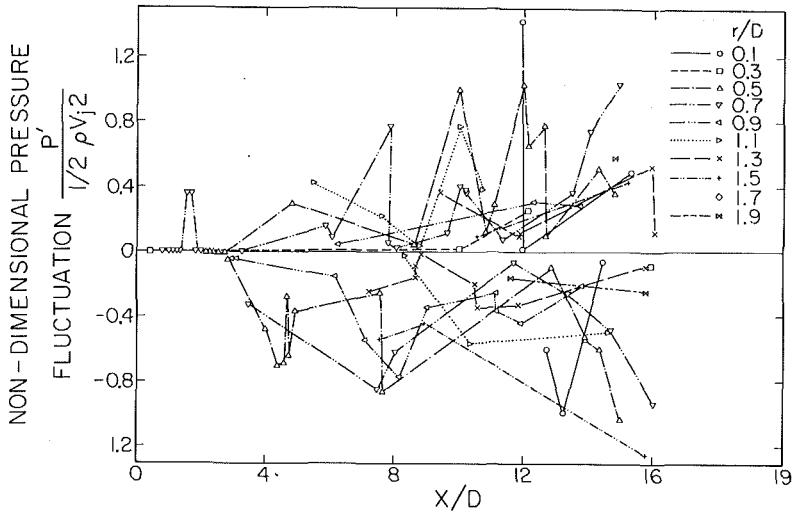

Fig. 8 Graphs of the instantaneous local pressure fluctuations as a function of the dimensionless axial position in the 3.17 mm jet

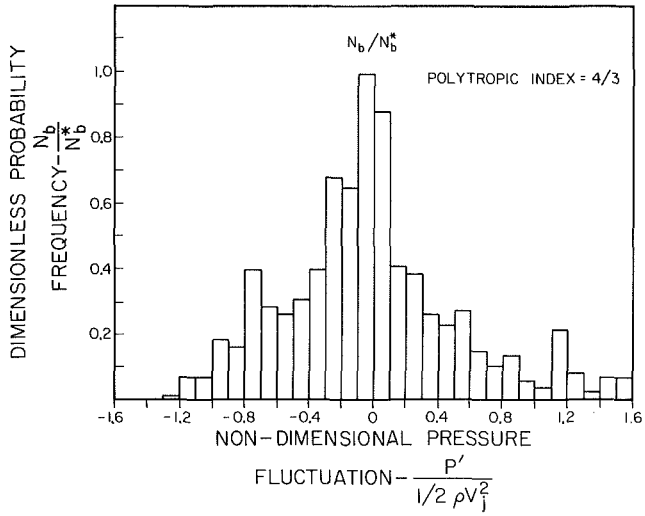

Fig. 9 Probability histogram showing the distribution of the pressure fluctuation intensities in jet. (Polytropic index of 4/3)

analysis. It has also been found that to some degree the tendency of the bubble to distort from its spherical form increases with the bubble size at the point of injection.

Discussion and Conclusions

There is at present no known criteria of establishing the correct value of the polytropic index in equations (13) and (14). Consequently, in the present work, an arbitrary value of 4/3 was used. Figure 8 is a typical example of the measured static pressure fluctuations in the present jet. The pressure fluctuation is expressed as a ratio of the dynamic head and plotted against the non-dimensional axial position. The various lines on the figure join data points at constant radial positions in the jet. It can be clearly seen that a wide spectrum of pressure fluctuations is present at any one instant. It should also be noted that peak fluctuations as intense as 160% of the dynamic head were also recorded although they are not shown in this plot.

A probability histogram which shows the distribution of the intensities of the pressure fluctuations is shown in Fig. 9. This curve was obtained by incorporating all the data from 17 holograms of the jet, under identical flow conditions. It can be inferred from this plot that the pressure fluctuation intensities have a Gaussian-like distribution, but is skewed somewhat. Notice also that the fluctuations peak at a higher positive value than a negative one. A similar histogram of the peak pressure fluctuations has been used to some degree of success in the scaling of cavitation inception data in jets. The details are found in [11].

To have an indication of the rms of the pressure fluctuations, the jet was divided into various regimes as shown in Table 1. The calculation was then performed using the expression:

$$\left\langle\left(\frac{P'}{\tfrac{1}{2}\rho V_j^2}\right)\right\rangle = \left[\frac{1}{(m-1)}\sum_{m=1}^{m}\left(\frac{P'}{\tfrac{1}{2}\rho V_j}\right)^2\right]^{\frac{1}{2}} \qquad (15)$$

where $\langle(P'/\tfrac{1}{2}\rho V_j^2)\rangle$ denotes the rms of the dimensionless pressure fluctuation in a particular regime of the jet and m is the number of data points in that region. The computed results are tabulated in Table 1. It can be seen from this table that there are two entries in each region of the jet. The first entry is the calculated rms fluctuation when all the measured data were used. The second entry corresponds to the calculated rms value when a few of the data points were not included in the computation because they exhibited values that were significantly different from the majority of the data in that group. A quick comparison of these two entries clearly shows that in many instances, there is a sizeable difference in the two rms values. This clearly implies that the results are not very accurate due to the limited number of data points. It should be pointed out that the number in parentheses represents the sampling size.

In the rms pressure measurements made to date by conventional means, it has been reported in [2] and [12] that the magnitude of the fluctuation decreases with increasing distance from the jet exit. However, this trend is not apparent in the present case. The cause of this discrepancy is not known. In addition, the currently calculated rms level is considerably higher than those reported by the other authors. It is believed that the lower rms values of the other investigators is due to spatial averaging, since the pressure transducers that they used were much larger by comparison.

It should be apparent by now that the present technique does permit the static pressure in a jet, or any shear flow for that matter, to be measured. Although the pressure measurements in this work were carried out at a jet velocity of only 12.2 m/s, higher velocities could be used if the surrounding ambient pressure was higher. This technique could also be utilized to measure the static pressure in a Lagrangian frame. As a final remark, it should be mentioned that the present method does have a set back which is the time

Downloaded 02 Jun 2010 to 171.66.16.91. Redistribution subject to ASME license or copyright; see http://www.asme.org/terms/Terms_Use.cfm

Table 1 A tabulation of the rms pressure fluctuations in various regions of the present jet (polytropic index = 4/3)

	$0 \le r/D \le 0.5$	$0.5 \le r/D \le 1.0$	$1.0 \le r/D \le 1.5$	$1.5 \le r/D \le 2.0$	$2.0 \le r/D \le 2.5$	$2.5 \le r/D \le 3.0$
$4.0 \le X/D < 6.0$	0.25(95)	0.43(38)	0.64(13)	–	–	–
	0.20(92)	0.32(35)	0.45(11)			
$6.0 \le X/D < 8.0$	0.39(43)	0.56(45)	0.76(25)	0.48(3)	–	–
	0.31(41)	0.39(42)	0.65(22)	–		
$8.0 \le X/D < 10.0$	0.56(24)	0.53(35)	0.56(33)	0.63(14)	–	–
	0.40(20)	0.40(32)	0.43(30)	0.56(13)		
$10.0 \le X/D < 12.0$	0.66(13)	0.69(38)	0.73(31)	0.83(20)	0.94(3)	–
	0.40(11)	0.54(35)	0.61(28)	0.68(17)	0.77(2)	
$12.0 \le X/D < 14.0$	0.64(12)	0.65(28)	0.78(18)	0.59(14)	0.69(1)	0.65(7)
	–	0.51(24)	0.49(14)	–	0.58(10)	–
$14.0 \le X/D < 16.0$	0.60(6)	0.69(10)	0.46(25)	0.68(25)	0.65(9)	0.76(13)
	0.43(5)	–	0.50(22)	–	0.56(8)	0.57(10)

required to analyze the holograms. As an example, it takes approximately ten hours to record all the bubble sizes in a single hologram. This puts a limit to the number of holograms that could be realistically analyzed and consequently affects the accuracy of the statistical results. It is true that an automated, computer aided system could be used to scan the hologram and record the bubble sizes simultaneously as a function of jet position. Unfortunately, such a system is at present unavailable.

Acknowledgments

The authors would like to take this opportunity to thank Professor Sabersky and Dr. Oldenziel for providing many useful suggestions and comments. Dr. J. Katz is deserving of special mention for his valuable assistance on the holographic work. The authors are grateful to Susan Berkley for her help in organizing the manuscript. This work was supported by Naval Sea Systems Command General Hydromechanics Research Program administered by the David Taylor Naval Research and Development Center under Contract No. N00014-75-C-0378, which was greatly appreciated.

References

1 Arndt, R. E. A., and George, W. K., "Pressure Fields and Cavitation in Turbulent Shear Flows," 12th Symp., Naval Hydrodynamics, Washington, D.C., 1978, pp. 327-39.

2 Barefoot, G. L., "Fluctuating Pressure Characteristics in the Mixing Region of a Perturbed and Unperturbed Round Free Jet," Appl. Res. Lab., Tech. Memo., File No. TM 72-165, Penn State Uni., Aug. 1972.

3 Barthes-Biesel, D., and Acrivos, A., "Deformation and Burst of a Liquid Droplet Freely Suspended in a Linear Shear Field," *J. Fluid Mech.*, Vol. 61, Part 1, 1973, pp. 1-21.

4 Clay, C. S., and Medwin, H., *Acoustical Oceanography: Principles and Applications*, Wiley, p. 191.

5 Devin, C., Jr., "Survey of Thermal, Radiation and Viscous Damping of Pulsating Air Bubbles in Water," *J. Acous. Soc. Am.*, Vol. 31, No. 12, Dec. 1959, pp. 1654-1677.

6 Epstein, P. S., and Plesset, M. E., "On the Stability of Gas Bubbles in Liquid-Gas Solutions," *J. Chem. Phys.*, Vol. 18, No. 11, Nov. 1950, pp. 1505-1509.

7 Franklin, R. E., and McMillan, J., "Noise Generation in Cavitating Flows. The Submerged Water Jet I.," Oxford Uni. Engrg. Lab. Report No. 1312/80.

8 Fuchs, H. V., "Space Correlations of the Fluctuating Pressure in Subsonic Turbulent Jets," *J. Sound and Vib.*, Vol. 23, No. 1, 1972, pp. 77-99.

9 Katz, J., "Construction and Calibration of an Holograph Camera Designed for Micro Bubbles Observation in Cavitation Research," CIT Rept. No. Eng. 183-4, Oct. 1979.

10 Lau, J. C., Fisher, M. J., and Fuchs, H. V., "The Intrinsic Structure of Turbulent Jets," *J. Sound and Vibration*, Vol. 22, 1972, pp. 379-406.

11 Ooi, K. K., "Scale Effects on Cavitation Inception in Submerged Jets," CIT Engineering Report, 183-6, Dec. 1981.

12 Sami, S., Carmody, T., and Rouse, H., "Jet Diffusion in the Region of Flow Establishment," *J. F. Mech.*, Vol. 27, Part 2, 1967, pp. 231-252.

13 Strasberg, M., "The Pulsation Frequency of Nonspherical Gas Bubbles in Liquids," *J. Acous. Soc. Am.*, Vol. 25, No. 3, May 1953, pp. 536-537.

Downloaded 02 Jun 2010 to 171.66.16.91. Redistribution subject to ASME license or copyright; see http://www.asme.org/terms/Terms_Use.cfm

Table 1 A tabulation of the rms pressure fluctuations in various regions of the present jet (polytropic index = 4/3)

	$0 \le r/D \le 0.5$	$0.5 \le r/D \le 1.0$	$1.0 \le r/D \le 1.5$	$1.5 \le r/D \le 2.0$	$2.0 \le r/D \le 2.5$	$2.5 \le r/D \le 3.0$
$4.0 \le X/D < 6.0$	0.25(95)	0.43(38)	0.64(13)	–	–	–
	0.20(92)	0.32(35)	0.45(11)			
$6.0 \le X/D < 8.0$	0.39(43)	0.56(45)	0.76(25)	0.48(3)	–	–
	0.31(41)	0.39(42)	0.65(22)			
$8.0 \le X/D < 10.0$	0.56(24)	0.53(35)	0.56(33)	0.63(14)	–	–
	0.40(20)	0.40(32)	0.43(30)	0.56(13)		
$10.0 \le X/D < 12.0$	0.66(13)	0.69(38)	0.73(31)	0.83(20)	0.94(3)	–
	0.40(11)	0.54(35)	0.61(28)	0.68(17)	0.77(2)	
$12.0 \le X/D < 14.0$	0.64(12)	0.65(28)	0.78(18)	0.59(14)	0.69(1)	0.65(7)
	–	0.51(24)	0.49(14)	–	0.58(10)	–
$14.0 \le X/D < 16.0$	0.60(6)	0.69(10)	0.46(25)	0.68(25)	0.65(9)	0.76(13)
	0.43(5)	–	0.50(22)	–	0.56(8)	0.57(10)

required to analyze the holograms. As an example, it takes approximately ten hours to record all the bubble sizes in a single hologram. This puts a limit to the number of holograms that could be realistically analyzed and consequently affects the accuracy of the statistical results. It is true that an automated, computer aided system could be used to scan the hologram and record the bubble sizes simultaneously as a function of jet position. Unfortunately, such a system is at present unavailable.

Acknowledgments

The authors would like to take this opportunity to thank Professor Sabersky and Dr. Oldenziel for providing many useful suggestions and comments. Dr. J. Katz is deserving of special mention for his valuable assistance on the holographic work. The authors are grateful to Susan Berkley for her help in organizing the manuscript. This work was supported by Naval Sea Systems Command General Hydromechanics Research Program administered by the David Taylor Naval Research and Development Center under Contract No. N00014-75-C-0378, which was greatly appreciated.

References

1 Arndt, R. E. A., and George, W. K., "Pressure Fields and Cavitation in Turbulent Shear Flows," 12th Symp., Naval Hydrodynamics, Washington, D.C., 1978, pp. 327-39.

2 Barefoot, G. L., "Fluctuating Pressure Characteristics in the Mixing Region of a Perturbed and Unperturbed Round Free Jet," Appl. Res. Lab., Tech. Memo., File No. TM 72-165, Penn State Uni., Aug. 1972.

3 Barthes-Biesel, D., and Acrivos, A., "Deformation and Burst of a Liquid Droplet Freely Suspended in a Linear Shear Field," *J. Fluid Mech.*, Vol. 61, Part 1, 1973, pp. 1-21.

4 Clay, C. S., and Medwin, H., *Acoustical Oceanography: Principles and Applications*, Wiley, p. 191.

5 Devin, C., Jr., "Survey of Thermal, Radiation and Viscous Damping of Pulsating Air Bubbles in Water," *J. Acous. Soc. Am.*, Vol. 31, No. 12, Dec. 1959, pp. 1654-1677.

6 Epstein, P. S., and Plesset, M. E., "On the Stability of Gas Bubbles in Liquid-Gas Solutions," *J. Chem. Phys.*, Vol. 18, No. 11, Nov. 1950, pp. 1505-1509.

7 Franklin, R. E., and McMillan, J., "Noise Generation in Cavitating Flows. The Submerged Water Jet I.," Oxford Uni. Engrg. Lab. Report No. 1312/80.

8 Fuchs, H. V., "Space Correlations of the Fluctuating Pressure in Subsonic Turbulent Jets," *J. Sound and Vib.*, Vol. 23, No. 1, 1972, pp. 77-99.

9 Katz, J., "Construction and Calibration of an Holograph Camera Designed for Micro Bubbles Observation in Cavitation Research," CIT Rept. No. Eng. 183-4, Oct. 1979.

10 Lau, J. C., Fisher, M. J., and Fuchs, H. V., "The Intrinsic Structure of Turbulent Jets," *J. Sound and Vibration*, Vol. 22, 1972, pp. 379-406.

11 Ooi, K. K., "Scale Effects on Cavitation Inception in Submerged Jets," CIT Engineering Report, 183-6, Dec. 1981.

12 Sami, S., Carmody, T., and Rouse, H., "Jet Diffusion in the Region of Flow Establishment," *J. F. Mech.*, Vol. 27, Part 2, 1967, pp. 231-252.

13 Strasberg, M., "The Pulsation Frequency of Nonspherical Gas Bubbles in Liquids," *J. Acous. Soc. Am.*, Vol. 25, No. 3, May 1953, pp. 536-537.

DISCUSSION

Reza Taghavi and R. E. A. Arndt[1]

We would like to congratulate the authors for providing a significant piece of information on pressure fluctuations in turbulent jets. However, we do take issue on the authors argument that the discrepancy between their value of the pressure fluctuations R.M.S. and that obtained by other investigators such as Jones et at. [1] and Michalke et al. [2] are merely due to a probe size resolution effect.

Indeed, in a paper by George et al. (3) soon to be published in the *Journal of Fluid Mechanics*, a thorough investigation of the available information obtained from various sources indicates a common value of $\langle p'/\frac{1}{2}\rho U^2 \rangle$ of 0.06. Therefore, something other than probe size is responsible for this discrepancy.

As stated by Tennekes and Lumley [4], in order for a Lagrangian measurement to be stationary, it is necessary that the flow be homogeneous and steady. These conditions are not fulfilled in a turbulent jet flow.

In the experiments reported by the authors, the pressure measurement probes, that is the air bubbles, follow the organized structures of the turbulent jet. Indeed, within a few diameters travel time, uniformly distributed air bubbles tend to migrate toward the core of vortices under the effect of radial pressure gradients [5]. Simple dimensional considerations, as well as photographic data, also tend to prove this argument. When a coordinate system moving with a vortex is considered, it is readily seen that fluid is continuously entering from one side and leaving from the other side of the vortex. Therefore, the pressure measurements reported by the authors are in fact Lagrangian measurements done along immaterial paths (those of vortices), along which the pressure is more likely to deviate from its mean value. That explains the apparent discrepancy between the results of these measurements and (Eulerian) measurements reported by others [1, 2].

[1] St. Anthony Falls Hydraulic Laboratory, University of Minnesota, Minneapolis, Minn. 55414.

Copyright © 1984 by ASME

Downloaded 02 Jun 2010 to 171.66.16.91. Redistribution subject to ASME license or copyright; see http://www.asme.org/terms/Terms_Use.cfm

The technique described by the authors seems to lead to a de Facto conditional sampling in which pressure is only measured when the probe is in the vicinity of vortex cores. The further the bubbles are from the nozzle lip, the closer they are to the core and the larger the measured pressure R.M.S. is. This could explain the increase $\langle p'/\frac{1}{2}\rho U^2 \rangle$ with downstream distance reported by the authors.

Fortunately, pressure measurements obtained with this technique are most relevant to the study of turbulence governed cavitation since the actual sites of cavitation are measurement probes themselves. The resulting value of the non-dimensional pressure R.M.S. should therefore be used for such studies [6].

Additional References

1 Jones et al., "Spectra of Turbulent Static Pressure Fluctuations in Jet Mixing Layers," *AIAA Journal*, Vol. 17, No. 5, 1979.

2 Michalke, A., and Fuchs, H., "On Turbulence and Noise of an Axisymmetric Shear Flow," *Journal of Fluid Mechanics*, Vol. 70, Part 1, 1975.

3 George, W. K., et al., "Pressure Spectra In Turbulent Shear Flow," AIAA Paper No. 80-0985, 1980.

4 Tennekes, H., and Lumley, J. L., *A First Course in Turbulence*, MIT Press, 1972.

5 Cook, T., and Harlow, F., "Vortex Behaviour in Two Phase Bubbly Flow," *Bulletin of the American Physical Society*, Vol. 28, No. 9, 1983.

6 Arndt, R. E. A., and Taghavi, Reza, "Cavitation Inception in Various Types of Shear Flow," To be presented at the ASCE Speciality Conference in Coeur d'Alene, Idaho, 1984.

Authors' Closure

We welcome Professor Arndt's interest in our jet-flow work, a subject which he himself has contributed to so greatly. We did not mean to put too much weight on the comments with which he takes issue. However, in numerous publications to date, for example, Bradshaw [14] and Knapp et al. [15], it has been clearly stated that the measured values of the probes that are similar to those used by the investigators cited by Professor Arndt are caused by two effects, namely, the effects of the fluctuating pressure and velocity effects caused by variations in the local angle of attack at the probe. Since these probes are unable to differentiate between these two effects, the fluctuating pressure measurements would therefore depend on the probe size relative to the scale of turbulence. In addition, Knapp et al. [15] stressed that "the relation between the fluctuating turbulent pressure and the magnitude sensed by a fixed probe includes a factor that depends on the local deceleration of the fluid element approaching the flow. This unsteady quantity is unknown." As a consequence, errors are introduced into the pressure measurements. It was discussed by Strasberg [16] that the probe errors stated above are probably of the *same order of magnitude* as the pressure fluctuations. If this is the case, then any probe size resolution effects could easily have been masked.

Certainly we would agree that the small air bubbles of our experiment do not follow the fluid trajectories—as is well known. It is quite interesting though that both positive as well as negative pressure excursions are observed showing that the bubbles are not simply entrained in the vortices of the flow. Admittedly, we do not know the actual history of this motion and consequently we do not have the true fluid Lagrangian pressure time history. But that it is "conditioned" to report "core" pressures predominantly seems unlikely for the above reasons. We would, of course, welcome quantitative estimates of this effect but the turbulent mixing structure of such flows is still in a developmental state and so this way prove to be difficult to carry out. We would look forward to the opportunity to review Professor Arndt's own recent work in this field and hope that it may soon become generally available.

Additional References

14 Bradshaw, P., *Experimental Fluid Mechanics*, Pergamon Press, Oxford, 1970.

15 Knapp, R. T., Daily, J. W., and Hammit, F. G., *Cavitation*, McGraw-Hill, New York, 1970.

16 Strasberg, M., "Measurements of Fluctuating Static and Total-head Pressure Gradient in a Turbulent Fluid," DTMB Rept. 1779, 1963.

Downloaded 02 Jun 2010 to 171.66.16.91. Redistribution subject to ASME license or copyright; see http://www.asme.org/terms/Terms_Use.cfm

An Acoustic Detection Method of Cloud Cavitation

C. Arai
Ship Propulsion Division,
Ship Research Institute,
Ministry of Transport,
Mitaka, Tokyo, Japan

This paper deals with an investigation of a method which detects the generation of cloud cavitation by the measurement of cavitation noise. Cavitation noise consists of a pulse train with approximately 1 μs rise time and 10 μs duration and has almost ultrasonic characteristics. By utilizing these chracteristics, the pulses of cavitation noise were measured, and a chart of cumulative pulseheight frequency was obtained. On this chart, the noise pattern due to cloud cavitation on a propeller working in nonuniform flow was clearly distinguished from other cavitation patterns.

Introduction

It is well-known that noise is generated when cavitation takes place [1]. Until recently the noise due to cavitation has not been utilized to clarify the mechanism of cavitation and to determine the generating condition of cavitation patterns. Therefore, an attempt has been made for classifying cavitation conditions through the measurement of cavitation noise generated by propellers and other devices. The aim of this research is to detect cloud cavitation (closely related with the erosion of propellers) by means of comparatively simple measurement of noise instead of laborious observation of cavitation at sea. In this paper, a new acoustic method for detecting cloud cavitation is proposed.

Mechanism of the Generation of Cavitation Noise

Minute gas nuclei in water move into a low pressure zone (where the pressure is less than the vapor pressure of water) around a propeller blade, and there grow into vapor cavity bubbles. Then they move into a high pressure zone where they immediately collapse.

Accordingly, it is considered that the transient deformation of the gas bubbles due to their rapid growth and collapse brings about a variation of pressure in the surroundings, and cavitation noise is generated [1]. Further, it is well known that the variation of pressure due to the deformation of the cavity is an impulse type [1]. Since the size and the distribution of the cavitation nuclei present in water are random, cavitation noise consists of a random train of acoustic pulses, even when it is generated in a steady flow condition. In addition, it can be said that even if all of the nuclei in water have the same size, different noises are generated if the cavitating condition varies. When the propeller blades are eroded by cavitation, a strong impact pressure is presumed to act on the propeller blade. Therefore, it is expected that by measuring the noise having a high pressure pulse which consists of high frequency components, a clue to the relationship between cavitation noise and cavitation pattern will be obtained.

Contributed by the Fluids Engineering Division and presented at the Winter Annual Meeting, Phoenix, Ariz., November 14.18, 1982 of THE AMERICAN SOCIETY OF MECHANICAL ENGINEERS. Manuscript received by the Fluids Engineering Division, February 9, 1984.

Condition of Experiments

Table 1 Types of experiments

Experimental object	Characteristic of flow	Test kinds	Test Place
Model propeller	Nonuniform flow	O, M	Small cavitation tunnel of SRI [2]
Full-scale propeller	Nonuniform flow	O, M	Full scale experiment of Ship A and Ship E
Oscillating hydrofoil	Nonuniform flow	M	High Speed Cavitation Tunnel, Dept. of Naval Architecture, Faculty of Engineering, University of Tokyo [3]
Water power turbine model	Nonuniform flow	M	Water Power Lab., Kobe Research Institute, Mitsubishi Heavy Industries, Ltd.

Abbreviations O: Observation of waveform
M: Measurement of waveheight frequency distribution

Table 1 shows the facilities in which the measurement of cavitation noise was carried out, and the types of experiments. The method of installing hydrophones in each experiment will be described below.

Hydrophone. The hydrophone used is a lithium-sulfate ultrasonic vibrator for nondestructive inspection (resonant frequency 10 MHz) [4]. The calibration of hydrophone was made by the reciprocity calibration method. In the calibration, the distance between two hydrophones were arranged so that the acoustic field may be regarded as spherical. Figure 1 shows the result of calibration. Four calibration curves in the figure correspond to different frequency bands. In Case I, the distance between two hydrophones was set at 320 mm, in Case II, at 60 mm and in Case III, at 10 mm. However, in Case III the distance between the hydrophones was almost equal to the diameter of the hydrophone. Therefore, verification was made using the facility at the Defence Technical Research Institute (D.T.R.I.). There the distance between the previously calibrated transmitter and the hydrophone was set at 200 mm,

Copyright © 1984 by ASME

Downloaded 02 Jun 2010 to 171.66.16.91. Redistribution subject to ASME license or copyright; see http://www.asme.org/terms/Terms_Use.cfm

and only the calibration for receiving sensitivity was made. Case IV in Fig. 1 shows the result of calibration. The uncertainty of this calibration is estimated within 3 dB in Case I to III, and within 0.1 dB in Case IV.

Installation of Hydrophone. The installation of hydrophone in each case is shown in Fig. 2. The upper part of Fig. 2 shows the method in the small cavitation tunnel of Ship Research Institute (SRI). A few drops of spindle oil were applied on the plexiglass wiindow of the top side of the cavitation tunnel before the hydrophone was installed with its face on the window pane to prevent the formation of air layer.

In full-scale ship experiments shown in Fig. 2, a plexiglass window was fitted in the hull plate on the starboard side above the propeller. On the window pane was placed a helmet-shaped container filled with water, and the hydrophone was installed in it.

In the oscillating hydrofoil experiments shown in Fig. 2, the observation window was located on the tunnel side, and jigs supported the hydrophone.

In the water power turbine model experiments shown in Fig. 2, the entire casing was made of plexiglass. The hydrophone was installed with its face attached on the portion where cavitation was most likely to occur.

Determination of Conditions. In the experiment on a model propeller in a nonuniform flow, the thrust coefficient K_T[1] was scaled from the full-scale propeller. At the corresponding thrust coefficient and the cavitation number σ [2], the noise measurement was carried out in a simulated ship wake field.

With the full-scale propeller, the cavitating conditions were divided into four types, realized by changing the propeller rpm, and were confirmed by the observation through the window above the propeller.

In the cases of an oscillating hydrofoil and a water power turbine model, four types of cavitation conditions were studied. These are, the condition just before cavitation is observed visually, the condition in which cavitation is fully developed, and two other conditions between these two limiting cases.

Type of Cavitating Conditions. Four types of experimental conditions were employed in the measurements.

Incipient Cavitation Condition. The cavitation number in which the incipient cavitation visually confirmed is designated as σ_i, and $2 * \sigma_i$ was adopted as the cavitation-free condition. The alteration of σ was realized by changing pressure. At $2 * \sigma_i$, the measuring instruments were tuned so that all the electrical disturbances were eliminated. Then it was found that there was no component in the background noise having a rise time as rapid as that of cavitation noise. However, when the test condition was set near $1.5 * \sigma_i$, impulses having a rapid rise time and considered to be due to cavitation became perceivable. Therefore, when the inception of cavitation is visually recognized, the impulse has already reached a considerable strength.

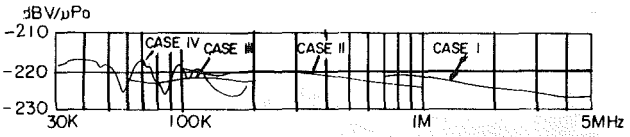

Fig. 1 Calibration result of hydrophone

Case	Distance	Place of Calibration
I	320 mm	Ship Research Institute (SRI)
II	60 mm	SRI
III	10 mm	SRI
IV	200 mm	D.T.R.I.

[1] $K_T = T/\rho n^2 D^4$

[2] $\sigma_{(i)} = (P_{(i)} - P_v)/0.5\rho n^2 D^2$ where T: thrust of propeller in N, ρ: density of water in kg/m^3, n: revolution of propeller in 1/s, D: diameter of propeller in m, $P_{(i)}$: ambient pressure at the depth of propeller (at Incipient Condition) in Pa, and P_v: vapor pressure of water in Pa.

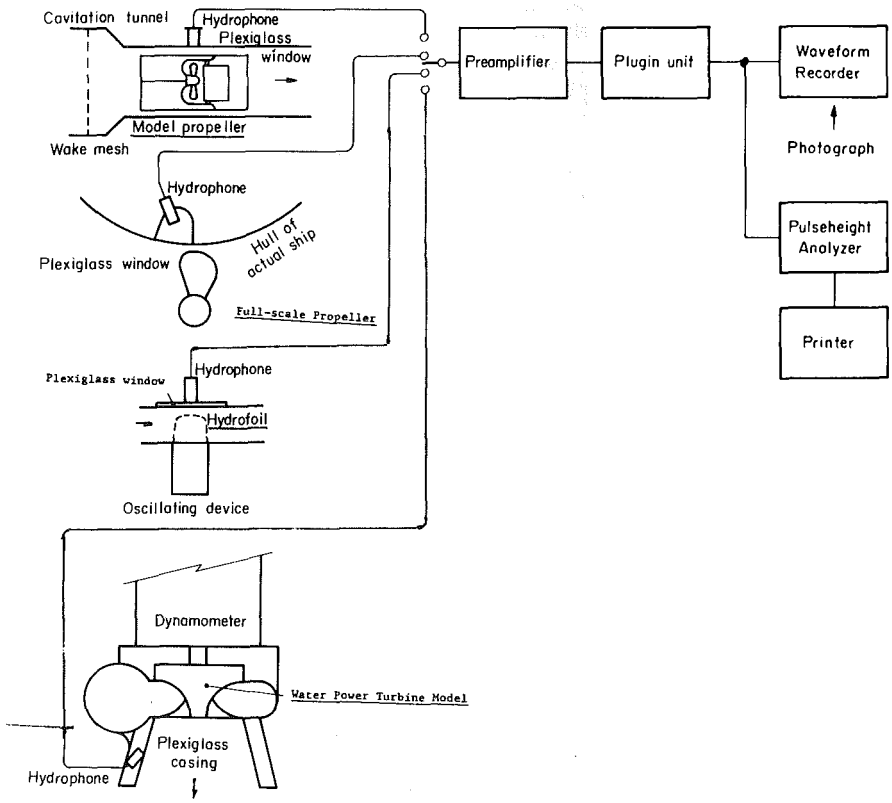

Fig. 2 Installation of hydrophone and block diagram of instrumentation

Downloaded 02 Jun 2010 to 171.66.16.91. Redistribution subject to ASME license or copyright; see http://www.asme.org/terms/Terms_Use.cfm

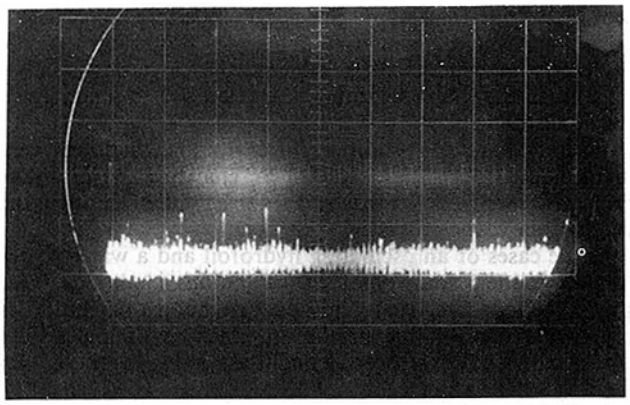

Photo 1 Noise waveform due to cavitation (model propeller in nonuniform flow)
sensitivity of vertical axis: 10 mV/div
" horizontal axis: 1 ms/div

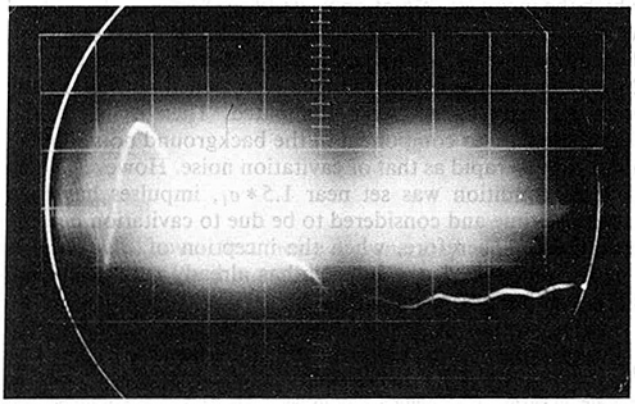

Photo 2 Noise waveform due to cavitation (model propeller in nonuniform flow)
sensitivity of vertical axis: 10 mV/div
" horizontal axis: 1 μs/div

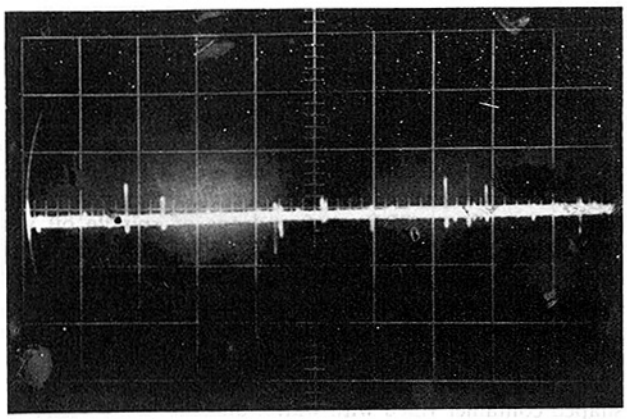

Photo 3 Noise waveform due to cavitation (full-scale propeller in nonuniform flow)
sensitivity of vertical axis: 1 V/div
" horizontal axis: 1 ms/div

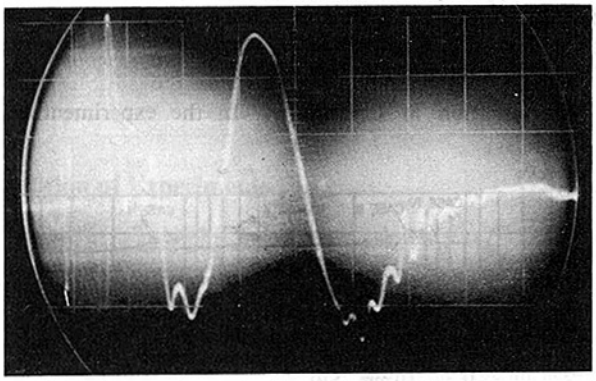

Photo 4 Noise waveform due to cavitation (full-scale propeller in nonuniform flow)
sensitivity of vertical axis: 1 V/div
" horizontal axis: 1 μs/div

Accordingly, the state in which the cavitation is not visually recognized but its noise is perceived ($1.5 * \sigma_i$), will be called "Incipient Cavitation Condition."

Tip Vortex Cavitation Condition. When the cavitation number of the model propeller is made smaller than σ_i, tip vortex cavitation takes place in a spiral fashion, and is gradually stabilized. This state will be called "Tip Vortex Cavitation Condition."

Sheet Cavitation Condition. When the cavitation number of a model propeller is made smaller than that of the tip vortex cavitation condition, a thin cavity spreads on the back side of the blade toward the root from the tip. This state will be called "Sheet Cavitation Condition."

Cloud Cavitation Condition and Others. In the case of a model propeller working in a nonuniform flow, if the cavitation number is made sufficiently small, cloud or mistlike cavities appear in the portion of the blade where cavities collapse. This state will be called "Cloud Cavitation Condition."

In the experiment on a two dimensional oscillating hydrofoil, the condition of the lowest cavitation number will be called "Supercavitation Condition," because the cavity is longer than the hydrofoil.

An intermediate condition between the incipient and sheet cavitation conditions with the oscillating hydrofoil and the water power turbine model, will be called "Semi-Sheet Cavitation Condition," because there is no tip vortex cavitation in either case.

Observation of Cavitation Noise Waveform

Using a storage oscilloscope, the observation of noise waveform due to cavitation was made. Two kinds of recording time – 10 ms and 10 μs – were employed in the experiments. In the case of 10 μs, several noticeable waveforms were obtained in the model propeller and full-scale propeller experiments. The discussion will focus on these results.

Photos 1 and 2 show the waveforms of cavitation noise in the model propeller experiment. The sweep rates (Horizontal axis) are 1 ms/div and 1 μs/div, respectively. They are the cases in which remarkable variation in waveforms was obtained. Photos 3 and 4 show the waveforms of cavitation noise in the full-scale propeller experiment.

It is seen from these photos that the duration of pressure variation due to the growth and collapse of a cavity bubble is several μs, and the rise time of pressure variation is impulsive having a duration of about 1 μs. Further, both the occurrence and the pulseheight of cavitation noise are random.

There is no significant difference in the rise time of pressure pulses in model propeller and fullscale propeller experiments, although the amplitude ratio is 1:10-100 (the scale ratio of model to fullscale propeller is 1:34.483). The reason that the base line of Photo 1 is thick is that the amplifier gain was increased, resulting in the increase of the amplifier noise.

From the above results, the followings may be stated:

(*a*) In order to catch the pulse having a rise time of 1 μs, a detector and an amplifier with 5 MHz as the upper limit of the

Downloaded 02 Jun 2010 to 171.66.16.91. Redistribution subject to ASME license or copyright; see http://www.asme.org/terms/Terms_Use.cfm

frequency band are required.[3] Furthermore, since the duration of the phenomenon is estimated to be 7–10 μs, 15–20 kHz is required as the lower limit of the frequency band.[4]

The reason that the lower limit of frequency band was set is to prevent mechanical vibrations from entering into input signals. Most of the mechanical vibrations are at 10 kHz or less.

(*b*) There is no theoretical evidence that the waveforms thus obtained are from cavitation noise. However, there are no noise sources in the acoustic field around the propeller having rise time of 2 μs or less, except cavitation. Therefore, these waveforms may be treated as those of cavitation noises.

(*c*) Photos 1 and 3 show that the waveform of cavitation noise is not necessarily uniform and includes a variety of pulseheights. The reason is the difference in cavitating conditions, in addition to the random size of the cavities. Thus when the cavitatin conditions (for example, cloud cavitation, sheet cavitation, etc.) differ, the height of cavitation noise pulses varies. Further, it is expected that by inspecting the distribution of the pulseheight, the condition in which erosion occurs on a propeller will be identified.

(*d*) The ratio of pulseheight in cavitation noise between model propeller and full-scale propeller is about 1:100. However, the required frequency band is the same, so that the same measuring instruments can be used simply by adjusting the gain of the amplifier. Although the characteristics of this noise seems to have a law of similarity, it is still necessary to accumulate more data having high accuracy.

Measurement and Analysis of Pulseheight Frequency Distribution

The pulseheight frequency distribution of cavitation noise was measured in each test with a pulseheight analyzer which is used in the atomic field.

In an initial test stage (i.e., a propeller shaft turning condition in full-scale propeller experiment) in which no cavitation took place, the earth point of measuring circuit and others were regulated so that there were no input signals. When cavitation noise was measured, the stroboscope was turned off so that the stroboscope pulse did not disturb the cavitation noise measurement.

The error in the measured values of the pulseheight (horizontal axis) shown in Figs. 3–7 is estimated to be ± 2.5 percent of measured maximum value. The measured maximum value is about 200 Pa in model experiments and 1 kPa in full-scale experiments. Therefore, the estimated error is ± 5 Pa in Figs. 3, 6, and 7, and ± 25 Pa in Figs. 4 and 5. The estimated errors in Figs. 8–12 are the same with those of the corresponding figures.

Analysis of Pulseheight Frequency Distribution on Semi-Logarithmic Paper. Figures 3–7 show the pulseheight frequency distribution plotted on semi-logarithmic scales and the sketches representing several types of cavitation. As the range of the frequency is considerably wide, a logarithmic frequency scale is used. The symbols ○, △, □, and ◇ represent the incipient, the tip vortex (or semi-sheet), the sheet, and the cloud (or super-) cavitation conditions, respectively. Figure 3 shows the model experiment of Ship A. Figures 4–5 show the full-scale experiments of Ship A and Ship E. Figure 6 shows the oscillating hydrofoil. Figure 7 shows the water power turbine model.

What may be said from Figs. 3–7 is that the cloud cavitation condition (◇) shows the existence of the components which are small in number but large in pulseheight. Analysis of these components will be described below.

Analysis of Pulseheight Frequency Distribution on Logarithmic Probability Paper. In the case of a phenomenon containing the component of a large variance, the use of logarithmic normal probability paper is more suitable than normal probability paper. Therefore, the generating frequency of the acoustic pulseheight of cavitation noise was plotted using logarithmic normal probability paper.[5] An approximately linear distribution was obtained in the logarithmic normal probability paper. This means that the distribution of the intensity of cavitation noise pulse is logarithmically random.

From the above discussion, the pulseheight frequency distribution of cavitation noise in each experiments shown in Figs. 3–7 is arranged on the logarithmic normal probability

[3] The upper limit of the frequencies constituting a pulse whose rise time and fall time are 1 μs, respectively, does not exceed 500 kHz. And if the minimum resonant frequency of the measuring system is more than ten times greater than the constituting frequencies of the pulse, the measurement error does not exceed 1 percent.

[4] In the present measuring system, the time constant of the rate network was made equal to the duration of the phenomenon, in order to cut off the low frequency band (noise). However, this introduces an error of 1.3 percent (for sine waves) to 37 percent (for rectangular waves) in general. Though it is not likely that the measurements error above mentioned actually occurs because the cavitation noise has a waveform of a unit pulse, it would have been safer to adopt a longer time constant for the rate network of the measuring system.

[5] A section paper having $100*\int_{-\infty}^{u} 1/\sqrt{2\pi}\, e^{-u^2/2}$ scale on a vertical axis and a logarithmic scale on a horizontal axis.

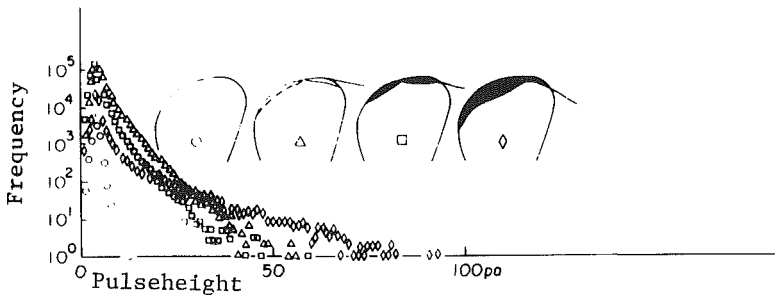

Condition of cavitation		σ	K_1
Incipient	○	6.4	0.104
Tip vortex	△	4.5	0.143
Sheet	□	3.5	0.132
Cloud	◇	2.1	0.150

Fig. 3 Pulseheight distribution (model propeller of Ship A)

Downloaded 02 Jun 2010 to 171.66.16.91. Redistribution subject to ASME license or copyright; see http://www.asme.org/terms/Terms_Use.cfm

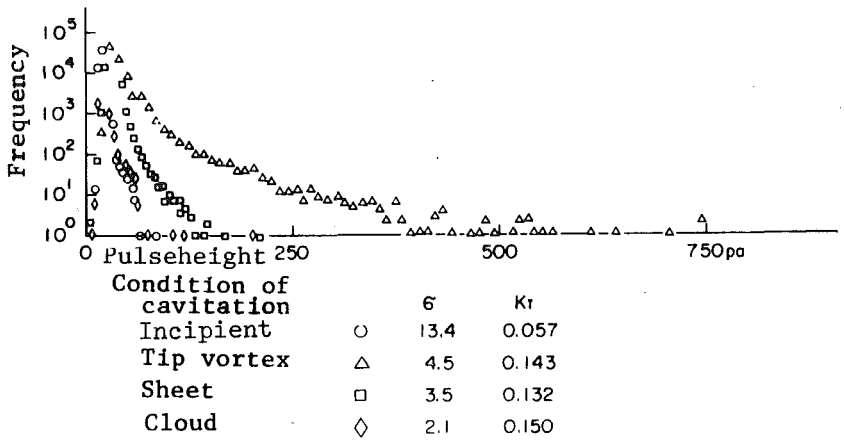

Fig. 4 Pulseheight distribution (full-scale propeller of Ship A)

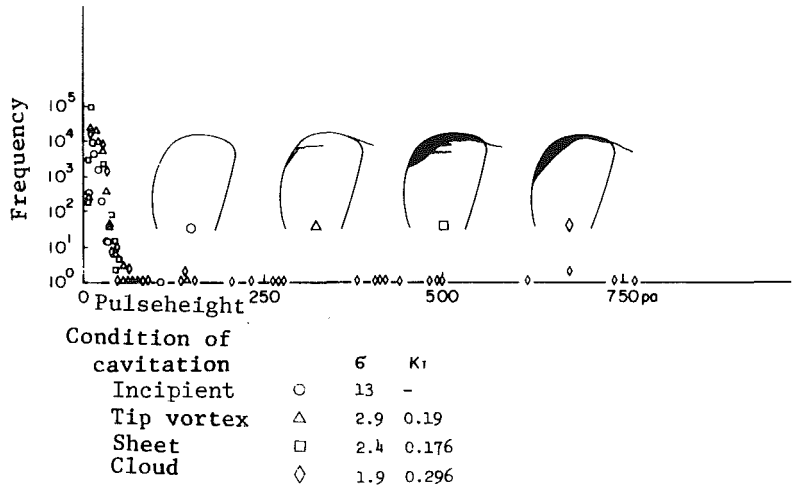

Fig. 5 Pulseheight distribution (full-scale propeller of Ship E)

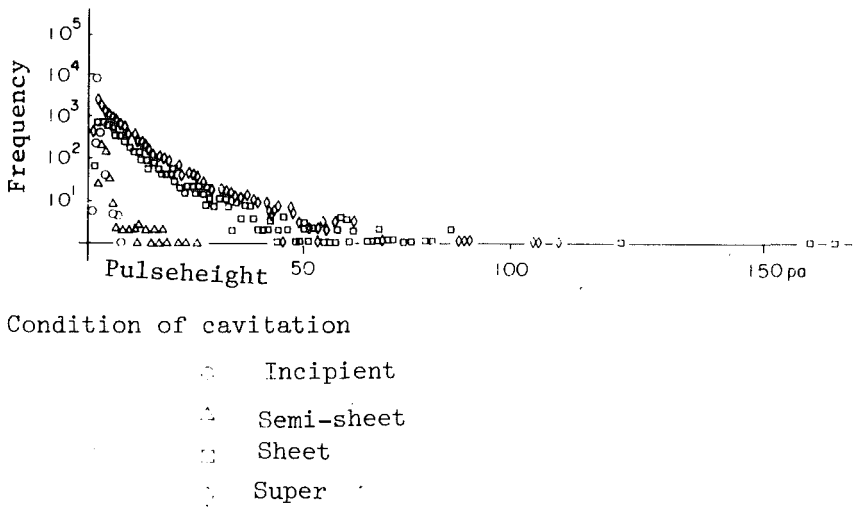

Fig. 6 Pulseheight distribution (oscillating hydrofoil)

paper (Figs. 8–12). These figures are sometimes called cumulative frequency charts because the vertical axes show cumulative frequency. From these results, it may be said that in any experimental condition, almost linear distribution is obtained in the cumulative pulseheight frequency range of 20–80 percent.

The characteristic of the distribution on logarithmic normal probability paper will be described below, focusing on the "sag" and break point in the upper portion.

(*a*) The cavitation experiment on the model propeller of Ship A, shown in Fig. 3, and the full-scale experiment on Ship A, shown in Fig. 4, correspond to Figs. 8 and 9. The incipient cavitation condition data (○) of these figures can be regarded as a linear distribution, i.e., logarithmic normal distribution,

Downloaded 02 Jun 2010 to 171.66.16.91. Redistribution subject to ASME license or copyright; see http://www.asme.org/terms/Terms_Use.cfm

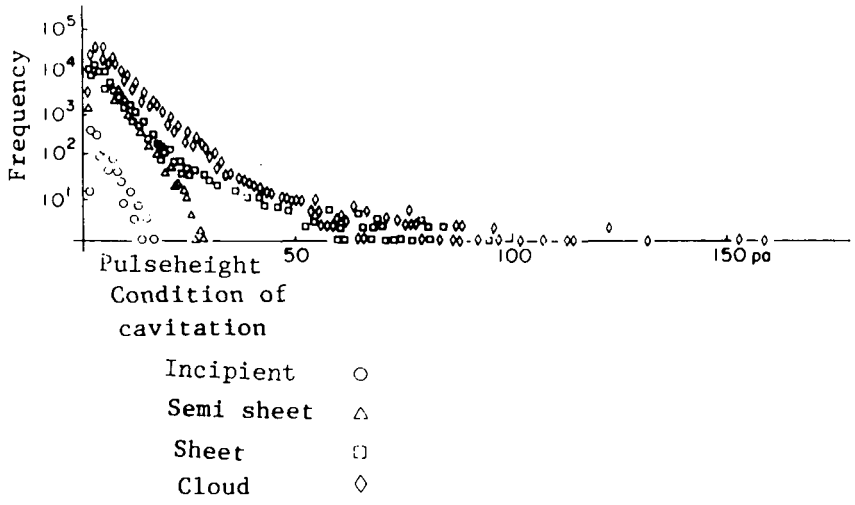

Fig. 7 Pulseheight distribution (water power turbine model)

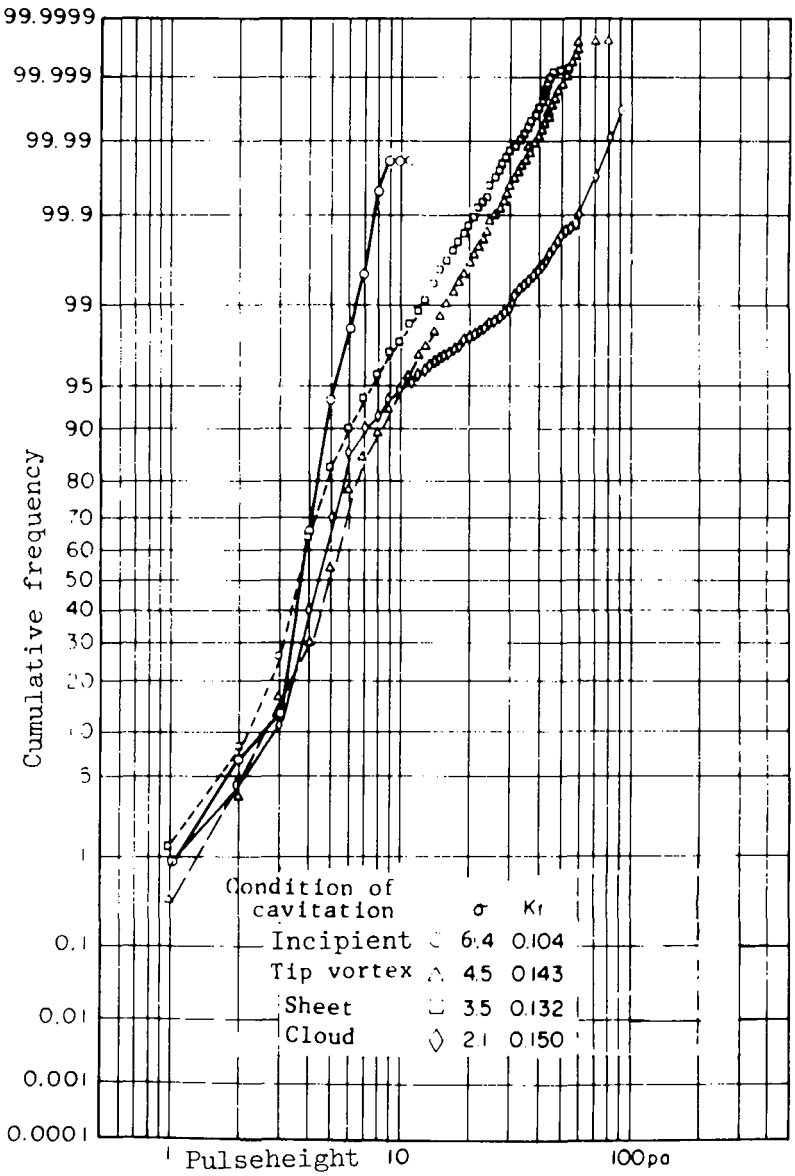

Fig. 8 Plot on a logarithmic probability paper (model propeller of Ship A)

Downloaded 02 Jun 2010 to 171.66.16.91. Redistribution subject to ASME license or copyright; see http://www.asme.org/terms/Terms_Use.cfm

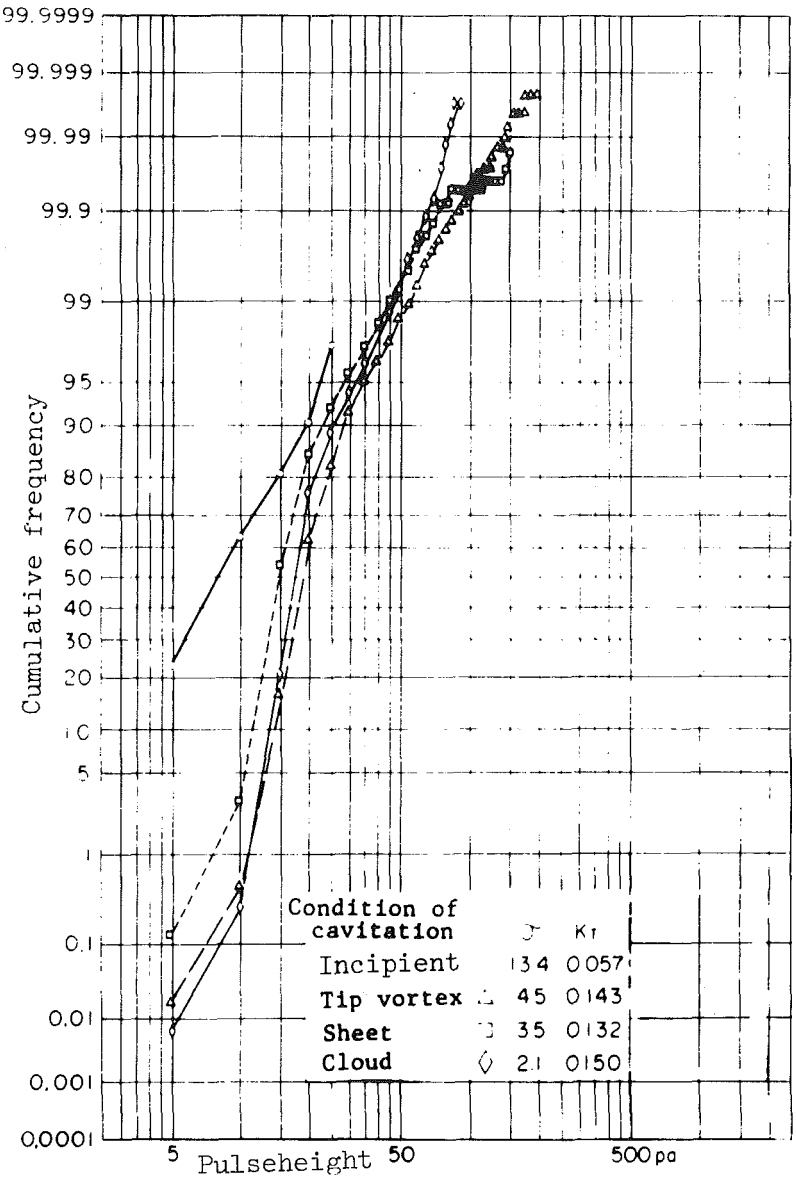

Fig. 9 Plot on a logarithmic probability paper (full-scale propeller of Ship A)

except for the two lowermost points in Fig. 8 and one uppermost point in Fig. 9. In the tip vortex cavitation condition (△) and in the sheet cavitation condition (□) in these figures, the distributions are linear, except for the breakpoints in 90 and 10 percent in Fig. 8 and the breakpoint in 5–0.5 percent in Fig. 9.

The distribution in the cloud cavitation condition (◇) in Fig. 8 clearly shows a "sag" in the upper portion, which is typical of components small in number but large in pulseheight. This is considered to show the existence of the impulsive pressure which is generated by cloud cavitation.

The distribution in the cloud cavitation condition (◇) of Fig. 9 looks not very different from those in the tip vortex or sheet cavitation condition, but a mild sag starting near 90 percent is still observed. When the measurement of the cloud cavitation condition of Ship A was made, a lot of air bubbles were present in the flow field near the propeller because the draft was shallow. Air bubbles in the transmission path of cavitation noise reduce the intensity of the noise, especially in the ultrasonic range. As the result, the presence of the sag is not so obvious as in the model experiment. The measurement time should have been longer in order to get more instances in which there were few bubbles in the transmission path.

(*b*) The result of the full-scale experiment in Ship E is shown in Figs. 5 and 10. In the incipient cavitation condition (○), the points lower than 99.7 percent are linearly distributed. The distributions in the tip vortex cavitation condition (△) and in the sheet cavitation condition (□) are similar to that in the incipient cavitation condition (○), except that the components of large pulseheight are fewer, and that the gradient of the component in 80–99.9 percent is greater, (i.e., smaller standard deviation). In the cloud cavitation condition (◇), the distribution has a clear "sag." In that condition, the cloud cavitation was visually confirmed. A small amount of cloud cavitation was observed in the tip vortex cavitation condition (△) and in the sheet cavitation condition (□). The existence of cloud cavitation seems to be indicated also in Fig. 10.

The clearness of the sag on logarithmic normal probability paper does not necessarily reflect the intensity of erosion. The range of the sag, i.e., the amount of the pulses which are due to cloud cavitation seems to be more important. Although the sag in Fig. 9 is much less evident than that in Fig. 10, the range of the sag in Fig. 9, starting at 90 percent, is wider than that in Fig. 10, starting at 99.9 percent. The erosion of the propeller

Downloaded 02 Jun 2010 to 171.66.16.91. Redistribution subject to ASME license or copyright; see http://www.asme.org/terms/Terms_Use.cfm

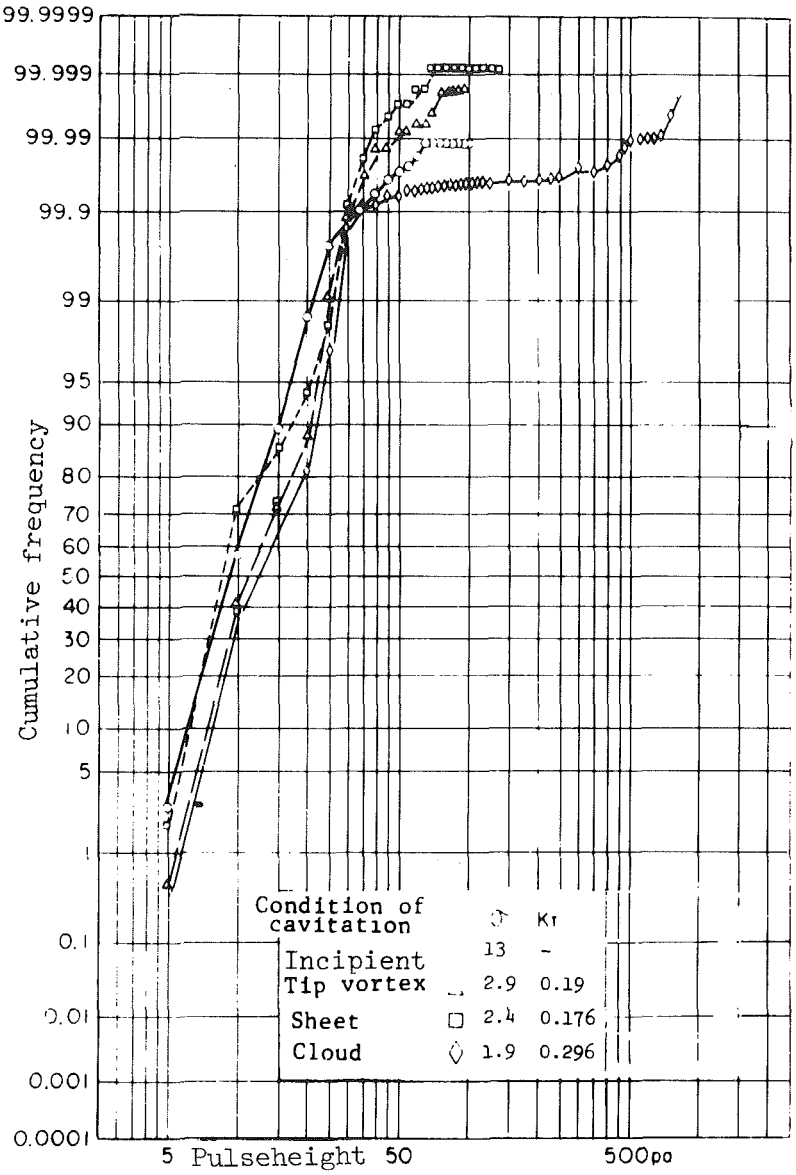

Fig. 10 Plot on a logarithmic probability paper (full-scale propeller of Ship E)

of Ship A (Fig. 9) after one year service was found to be much severer than that of Ship E (Fig. 10) [5].

(*c*) In the results of oscillating hydrofoil experiments shown in Figs. 6 and 11, the distribution in the incipient cavitation condition (○) is almost linear. In the semi-sheet cavitation condition (△), a considerable "sag" exist in the region 95 percent or higher, which shows the existence of components small in number but large in pulseheight. On the other hand, in the sheet cavitation condition (□) and super-cavitation condition (◇), the gradient somewhat decreases and the standard deviation increases. Overall, linear distributions are formed.

In the super-cavitation condition, severe erosion cannot be expected to occur because the cavity is longer than the hydrofoil, and no sag is seen in the distribution. An interesting point is that there is a sag in the semi-sheet cavitation condition where the cavities are much less developed than in the sheet cavitation condition, where the distribution is quite linear.

(*d*) In the water power turbine model experiment shown in Figs. 7 and 12, almost linear distributions are seen in the incipient cavitation condition (○) and in the semi-sheet cavitation condition (△). In the sheet cavitation condition (□), a sag is clearly seen near 99 percent, which suggests that the cloud cavitation has started to occur. In the cloud cavitation condition (◇), though it appears that there is no sag at first glance, there is a slight sag starting at 95 percent. Therefore, it is suspected that the cloud cavitation which already appears in the sheet cavitation condition is more frequently generated in the cloud cavitation condition.

Discussion

From the above experimental results, the following points may be made:

(*a*) As the acoustic pulses of cavitation noise have a logarithmic normal probability distribution, the existence of components small in number but large in pulseheight in the cavitation noise generated by a propeller working in nonuniform flow was made clear on the cumulative pulseheight frequency chart, and the cloud cavitation was successfully detected through its characteristic distribution

Downloaded 02 Jun 2010 to 171.66.16.91. Redistribution subject to ASME license or copyright; see http://www.asme.org/terms/Terms_Use.cfm

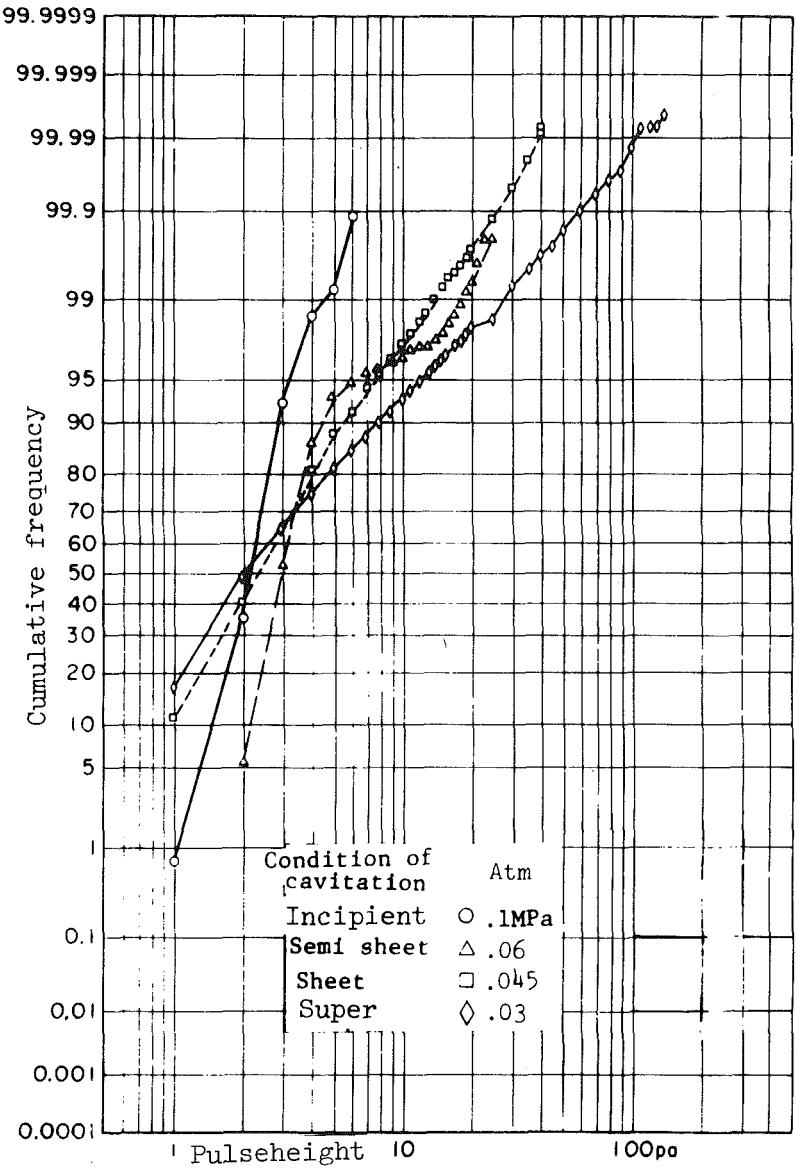

Fig. 11 Plot on a logarithmic probability paper (oscillating hydrofoil)

shown on the chart. At the same time, a part of the cloud cavitation was visually confirmed.

(*b*) The pulse generation frequency of cavitation noise increases from an incipient cavitation condition (○) to a tip vortex cavitation condition (△). Although the pulse generation frequency often becomes smaller in a sheet cavitation condition (□) than in a tip vortex cavitation condition, large pulseheight components begin to be generated. Therefore, the sheet cavitation condition (□) may be characterized by the generation of large pulseheight components. The shift to cloud cavitation condition (◇) may be characterized by further increase of the large pulseheight components. In a cloud cavitation condition, cavitation noise is often damped by air bubbles, in which case the measurement should be prolonged.

(*c*) The comparison of the results of Ship A and Ship E after one year service of operation shows that a propeller whose cavitation noise has more large-pulseheight components suffers from severer cavitation erosion, since the erosion of the propeller of Ship A was found to be severer than that condition.

(*d*) With regards to the instrumentation, the author recommends the use of a hydrophone with a similar character but with better shielding, a logarithmic preamplifier with rapid response in pulseheight measurement to make data processing easier, a noiseless linear preamplifier and a digital type analogue recorder for the measurement of noise waveform and a micro computer system for processing the measured data.

Conclusion

In order to detect the condition of cavitation by the measurement of cavitation noise of a ship's propellers, foil and water power turbine model, the pulseheight frequency of the cavitation noise was measured by utilizing the fact that such ultrasonic impulse components are scarcely influenced by other disturbances. As a result, a logarithmic normal probability distribution was obtained on a logarithmic probability paper, and the cloud cavitation induced by the propeller working in a nonuniform flow was clearly distinguished. However, the examples used are limited and various problems still remain unsolved, especially with regard to other test bodies like an oscillating hydrofoil or a water power turbine model. Therefore, it will be necessary to extend this study by applying the method to many other cases and

Downloaded 02 Jun 2010 to 171.66.16.91. Redistribution subject to ASME license or copyright; see http://www.asme.org/terms/Terms_Use.cfm

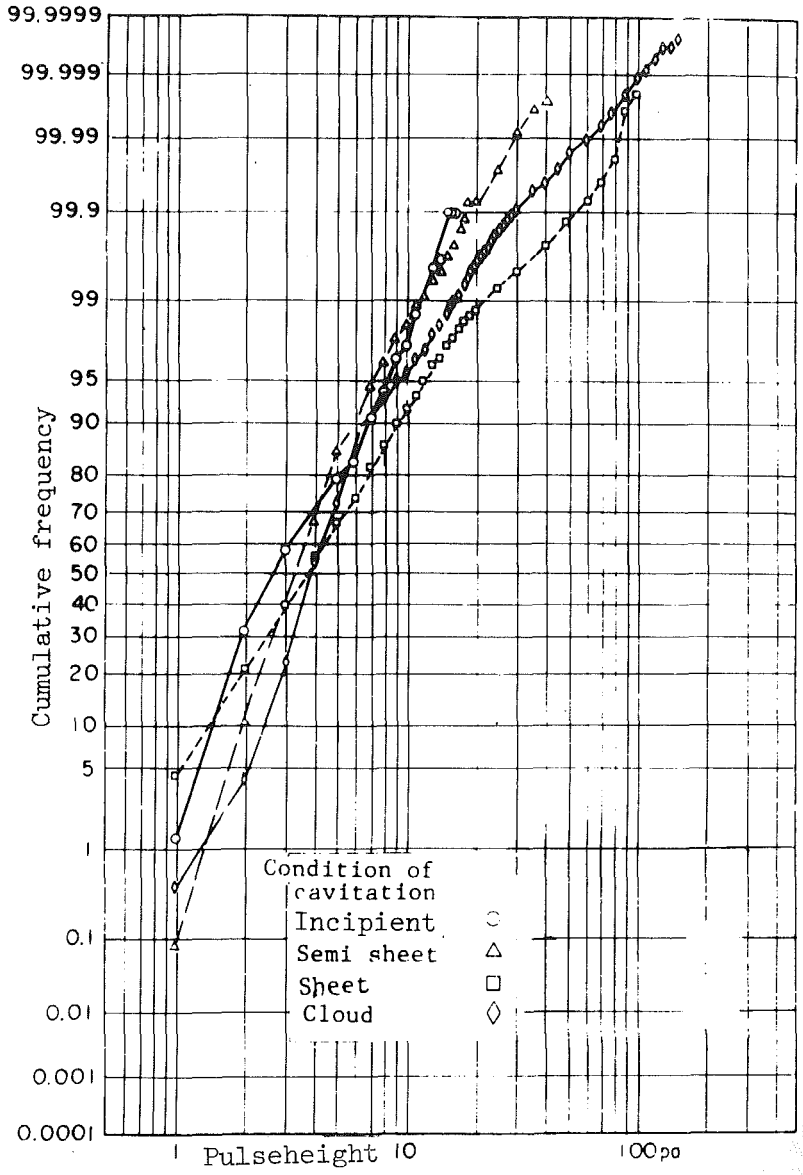

Fig. 12 Plot on a logarithmic probability paper (water power turbine model)

accumulating more data. That is required both in order to develop the method's ability to distinguish cavitation noise, and to establish a more accurate and easily applicable method for detecting cavitation noise.

Acknowledgments

The author is grateful for the support, given by the SRI staff in conducting this research, especially, the late Mr. T. Ito who was Director General of Ship Research Institute, and Dr. H. Takahashi, Director of Ship Propulsion Division, SRI. Dr. Y. Kodama, a staff of Cavitation Section of Ship Propulsion Division was very helpful in discussion for completion of this paper. The author also acknowledges Dr. Robert Latorre for his kind advice and suggestions.

References

1 Fitzpatrick, H. M., and Strasberg, M., "Hydrodynamic Source of Sound," *1st Symposium on Naval Hydrodynamics*, Sept. 1957, pp. 247-257, and pp. 278-279.

2 van Manen, J. D., "Questionnaire of Water Tunnels," *Report of Cavitation Committee*, 12th International Towing Tank Conference (ITTC), 1969, pp. 38-45.

3 Latorre, R., "TVC Noise Envelope—An Approach to Tip Vortex Cavitation Noise Scaling," *Journal of Ship Research*, Vol. 26, No. 1, Mar. 1982, pp. 65-75.

4 Kasai, C., and Okuyama, D., "Active Damping by Utilizing Transient-Response Characteristics of Piezoelectric Vibrator," *Annual Proceedings of Acoustic Society of Japan*, Vol. 1, 1969 (in Japanese).

5 Takahashi, H., et al., "Comparison of Cavitation Phenomena Between the Actual and Model Propeller and Erosion Survey on the Actual Propeller," *Proceeding of 14th ITTC*, Vol. 2, 1975, pp. 261-279.

Downloaded 02 Jun 2010 to 171.66.16.91. Redistribution subject to ASME license or copyright; see http://www.asme.org/terms/Terms_Use.cfm

DISCUSSION

R. Latorre[1]

The author is to be congratulated on the development of a diagnostic technique for detecting cloud cavitation on marine propellers. Previous studies have linked intense cavitation erosion with the appearance of cloud cavitation. In the past the presence of cloud cavitation would be detected by observation of the scale model propeller operating in a simulated shipwake or by actual full-scale observation. While there has been progress in numerical analysis using lifting surface propeller design programs, it is not clear how to describe the limiting conditions for cloud cavitation in the programs. The acoustic technique of the author should contribute to establishing the presence of cloud cavitation as well as providing a basis for determining the limiting conditions required for numerical analysis. My discussion concerns 3 items presented in the paper.

1) The data presented in the paper are useful to increase our understanding of the structure of cavitation and the characterization of its noise. In the study of tip vortex cavitation, reference [3] of the author's paper, noise measurements were presented showing cavitation noise would be recorded before the visible appearance of tip vortex cavitation. The threshold was the background cavitation tunnel noise level. The author's measurements of noise at the "incipient cavitation condition" further supports this observation. Does he feel the inception of cavitation should be determined by acoustic measurement?

2) The collapse of isolated cavitation bubbles has been the basis of our understanding of the mechanism of cavitation noise. The author's photos T-4 showing the cavitation noise waveforms for model and full scale propellers are useful to further our understanding. In item *d* of the discussion on the cavitation noise wave form observation, the author mentions that the pulse height seems to have a law of similarity. In order to qualify this, it is necessary to specify the velocity V, pressure P, distance from propeller to hydrophone r, and the fluid density ρ, for both the model and full scale propeller measurements. Could the author give the values of these parameters corresponding to Photos 1.2 and 3.4 in a table? Based on this information which of the scaling relationships KMW [D-1] or Levkovskii's [D-2], [D-3] correctly predicts the measured full scale pulse height from the scale model propeller measurements? In [3], I found the KMW method best fitted the experimental tip vortex cavitation noise measurements.

3) I would like to ask the author if he has measured, or if he would expect large distortion in the pulse height distribution when model or full scale propellers with soft, elastic, or paint-ink coatings are tested? Hammitt [D-4] discusses cavitation resistance in terms of surface hardness and indicates that soft surfaces effect the bubble collapse and formation of micro-jets. Recent work in the USA [D-5] has shown the feasibility of using soft elastometric materials to eliminate cavitation erosion on commercial ship propellers. The author's acoustic technique could provide a means to evaluate the effectiveness of these coatings in service.

In closing I thank the author for giving me this opportunity for discussing his research and look forward to further results from his studies on cavitation noise in the future.

[1] Associate Professor, School of Naval Architecture and Marine Engineering, University of New Orleans, New Orleans, La.

Additional References

D-1 Bjorheden, O., and Astrom, L., "Prediction of Propeller Noise Spectra," Det-Norske Veritas Symposium on "Hydrodynamics of Ship and Offshore Propulsion Systems," Paper 1/2, Session 4, Oslo, Mar. 1972.

D-2 Levkovskii and Yu. L., "Modeling of Cavitation Noise," *Soviet-Physics Acoustics*, Vol. 13, No. 3, 1968, pp. 337–339.

D-3 Levkovskii, Yu. L., "Prediction of the Spectral Levels of Cavitation Noise," *Soviet-Physics Acoustics*, Vol. 26, No. 6, 1980, pp. 495–497.

D-4 Hammitt, F. G., *Cavitation and Multiphase Flow Phenomena*, McGraw-Hill, New York, 1980.

D-5 Dashnaw, F. T., et al., "Development of Protective Covering Systems for Steel and Bronze Ship Propellers," *Transactions SNAME*, Vol. 88, 1980, pp. 55–74.

Authors Closure

Thank you for your valuable discussion which I am happy to reply.

1) The acoustic detection of cavitation is limited to determining the existence of cavitation noise. Cavitation inception is typically defined as the condition when cavitation is continuously visible on an object.

There are several differences between these two cases. The first detects if a cavitation nucleus under goes collapse, while the second is more continuous process of cavitation formation and collapse.

Therefore, it is best to introduce a new definition for cavitation inception based an acoustic measurement or treat this acoustic cavitation inception measurement data separately.

2) The pulse-height of each cavitation event is random, which makes it difficult to compare the pulse-height shown in each photograph. However, using the most frequently measured value of cavitation noise for such comparison should provide useful data. Unfortunately, this requires that the instrumentation be linear and stable which was not always the case in my measurements. I regret that I am unable to reach a definite answer due to my instrumentation.

3) I have not made experiments where the cavitation noise from model or full-scale propeller with soft surface – soft coatings – was measured. Such experiments would be of great value to study the relationship between the collapse of cavitation and the acoustic revibration – propagation of noise from the surface.

Again, I appreciate your interest in my work.

Copyright © 1984 by ASME

Downloaded 02 Jun 2010 to 171.66.16.91. Redistribution subject to ASME license or copyright; see http://www.asme.org/terms/Terms_Use.cfm

S. M. Ghiaasiaan
Science Applications International Corporation,
Hermosa Beach, CA 90254

I. Catton
School of Engineering and Applied Science,
University of California,
Los Angeles, Calif. 90024

R. B. Duffey
Electric Power Research Institute,
Palo Alto, Calif. 94303

Thermal Hydraulic and Two-Phase Phenomena in Reflooding of Nuclear Reactor Cores

A quasi-steady, two-dimensional thermal hydraulic analysis of the two-phase region formed ahead of a quench front during reflooding of a slab or cylindrical core is carried out, and the results for slab geometry are compared with the experiment. It is shown that the two-phase level variation in the core is due to the transverse heat flux power profile, and is sensitive to the assumed pressure-drop boundary condition for the bundle, while the effects of crossflow and axial friction are small. Implicit expressions are given for predicting the quasi-steady two-phase level variation across slab and cylindrical cores.

Introduction

Two-phase phenomena govern many processes of importance to thermal hydraulic aspects of nuclear safety as well as other energy related processes. In this work, reflooding of a nuclear reactor core after a loss of coolant accident is studied.

Reflooding of a reactor core has been the subject of a number of studies. References [1–4] represent reviews of the bulk of the experimental and theoretical studies of reflooding. For the most part, the process of reflooding has been reduced to a one or two-dimensional conduction problem coupled to the flow by heat transfer coefficients representing different flow regimes. The level of sophistication of a given study is related to the number of heat transfer regions or regimes used. Observations of the reflood process show that a two phase region forms ahead (above) of the quench front, except for very low flooding rates, (the quench front being the location where water contacts the hot surface in more than a dropwise manner). The cooling which takes place in the two-phase region is higher than normally found in film boiling and is commonly called precursory cooling. Describing the precursory cooling and the reflood process requires knowledge of the thermal hydraulic behavior occurring in the two-phase region. The upper boundary of the two-phase region is the lower boundary of a region of low heat transfer coefficient where only vapor and isolated droplets are available for cooling.

The thermal hydraulic processes governing the two-phase region have recently been the subject of several studies. A one-dimensional quasi-steady model for predicting the two-phase region boundary under low flow conditions was proposed by Sun et al. [5]. Heat transfer correlations have been proposed by Sudo [6] and Murao and Sugimoto [7]. The proposed correlation of Murao and Sugimoto [7] shows the significant effect of local void fraction on heat transfer coefficient.

This paper presents results of experiments carried out with a scaled 1692-rod slab core, and describes a two-dimensional analytical treatment of the two-phase region forming ahead of the quench front during reflooding of cylindrical and slab cores. Effects of crossflow and axial friction are examined. The theoretical approach is compared with experimental results for the 1692-rod slab core.

Contributed by the Fluids Engineering Division of THE AMERICAN SOCIETY OF MECHANICAL ENGINEERS and presented at the Fluids Engineering Conference, Saint Louis, Mo., June 1982. Manuscript received by the Fluids Engineering Division, September 22, 1982. Paper No. 82-FE-1.

Experimental Study

Experimental Apparatus. The experimental facilities used in this study are described in detail elsewhere [8]. The test section consisted of an 18 × 94 rod slab core with the dimensions indicated in Fig. 1. The pitch to diameter ratio, as well as the core aspect ratio, was in agreement with most PWR open lattice designs. The rods and all structural components were made from 304 stainless steel. The test section was contained in a quartz box which made viewing possible. Water was heated to the desired temperature in a tank. At the start of each run, a solenoid valve was opened to allow the water to flow into the bottom of the test section. A pump and pre-adjusted globe valve maintained a constant flow of the water to the test section.

The outlet nozzle at the top of the test section, having an area of 0.0161 m^2, guided the carry-over water into a barrel for collection. The test section was heated to the desired temperature by induction heating before each run. Due to the existence of radiation heat loss from the test section, the initial temperature at the start of experimental runs was not uniform, being higher in the center.

The test instrumentation consisted of several thermocoules sheathed with 304 stainless steel located in the test section so as to cover three planes at the 1/3, 1/2, and 2/3 test section height. A data acquisition computer system, consisting of a PDP-11 Digital Corporation computer, was used for recording temperature histories.

Photographs using a high speed camera were taken during selected experiments and provide indicators of the behavior of the quench front and the two-phase system ahead of the

Copyright © 1984 by ASME

Downloaded 02 Jun 2010 to 171.66.16.91. Redistribution subject to ASME license or copyright; see http://www.asme.org/terms/Terms_Use.cfm

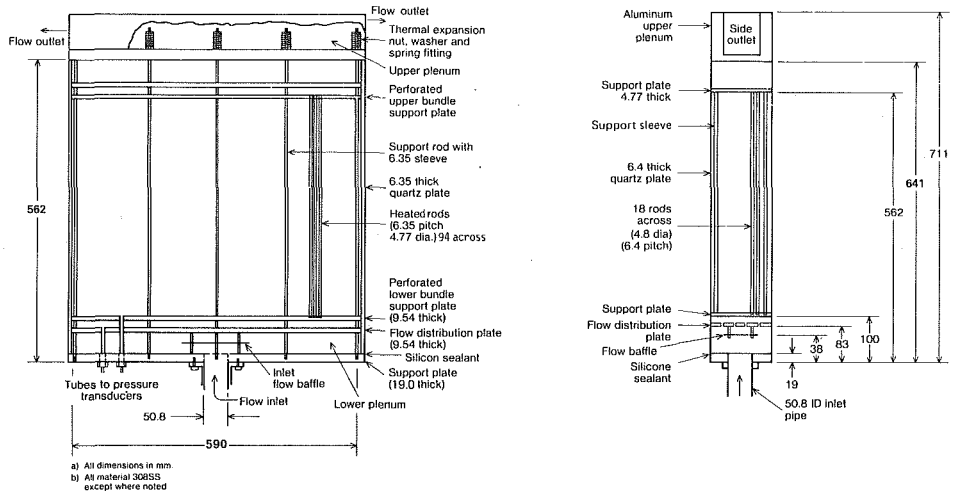

SCHEMATIC OF 1692 PIN TEST SECTION (ELEVATION)

SCHEMATIC OF 1692 PIN TEST SECTION (SIDE)

Fig. 1 Schematic of the UCLA 1692-rod slab core (elevation and side)

quench front for analysis. Experimental convective heat transfer coefficients and convective heat fluxes were computed by a lumped parameter method. The use of a lumped parameter method in the two-phase region is justified because the Biot number in this region is less than 0.1.

Void Fraction Measurement. In separate runs, variation of void fraction with time at specific altitudes of the test section was recorded by a gamma ray attenuation technique. The fundamentals of photon attentuation techniques in density measurements are described elsewhere [9].

The gamma densitometer consisted of a 150 microcurie Cs-137 source and a two inch NaI detector, both encased in lead and mounted on a lift truck. The electronics consisted of a 1024-channel Pulse Height Analyzer manufactured by Technical Measurement Corporation. Figure 2 shows the configuration of the densitometer and the test section. The collimation apertur of the densitometer is 0.635 cm.

In order to make the alignment of the densitometer possible, a row of rods was removed in the desired location of the test section, leaving enough free space to make the densitometer's adjustment easy. The densitometer's height would be kept constant during the test, while the pulse counts were recorded on the multi-channel analyzer. The density

Nomenclature

B = parameter used for fitting the convective heat flux (equation (6)) (1/s)
C = constant of proportionality between lateral (radial) velocity and radial drift flux
C_0 = distribution coefficient in the drift flux model formulation of the void fraction (equation (19))
D = cylindrical core diameter (m)
D_e = flow channel hydraulic diameter (m)
$\bar{f}_r$ = radial friction factor, slab geometry
$\bar{f}_y$ = lateral friction factor, slab geometry
f_z = modified axial friction factor (equation (11))
$f_n(z)$ = functions representing the crossflow Z dependence (equations (12) and (13))
$f_n'(z)$ = derivative of $f(z)$ with respect to Z
g = gravitational acceleration (m/s^2)
H = two-phase region's thickness (m)
H_f = quench front height normalized with core height
h_{fg} = latent heat of vaporization (J/kg)
j_{gr} = radial superficial velocity (m/s), normalized radial superficial velocity
j_{gr}^* = normalized radial superficial velocity
j_{gy} = lateral superficial velocity, normalized lateral superficial velocity
j_{gy}^* = normalized lateral superficial velocity
j_{gz} = axial superficial velocity (m/s), normalized axial superficial velocity
j_{gz}^* = normalized axial superficial velocity
K_r, K_y = factors accounting for flow channel to flow channel geometric change
N = number of terms in the crossflow expansion
n = index of crossflow expansion terms
n_0 = nondimensional parameter used for fitting the convective heat flux (equation (6))
P = pressure (N/m^2)
q'' = convective heat flux (W/m^2)
R = cylindrical core radius (m)
r = radial coordinate (m), normalized radial coordinate
u = axial velocity (m/s)
v = lateral or radial velocity (m/s)
V_{gj} = vapor axial drift velocity (m/s)
y = lateral coordinate (m), normalized lateral coordinate in slab geometry
Y_B = slab core width or half width (m)
z = axial coordinate (m), normalized axial coordinate
Z_B = core height (m)
Z_2 = two-phase region thickness (m), normalized two-phase region thickness
α = void fraction
$\bar{\alpha}$ = void fraction in two-phase region averaged in z direction
ϵ = nondimensional parameter used for fitting the convective heat flux (equation (6))
Γ = volumetric vapor generation rate (kg/m^3.s)
γ_n = coefficients in polynomials representing the crossflow (equations (18) and (23))
ΔP_0 = pressure drop across the two-phase region (N/m^2)
ζ = normalized lateral or radial coordinates
ρ_l = liquid density (kg/m^3)
ρ_g = vapor density (kg/m^3)
σ = surface tension (N/m)

Downloaded 02 Jun 2010 to 171.66.16.91. Redistribution subject to ASME license or copyright; see http://www.asme.org/terms/Terms_Use.cfm

Table 1 Run conditions of experiments with UCLA slab core used for comparison with theory

Run number	Flooding velocity cm/s	Core average initial temperature °C	Inlet-water subcoling °C	Initial temperature difference between core center and edge
34	1	500	70	~185
38	1.8	650	10	~220
41	2.0	650	30	~220
101	2.0	520	60	~190
104	5	520	70	~190

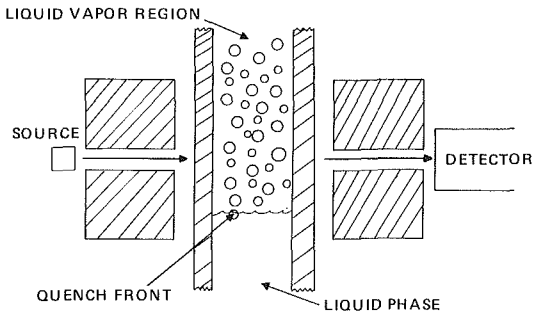

Fig. 2 Configuration of gamma ray densitometer and the slab core during experiments

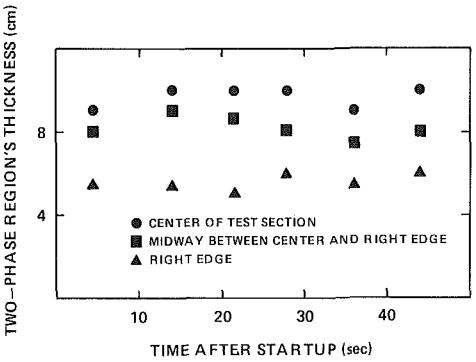

Fig. 3 Variation of two-phase region's thickness with time in 1692-rod slab core during run 34 (uncertainty in two-phase region's thickness = ± 1.5 cm)

calculated at each time would be the average across the slab core's thickness.

Experimental Results and Discussion. Except for very low flooding rates, the rate of quench front advance is smaller than the flooding rate. The surplus water is partially carried out of the test section by the steam flow, and the remaining water forms a two-phase region ahead of the quench front. The two-phase region refers to the portion of the core above the quench-front. The two-phase region refers to the portion of the core above the quench-front where the liquid phase is quasi-stationary, and below the upper portion of the core where the liquid droplets are carried by steam flow with very little slip. The two-phase region as defined here covers a void fraction range from near zero to approximately 0.95 (see [10] for further details).

The nonuniform initial rod temperature across the test section results in faster quench front advance in cooler parts of the test section. This gives rise to the "chimney effect" in which, below the quench front, water flows towards the center where the rod surface is hotter, and is thereby fed into the two-phase region. In experiments in which the inlet velocity is low enough, a quasi-steady state is obtained where the quench front advance velocity (as well as the two-phase region's thickness) does not change significantly with time. As will be shown in the analysis section, the slow variation of

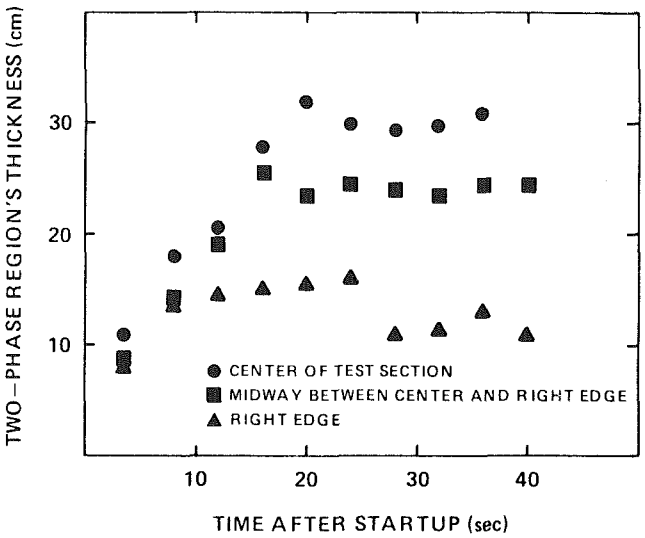

Fig. 4 Variation of two-phase region's thickness with time in 1692-rod slab core during run 38 (uncertainty in two-phase region's thickness = ± 2.5 cm)

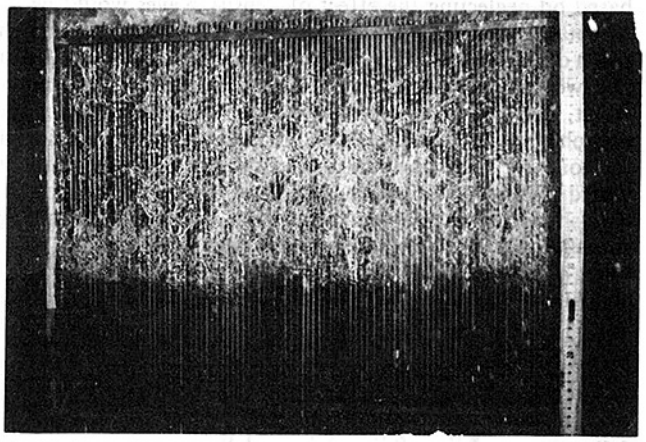

Fig. 5 Two-phase distribution across the 1692-rod slab core during reflooding in run 104

parameters with time allows us to neglect the time dependent terms in the conservation equations. Run conditions of the experiments with UCLA Slab Core used for comparison with theory in this paper are summarized in Table 1. Further details about the core initial temperature can be found in [8, 10]. Figures 3 and 4 show the typical two-phase behavior with time for the 1692-rod slab core. In cases where the inlet velocity is relatively high, the two-phase system covers the whole test section before the quasi-steady state case is reached.

In some circumstances side-to-side undamped density oscillations were observed in the two-phase flow region; the conditions under which these oscillating effects occurred cannot be generalized to cover a different geometry since the appropriate scaling parameters are unknown. In any case, the duration of the density waves was found to be small compared with the period of cycles, implying that a theoretical approach

Downloaded 02 Jun 2010 to 171.66.16.91. Redistribution subject to ASME license or copyright; see http://www.asme.org/terms/Terms_Use.cfm

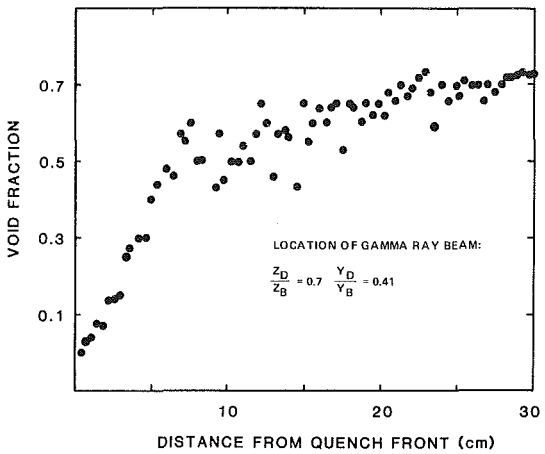

Fig. 6 Quasi-steady void fraction distribution in the two-phase region in run 101 with UCLA slab core

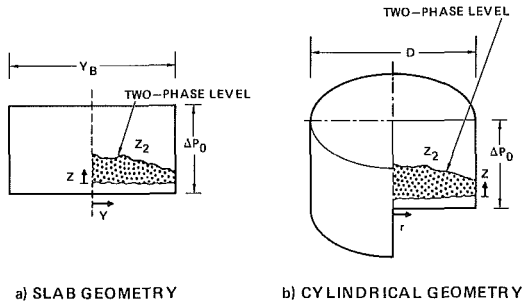

Fig. 7 Definition of theoretical idealization for crossflow analysis

based on neglecting the effect of density waves would be an acceptable approximation. Figure 5 is a typical photograph taken during experiments, which shows the non-uniformity of the two-phase region's thickness as a result of the chimney effect. Figure 6 shows typical void fraction behavior in the two-phase region. Thorough understanding of the behavior of the void fraction in the two-phase flow ahead of quench front would require investigation. However, the measurements to date show that an average value of the void fraction ranging from 0.4 to 0.6 is appropriate for the two-phase region.

Theoretical Model and Basic Assumptions

The underlying method will be reviewed here in a general form for both cylindrical and slab geometries. Figure 7 shows the theoretical idealization definitions for both geometries.

The simplifying assumptions used in the analysis are as follows:

(*a*) The core is treated as two-dimensional; (z, y) in the slab geometry, and (z, r) in the cylindrical geometry.
(*b*) The flow is considered incompressible and quasi-steady.
(*c*) At any time t, there is a saturated two-phase region ahead of the quench front with thickness $Z_2(r)$ for the cylinder and $Z_2(y)$ for the slab. Above the two-phase region there is saturated steam flow.
(*d*) In the vertical direction z, phase separation is treated with a void fraction correlation, and in the lateral direction, r or y, phase velocities are equal. The drift flux formulation for void fraction is used.
(*e*) Transverse velocities are small compared to axial flow velocities.
(*f*) In the two-phase region, hydrostatic pressure losses dominate the axial pressure gradient. Above the two-phase region, frictional losses dominate.
(*g*) The boundary condition for the bundle is a steady imposed axial pressure drop, which is identical for all channels.

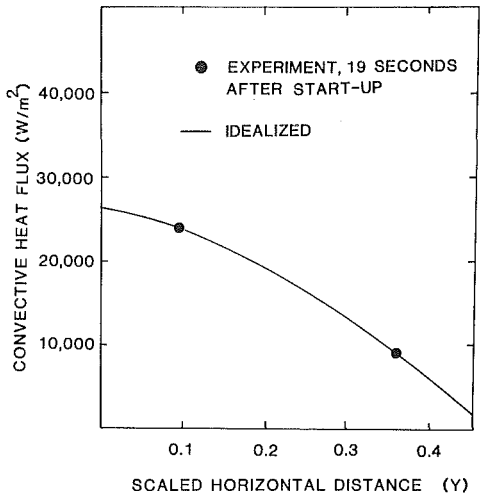

Fig. 8(*a*) Average convection heat flux distribution across the two-phase region (19 seconds after start-up). Uncertainty in q'' is +3500, −1800 W/m^2.

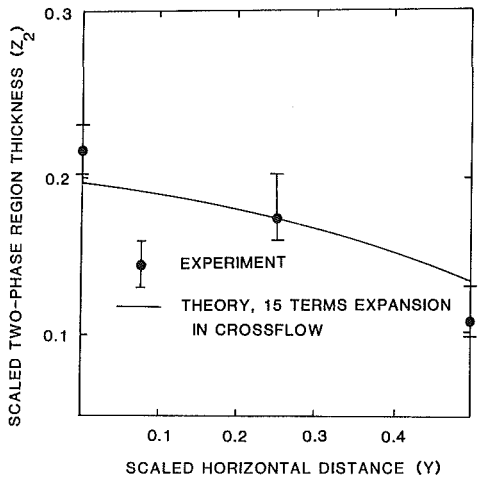

Fig. 8(*b*) Quasi-steady two-phase region thickness distribution across the core

Fig. 8 Comparison of theoretical and experimental quasi-steady two-phase region thickness distribution in slab core in run 34

Analysis. Analysis of cylindrical geometry is presented in detail in the following paragraphs; the slab geometry is only mentioned briefly.

Vertically averaging the convective heat flux, $q''(r)$, and defining a vapor production parameter

$$\Gamma(r) = \frac{4q''(r)}{h_{fg}D_e}.$$

allows the vapor conservation equation to be written as

$$\frac{\partial j_{gz}}{\partial z} + \frac{1}{r}\frac{\partial}{\partial r}(rv) = \frac{\Gamma(r)}{\rho_g}.$$

Based on the listed assumptions, the axial and radial momentum equations are

$$-\frac{1}{\rho_g}\frac{\partial P}{\partial z} = \frac{\rho_l(1-\alpha)g}{\rho_g} + \bar{f}_z j_{gz}^2 + \frac{\partial j_{gz}^2}{\partial z} + \frac{1}{r}\frac{\partial}{\partial r}(rvj_{gz}), \quad (3)$$

$$-\frac{1}{K_r}\frac{1}{\rho_g}\frac{\partial P}{\partial r} = \frac{1}{r}\frac{\partial}{\partial r}(rv^2) + \frac{\partial}{\partial z}(vj_{gz}) + \bar{f}_r\rho_g v^2. \quad (4)$$

The friction term in the radial direction is assumed small

Downloaded 02 Jun 2010 to 171.66.16.91. Redistribution subject to ASME license or copyright; see http://www.asme.org/terms/Terms_Use.cfm

Table 2 Values of γ_n in slab geometry for the case with five term expansion representation of crossflow[a]

n \ n_0	0.25	0.5	1.0	2.0
1	−7.69	−3.21	−0.179	0.367
2	41.20	16.84	0.293	1.01
3	−97.47	−39.99	−1.49	1.26
4	102.26	42.55	2.8	0.704
5	−38.99	−16.57	−1.70	−0.695

[a]Method of colocation applied at points represented by $Y_n = \frac{n-1/2}{N}$, $n = 1, 2, \ldots,$ where N is the total number of terms in the expansion.

Table 3 Values of γ_n in cylindrical geometry for the case with five term expansion representation of crossflow[a]

n \ n_0	0.25	0.5	1.0	2.0
1	−7.78	−5.084	−3.18	−4.50
2	27.37	20.58	17.87	26.81
3	−50.57	−42.65	−43.27	−64.90
4	46.39	42.66	47.03	70.55
5	−16.59	−16.17	−18.80	−28.22

[a]Method of colocation applied at points represented by $Y_n = \frac{n-1/2}{N}$, $n = 1, 2, \ldots,$ where N is the total number of terms in the expansion.

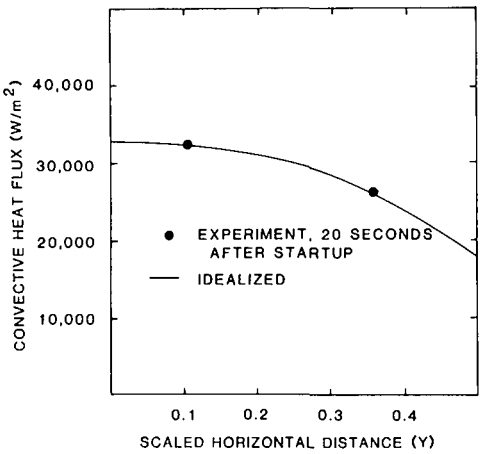

Fig. 9(a) Average convective heat flux distribution across the two-phase region (20 seconds after start-up). Uncertainty in q'' was ± 5500 W/m².

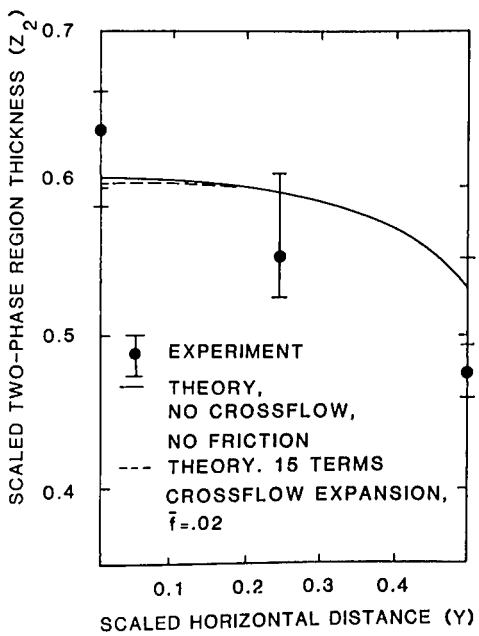

Fig. 9(b) Quasi-steady two-phase region thickness distribution across the core

Fig. 9 Comparison of theoretical and experimental quasi-steady two-phase region thickness distribution in slab core in run 41

and will be neglected. The form factor for flow channel to flow channel geometric change, K_r, is assumed to be of order unity following Weisman [11]. The radial velocity, again following Weisman, is assumed to be proportional to j_{gr},

$$v = Cj_{gr}, \tag{5}$$

The radial variation in heat flux is assumed to be of the form

$$4q''(r) = \rho_g B h_{fg} D_e \left(1 - \epsilon\left(\frac{r}{R}\right)^{n_0+1}\right). \tag{6}$$

with B, ϵ, and n_0 being chosen to give a particular distribution. The conservation equations are normalized as follows:

$$j_z^* = \frac{j_{gz}}{BZ_B}, \; j_r^* = \frac{Cj_{gr}}{BR}, \; Z^* = \frac{z}{Z_B}, \; r^* = \frac{r}{R}, \tag{7}$$

$$\text{and } p^* = \frac{P}{B^2 Z_B^2 \rho_g}$$

The normalized conservation equations then become, dropping asterisks for convenience,

$$\frac{\partial j_z}{\partial z} + \frac{1}{r}\frac{\partial}{\partial r}(rj_r) = \left(1 - \epsilon\left(\frac{r}{R}\right)^{n_0+1}\right), \tag{8}$$

$$-\frac{\partial P}{\partial z} = \frac{\rho_l(1-\alpha)g}{\rho_g B^2 Z_B} + f_z j_z^2 + \frac{\partial j_z^2}{\partial z} + \frac{1}{r}\frac{\partial}{\partial r}(rj_r j_z), \tag{9}$$

$$\text{and} \quad -\frac{\partial P}{\partial r} = \frac{K_r R^2}{Z_B^2}\left[\frac{\partial}{\partial z}(j_r j_z) + \frac{1}{r}\frac{\partial}{\partial r}(rj_r^2)\right]. \tag{10}$$

Here, f_z is defined as

$$f_z = \frac{Z_B}{2D_e}\bar{f}_z. \tag{11}$$

Downloaded 02 Jun 2010 to 171.66.16.91. Redistribution subject to ASME license or copyright; see http://www.asme.org/terms/Terms_Use.cfm

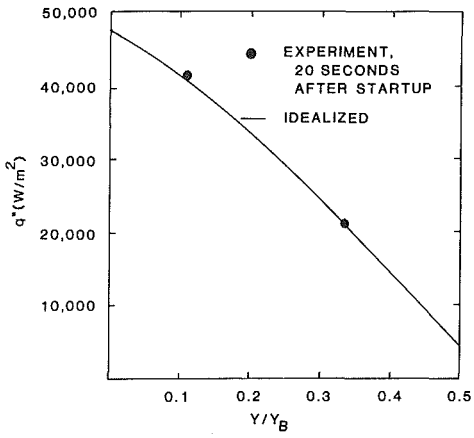

Fig. 10(*a*) Average convective heat flux distribution across the two-phase region (20 seconds after start-up). Uncertainty in q'' was ± 1600 W/m^2.

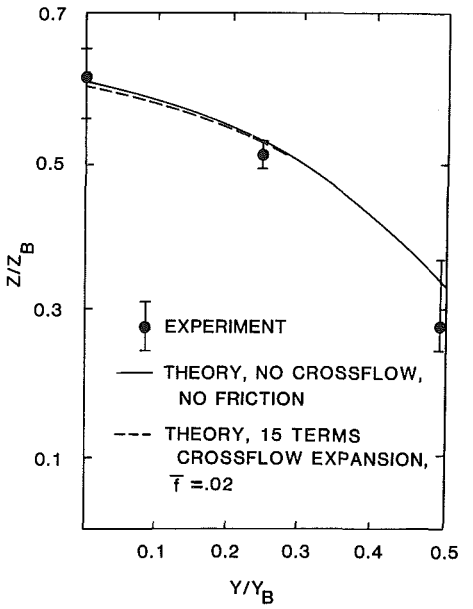

Fig. 10(*b*) Quasi-steady two-phase region thickness distribution across the core

Fig. 10 Comparison of theoretical and experimental quasi-steady two-phase region thickness distribution in the slab core in run 38

Solution. The drift fluxes j_z and j_r are assumed to be

$$j_z = Z\left[1-\epsilon\, r^{n_0+1}\right] - \sum_{n=1}^{N} f_n(z)\left[2-(n+2)r^n\right] \tag{12}$$

$$j_r = \sum_{n=1}^{N}\left[r-r^{n+1}\right]f_n'(z). \tag{13}$$

Substituting j_z and j_r in (9), neglecting friction, consistant with assumption f, and retaining only first order terms, one obtains

$$-\frac{\partial P}{\partial z} = \frac{\rho_l(1-\alpha)g}{\rho_g B^2 Z_B} + 2z(1-\epsilon\, r^{n_0+1})^2. \tag{14}$$

Combining (14) and (10) after integration over Z and r respectively and neglecting second order terms yields

$$\sum_{n=1}^{N}\left(\bar{f}_n'(z)+z\bar{f}_n(z)\right)\left[\left(r^{1-n_0}\right)-r^{n-n_0+1}\right] = -z^2 \tag{15}$$

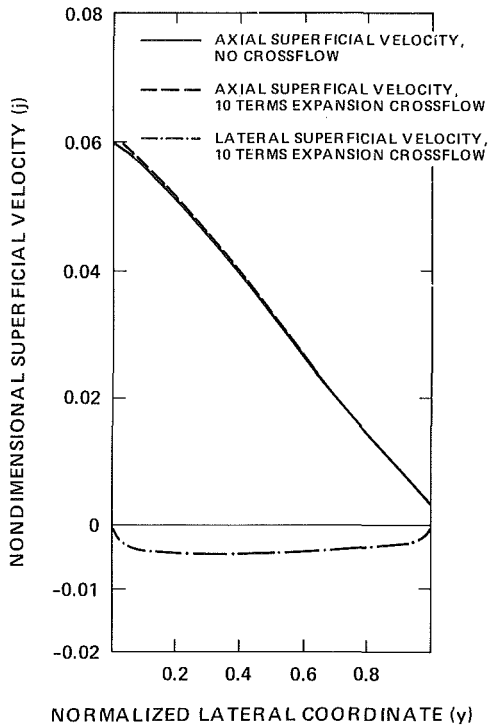

Fig. 11 Predicted quasi-steady normalized axial and lateral superficial velocity distributions in the slab core during run 38 at 10 percent of two-phase region's height (K_y = 1.0, lateral distance normalized with half width)

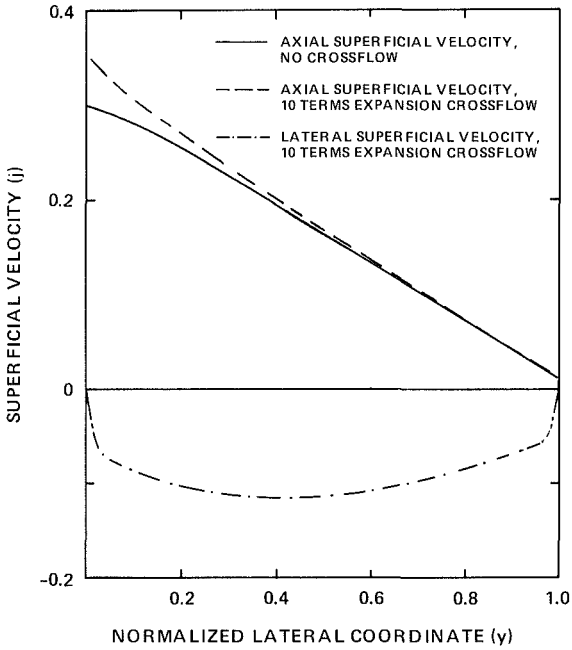

Fig. 12 Predicted quasi-steady axial and lateral superficial velocity distributions in the slab core during run 38 at two-thirds of two-phase region's height (K_y = 1.0, lateral distance normalized with half width)

where

$$\bar{f}_n(z) = \frac{K_r R^2}{\epsilon Z_B^2}\cdot\frac{1}{2(n_0+1)}f_n(z). \tag{16}$$

A form of $\bar{f}_n(z)$ that partially satisfies (14) is

$$\bar{f}_n(z) = \gamma_n z^3. \tag{17}$$

Values of γ_n that complete the solution are found by applying the method of collocation [12] to the following expression

Downloaded 02 Jun 2010 to 171.66.16.91. Redistribution subject to ASME license or copyright; see http://www.asme.org/terms/Terms_Use.cfm

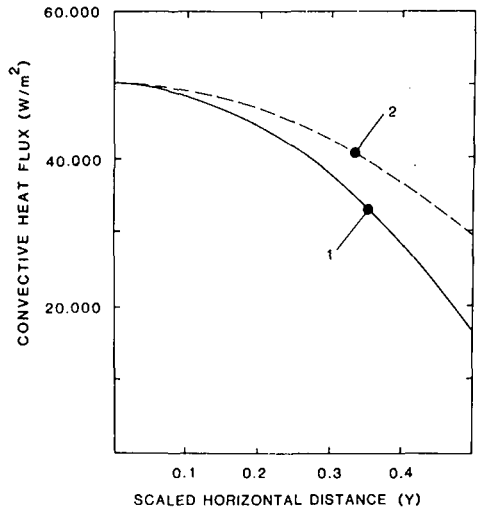

Fig. 13(*a*) Two assumed convective heat flux distributions across the 1692-rod slab core

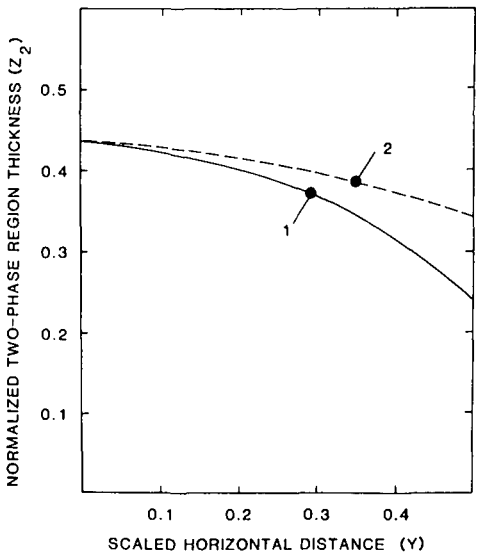

Fig. 13(*b*) Two-phase region thickness distribution from theory resulting from convective power distributions of Fig. 13(*a*)

Fig. 13 Effect of average two-phase region's convective heat flux distribution across the slab core on theoretical two-phase region's thickness

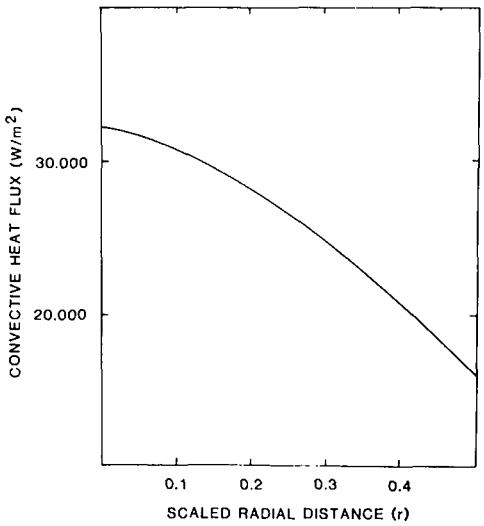

Fig. 14(*a*) Assumed convective heat flux distribution in the two-phase region across a cylindrical core with dimensions typical of pressurized water reactors (radial distance normalized with D)

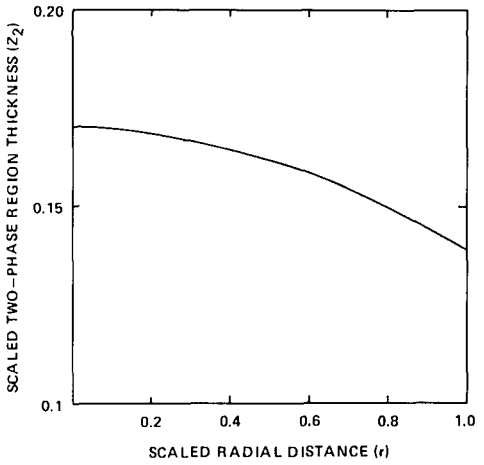

Fig. 14(*b*) Predicted two-phase region thickness distribution across the cylindrical core resulting from convective power distribution of Fig. 14(*a*) (Radial distance normalized with R)

Fig. 14 Theoretical prediction of quasi-steady two-phase region thickness distribution across a typical PWR core during reflooding with a low reflooding velocity

$$\sum_{n=1}^{N} 9\gamma_n \left[r^{1+n_0} - r^{1+n-n_0} \right] = -1 \tag{18}$$

The drift flux formulation for void fraction given by Zuber and Findlay [13] is assumed to be valid throughout the two-phase region:

$$\alpha = \frac{j_z}{C_0 j_z + \dfrac{V_{gj}}{BZ_B}} \tag{19}$$

An expression for V_{gj} for churn-bubbly flow, following Zuber [14] is

$$V_{gj} = 1.53 \left[\frac{\sigma g (\rho_l - \rho_g)}{\rho_l^2} \right]^{1/4}. \tag{20}$$

which is assumed to represent the conditions in a rod bundle. Substitution of equations (15)–(19) in (9), and integrating between zero and Z_2 yields

$$\Delta P_0 = \frac{\rho_l g}{\rho_g B^2 Z_B} \left\{ \left(\frac{C_0 - 1}{C_0} \right) Z_2 + \left(\frac{V_{gj}}{B(1 - \epsilon\, r^{n_0+1}) Z_B C_0^2} \right) \ln \left[1 + \left(\frac{C_0 B Z_B (1 - \epsilon\, r^{n_0+1})}{V_{gj}} \right) Z_2 \right] \right\}$$

$$+ \left[1 + f_z (1 - H_f - Z_2) \right]$$

$$\cdot \left[Z_2^2 \left((1 - \epsilon\, r^{n_0+1})^2 \right) - \left(\frac{4\epsilon Z_B^2}{K_r R^2} \right) (n_0 + 1) \right.$$

$$\cdot (1 - r^{n_0+1}) Z_2^4 \sum_{n=1}^{N}$$

$$\left. \gamma_n \left(2 - (n+2) r^n \right) \right] + \frac{3}{2} \frac{\epsilon Z_B^2}{K_r R^2} (n_0 + 1)$$

Downloaded 02 Jun 2010 to 171.66.16.91. Redistribution subject to ASME license or copyright; see http://www.asme.org/terms/Terms_Use.cfm

$$\left[\left(1-\epsilon\, r^{n_0+1}\right)\sum_{n=1}^{N}\gamma_n\left(2-(n+2)r^n\right)\right.$$

$$\left.-\epsilon(n_0+1)(r^{n0})\cdot\sum_{n=1}^{N}\gamma_n(r-r^{n+1})\right]Z_2^4. \tag{21}$$

ΔP_0 is the normalized pressure drop across the bundle above the quench front, and H_f is the quench front height normalized with core height.

Following an analysis similar to the above, the final result for slab geometry is

$$\Delta P_0=\frac{\rho_l g}{\rho_g B^2 Z_B}\left\{\left(\frac{C_0-1}{C_0}\right)Z_2+\left(\frac{V_{gj}}{B(1-\epsilon\, y^{n_0+1})Z_B C_0}\right)\ln\left[1+\left(\frac{C_0 BZ_B(1-\epsilon\, y^{n_0+1})}{V_{gj}}\right)Z_2\right]\right\}$$

$$+\left[1+f_z(1-H_f-Z_2)\right]$$

$$\cdot\left[Z_2^2\left((1-y^{n_0+1})^2\right)-4Z_2^4\left(\frac{Z_B^2\epsilon}{K_y Y_B^2}\right)(n_0+1)\right.$$

$$\cdot(1-\epsilon\, y^{n_0+1})\cdot\sum_{n=1}^{N}\gamma_n\left(1-(2n+1)y^{2n}\right)\Big]$$

$$+\left\{\frac{3(n_0+1)}{2}Z_2^4\left(\frac{Z_B^2\epsilon}{K_y Y_B^2}\right)\right\}\cdot\left[(1-y^{n_0+1})\right.$$

$$\sum_{n=1}^{N}\gamma_n\left(1-(2n+1)y^{2n}\right)-\epsilon(y^{n0})(n_0+1)$$

$$\left.\cdot\sum_{n=1}^{N}\gamma_n(y-y^{2n+1})\right] \tag{22}$$

The γ_n are selected so that

$$\sum_{n=1}^{N}9\gamma_n\left[(y^{1-n_0})-y^{2n+1-n_0}\right]=-1 \tag{23}$$

In equations (22) and (23) the normalizing characteristic length in the y direction Y_B, is the slab core's half width. Values of γ_n for case of five term expansion representation of crossflow are given in Tables 2 and 3 for slab and cylindrical geometries, respectively.

For both slab and cylindrical geometries, if friction and crossflow terms are neglected

$$\Delta P_0=\frac{\rho_l g}{\rho_g B^2 Z_B}\left[\left(\frac{C_0-1}{C_0}\right)Z_2+\left(\frac{V_{gj}}{B(1-\epsilon\,\zeta^{n_0+1})Z_B C_0^2}\right)\right.$$

$$\left.\cdot\ln\left(1+\left(\frac{C_0 BZ_B(1-\epsilon\,\zeta^{n_0+1})}{V_{gj}}\right)Z_2\right)\right], \tag{24}$$

where ζ is y or r for slab or cylindrical geometries, respectively.

Equations (21), (22), and (24) are transcendental equations in terms of Z_2, provided ΔP_0, which is the pressure drop across the tube bundle ahead of the quench front, is known. For calculations, it was assumed that the dimensional pressure drop is

$$\Delta P_0=(1-\bar{\alpha})H\rho_l g \tag{25}$$

where H is the average two-phase region height and $\bar{\alpha}$ is the average void fraction. Both H and $\bar{\alpha}$ are based on experimental observations.

Comparisons of the results obtained from the model with experimental results from the slab core tests are shown in Figs. 8 through 10. In the comparisons, parameters B, ϵ, and n_0 were adjusted so that equation (6) would approximately represent the experimental heat fluxes (see Figs. 8(*a*), 9(*a*), and 10(*a*)). Following Maitra and Subba-Raju [15], the constant C_0 for the rod bundle was assumed to be constant and equal to 1.5. The comparisons show that the crossflow in the two-phase region has little effect on the boundaries of the two-phase region. The insensitivity of the results to crossflow lead to an insensitivity of the results to the value chosen for K_y. A change in its value from 1 to 1.5 changed the computed value of Z_2 by less than 0.5 percent.

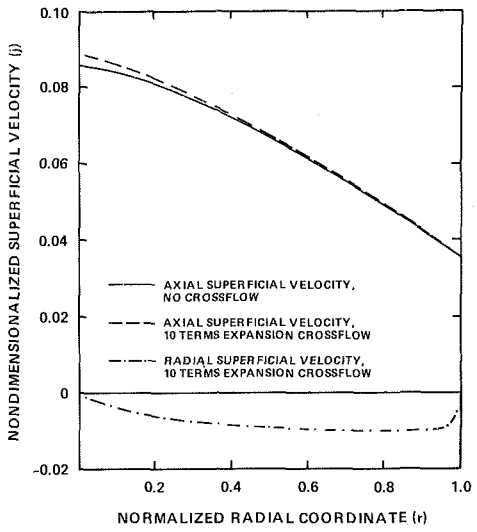

Fig. 15 Normalized axial and radial superficial velocity distributions in cylindrical geometry at two-thirds of two-phase region's height for the assumed conditions of Fig. (14 (K_y = 1.0)

Computed values of normalized superficial velocities for Run 38 are compared on Figs. 11 and 12 for two different locations in the two-phase flow region. Run 38, during which the two-phase flow system is relatively thick (Fig. 10(*b*)) and the idealized convective heat flux is very uneven (Fig. 10(*a*)) represents the most unfavorable case studied here with respect to the validity of the assumption that transverse velocities are negligible compared to axial flow velocities. Nevertheless, it can be observed from Figs. 11 and 12 that the assumption is valid in the greater part of the two-phase flow region. It can be seen that the effect of crossflows on the magnitude of axial superficial velocity is small. It should be noted that, since axial and lateral superficial velocities are normalized differently (see equations (7)), the comparison represented on Figs. 11 and 12 are exaggerated as compared with non-normalized velocities.

The effect of friction was also found to be insignificant. Using values of $\bar{f}$ = 0 and $\bar{f}$ = 0.02, with other parameters constant, never gave more than a 1 percent change in the value of Z_2.

Pressure drop across the two-phase region, ΔP_0, and the distribution of convective heat flux across the core, $q''(r)$, are the factors that determine the two-phase region boundaries. Figure 13 compares model results for two-phase region.

Figure 14 represents the quasi-steady behavior of two-phase region during reflooding of a reactor core for which the fuel elements dimensions and pitch are the same as those in FLECHT experiments, but the core dimensions are those for a 4-loop pressurized water reactor. The value of B corresponds to an average value of heat flux in the two-phase region of about 20000 W/m^2. The effects of crossflow and friction on two-phase region thickness distribution were

Downloaded 02 Jun 2010 to 171.66.16.91. Redistribution subject to ASME license or copyright; see http://www.asme.org/terms/Terms_Use.cfm

found to be negligibly small, and could not be shown on the graph.

Computed distributions of superficial velocities for this test are shown on Fig. 15. It can be observed that the crossflow is small, and has a negligible effect on the magnitude of axial flow.

Conclusions

Reflooding experiments have been carried out with a 1692-rod slab core in order to understand the thermal hydraulic behavior of the two-phase region which forms ahead of the quench front. Nonuniform distribution of the two-phase region's thickness was observed, with thicker two-phase regions in hotter areas. A chimney effect and higher vapor velocities in hotter areas were the mechanisms responsible for the nonuniformity of the two-phase region's thickness.

A two-dimensional quasi-steady analysis of the two-phase region has been carried out for slab and cylindrical geometries, resulting in expressions for predicting the distribution of the two-phase region's thickness across the core. Model predictions compare favorably with the results of 1692-rod slab core experiments. Numerical results also prove that the effects of crossflow, as well as friction, are small. As a result of the insignificance of crossflow and friction in a thermal hydraulic modeling of reflooding, the collapsed water head ahead of the quench front should be normalized and used as ΔP_0 and equation (24) solved for Z_2. The collapsed water heat should be computed from conservation of liquid water ahead of the quench front. The success of the semi-analytical treatment of the two-phase thermal-hydraulics presented here demonstrates that simple models can be used to obtain solutions that contain all the major features of the physical phenomena. The simple models yield relatively inexpensive solutions to very complex problems.

Acknowledgments

The authors gratefully acknowledge EPRI for its support through Project RP1118-1 and William Toman for many helpful discussions.

References

1 Sawan, M., and Carbon, M. W., "A Review of Spray Cooling and Bottom-Flooding Work for LWR Cores," *J. Nuc. Eng. Des.*, Vol. 32, 1975, pp. 191-207.

2 Yadigaroglu, G., "The Reflooding Phase of LOCA in PWRs. Part I: Core Heat Transfer and Fluid Flow," *J. Nuc. Safety*, Vol. 19, Jan.-Feb. 1978, pp. 20-36.

3 Elias, E., and Yadigaroglu, G., "The Reflooding Phase of LOCA in PWRs. Part II: Rewetting and Liquid Entrainment," *J. Nuc. Safety*, Vol. 19, Mar.-Apr. 1978, pp. 60-75.

4 Carbajo, J. J., and Siegel, A. D., "A Review and Comparison Among the Different Models for Rewetting in LWRs," *Nuc. Eng. Des.*, Vol. 58, 1980, pp. 33-44.

5 Sun, K. H., Duffey, R. B., and Peng, C. M., "Prediction of Two-Phase Mixture Level and Hydrodynamically Controlled Dryout Under Low Flow Conditions," EPRI-NP-1359-SR, 1980.

6 Sudo, Y., "Film Boiling Heat Transfer During Reflooding Phase in Postulated PWR Loss of Coolant Accident," *J. Nuc. Sci. Tech.*, Vol. 17, 1980, pp. 516-530.

7 Murao, Y., and Sugimoto, J., "Correlation of Heat Transfer Coefficient for Saturated Film Boiling During Reflood Phase Prior to Quenching," *J. Nuc. Sci. Tech.*, Vol. 18, 1981, pp. 275-284.

8 Toman, W. I., Catton, I., and Duffey, R. B., "Multidimensional Thermal-Hydraulic Reflood Phenomena in a 1692-Rod Slab Core," EPRI-NP-2392, 1982.

9 Stephens, A. G., Emery, M. A., and Hochreiter, L. E., "Local Density in a Steam Water Mixing Zone Using the Photon Attenuation Technic," presented at the ASME Winter Annual Meeting, San Francisco, CA, Dec. 1978.

10 Ghiaasiaan, S. M., "On Multi-Dimensional Thermal-Hydraulics and Two-Phase Phenomena During Reflooding of Nuclear Reactor Cores," Ph.D. thesis, School of Engineering, University of California at Los Angeles, 1983.

11 Weisman, J., "Cross Flow Resistance in Rod Bundle Cores," *J. Nuc. Tech.*, Vol. 15, 1972, pp. 465-469.

12 Findlayson, B. A., *The Method of Weighted Residuals and Variational Parameters*, Academic Press, New York, 1972.

13 Zuber, N., and Findlay, J. A., "Average Volumetric Concentration in Two-Phase Flow System," *J. Heat Trans.*, Vol. 87, 1965, pp. 453-468.

14 Zuber, N., Staub, F. W., Bijwaard, G., and Kroeger, P. G., "Steady State and Transient Void Fraction in Two-Phase Flow Systems," GEAP 5417, 1967.

15 Maitra, D., and Subba-Raju, K., "Vapor Void Fraction in Sub-cooled Flow Boiling," *J. Nuc. Eng. Des.*, Vol. 32, 1975, pp. 20-38.

Downloaded 02 Jun 2010 to 171.66.16.91. Redistribution subject to ASME license or copyright; see http://www.asme.org/terms/Terms_Use.cfm

ERRATA

Journal of Fluids Engineering, Vol. 106, No. 2, p. 217.

On page 217 of the June 1984 issue, the initial of the senior author is incorrectly listed as Y. Yildirim. The correct name is Nevzat Yildirim.

Copyright © 1984 by ASME

Downloaded 02 Jun 2010 to 171.66.16.91. Redistribution subject to ASME license or copyright; see http://www.asme.org/terms/Terms_Use.cfm

Collective Effects on the Growth of Vapor Bubbles in a Superheated Liquid

G. L. Chahine

H. L. Liu

Tracor Hydronautics, Inc., Laurel, MD

The problem of the growth of a spherical isolated bubble in a superheated liquid has been extensively studied. However, very little work has been done for the case of a cloud of bubbles. The collective behavior of the bubbles departs considerably from that of a single isolated bubble, due to the cumulative modification of the pressure field from all other bubbles. This paper presents a theoretical study on bubble interaction in a superheated liquid during the growth stage. The solution is sought in terms of matched asymptotic expansions in powers of ϵ, the ratio between r_{b0}, a characteristic bubble radius and l_0, the interbubble distance. Numerical results show a significant inhibition of the bubble growth rate due to the presence of interacting bubbles. In addition, the temperature at the bubble wall decreases at a slower rate. Consequently, the overall heat exchange during the bubble growth is reduced.

Introduction

In hydrodynamic applications as with propellers, pumps, channels, pipes, submerged jets, etc., cavitation occurs when the liquid experiences significant pressure drops due to local high flow velocities. In this case the growth of the nuclei to macroscopic bubbles is mainly controlled by inertia. Heat transfer during the phase change at the bubble wall is negligible because of the low value of the vapor density at the ambient temperatures, and does not affect the bubble-wall motion. The phase change is then called "cavitation" and the liquid is described as "cold." Conversely in applications where heat exchange, rather than the liquid inertia, controls the vapor-bubble dynamics, the phase change is called "boiling."

In many modern processes such as power plants and nuclear engineering the liquids involved are in such conditions that the liquid is described as "superheated" and both heat transfer as well as inertia contribute to controlling the bubble behavior. Phase change and cavity growth appear in these liquids in applications such as high speed flow of sodium cooled fast-breeder reactors in nuclear power engineering, and flow of hot water in nozzles and pipes in steam power plants. Accidents such as loss of coolant, or rupture of a pipe, are sources of boiling nucleation and evidently of major safety concern.

The problem of the growth of a spherical isolated bubble in a superheated liquid has been extensively studied, [1, 2] and both exact numerical solutions [2] as well as approximate solutions have been obtained. However, very little work has been done on the subject for the more realistic case of a cloud of bubbles. The collapse of an inertia-controlled bubble cloud or cluster has been studied recently and papers on this subject were presented at the ASME meetings the past two years [3, 4]. We proposed to the National Science Foundation to use the same approach we have developed to study the inertial behavior of a multibubble system to investigate bubble interaction in a superheated liquid. We present here the first results of this study. The collective behavior of the bubble is expected to depart significantly from that of a single isolated bubble due to the cumulative modification of the pressure field at the location of a bubble due to the other bubbles [4, 5]. However, this effect which is very important during the collapse phase is expected to be more moderate during the growth phase. The bubble departure from sphericity is also expected to be smaller in the growth case.

Formulation of the Problem

Let us consider the case of low void fraction in an unbounded medium of uniform pressure, P_∞ and temperature T_∞. We assume the fluid to be inviscid and incompressible and the flow to be irrotational. These assumptions are usual [1, 6] and can be justified in boiling heat transfer and cavitation studies except in the last phase of the bubble collapse and in the very early phase of bubble growth where the corresponding Reynolds number is small. At $t = 0$ a sudden variation in the ambient pressure, $P_\infty(t)$, is introduced and the cloud dynamics is sought. Provided that the characteristic size r_{b_0} of a bubble is small compared to its characteristic distance l_0 from its neighbors, we can assume that interbubble interactions are weak enough so that, to the first order of approximation, and in the absence of relative velocity with the surrounding fluid, each of the individual bubbles reacts to the local pressure variations spherically, as if isolated. Mutual bubble interactions, individual bubble

Contributed by the Fluids Engineering Division and presented at the Cavitation and Polyphase Flow Symposium, Houston, Texas, June 20-22, 1983. Manuscript received by the Fluids Engineering Division, June 27, 1983.

Copyright © 1984 by ASME

Downloaded 02 Jun 2010 to 171.66.16.91. Redistribution subject to ASME license or copyright; see http://www.asme.org/terms/Terms_Use.cfm

motions and deformations are taken into account in the following orders of approximation.

The solution of the problem is sought in terms of matched asymptotic expansions in powers of ϵ, the ratio between r_{b_0} and l_0. Two regions of the fluid are defined for each individual bubble of the cloud. In the "inner region," of scale r_{b_0}, boundary conditions on pressures, velocities and heat transfer can be written at the bubble wall. In the "outer region," of scale l_0, the cloud appears as a distribution of singularities, whose strength is determined by solving the "inner problem." In each order of approximation an "inner problem" reduces to the study of an isolated bubble with conditions imposed at infinity and determined from the "outer problem" at the preceding order. By application of the matching principle these conditions are obtained as the expansions of the preceding order "outer solution" near the bubble singularity. The process is started by the first order approximation whose solution is known since all bubbles behave then as if isolated. Knowing the behavior to this first order of all the bubbles, one obtains the solutions of the first order "outer problem." The corresponding potential is the sum of the potentials due to the sources representing all the spherical bubbles. These sources are each located at a bubble center and their intensity is related to the bubble radius and the growth rate. The behavior of this first order "outer solution" in the vicinity of a particular bubble provides, through the matching condition, the condition at infinity to satisfy when solving the second order "inner problem" corresponding to this bubble. Obtaining the solution for all second order "inner problems" one can pursue the same procedure to solve all following higher orders. This approach is similar to the one we have developed for the study of the collapse of two bubbles [8] and that we have extended to a bubble cloud [7]. These two earlier papers [7, 8] give more details about the method concerning the expansions at each order and the matching procedure.

With our above assumptions both inner and outer flows are potential flows. Practically this applies for the usual ranges of Reynolds numbers where the liquid can be considered as inviscid. The equations of the problem are the following. In the inner problem in order to determine the flow field around any individual bubble, as well as its motion and deformation in the cloud, one has to solve the Laplace equation

$$\Delta\Phi_{\text{in}} = 0, \tag{1}$$

subjected to kinematic and dynamical conditions on the bubble's surface.

$$\nabla\Phi_{\text{in}} \cdot n^i \mid_{r=R^i(\theta,\phi,t)} = [\dot{R}^i e_r + \dot{b}^i e_z] n^i \tag{2}$$

$$\rho[\dot{\Phi}_{\text{in}} - \dot{b}^i e_z + 1/2 \mid \nabla\Phi_{\text{in}} \mid^2_{r=R^i(\theta,\phi,t)}] = P_\infty(t) - P^i_v - P^i_g + 2\gamma\mathcal{C}^i(\theta,\phi,t) \tag{3}$$

where $\mathcal{C}^i$ and $\mathbf{n}^i$ are, respectively, the local curvature of the surface of bubble B^i and its unit vector at the point $M(r, \theta, \phi)$. The equation of the bubble surface in a coordinate system moving with velocity $\dot{b}^i$ in the direction $\mathbf{e}_z$, is $r = R^i(\theta, \phi, t)$. γ is the surface tension and dots denote time differentiation. Φ_{in} and the operator ∇ are expressed in the moving coordinates system. P_g can be related to its initial value, P_{g_0}, and to the bubble volume v by the equation

$$P_g(t) = P_{g_0}\left[\frac{v(0)}{v(t)}\right]^{3\kappa}; \quad 1 < \kappa < \frac{c_p}{c_v}, \tag{4}$$

To solve the heat problem, in the inner region, one needs to determine the temperature at the bubble wall, $T_R(\theta, \phi, t)$, when temperatures deviate significantly from T_∞. The energy equation can be written:

$$\dot{T} + \nabla\Phi_{\text{in}} \cdot \nabla T = D \cdot \Delta T, \tag{5}$$

where $\mathbf{V} = \nabla\Phi_{\text{in}}$ is the fluid velocity given by equations (1-4), and D is the thermal diffusivity of the liquid. Equation (5) is subjected to a boundary condition on the bubble wall stating that the heat locally lost at any point of the interface is used to vaporize an amount of liquid determined by the local bubble volume expansion rate. This can be written:

$$\frac{\partial T}{\partial n^i}\Big|_{r=R^i(\theta,\phi,t)} = \frac{\rho_v L}{K}\dot{R}^i \tag{6}$$

In the outer problem, one needs to be concerned with the macrobehavior of the cloud. Here the bubbles appear only as singularities (dynamic sources and heat sinks) whose intensities are determined by the resolution of the various inner problems. The equations of the problem are therefore limited in the outer region to the Laplace equation

$$\Delta\Phi_{\text{out}} = 0,$$

only submitted to the at-infinity (far from the cloud) boundary conditions in addition to the presence of the distributed singularities condition between the inner and the outer problem can be simply stated:

$$\begin{aligned} &\text{behavior } \phi_{\text{in}} \quad = \text{behavior } \phi_{\text{out}} \\ &\tilde{r} = r/r_{b_0} \to \infty \qquad\quad \epsilon \to 0 \end{aligned} \tag{7}$$

In order to make asymptotic expansions (and thus to compare orders of magnitudes) an accurate choice of characteristic scale variables is fundamental. For the length scales the choice is immediate: r_{b_0} in the inner problem, l_0 in the outer. However, the relationship between r_{b_0} and the characteristic initial bubble radius, R_0, is less obvious. Indeed, while in the case of bubble collapse, the bubble radius stays of order R_0 in the mathematical sense, [$R(\epsilon) = 0(R_0)$; if there exists a constant λ independent of ϵ such that $|R| \leq \lambda|R_0|$], this is not the case for the bubble cloud growth studied here. The problem is approached in the following way. r_{b_0} is chosen arbitrarily (independent of R) such that the inequality, $r_{b_0}/l_0 = \epsilon << 1$ is valid. When doing this we must keep in mind that the results of the computations will be valid only as long as the radius of any bubble in the cloud does not exceed too much r_{b_0}. Concerning the time scale, the choice is simple once r_{b_0} is known. For the problem of a sudden depressurization, this time scale is related to the pressure drop, ΔP, by the relation: $\tau_0 = r_{b_0}(\rho/\Delta P)^{1/2}$. In the numerical examples considered here the pressure drops from its initial value, $P_{\infty 0}{}'$ to a constant value P_∞, in which case ΔP is defined as: $\Delta P = P_{\infty 0} - P_\infty$.

The equation of the surface of any bubble in the cloud is expanded in spherical harmonics and can be shown [4, 5] to be written up to the order ϵ^3 as follows

$$\tilde{R}(\theta,t) = a_0(t) + \epsilon a_i(t) + \epsilon^2[a_2(t) + f_2(t)\cos\theta] + \epsilon^3[a_3(t) + f_3(t)\cos\theta + g_3(t)\mathcal{P}_2(\cos\theta)] + \sigma(\epsilon^3) \tag{8}$$

where $\mathcal{P}_2$ is the Legendre polynomial of order 2 and θ is the angle seen from the bubble center between the direction of a field point on the bubble surface and the "center of the cloud" (direction of motion of the bubble) [5, 7]. The nondimensional radius $a_0(t)$ (reference length, r_{b_0}) is given by the Rayleigh-Plesset equation:

$$a_0\ddot{a}_0 + \frac{3}{2}\dot{a}_0^2 = -\bar{P}_\infty(t) + \pi_0(t) + -\mathcal{P} - \frac{2\mathrm{W}_e{}^{-1}}{a_0} + \left(\mathcal{P} + \frac{2\mathrm{W}_e{}^{-1}}{R_0}\right)\left(\frac{a_0}{R_0}\right)^{-3k}, \tag{9}$$

where R_0 is the initial nondimensional bubble radius and k the polytropic gas coefficient. The nondimensional parameters are given by:

Downloaded 02 Jun 2010 to 171.66.16.91. Redistribution subject to ASME license or copyright; see http://www.asme.org/terms/Terms_Use.cfm

$$\left.\begin{aligned} \bar{P}_\infty(t) &= \frac{P_\infty(t)-P_\infty(0)}{\Delta P}, \qquad \mathcal{P} = \frac{P_\infty(0)-P_v(0)}{\Delta P}, \\ \pi_0(t) &= \frac{P_v(t)-p_v(0)}{\Delta P}, \qquad \mathrm{W}_e^{-1} = \frac{\gamma(t)}{r_{b_0}\Delta P}, \end{aligned}\right\} \quad (10)$$

where $P_\infty(t)$ is the imposed ambient pressure and ΔP is the characteristic size of the pressure variations. $\gamma(t)$ and $p_v(t)$ are the surface tension coefficient and the vapor pressure at the temperature of the bubble wall at time t. When the temperatures at the surface of the bubble depart significantly from the ambient, and for liquids where the dependence of p_v and γ on temperature is important, it is necessary to couple equation (9) with the heat equation to obtain a solution. As an example, for a 1 mm bubble in water at 20°C the temperature drop, ΔT, 1 ms after the beginning of the growth process is 0.2 degrees and P_v drops 1 percent. However, near 100°C, ΔT is 13 degrees and P decreases by half [6]. In the first case water is "cold" and there is no need to solve for the temperature. This is, however, necessary for "hot" water. The dependence of γ on temperature is very weak and could therefore be neglected. The Weber number, W_e, will therefore be considered constant in the following.

After accounting for the spherical symmetry of the problem the energy equation reduces in first approximation to the following equation:

$$\frac{\partial T}{\partial t} - \frac{a_0^2\dot{a}_0}{r^2}\frac{\partial T}{\partial r} = \mathrm{P_e}^{-1}\frac{1}{r^2}\frac{\partial}{\partial r}\left(r^2\frac{\partial T}{\partial r}\right), \quad (11)$$

where the Peclet number, $\mathrm{P_e}^{-1}$ is related to the thermal diffusivity, D, and the bubble characteristic size, r_{b_0} and time scale τ_0 by the relation

$$\mathrm{P_e} = r_{b_0}^2/D\tau_0. \quad (12)$$

If the influence of noncondensables inside the bubble is neglected, which is justifiable during the bubble growth, the last term in equation (9) is negligible, and a simple equation for the heat balance on the bubble-liquid interface can be formulated. It states that the heat locally lost at any point of the interface is used to vaporize an amount of liquid determined by the local bubble volume expansion rate. Since the problem is spherical in first approximation, this is expressed by the equation:

$$\frac{\partial T_0}{\partial r} = \frac{\rho_v L}{K}\frac{r_{b_0}^2}{T_{\mathrm{ref}}\tau_0}\dot{a}_0 = \mathcal{C}\cdot\dot{a}_0 \quad (13)$$

where K and L are, respectively, the thermal conductivity and the latent heat of vaporization of the liquid, and ρ the density of its vapor at the bubble wall temperature. T_{ref} is the reference temperature which we will choose equal to the amount of superheat.

$$T_{\mathrm{ref}} = T_\infty - T_b \quad (14)$$

T_∞ is the initial ambient and at infinity temperature, while T_b is the "boiling temperature," or the temperature at which the vapor pressure is equal to the imposed ambient pressure. For a sudden pressure drop from $P_\infty(0)$ to a constant pressure, P_∞, T_b can be defined by:

$$P_\infty(t) = P_\infty = p_v(T_b) \quad (15)$$

Interactions

Once equations (9), (11), and (12) are solved the first approximation of the variation with time of any bubble radius, $a_o^{(i)}$, in the cloud is determined. This allows us to proceed as described in the preceding paragraph, to determine at the following order the boundary conditions at infinity for the inner problem concerning any bubble, $B^{(i)}$. This is obtained by expanding the outer solution obtained at order zero in the vicinity of $B^{(i)}$. To the first order, ϵ, the correction amounts to just a change of the ambient pressure for the inertia problem. This implies a correction of the strength of both the dynamical source and the thermal sink representing $B^{(i)}$ in the outer problem. The "inner problems" remain, therefore, spherical to this order and in absence of condensables the bubble radius correction, $a_1^{(i)}$, is given by the following equation where the subscript (i) has been omitted for convenience.

$$a_0\ddot{a}_1 + 3\dot{a}_0\dot{a}_1 + a_1\left(\ddot{a}_0 - \frac{2\mathrm{W}_e^{-1}}{a_0^2}\right) = -\sum_j\left(\frac{l_0}{l_0^{ij}}\right)\dot{q}_0^{(j)} + \pi_1(t), \quad (16)$$

where l_0^{ij} is the distance between the bubbles $B^{(i)}$ and $B^{(j)}$, and $q_0^{(j)}$ is the strength of the oscillating source in $B^{(j)}$. $\pi_1(t)$ is a correction of $\pi_0(t)$ and expresses the second approximation of the vapor pressure at the bubble wall. With the temperature expanded in powers of ϵ as $R(\theta, t)$,

$$\begin{aligned} T(r,\theta,t) = T_0(r,t) + \epsilon T_1(r,t) + \epsilon^2[T_2(r,t) + T_{21}(r,t)\cos\theta] \\ + \epsilon^3[T_3(r,t) + T_{31}(r,t)\cos\theta + T_{32}(r,t)\mathcal{P}_2(\cos\theta)] + \sigma(\epsilon^3), \end{aligned} \quad (17)$$

$\pi_0(t)$ and $\pi_1(t)$ can be expressed as:

$$\pi_0(t) = [p_v(T_0(a_0,t)) - p_v(T_\infty)]/\Delta P, \quad (18)$$

$$\pi_1(t) = \left[p_v(T_1(a_0,t)) + a_1\frac{\partial T}{\partial r}(a_0,t) \cdot \frac{dp_v}{dT}(T_0(a_0,t))\right]/\Delta P, \quad (19)$$

Since the "inner problem" is spherical at this order and at the preceding one, the heat equation can be written after using the Lagrange transformation:

$$y = \frac{1}{3}[r^3 - R^3(t)], \quad (20)$$

$$\frac{\partial T_n}{\partial t} = \mathrm{P_e}^{-1}\frac{\partial}{\partial y}\left(r^4\frac{\partial T_n}{\partial y}\right); \quad n = 0,1 \quad (21)$$

The heat balance at the bubble wall can be expressed with the same variables as follows:

$$a_0^2\frac{\partial T_0}{\partial y}\bigg|_{y=0} = \mathcal{C}\dot{a}_0, \quad (22)$$

$$a_0^2\left(\frac{\partial T_1}{\partial y} + 2\frac{a_1}{a_0}\frac{\partial T_0}{\partial y}\right)\bigg|_{y=0} = \mathcal{C}\dot{a}_1. \quad (23)$$

Following the same procedure, once $a_0^{(i)}$ and $a_1^{(i)}$ are known, one can determine the governing equations of motion at higher orders of approximation. For instance, the order ϵ^2 correction will reflect first, a change of the strength of the source located in $B^{(i)}$ due to the source strength corrections at the preceding order of the other singularities located in $B^{(j)}$. Secondly a nonspherical correction is to be applied which is due to an imposed uniform velocity which results from compounding the velocities induced by all the other bubbles $B^{(j)}$ at the location of $B^{(i)}$. For this reason, the nonspherical component of the velocity potential which is in cos θ, can be interpreted as both a translation velocity and a deformation of the bubble. At order ϵ^3, another additional nonspherical correction appears, which is due to a velocity gradient generated by the flow field associated with the motion of the other bubbles.

Downloaded 02 Jun 2010 to 171.66.16.91. Redistribution subject to ASME license or copyright; see http://www.asme.org/terms/Terms_Use.cfm

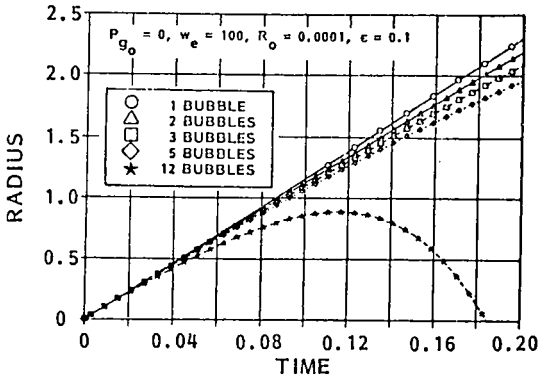

Fig. 1 Growth of an *N*-bubble cloud following a sudden pressure drop

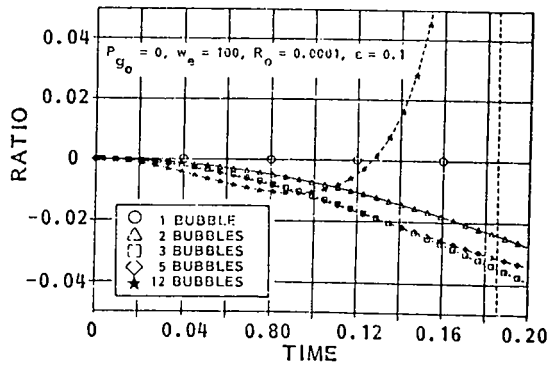

Fig. 2 Growth of an *N*-bubble cloud, ratio of deformation to radius

The dynamical equations at order ϵ^2 can be written:

$$a_0\ddot{a}_2 + 3\dot{a}_0\dot{a}_2 + a_2\left(\ddot{a}_0 - \frac{2W_e^{-1}}{a_0^2}\right) + \left(\frac{3}{2}\dot{a}_1^2 + a_1\ddot{a}_1 + 2W_e^{-1}\frac{a_1^2}{a_0^3}\right) = \pi_2(t) - \sum_j \left(\frac{l_0}{l_0^{jj}}\right)\dot{q}^{(j)}, \tag{24}$$

$$a_0\ddot{f}_2 + 3\dot{a}_0\dot{f}_2 = \pi_{21}(t) + -3\sum_j\left(\frac{l_0}{l_0^{jj}}\right)^2 (\dot{a}_0 q_0^{(j)} + a_0\dot{q}_0^{(j)}), \tag{25}$$

where $q_0^{(j)}$ and $q^{(j)}$ are the strengths of the sources of order 1 and ϵ (related to $a_0^{(j)}$ and $a_1^{(j)}$). The energy equation is then expanded as follows

$$\dot{T}_1 = P_e^{-1}\frac{\partial}{\partial y}\left[4a_1a_0^2\eta^{1/3}\frac{\partial T_0}{\partial y} + \eta^{4/3}\frac{\partial T_1}{\partial y}\right], \tag{26}$$

$$\dot{T}_2 + \frac{\partial T_0}{\partial y}[q_2 - \dot{a}_0a_1^2 - a_0^2\dot{a}_1 - a_1\dot{a}_1] = P_e^{-1}\left\{\frac{\partial}{\partial y}\left(\eta^{4/3}\frac{\partial T_2}{\partial y}\right) + \frac{\partial}{\partial y}[(4a_2a_0^2 + 4a_1^2a_0)\eta^{1/3} + 2a_1^2a_0^4\eta^{2/3}]\frac{\partial T_0}{\partial y} + \frac{\partial}{\partial y}\left[4a_1a_0^2\eta^{1/3}\frac{\partial T_1}{\partial y}\right]\right\}, \tag{27}$$

$$\dot{T}_{21} + \frac{\partial}{\partial y}T_0\left[-2h_2\eta^{-1/3} - \sum_j\left(\frac{l_0}{l_0^{jj}}\right)^2 q_0^{(j)}\eta^{2/3}\right] = P_e^{-1}\left[\eta^{2/3}\left(-2T_2 + 2f_2a_0^2\frac{\partial T_0}{\partial y}\right) + \frac{\partial}{\partial y}(4f_2a_0^2\eta^{1/3})\frac{\partial T_0}{\partial y}\right], \tag{28}$$

where, $\eta = a_0^3 + 3y$, and q_2 and h_2 are terms appearing in the expressions of the potential flow ϕ_2. The heat balance on the bubble interface can be written:

$$a_0^2\frac{\partial T_2}{\partial y} + 2\frac{a_1}{a_0}\frac{\partial T_1}{\partial y} + \left(2\frac{a_2}{a_0} + \frac{a_1^2}{a_0^2}\right)\frac{\partial T_0}{\partial y}\bigg|_{y=0} = \mathcal{C}\dot{a}_2 \tag{29}$$

$$2\frac{f_2}{a_0}\frac{\partial T_0}{\partial y}\bigg|_{y=0} = \mathcal{C}\dot{f}_2. \tag{30}$$

As for the dynamical problem [4, 7] we have derived the expansions up to and including the order ϵ^3. In order to be brief we will not present here any further expansions.

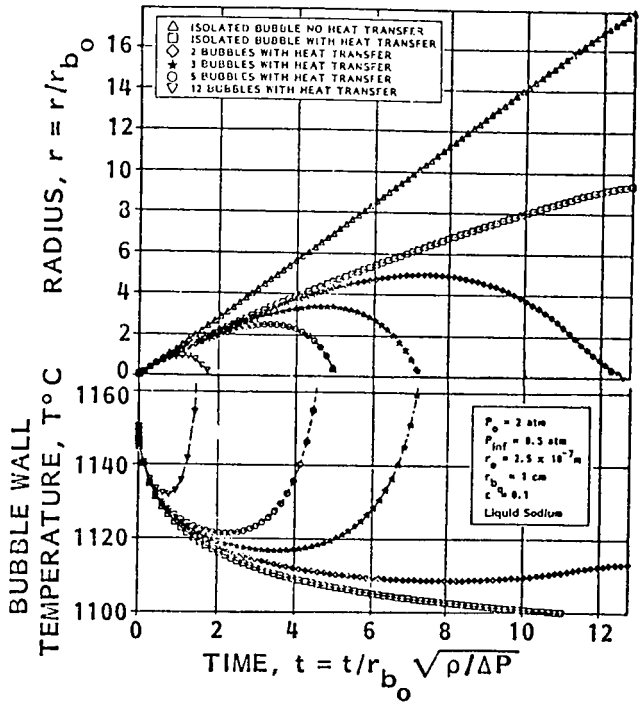

Fig. 3 Growth of an *N*-bubble cloud in a superheated liquid

Approximate Solution: Thermal Boundary Layer

In order to solve the various equations of the problem one needs to couple the resolution of the dynamical problem (by a multi-Runge-Kutta procedure for example) to a resolution method for the heat equation. We are presently considering two approaches to solve the equations appearing at each order of approximation. The first approach, similar to that used in [2] for an isolated bubble, is exact in that it does not consider any assumption on the thickness of the thermal boundary layer at the bubble wall. It consists of solving the heat equation in the fluid through a space marching procedure. The domain of applicability of this method is very large but the corresponding computing time could be considerable.

The second method is based on the assumption that the amount of superheat is large enough so that the distance δ in which the temperature rises from the bubble wall temperature to the ambient temperature is small relative to the bubble radius. In that case a thermal boundary layer assumption is introduced [1] and its thickness can be approximated by:

Downloaded 02 Jun 2010 to 171.66.16.91. Redistribution subject to ASME license or copyright; see http://www.asme.org/terms/Terms_Use.cfm

$$\frac{\delta}{R} \simeq \frac{\rho_v}{\rho} \frac{L}{C(T_\infty - T_b)} \simeq \frac{1}{J}, \tag{31}$$

where C is the specific heat of the liquid and ρ its density (the other variables have been defined earlier). An analytical expression of the temperature at the bubble wall has been derived in this case and can be written for a sphere of radius $a(t)$,

$$T_a = T_\infty - \sqrt{D\pi}\left[\int_0^t \frac{L\rho_v}{K} \frac{a^2 \dot{a}}{\left(\int_x^t a^4 dy\right)^{1/2}} dx\right]. \tag{32}$$

Prosperetti and Plesset [1] showed that this expression is valid for Jacob numbers, J, as low as 3. This same equation applies for $T_0(a)$, and $a_0(t)$ in our approach and similar equations are derived at the following orders [5]. We will not consider here this relatively accurate but laborious approach. We will rather consider a further simplification for the study of collective bubble growth. Solutions of the dynamical equation in the absence of heat transfer show that during the growth phase bubble deformations are negligible at least as far in the time history as the asymptotic method is valid. Figure 1 presents the example of the growth of initially spherical bubbles of initial nondimensional radius 10^{-4}, symmetrically located on a sphere. For the case of an isolated bubble, the growth follows the asymptotic linear behavior. However, when the number of interacting bubble increases, the pressure field associated with the growth of the other bubbles in the cloud reduces the growth rate. Finally for $N = 12$, the method apparently fails for $t > 0.1$, since the radius corrections become larger than the order zero radius. Figure 2 shows, for the same bubble configuration, the ratio of the deformations of type cos θ to the spherical part of $R(\theta, t)$ in the expansion (1). In all cases but the obvious case where the method breaks down the deformations are less than 4 percent where the bubble has attained 2,000 times its initial radius. This result depends obviously, in general, on R_0 and l_0, as well as on the number of interacting bubbles, N. The deformations are larger for larger R_0/l_0 and N. Therefore, based on the above observation we can consider equation (32) to be applicable for the corrected bubble radius, $\Sigma\epsilon^n a_n(t)$ for small ϵ, and as long as deviations from sphericity are negligible.

With this simplification, at any time step all dynamical equations (including the nonspherical part) are solved. The value of the vapor pressure is that corresponding to the bubble wall temperature computed at the preceding time step using equation (32). Figure 3 shows an example of the results obtained with the developed numerical code for the case of N symmetrically located bubbles on a spherical shell. Both, the motion of a characteristic point of the bubble wall and the bubble wall temperature are plotted versus time. The motion of different points on the bubble wall is not always the same, but space limitations do not allow us to elaborate here (see [5] and [9] for details). Basically one observes a flattening of the bubble and its elongation in the direction tangential to the sphere. The qualitative relative comparison of the cases of various numbers of bubbles, N, is however always the same for any point on the bubble surface. Figure 3 reconfirms the results of Fig. 1 on the inhibiting effect of the presence of interacting bubbles on the bubble growth rate. This result is important for any heat exchange prediction and is reflected by the bubble wall temperatures which are shown to decrease slower in the presence of the other bubbles. The comparison of the growth of a bubble in a superheated liquid to that in a cold liquid is satisfactory, both showing the known asymptotic behavior. The results concerning the last phase of the growth of multiple bubbles, namely collapse insteady of growth and consequently temperature surge, are, however, doubtful and instead reflect the expected failure of the asymptotic method in describing correctly the bubble behavior when the two-phase medium becomes dense. As we have concluded in the case of inertia-controlled bubble clouds [7], this failure is probably due to the compressibility of the bubbly medium which was not taken into account. Indeed, the propagation of the information from one bubble to another takes place, in fact, in a finite time due to the finite wave speed in the medium. As a result, the effects of the various bubbles add up with retarded times. Once this is accounted for, the cumulative modification of the pressure field surrounding a particular bubble will be significantly reduced. Another source of method failure is inherent in the growth phenomenon since the ratio of bubble radius to inter-bubble distance constantly increases, necessarily inducing nonvalidity of an asymptotic approach beyond a time limit.

Acknowledgment

This work was supported by a National Science Foundation Grant No. MEA-8260689.

References

1 Prosperetti, S., and Plesset, M. S., "Vapor-Bubble Growth in Superheated Liquid," *J. Fluid Mechanics*, Vol. 85, No. 2, 1978, pp. 249-268.

2 Dalle Donne, M., and Ferranti, M. P., "The Growth of Vapor Bubbles in Superheated Sodium," *Int. J. Heat and Mass Transfer*, Vol. 18, 1975, pp. 477-493.

3 Morch, K. A., "Cavity Cluster Dynamics and Cavitation Erosion," ASME, Cavitation and Polyphase Flow Forum, Boulder, 1981, pp. 1-11.

4 Chahine, G. L., "Pressure Generated by a Bubble Cloud Collapse," ASME, Cavitation and Polyphase Flow Forum, St. Louis, 1982, pp. 27-31.

5 Chahine, G. L., and Liu, H. L., "A Singular Perturbation Theory of the Growth of a Bubble-Cluster in a Superheated Liquid," NSF Grant No. MEA-8260689, Hydronautics Technical Report 83020, Apr. 1983.

6 Plesset, M. S., and Prosperetti, A., "Bubble Dynamics and Cavitation," *Annual Review of Journal Fluid Mechanics*, Vol. 9, 1977, pp. 145-185.

7 Chahine, G. L., "Cloud Cavitation Theory," 14th Symposium Naval Hydrodynamics, Ann Arbor, Mich., Aug. 1982, National Academy Press, Washington, D.C., 1983, pp. 165-195.

8 Chahine, G. L., and Bovis, A. G., "Pressure Field Generated by Non-spherical Bubble Collapse," ASME JOURNAL OF FLUIDS ENGINEERING, Vol. 105, No. 3, Sept. 1983, pp. 346-363.

9 Chahine, G. L., and Liu, H. L., "Collective Bubble Growth in a Superheated Liquid Following a Sudden Depressurization," Sixth International Symposium on Hydraulic Transients in Power Plants, Gloucester, England, Sept. 1983, pp. 19-20.

Downloaded 02 Jun 2010 to 171.66.16.91. Redistribution subject to ASME license or copyright; see http://www.asme.org/terms/Terms_Use.cfm

Simulation of the Pressure Field Due to a Submerged Oscillating Jet Impacting on a Solid Wall

Ph. F. Genoux[1]
Direction des Recherches Etudes et Techniques, Paris, France

G. L. Chahine
Tracor Hydronautics, Inc., Laurel, Md.

This paper presents some results obtained with the simulation of a submerged oscillating jet impacting on a solid wall. The oscillating jet which organizes into large vortical structures is simulated by the emission of vortex rings at a constant frequency. Outside of the cores of the rings the fluid is assumed to be inviscid and irrotational. The positions of the tori are obtained by combining for each torus its self-induced velocity with the velocity induced by all other rings and ring-images in the wall. The tangential velocities and the pressures in the fluid at the wall are then computed. The high shearing and suction forces found at the wall may explain the enhanced erosivity and cleaning action of oscillating jets.

Introduction

Experimental observations of air jets show the tendency of the turbulent eddies in their shear layer to organize in large structures. Excitation of a jet with periodic acoustic signals produced upstream of the nozzle by transducers or loud speakers shows a remarkable change of the jet structure into discrete ring vortices, when the excitation frequency, f, matches the predominant natural frequencies of the nonexcited jet [1, 2]. This corresponds to a Strouhal number, S_d, close to 0.3 or one of its first integer multiples. (The Strouhal number is defined as $S_d = fd/V$, where V and d are the velocity and the diameter of the jet.) Based on these observations, several attempts have been carried out to model a jet with a discrete distribution of vortex rings. Axially symmetric vortex rings with a viscous core have been investigated and the numerical schemes were able to satisfactorly reproduce experimental measurements or observations [3–5]. For instance, the fluctuating pressure field in the jet vicinity was simulated by Fung et al. [3]. Acton [4] simulated the upstream portion of the jet with a double row of ring vortices which were allowed to interact and move freely downstream of the nozzle exit. The roll up of the vortex sheet into large axisymmetric structures was numerically demonstrated. Artificial excitation of the jet by periodically modulating the strength of the emitted vortices exhibited the same features as obsrved experimentally, namely the existence of an optimal Strouhal number.

Under an effort for the Department of Energy, in order to improve the erosive and cleaning power of submerged water jets in deep drilling technology, the same ideas were applied to cavitating jets [6]. Here, the cavitation appears in the shear layer in randomly oriented vortex filaments in which gas and vapour cavities grow. The studies conducted at Tracor Hydronautics have shown very clearly that a cavitating jet can be organized in well defined bubble ring vortices when excited (Fig. 1). This has augmented the erosive and cleaning power of these jets. Both external excitation with a transducer and self induced oscillations have been considered [6]. In previous work we modelled the growth and collapse of a toroidal bubble in an infinite medium. A dynamic equation was derived and the importance of the various parameters investigated. The characteristic time of the collapse of the toroidal cavity, and its self induced translation velocity were obtained [7, 8].

This paper is one of the first steps towards the understanding of the enhancement of the cleaning effects associated with the excited jets and is mostly concerned with the interaction of an organized jet with a solid wall. Taking advantage of the numerical results obtained in previous studies and of experimental observations one can simplify the problem by neglecting the fine structure of the jet's shear layer and assuming that the major features of the flow field are associated with the large structures. Thus, the excited jet is modelled with large vortex rings emitted from the nozzle orifice at constant time intervals which correspond to the

Fig. 1 Cavitating vortex rings in the shear layer of an excited submerged jet. $\sigma = 0.94$, $M = 0.082$, and $F = 14$ kHz

[1] This work was done while on leave at Tracor Hydronautics, Incorporated.

Contributed by the Fluids Engineering Division and presented at the Cavitation and Polyphase Flow Symposium, Houston, Texas, June 20–22, 1983. Manuscript received by the Fluids Engineering Division July 19, 1983.

Copyright © 1984 by ASME

Downloaded 02 Jun 2010 to 171.66.16.91. Redistribution subject to ASME license or copyright; see http://www.asme.org/terms/Terms_Use.cfm

frequency of the pulsing jet. Each of these vortex rings has in its center a gas and vapor filled toroidal cavity and is allowed to move and change shape under the influence of its self induced velocity as well as the velocities induced by the other ring vortices present in the field. The presence of the wall is accounted for by applying the method of images since no viscous effects are considered. Knowing the location and characteristics of all rings at any time allows the computation of the generated pressure field. We present here the model used and some results on the interactions of the large structures between each other and with the wall, as well as the generated pressures on several arbitrary locations on the solid wall.

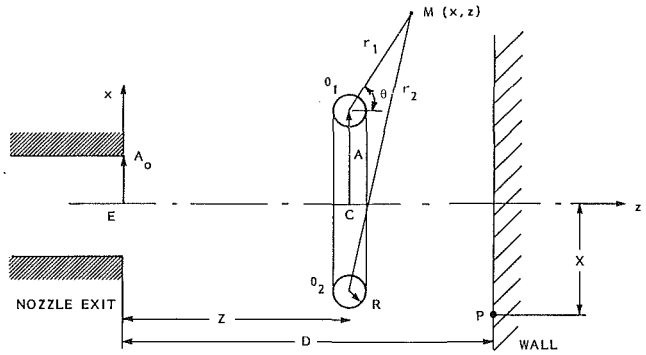

Fig. 2 Definition diagram of the geometry

Formulation of the Problem

Let us consider a vortex ring of radius A_0 and of circulation, Γ, constant in time. The core of the ring is gas and vapor filled and has a circular section of radius R_0. The surface tension coefficient at the bubble liquid interface is γ, and the initial partial gas and vapor pressures inside the bubble are P_{g0} and P_v. Outside the gaseous core we can assume that the liquid is inviscid and incompressible and that the flow is irrotational. Therefore the liquid flow is potential. In order to simplify the analytical and numerical approach we consider the case where the radius of the gaseous section is small compared to the torus radius and introduce the small parameter,

$$\epsilon = R_0/A_0 << 1 \tag{1}$$

We can then consider an asymptotic approach to the problem, and use the method of matched asymptotic expansions. Concerning the investigation of the bubble ring behavior two regions of the fluid field are introduced. In the "inner region" of characteristics length R_0, the problem is concerned with the torus core, and is two-dimensional, and the bubble appears as cylindrical. In the "outer region" of characteristic length A_0, the cavity cannot be distinguished and the problem reduces to the well-known potential problem of a circular vortex line. For this "outer problem" the expression of the stream function ψ is given by Lamb [9].

$$\psi = -\frac{\Gamma}{2\pi}(r_1+r_2)\left[K\left(\frac{r_2-r_1}{r_2+r_1}\right)-E\left(\frac{r_2-r_1}{r_2+r_1}\right)\right] \tag{2}$$

where E and K are complete elliptic integrals of the first and second kind respectively and where the geometric distances r_1 and r_2 are defined in Fig. 2. Similarly, the velocity potential can be written as

$$\phi^{\text{ext}} = \frac{-\Gamma}{4\pi}\int_S \frac{\mathbf{PM}\cdot e_z}{|\mathbf{PM}|^3}\,ds$$

$$= \text{sgn}(Z-z)\frac{\Gamma A_o}{2}\int_0^\infty e^{-k|z-Z|}J_0(kx)J_1(kA_o)dk \tag{3}$$

where J_0 and J_1 are the Bessel functions of order 0 and 1, and P is a point of any surface S limited by the circle of radius A_0.

In order to determine the self-induced translation velocity of the vortex ring one has to solve both the inner and outer problems using a matching condition at the boundary of the two regions. For instance, when no bubble growth occurs the behavior of the outer solution in the vicinity of the bubble wall can be obtained by expanding ϕ^{ext} in powers of ϵ and Log ϵ, [8], and can be written:

$$\lim_{\epsilon\to 0}\ \phi^{\text{ext}}(\epsilon A_o\tilde{r},\theta)$$

$$= \frac{\Gamma}{2\pi}\left[\theta-\epsilon\text{Ln}\left(\frac{\epsilon}{8}\right)\frac{\tilde{r}}{2}\cos\theta-\epsilon\frac{\tilde{r}\cos\theta}{2}\text{Ln}\,\tilde{r}+\sigma(\epsilon)\right], \tag{4}$$

where the nondimensional distance, $\tilde{r}$, from the bubble center to the field point M is defined by:

$$\tilde{r} = r/R_0 = r/\epsilon A_0 \tag{5}$$

Expression (4) is used for writing the boundary conditions at

Nomenclature

d = jet diameter
e_z = unit vector along z-axis
E = complete elliptical integral of the second kind
f = frequency
Jo = Bessel function of order 0
J_l = Bessel function of order 1
K = complete elliptical integral of the first kind
$\mathbf{n}$ = normal unit vector
P_{g0} = initial partial gas pressure inside the ring
P_v = vapor pressure inside the ring
P_∞ = pressure at infinity
R = vortex ring section radius
R_0 = initial ring section radius
$r_{1,2}$ = geometric distance between the field point and the ring center
A = vortex ring radius
A_0 = initial vortex ring radius
$\mathcal{S}$ = vortex ring surface
S_d = Strouhal number $= fd/V$
t = time
V = jet velocity
Z = axial distance of the ring center
z = axial distance of the field point
$\mathcal{W}_s^{-1}$ = inverse of the Weber number $= \gamma/R_0P_\infty$
X = radial distance from the ring axis
ϵ = asymptotic parameter, defined as the ratio of the ring section radius to the ring radius
γ = surface tension
Γ = circulation of the vortex ring
ψ = stream function
ϕ = velocity potential
θ = field angle
∇ = gradient operator
Δ = Laplacian operator
ρ = density of the liquid
δ = ratio between the core size and the ring radius
Ω_s = circulation parameter $= \frac{\rho}{P_\infty}\left(\frac{\Gamma}{2\pi R_0}\right)^2$

Superscripts

ext = outer problem
int = inner problem
~ = tilde, normalization in reference to the outer problem
— = bar, normalization in reference to the inner problem

Downloaded 02 Jun 2010 to 171.66.16.91. Redistribution subject to ASME license or copyright; see http://www.asme.org/terms/Terms_Use.cfm

infinity for the inner problem, and contains most of the information needed to compute the bubble translation velocity. Besides the vortical motion which is given by the first order term, a uniform velocity appears to the following order, ϵLn ($\epsilon/8$). More complicated terms appear at the higher orders. If the bubble ring is not isolated the second term is modified by an additional constant multiplying $\bar{r}\cos\theta$.

In the "inner problem", one has to solve the Laplace equation along with kinematic and dynamic boundary conditions on the bubble wall:

$$\Delta\phi^{\text{int}} = 0, \tag{6}$$

$$\nabla\phi^{\text{int}} \cdot \mathbf{n}\Big|_{r=R} = \mathbf{V}_t \cdot \mathbf{n}, \tag{7}$$

$$\rho\left[\frac{\partial\phi^{\text{int}}}{\partial t} - \mathbf{V}_t \cdot \nabla\phi^{\text{int}} + \frac{1}{2}\,|\nabla\phi^{\text{int}}|^2\right]_{r=R} = p_\infty - p_v - p_g - 2\gamma\mathcal{C}, \tag{8}$$

where $\mathbf{n}$ is the normal vector to the bubble wall, $\mathcal{C}$ the bubble curvature, and $\mathbf{V}_t$ the translation velocity of the ring which is chosen as the translation velocity of the origin of coordinates. Equations (6) to (8) are expanded in powers of ϵ and Logϵ, and ϕ^{int} and $R(\theta, t)$ decomposed in spherical harmonics. One finds, [8], after using the boundary condition at infinity derived from (4) that the circular shape of the bubble section is a stable solution, up to the order ϵ, and that the self-induced velocity of the ring is

$$V_{\text{self}} = \frac{\Gamma}{4\pi R_0}\left\{\frac{\epsilon}{\bar{A}}\left[\text{Ln}\frac{8\bar{A}}{\epsilon} - \frac{1}{2} + \frac{\mathcal{W}_s^{-1}}{\Omega_s}\right] + 0(\epsilon)\right\}, \tag{9}$$

where $\mathcal{W}_s^{-1}$ is the inverse of the Weber number and Ω_s the circulation number measuring respectively the relative importance of the surface tension and the pressure drop due to circulation relative to the ambient pressure. These are written as:

$$\mathcal{W}_s^{-1} = \gamma/R_0 P_\infty, \tag{10}$$

$$\Omega_s = \rho(\Gamma/2\pi R_0)^2/P_\infty. \tag{11}$$

A similar expression has been obtained for vortex rings with a viscous liquid core. In that case ϵ is replaced by δ, the ratio between the core size and the torus radius, A, the surface tension term is null and the constant 1/2 is replaced by 1/4 [10]

$$V_{\text{viscous}} = \frac{\Gamma}{4\pi R_0}\left\{\delta\left[\text{Ln}\frac{8}{\delta} - \frac{1}{4}\right] + 0(\delta)\right\} \tag{12}$$

Numerical Procedure and Remarks

In order to simulate the behavior of the jet and its interaction with the wall we used the following procedure. At $t = 0$, a ring is emitted from the location $Z = 0$ and is allowed to move under the influence of its self-induced velocity. The velocity due to the ring image is to be added when a solid wall is present. Subsequently at the discrete instants $t_n = n/f$, (f is the jet oscillation frequency and n an integer number) an additional ring is emitted and is allowed to interact with the rings already in field and their images. At every time step the locations of all the rings are computed, as well as their translation velocities which in turn determine their subsequent positions. The self-induced velocity of any ring is computed using equation (9), while its translation velocity due to the other rings and the ring images is derived using equations (4) or (5) since the analysis show that the translation velocity of the bubble ring due to an imposed incoming flow is equal to the fluid velocity at its location.

As expected the behavior of the emitted rings is at first unsteady and does not represent the jet behavior. However, after certain computation time has elapsed the system becomes steady and a periodic behavior of the various emitted ring is exhibited. Once the location of all the rings are determined, the pressure at any location can be obtained using the Bernoulli equation:

$$p(M) - p_\infty = -\rho\left[\frac{\partial\phi^{\text{ext}}}{\partial t} + \frac{1}{2}\,|\nabla\phi^{\text{ext}}|^2\right] \tag{13}$$

where ϕ^{ext} is given using (3).

Let us note that in the procedure and the analytical expressions presented above we have neglected both the influence of the nozzle and the bubble growth. The first effect is too complicated to account for with accuracy at the present time and will constitute a future subject of investigation. The bubble growth effect which we have studied earlier [7] can be neglected if the variation of the local pressure around the bubble ring and the influence on the vortex ring motion are small compared to ϵ, the highest order term considered in the above expressions. This is true as long as the distance between two tori is of higher order of magnitude than ϵ, (i.e., as long as the distance is greater than the section radius). This assumption, as we will see below is valid in all the cases studied and fails only when the vortex ring becomes very close to the wall. In fact, in that case not all assumptions are valid and viscous effects on the wall must be considered.

Results and Discussion

In all results presented below, distances are normalized with the nozzle radius, $A_0 = d/2$, and velocities with the self-induced velocity of an isolated ring, V_{selfo}, from (9). Thus the time scale is A_0/V_{selfo}. For comparison purposes, Fig. 3 shows the behavior of the simulated jet in absence of a solid wall. In this case a steady periodic solution appears after about seventeen time steps. Then the multiple rings exhibit similar behavior to two equal rings, namely successive threading and overpassing of one ring through the other. Here all rings emitted at an odd number normalized time follow the same path while all even numbered ones follow a different path. At a given subsequent time the rings are located as those numbered in the figure. The arrowed lines in the figure join two successive rings and show that the closest to each other these rings get is at the moment they pass each other and that even then they stay at a distance of order unity. Figures 4 and

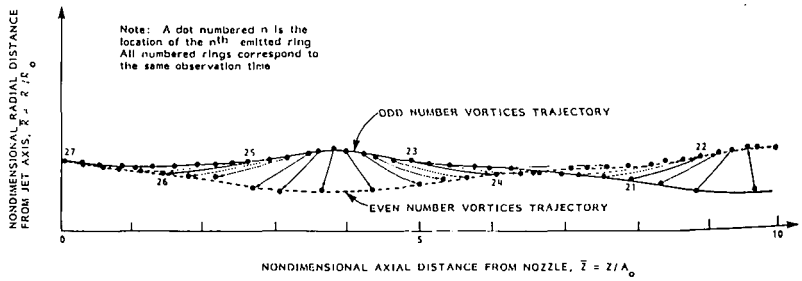

Fig. 3 Trajectories of ring vortices emitted at constant frequency, ϵ = 0.1, W_e = 200, Ω = 20, f = 1

Downloaded 02 Jun 2010 to 171.66.16.91. Redistribution subject to ASME license or copyright; see http://www.asme.org/terms/Terms_Use.cfm

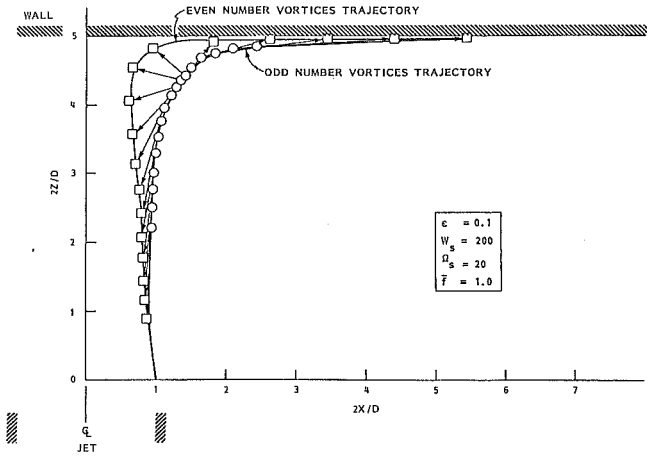

Fig. 4 Trajectories of ring vortices emitted at constant frequency ($S_d = 2\bar{f} = fd/V\,self_0 = 2$)

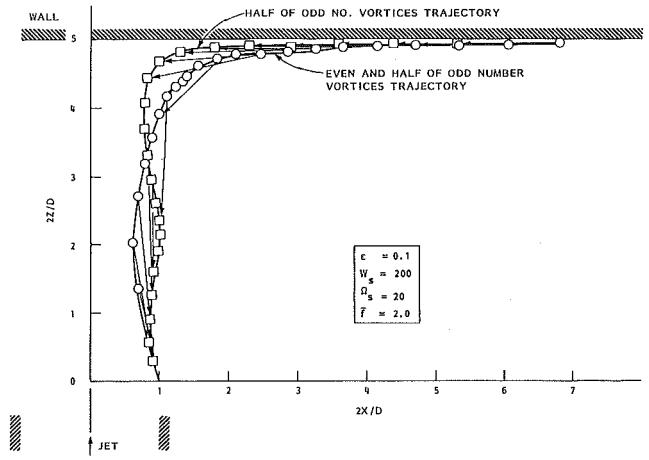

Fig. 5 Trajectories of ring vortices emitted at constant frequency ($S_d = 2\bar{f} = fd/V\,self_0 = 4$)

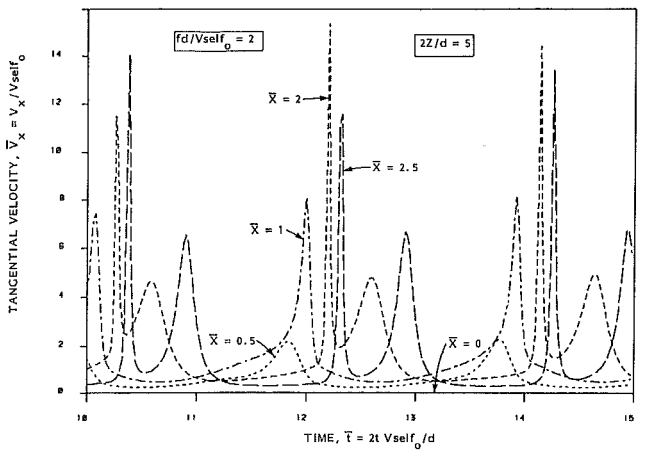

Fig. 6 Tangential velocities induced at different locations, $\bar{X}$, on the impacted wall versus time

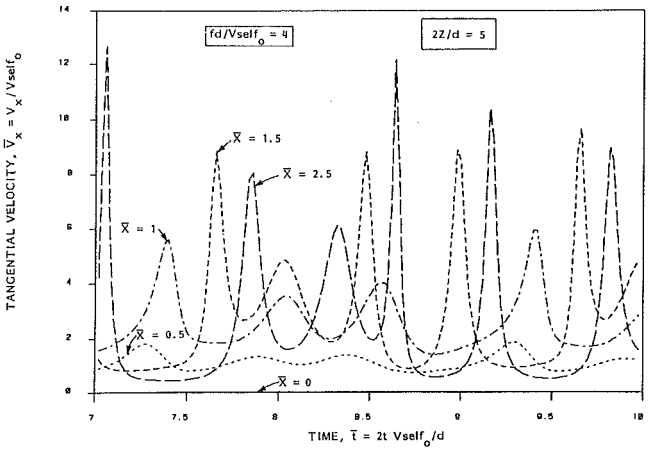

Fig. 7 Tangential velocities induced at different locations, $\bar{X}$, on the impacted wall versus time

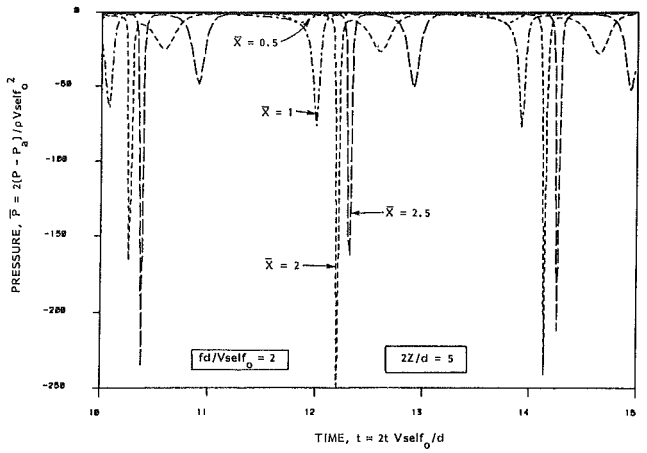

Fig. 8 Pressures induced at different locations, $\bar{X}$, on the impacted wall, versus time

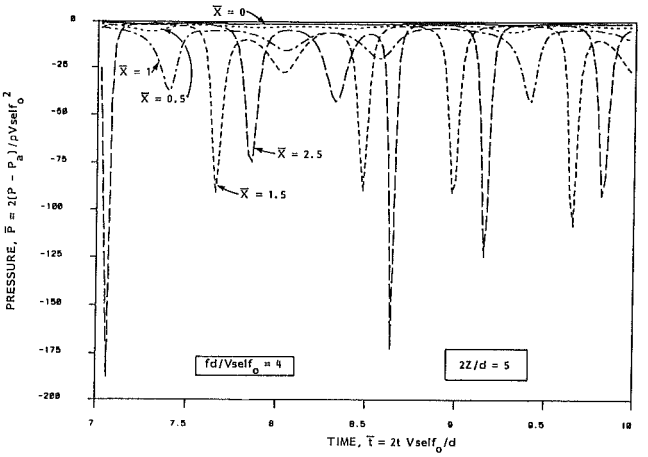

Fig. 9 Pressures induced at different locations, $\bar{X}$, on the impacted wall, versus time

5 show the same type of trajectories represented in-presence of a solid wall and for two reduced frequencies, $\bar{f} = 1$ and 2 (or $\bar{S}_d = f\,V_{self_0}/d = 0.5$ and 1). In both cases the standoff distance, $\bar{Z} = Z/A_0$, is equal to 5. The importance of the Strouhal number on the jet behavior is very clear in this example. Obviously the optimum location of the wall for maximum erosion and cleaning power is not the same for both cases. This optimum is for either maximum pressure fluctuations or maximum tangential velocity (shear) at the wall. In Fig. 4, two distincts trajectories for odd and even number rings is seen as in the free jet case. This is not the case for $S_d \sim 1$, Fig. 5, where all even number rings and one out of two odd number rings follow one trajectory while the other half of the odd number rings follow another. In both cases the steady solution was attained much faster than for the free jet, after

Downloaded 02 Jun 2010 to 171.66.16.91. Redistribution subject to ASME license or copyright; see http://www.asme.org/terms/Terms_Use.cfm

about seven time steps. We can notice also that in both cases two successive rings are always much further apart than ϵ. However their distance to the wall becomes of this order at a radial distance to the jet center, $\bar{X}$, of about 2.5.

Figures 6 and 7 show the tangential velocities induced on five different locations on the solid wall versus time. The spikes correspond to the passage of a vortex ring. It is interesting to notice that both the amplitude and the frequencies of the locally sensed velocity spikes are dependent on the point of observation. The same observations can be made concerning the generated pressures represented in Figs. 8 and 9. The occurrence of the pressure and velocity spikes for both frequencies are very much correlated as well as their amplitudes. Both indicate that the predominant term is the steady term $|\nabla\phi|^2$ and that the major factor with our assumptions appears to be the distance at a given time between the ring and the wall. This explains why the highest negative pressure peaks are at an optimum (in the analyzed range) value of $\bar{X}$. Both, the high intensification of the tangential velocities and of the suction pressures on the wall due to the passage of organized structures indicate a significant enhancement of the cleaning capability of water jets through excitation. This is possible through an increased shearing action of the jet on the solid chips on the wall as well as increased lifting forces. These first results of the developed program are being presently refined through accounting for the bubble volume change near the wall and are being extended to obtain relationships between Strouhal numbers, optimum standoff distances and maximum pressure drop on the wall. The same numerical program can be used for noncavitating vortex rings by replacing equation (9) by (12).

Acknowledgments

This work was supported in part by the U.S. Department of Energy, Division of Geothermal Energy, under SANDIA Laboratories Contract No. 13-5129. We would like to thank V. E. Johnson, H. L. Liu, and W. R. Sirian from Tracor Hydronautics, Incorporated for useful discussions and contributions to the presentation.

References

1 Crow, S. C., and Champagne, F. H., "Orderly Structure in Jet Turbulence," *Journal of Fluid Mechanics*, Vol. 48, Part 3, Aug. 1971, pp. 547-591.

2 Kibens, V., "Discrete Noise Spectrum Generated by an Acoustically Excited Jet," Paper 75-0592, *AIAA Fifth Aeroacoustics Conference*, Mar. 12-14, 1979.

3 Fung, Y. T., Liu, C. H., and Gunzburger, M. D., "Simulation of the Pressure Near a Jet Randomly Distributed Vortex Rings," *AIAA, Journal*, 1979, Vol. 17, pp. 553-557.

4 Acton, E., "A Modelling of Large Eddies in an Axisymmetric Jet," *Journal of Fluid Mechanics*, Vol. 98, 1980, pp. 1-31.

5 Edwards, A. V. J., Morfey, C. L., and Davies, P. O. A. L., "A Computer Simulation of a Starting-Jet," University of Southampton, *ISVR Technical Report No. 89*, Apr. 1977.

6 Johnson, V. E., Jr., Chahine, G. L., Lindenmuth, W. T., Conn, A. F., Frederick, G. S., and Giacchino, G. J., Jr., "Cavitating and Structured Jets for Mechanical Bits to Increase Drilling Rate," ASME Paper 82-P35-13, 1982.

7 Chahine, G. L., and Genoux, Ph., "Collapse of a Vortex Ring," *ASME Cavitation and Polyphase Flow Forum*, Saint Louis, Missouri, June 1982, pp. 37-41. Journal of Fluids Engineering, Vol 105, pp. 400-405, Dec. 1983.

8 Genoux, Ph., and Chahine, G. L., "Equilibre Statique et Dynamique d'un tore de Vapeur Tourbillonnaire," *Journal de Mecanique théorique et Appliquée*, Vol. 2, No. 5, pp. 829-837, Sept. 1983.

9 Lamb, H., *Hydrodynamics*, Dover Publications, Inc., New York, 1932.

10 Safman, P. G., "The Velocity of Viscous Vortex-Rings," *Stud. Appl. Math.*, Vol. 49, 1970, p. 371-380.

Downloaded 02 Jun 2010 to 171.66.16.91. Redistribution subject to ASME license or copyright; see http://www.asme.org/terms/Terms_Use.cfm

Journal of Fluids Engineering

Technical Briefs

Cavitation Incipience in Submerged Orifice Flows

John H. Lienhard[1]

Goss and I [1 and 2] argued in 1972 that the cavitation inception coefficient, σ_i, for a shear layer, should depend upon the absolute size of a flow as well as on its configuration. This notion was not too well received at the time, but a recent paper by Katz and O'Hern [3] provides new data that give a basis for reopening the issue.

Background

Let us briefly review our previous dimensional analysis of cavitation inception. We take the deviation of the local pressure, p, (or of a characteristic system pressure) from the vapor pressure, p_v, as the dependent variable. Then:

$$p - p_v = f(\rho_f, u, d, D, n) \tag{1}$$

where:

- ρ_f is the liquid density.
- u is the relative velocity of the liquid across the shear layer in which inception begins.
- d and D are any two system dimensions required to define the flow configuration. The submerged orifice or nozzle occupies much of our attention (see Fig. 1). In it, d is the diameter of the vena contracta, and D is the diameter of the surrounding pipe.
- p is the static pressure in the conduit after the shear layer has diffused.
- We designate as n m^{-3}, the density of "weak spots" in the fluid. These are the sort of loci about which cavitation might form—tiny gas bubbles, impurities containing gas pockets, etc. Of course n is not a readily observable quantity, but one that might be fixed in a given flow by controlling the gas content or liquid preparation.
- The viscosity is not included in this list because cavitation is triggered by turbulent pressure fluctuations, and they in turn are known to be insensitive to viscosity.

There are six variables in N, m, and sec, so equation (1) must reduce to an equation among three dimensionless groups: the cavitation inception coefficient, σ_i, a configuration parameter, $\beta \equiv d/D$ and the scale parameter, $dn^{1/3}$. Thus:

$$\sigma_i \equiv 2(p - p_v)/\rho_f u^2 = f(\beta, dn^{1/3}) \tag{2}$$

The scale parameter, $dn^{1/3}$, is not a commonly recognized cavitation parameter; nor is it a very satisfactory one, owing to the presence of the very hard-to-measure quantity, $n^{1/3}$. The problem is that there is no other correct scale factor with which to nondimensionalize d. The lack of a better system scale-factor has probably dissuaded cavitation people from accepting size as a primary determinant of σ_i.

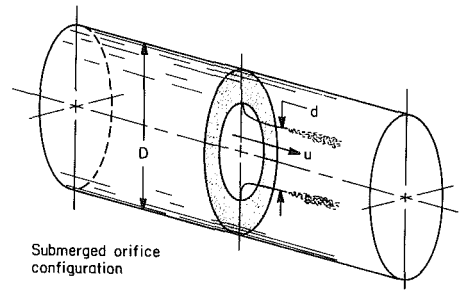

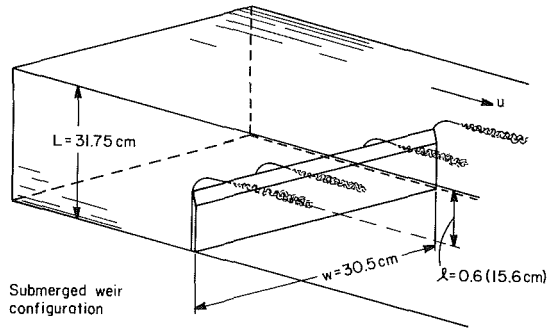

Fig. 1 Submerged orifice and weir configurations

The data (both original and reported) that were used in [1, 2] included both nozzle data [4–8] and orifice data with d corrected for contraction [2, 7, 8]. They represented substantial variations of d, D, and p_v. Thus the ranges of all parameters in equation (2) were varied; however the dimensional quantities ρ_f and n were not. All data were based on water, and data were only reported for experiments in which at least the oxygen content was fairly low—approximately 4 ppm.

The data correlation from [1] is reproduced in Fig. 2. These data have been fitted with the following empirical representation:

$$\sigma_i = \sigma_i^0 (dn^{1/3}) \cdot (3.5 - 2.5e^{-4\beta}) \tag{3}$$

where σ_i^0 $(dn^{1/3})$ is the limiting cavitation inception coefficient for a hole discharging into an infinite bath. Since $n^{1/3}$ is not known, σ_i^0 must be written in seemingly dimensional form:

$$\sigma_i^0 = (d \text{ cm})e^{-5.9(d \text{ cm})} + 0.264(d \text{ cm})^{1/3}(1 - e^{-4(d \text{ cm})}) \tag{4}$$

The unknown value of $n^{1/3}$ cm is thus absorbed into the

[1] Professor, Heat Transfer/Phase Change Laboratory, Mechanical Engineering Department, University of Houston, Houston, Texas 77004, Fellow ASME

Contributed by the Fluids Engineering Division of THE AMERICAN SOCIETY OF MECHANICAL ENGINEERS. Manuscript received by the Fluids Engineering Division July 26, 1983.

Copyright © 1984 by ASME

Downloaded 02 Jun 2010 to 171.66.16.91. Redistribution subject to ASME license or copyright; see http://www.asme.org/terms/Terms_Use.cfm

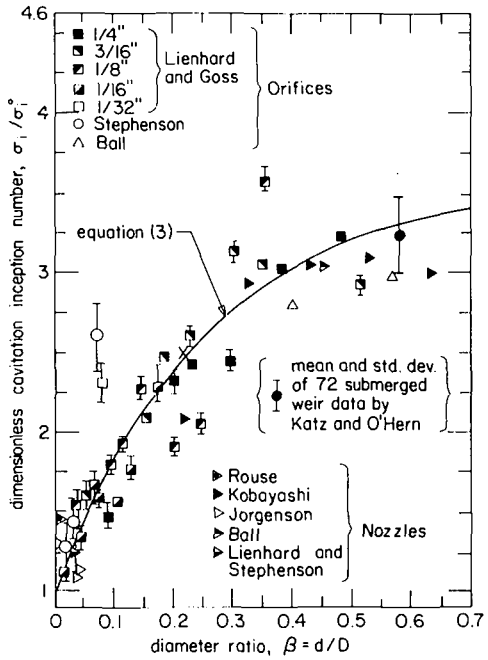

Fig. 2 Incipient cavitation coefficient data

constants of equation (3) which, in turn, is only valid for water with a fairly low gas content.

Submerged Weir Data

The submerged weir configuration studied by Katz and O'Hern is shown in[2] Fig. 1. This is equivalent to a submerged orifice flow with $\pi d^2/4 = l\,w$ and $\beta = \sqrt{l/L}$. This gives $\beta = 0.578$ and $d = 19$ cm. (Notice that in Fig. 2 we have applied a standard contraction coefficient of 0.60 to the slot dimension.) Equations (3) and (4) then give $\sigma_i = 2.29$ based upon these values.

The Katz and O'Hern inception coefficients (and their standard deviation) for an oxygen concentration of 3.6 ppm, are:

$$\sigma_i = 2.25 \pm 0.15$$

when they are converted to the form given in equation (2). These data are displayed in Fig. 2, in the form suggested by equation (3).

Thus these totally independent measurements in a different configuration can be predicted remarkably well by equations (3) and (4). As a matter of interest, the Katz and O'Hern data for an oxygen content of 9–11 ppm yield $\sigma_i \simeq 2.5$—a number that is only slightly higher. This reflects a relative insensitivity of σ_i to dissolved oxygen when the oxygen content is not high, and it suggests that equations (3) and (4) can be used fairly freely in undersaturated water.

Both Baker, Holl, and Arndt [9], and Ooi [10], provide evidence that support the claim that the influence of dissolved gas is weak in undersaturated liquids, although neither provide additional σ_i data for comparison with equation (3). (Only desinence data are given in [9]; and Ooi's nozzles permit the entrainment of liquid into the jet from behind the exit plane.) The investigations involve variations of the gas content from 2 to 14 ppm and both report only about a 10 percent average variation in σ with gas content in flows that are subsaturated or slightly beyond. In the range from 7 to 14 ppm, both sources show roughly a doubling in σ.

[2] There was a long shelf downstream of the weir, parallel to the floor of the flume and 2.54 cm above it, with a gap under it through which some of the flow escaped. We have taken the downstream channel dimensions as appropriate for this configuration.

References

1 Lienhard, J. H., and Goss, C. D., "Influences of Size and Configuration on Cavitation in Submerged Orifice Flows," ASME Preprint 71-FE-39, Fluids Engr. Conf., Pittsburgh, Pa., May 9–12, 1971.

2 Goss, C. D., "Effects of Size and Configuration Upon Cavitation in a Submerged Orifice Jet," M. S. thesis, University of Kentucky, Lexington, Ky., 1969.

3 Katz, J., and O'Hern, T. J., "Cavitation in Large Scale Shear Flows," ASME Preprint 83-FE-33, Fluids Engr. Conf., Houston, Tx., June 20–23, 1983.

4 Rouse, H., "Cavitation in the Mixing Zone of a Submerged Jet," *La Houille Blanche*, Vol. 8, No. 1, 1953, pp. 9–19.

5 Kobayashi, R., "Effect of Cavitation on the Discharge Coefficient of Standard Flow Nozzles," ASME *Journal of Basic Engineering*, Vol. 89. No. 3, 1967, pp. 677–685.

6 Jorgenson, D. W., "Noise from Cavitating Submerged Water Jets," *J. Acoustical Soc. Am.*, Vol. 33, No. 10, 1961, pp. 1334–8.

7 Ball, J. W., Discussion of paper by Numachi et al., ASME *Journal of Basic Engineering*, Vol. 84, No. 1, 1960, pp. 6–10.

8 Stephenson, J. M., "A Study of Cavitating and Flashing Flows," M. S. thesis, Washington State University, Inst. of Tech. Bull. 290, 1965.

9 Baker, C. B., Hill, J. W., and Arndt, R. E., "Influence of Gas Content and Polyethylene Oxide Additive upon Confined Jet Cavitation in Water," ASME Cavitation and Polyphase Flow Forum, New York, 1976, p. 68.

10 Ooi, K. K., "Scale Effects on Cavitation Inception in Submerged Jets," Ph.D. dissertation, California Institute of Technology, 1981.

Downloaded 02 Jun 2010 to 171.66.16.91. Redistribution subject to ASME license or copyright; see http://www.asme.org/terms/Terms_Use.cfm

Journal of Fluids Engineering

Discussion

Confined Flow in a Partially-Filled Rotating Horizontal Cylinder [1]

Roger F. Gans.[2] The authors have tackled a difficult and interesting problem using a combination of approximate analysis and experiment. The analysis is restricted to small Reynolds number. In that limit results depend on the parameter G, formally of order unity, but actually large. (For the experiments reported on Fig. 11, $G=250$, 480 and 1640.)

The data agree with analysis for $G=1640$; there is disagreement at the other two values. The discrepancies are attributed to "the boundary layer on the frontal plate, parallax error . . . secondary flow, uncertainties in the value of the properties, approximations in the theoretical model and surface tension." This would be more convincing were estimates of these errors constructed. This is important in view of the ad hoc and unsystematic manner in which equations (3) were obtained from equations (1).

The space limitations for discussion make this necessarily brief. I will discuss the analysis and then the experiments.

Equations (3) express a radial balance between gravity and differential pressure, and a tangential balance among gravity, pressure and viscous forces. To explore a hydrostatic balance why not scale the differential pressure by ρgL rather than $\mu\omega$ (where L denotes the scale of radial variation, not necessarily equal to r_0). In this scaling the inertial terms are multiplied by Re/G (equal to a Froude number), which can be taken to be small, leaving

$$\frac{\partial p}{\partial \eta}=\cos\phi+\frac{r_0}{LG}\left\{\frac{\partial^2 u}{\partial \eta^2}+\frac{L}{r_0}\left[\frac{1}{\eta}\frac{\partial u}{\partial \eta}-\frac{2}{\eta^2}\frac{\partial v}{\partial \phi}\right]+\left(\frac{L}{r_0}\right)^2\left(\frac{\partial^2 u}{\partial \phi^2}-u\right)\right\}$$

$$\frac{L}{r_0}\frac{1}{\eta}\frac{\partial p}{\partial \phi}=-\sin\phi+\frac{r_0^2}{L^2 G}\left\{\frac{\partial^2 v}{\partial \eta^2}+\frac{L}{r_0}\frac{1}{\eta}\frac{\partial v}{\partial \eta}+\left(\frac{L}{r_0}\right)^2\frac{1}{\eta^2}\left(\frac{\partial v}{\partial \phi^2}-v\right)+\left(\frac{L}{r_0}\right)^3\frac{2}{\eta^2}\frac{\partial u}{\partial \phi}\right\}$$

where the scaling for u has been taken to be $(L/r_0)(\omega r_0)$, a necessary consequence of the divergence condition, equation (2).

In the work under discussion $L=r_0$, and one may take $G=0(1)$ or $G>>1$. In either case the viscous terms in each equation are of the same order. If L/r_0 is taken to be small, $r_0/LG<<1$ and $r_0^2/L^2G\sim 1$, then one obtains the equivalent of equation (3*a*), and a pressureless equation (3*b*), with a vastly simplified viscous term. Pressure and velocity are decoupled at lowest order.

The reader will note a suggestive resemblance of equations (3) to the governing equations of lubrication theory. This can be made clearer by a redefinition of the pressure, before scaling. Let the dimensional pressure be

$$P=P_{\mathrm{atm}}+\rho g r_0[r\cos\phi+\pi(L/r_0)]$$

and further let $r=r_0\ [1+(L/r_0)y]$. Then the equivalent of equations (3) becomes

$$\frac{\partial \pi}{\partial y}=0[(L/r_0{}^2]$$

$$\frac{\partial \pi}{\partial \phi}=\frac{\partial^2 v}{\partial y^2}+0(L/r_0)$$

where I have taken $\mathrm{Re}/G<<(L/r_0)^2$.

The solution of this set, coupled to the divergence condition, with a free surface boundary condition, constitutes a novel problem, probably appropriate to the thin layer adhering to the upper walls of the cylinder. The recirculation region does not fit into this formulation very well. One certainly cannot apply the lubrication technique of using the integrated divergence condition.

It is difficult to assess fully the experiments because of inadequate reporting. If I assume off-the-shelf glycerine, typically about 96% pure with a kinematic viscosity of about 4 cm^2/s, I can deduce the following about the experiments reported in Fig. 11:

G	ω(rad/s)	Re	Re/G
1640	1.17	18	.011
480	3.98	61	.127
250	7.64	116	.464

These data suggest that the increasing discrepancy between theory and experiment with decreasing G may indeed be an inertial effect, scaled by Re/G. A formal expansion would be useful to explore this contention.

Authors' Closure

The authors wish to thank Dr. Gans for his penetrating observation and for providing a valuable addition to this paper. It is to be mentioned that the scaling, whether one uses $\rho g r_0$ or $\mu\omega$, does not alter the final results.

The value of $r_0^2\omega/\nu$, which is the Reynolds number, is given in Fig. 10 as 2.7, 9.3, and 15.5, therefore, the value of Re/G should be .0016, .019, and .062. The discrepancy is caused by a strong dependence of kinematic viscosity on temperature, hence the value of $\nu=4.0$ cm^2/s is different from the values used for the computation of Re in Fig. 10 for which the temperature is in the vicinity of 22°C. In addition, one may observe that the experimental location of the free surface for $G=920$ in Fig. 13, unlike those in Fig. 11, is higher than the

[1] By A. Haji-Sheikh, et al., published in the September 1984 issue of the JOURNAL OF FLUIDS ENGINEERING, Vol. 106, No. 3, pp. 270–278.

[2] Department of Mechanical Engineering, The University of Rochester, Rochester, NY 14627.

Copyright © 1984 by ASME

Downloaded 02 Jun 2010 to 171.66.16.91. Redistribution subject to ASME license or copyright; see http://www.asme.org/terms/Terms_Use.cfm

predicted value. The sensitivity of analysis to the variation of the kinematic viscosity and the low values of Re/G are the reasons these authors regarded the errors to be mainly due to factors mentioned in the text.

Experiments on the Buckling of This Fluid Layers Undergoing End-Compression[1]

A. Nachman.[2] Since two of my papers are referred to as references [7] and [8] of this article, I would like to offer the following rebuttal.

There is no connection between the experiments performed by Blake and Bejan and our own analysis of G. I. Taylor's experiment (reference [5] of the article). Taylor floated a thin thread of viscous fluid on a mercury bath and pushed the ends toward each other, causing the thread to deform in the plane of the mercury surface. Blake and Bejan[1] cover an entire rectangular water surface with viscous oil and push two entire opposite edges toward each other, thus causing vertical deformations. Their experiment works against gravity, Taylor's did not. I do not see how one could use data from one experiment to interpret results from the other.

[1] by K. R. Blake and A. Bejan, published in the March 1984 issue of the JOURNAL OF FLUIDS ENGINEERING, Vol. 106, pp. 74-78.

[2] Southwest Research Institute, San Antonio, TX 78284.

Authors' Closure

My apologies to Mr. Nachman who objects to having his work referenced. But to those interested in the universality of an exciting and relatively unknown flow phenomenon, let me stress precisely the point being made. Straight fluid layers and fibers buckle in a unique way (with a characteristic, reproducible, meander wavelength) regardless of whether the buckling plane is normal or parallel to gravity [1, 2]. This is the combined message of our experiments and G. I. Taylor's.

Additional References

1 Bejan, A., *Entropy Generation Through Heat and Fluid Flow*, Wiley, New York, 1982, Chapters 3, 4.

2 Bejan, A., *Convection Heat Transfer*. Wiley, New York, 1984, Chapters 6-8.

Downloaded 02 Jun 2010 to 171.66.16.91. Redistribution subject to ASME license or copyright; see http://www.asme.org/terms/Terms_Use.cfm

predicted value. The sensitivity of analysis to the variation of the kinematic viscosity and the low values of Re/G are the reasons these authors regarded the errors to be mainly due to factors mentioned in the text.

Experiments on the Buckling of This Fluid Layers Undergoing End-Compression[1]

A. Nachman.[2] Since two of my papers are referred to as references [7] and [8] of this article, I would like to offer the following rebuttal.

There is no connection between the experiments performed by Blake and Bejan and our own analysis of G. I. Taylor's experiment (reference [5] of the article). Taylor floated a thin thread of viscous fluid on a mercury bath and pushed the ends toward each other, causing the thread to deform in the plane of the mercury surface. Blake and Bejan[1] cover an entire rectangular water surface with viscous oil and push two entire opposite edges toward each other, thus causing vertical deformations. Their experiment works against gravity, Taylor's did not. I do not see how one could use data from one experiment to interpret results from the other.

[1] by K. R. Blake and A. Bejan, published in the March 1984 issue of the JOURNAL OF FLUIDS ENGINEERING, Vol. 106, pp. 74-78.

[2] Southwest Research Institute, San Antonio, TX 78284.

Authors' Closure

My apologies to Mr. Nachman who objects to having his work referenced. But to those interested in the universality of an exciting and relatively unknown flow phenomenon, let me stress precisely the point being made. Straight fluid layers and fibers buckle in a unique way (with a characteristic, reproducible, meander wavelength) regardless of whether the buckling plane is normal or parallel to gravity [1, 2]. This is the combined message of our experiments and G. I. Taylor's.

Additional References

1 Bejan, A., *Entropy Generation Through Heat and Fluid Flow*, Wiley, New York, 1982, Chapters 3, 4.

2 Bejan, A., *Convection Heat Transfer*. Wiley, New York, 1984, Chapters 6-8.

Downloaded 02 Jun 2010 to 171.66.16.91. Redistribution subject to ASME license or copyright; see http://www.asme.org/terms/Terms_Use.cfm